



Radiative and quantum electrodynamic effects in ultra-relativistic laser-matter interaction

Bertrand Martinez

► To cite this version:

Bertrand Martinez. Radiative and quantum electrodynamic effects in ultra-relativistic laser-matter interaction. Mathematical Physics [math-ph]. Université de Bordeaux, 2018. English. NNT : 2018BORD0442 . tel-02079791

HAL Id: tel-02079791

<https://tel.archives-ouvertes.fr/tel-02079791>

Submitted on 26 Mar 2019

HAL is a multi-disciplinary open access archive for the deposit and dissemination of scientific research documents, whether they are published or not. The documents may come from teaching and research institutions in France or abroad, or from public or private research centers.

L'archive ouverte pluridisciplinaire **HAL**, est destinée au dépôt et à la diffusion de documents scientifiques de niveau recherche, publiés ou non, émanant des établissements d'enseignement et de recherche français ou étrangers, des laboratoires publics ou privés.



THÈSE

Présentée en vue de l'obtention du grade de

DOCTEUR DE L'UNIVERSITÉ DE BORDEAUX

École doctorale Science Physique et de l'Ingénieur
Spécialité : Laser, matière et nanosciences

Réalisée au sein du

COMMISSARIAT À L'ÉNERGIE ATOMIQUE ET AUX ÉNERGIES ALTERNATIVES

En cotutelle avec le laboratoire

CENTRE LASERS INTENSES ET APPLICATIONS

Par **Bertrand MARTINEZ**

Effets radiatifs et quantiques dans l'interaction laser-matière ultra-relativiste

Sous la direction universitaire de Emmanuel d'HUMIÈRES
Et sous la responsabilité CEA de Laurent GREMILLET

Soutenance prévue le 18 décembre 2018 devant le jury composé de :

M. BONNAUD Guy	Université Paris-Saclay	Rapporteur
M. GREMILLET Laurent	CEA/DAM, Bruyères-le-Châtel	Encadrant CEA
M. GRISMAYER Thomas	Université Technique de Lisbonne	Examinateur
M. d'HUMIÈRES Emmanuel	Université de Bordeaux	Directeur de thèse
Mme RICONDA Caterina	Université Paris 6	Rapporteuse
M. TIKHONCHUK Vladimir	Université de Bordeaux	Président

Résumé : Effets radiatifs et d'électrodynamique quantique dans l'interaction laser-matière relativiste

Les futures installations laser multi-pétawatts, tel le projet Apollon (France) permettront d'atteindre des intensités sur cible dépassant 10^{22} W/cm^2 . Dans de telles conditions, l'interaction laser-matière met en jeu des processus plasmas ultra-relativistes couplés à des mécanismes radiatifs et d'électrodynamique quantique (QED). La plupart des études théoriques sur ce sujet ont porté sur l'émission synchrotron et la production de paires électron-positron par le processus de Breit-Wheeler, tous deux induits par un champ laser intense et censés dominer l'interaction à des intensités $> 10^{22} \text{ W/cm}^2$. À de plus faibles intensités ($\lesssim 10^{21} \text{ W/cm}^2$), l'émission de photons et la création de paires procèdent essentiellement du Bremsstrahlung et des processus de Bethe-Heitler/Trident, tous déclenchés sous l'action du champ Coulombien atomique. Cette thèse vise précisément à étudier ces processus à l'aide du code particle-in-cell (PIC) CALDER conçu au CEA/DAM.

Notre première étude permet d'étendre les capacités de simulation du code PIC CALDER à l'ensemble des mécanismes mentionnés ci-dessus. Nous nous intéressons ensuite à la compétition entre le Bremsstrahlung et l'émission synchrotron dans des feuilles de cuivre irradiées par un laser femtoseconde d'intensité 10^{22} W/cm^2 . Finalement, nous explorons le potentiel de cibles composées de nano-fils pour augmenter le rayonnement synchrotron.

Mots-clés : interaction laser-matière, plasma, électrodynamique quantique, Particle-In-Cell, Compton, Breit-Wheeler, Bremsstrahlung, Bethe-Heitler, nano-fils, Apollon.

Abstract: Radiative and quantum electrodynamic effects in relativistic laser-matter interaction

Forthcoming multi-petawatt laser systems, such as the French Apollon, are expected to deliver on-target laser intensities exceeding 10^{22} W/cm^2 . A novel regime of laser-matter interaction will ensue, where ultra-relativistic plasma effects are coupled with copious generation of high-energy photons and electron-positron pairs. In recent years, most theoretical studies performed in this field have focused on the impact of synchrotron photon emission and Breit-Wheeler pair generation, both directly induced by an intense laser field and believed to be dominant at intensities $> 10^{22} \text{ W/cm}^2$. At the lower intensities ($\lesssim 10^{21} \text{ W/cm}^2$) currently attainable, by contrast, photon and pair production mainly originate from, respectively, Bremsstrahlung and Bethe-Heitler/Trident processes, all triggered by atomic Coulomb fields. The purpose of this PhD is precisely to study those processes using the particle-in-cell CALDER code developed at CEA/DAM.

Our first study extends the simulation capabilities of CALDER to the whole range of photon and positron generation mechanisms aforementioned. We then address the competition between Bremsstrahlung and synchrotron emission from copper foils irradiated at 10^{22} W/cm^2 . Finally, we investigate the potential of nanowire-array targets to enhance the synchrotron yield of a 10^{22} W/cm^2 femtosecond laser pulse.

keywords: laser-matter interaction, plasma, quantum electrodynamics, Particle-In-Cell, Compton, Breit-Wheeler, Bremsstrahlung, Bethe-Heitler, nanowires, Apollon.

CEA, DAM, DIF, F-91297, Arpajon, France

CELIA, UMR 5107, Université de Bordeaux-CNRS-CEA, 33405, Talence, France

Acknowledgement

I wish to thank the people who gave me the opportunity to benefit from a thesis scholarship at CEA: Catherine Cherfils who funded it, Luc Bergé who first got in contact with me and Laurent Gremillet who accepted to supervise me.

I would especially like to thank my two supervisors: Laurent Gremillet and Emmanuel d'Humières.

Three years ago, Laurent gave me his trust to accomplish this PhD despite I only had a poor knowledge of plasma physics. He has shown patience teaching me key concepts of physics as well as proofreading scientific documents, which is a valuable quality for a supervisor. I keep a good memory of all the different conferences, in France and abroad, I took part in thanks to him, especially those in the mountains. In addition, I am grateful he is personally involved in order to help me continue my career in research.

Emmanuel regularly supervised me despite the distance. While he provided good advice on a scientific point of view, he also helped me to wisely manage my time. Among other things, he encouraged me to take a step back on my work and he introduced me to many researchers in conferences and at the CELIA laboratory. I enjoyed meeting new people which helped me to be more open-minded but, above all, to start developing a professional network.

My thanks go to the researchers I met and had fruitful discussion with. I am thinking of Yasuhiko Sentoku and Ryan Royle who welcomed me at the National Terawatt Facility and for our debates on radiative processes in particle-in-cell codes. It was also enriching to talk about gamma-ray sources with Xavier Ribeyre. I would like to address a special thanks to the jury members: Guy Bonnaud, Thomas Grismayer, Caterina Riconda and Vladimir Tikhonchuk who dedicated time to check my manuscript and comment it. I finally thank Roland Duclous for our discussions on the Bremsstrahlung process.

I would like to thank the people I worked with during three years at the CEA as I will keep many good memories from them. Mathieu who helped me to settle in well with the laboratory, Pedro who made me taste the original paella recipe, Simon for all the time we spent together, Antoine for the good experience we had at the winter school in Montgenèvre, Gaëtan who gave good tips on movies and brought many answers to my questions about (meta)physics, Jérémie with whom I shared my office as much as my mood swings, Pierre-Louis for our tea breaks, Alizée and Vivien who wrote their manuscript at the same time as me, Serge for his communicative sense of humor and for driving me back home sometimes, Arno for the nice time we spent together in Prague at the EPS conference, Xavier V. who gave me a lot of advice on post-doc research, Manuel, Mickaël, Charles, Arnaud for their invitations to have a drink, Fabien who worked on the same topic as mine, Xavier D. who was always available and provided a valuable help on how to use Calder, Jean-Etienne who regularly asked news, Benoit who is always ready to talk about ecology and the end of the world, Didier for his very pedagogical introduction to Hamiltonian dynamics. I wish also to thank Sylvie, Brigitte, Florian, Luc and Laurence who answered many of my interrogations on administrative procedures.

I also thank Quentin, Corentin, Maxime, Alessandro, Léo, Julien, Jonathan and Simon that I met at the CELIA laboratory. They made me discover quite nice restaurants and bars in Bordeaux and we had a great time during conferences.

I thank Narayan who is always motivated to go out for a drink and talk, Antoine who went through the same moments of success and doubts before me, Pascal who often went swimming and running with me, David, Alexandre, Baptiste, Olivier for all the good moments and holidays we shared that helped me to stay on track, especially during the

redaction of my manuscript.

I would like to thank my family: my mother, my aunt, my father, my brother, my sister and my cousin as they all support my career choice and are always available for me. In particular, I wish to thank my grandmother who passed away before I finished my PhD.

I address special thanks to my girlfriend, Athénaïs, who unconditionally provided support during my PhD. While I went through tough times, the numerous week-ends we spent together outside Paris helped me to carry on. Amongst other things, she revived my interest for comics, for french pop music, for cooking and travelling.

Contents

Résumé français	9
Introduction	13
Scientific context	13
Plasmas physics	13
Concise history of lasers	13
State of the art and forthcoming laser facilities	14
Radiative and Quantum Electrodynamics (QED) processes	15
Goal and plan of the thesis	16
I Theory and implementation of radiative and QED processes	19
1 Particle-in-cell method	21
1.1 Introduction	21
1.2 Interpolation steps	22
1.3 Resolution of Maxwell's equations	24
1.3.1 Explicit method from K. Yee	24
1.3.2 Improved resolution of Maxwell's equations	26
1.4 Resolution of particles' motion	27
1.5 Non-conservation of charge during interpolation	28
1.6 Photon transport for PIC codes	29
1.6.1 Radiative transport equation in the PIC framework	30
1.6.2 Monte Carlo scheme for elastic and inelastic processes	31
2 Processes induced in an electromagnetic field	35
2.1 Radiation of photons by nonlinear inverse Compton scattering	35
2.1.1 Physical model	36
2.1.2 Continuous radiation loss	41
2.1.3 Implementation of the continuous model	42
2.1.4 Implementation of the discontinuous model	43
2.2 Pair creation by the nonlinear Breit-Wheeler process	44
2.2.1 Physical Model	44
2.2.2 Monte Carlo implementation in the PIC code CALDER	46
2.3 Pair creation by the electromagnetic Trident process	46
3 Processes induced in a Coulomb atomic field	49
3.1 Elastic scattering	51
3.1.1 Nanbu's theory for Debye's screening	51

3.1.2	Description of bound electron screening	53
3.1.3	Monte Carlo implementation	57
3.1.4	Numerical tests with arbitrary ionized atoms	58
3.2	Impact ionization	60
3.2.1	Model for impact ionization	60
3.2.2	Monte Carlo implementation	61
3.2.3	Calculation of the electron collisional stopping power	62
3.3	Bremsstrahlung emission of photons	63
3.3.1	Cross-sections accounting for free and bound electron screening . . .	63
3.3.2	Implementation of Bremsstrahlung emission	72
3.3.3	Validation of the simulated electron radiative stopping power	74
3.4	Bethe-Heitler pair creation	75
3.4.1	Cross-sections accounting for free and bound electron screening . . .	75
3.4.2	Implementation of the Bethe-Heitler pair creation	76
3.5	Coulomb-Trident pair creation	78
3.5.1	Non-screened cross-sections	78
3.5.2	Implementation of the Coulomb-Trident pair creation	81
3.6	Application to fast electron relaxation in a solid target	82
3.6.1	Theoretical 0D model on positron creation	82
3.6.2	Self-consistent Particle-In-Cell simulations	86
II	Radiative processes induced by laser solid interaction	91
4	High-energy radiation in ultra-relativistic laser-solid interactions	93
4.1	Fundamentals of relativistic laser-plasma interaction	95
4.1.1	Dynamics of a single electron in an intense electromagnetic field . .	95
4.1.2	Relativistic self-induced transparency	96
4.1.3	Fast electron generation in undercritical plasmas	98
4.1.4	Fast electron generation in overcritical plasmas	99
4.1.5	Ion acceleration in overcritical plasmas	102
4.2	Laser-induced synchrotron radiation in uniform plasmas of varying density	107
4.2.1	Synchrotron emission in relativistically undercritical plasmas . . .	108
4.2.2	Synchrotron emission in overcritical plasmas	113
4.2.3	Conclusions	118
4.3	Competition between Bremsstrahlung and Synchrotron radiation in foils of varying thickness	120
4.3.1	Numerical setup	120
4.3.2	Target thickness dependence of the radiation yield	121
4.3.3	Influence of the target dynamics on the radiation processes	122
4.3.4	Opaque targets	129
4.3.5	Target thickness dependence of the radiation spectra	134
4.3.6	Conclusions	137
5	Improving the synchrotron process efficiency with nanowire arrays	139
5.1	Preliminary investigation of electron heating	141
5.1.1	2D PIC simulation setup	141
5.1.2	Evidence of different electron heating mechanisms with nanowires .	142
5.1.3	Dependence of electron heating on the nanowire parameters	146
5.2	Identification of the main synchrotron radiation regimes	148

5.3	Variations of the synchrotron yield with the nanowire parameters	153
5.3.1	Variation of the interwire spacing: from forward to backward directed radiation	153
5.3.2	Variation of the wire width: from RESE to SDE, through TOEE . .	155
5.3.3	Changing the ion mass and the laser intensity	158
5.3.4	Comparison with uniform-density targets	160
5.4	Extension to more realistic setups	162
5.4.1	Radiation enhancement by a reflective substrate	162
5.4.2	Effect of a finite focal spot and an oblique incidence angle	164
5.5	Ion acceleration in nanowire arrays	166
5.5.1	Numerical setup and optimized regime for flat targets	167
5.5.2	Substrate length dependence of ion acceleration	172
5.5.3	Nanowire length dependence of ion acceleration	176
5.5.4	Comparison of nanowire-foil and foam-foil targets	177
Conclusions and perspectives		183
Conclusions	183	
Perspectives	185	
Appendices		187
A Laser normalisation		189
B Screening angle in the limit of weak and strong ionization		191
B.1	Particular case of a single exponential potential	191
B.2	Generalisation to a double exponential potential	192
C List of communications		195
C.1	First author articles in peer-reviewed journals	195
C.2	Oral presentations	195
C.3	Poster presentations	196

CONTENTS

Résumé français

Contexte scientifique

Les futures installations laser multi-pétawatts, tels les projets Apollon (France) et Extreme Light Infrastructure (République Tchèque, Hongrie, Roumanie), permettront d'atteindre des intensités sur cible dépassant 10^{22} W/cm^2 . Dans de telles conditions, l'interaction laser-matière met en jeu des processus plasmas ultra-relativistes couplés à des mécanismes radiatifs et d'électrodynamique quantique (QED). Ce nouveau régime d'interaction laisse présager de nombreuses applications transdisciplinaires en recherche fondamentale et appliquée, incluant le développement de sources compactes et ultra-intenses de particules énergétiques, la reproduction de phénomènes astrophysiques relativistes ou des tests expérimentaux de divers aspects de la QED.

La plupart des études théoriques sur ce sujet ont porté sur l'impact de l'émission synchrotron et de la production de paires électron-positron par le processus de Breit-Wheeler, tous deux induits par le champ laser et censés dominer l'interaction à des intensités $> 10^{22} \text{ W/cm}^2$ (voir Fig. 6). À de plus faibles intensités ($\lesssim 10^{21} \text{ W/cm}^2$), l'émission de photons et la création de paires procèdent essentiellement du Bremsstrahlung et des processus de Bethe-Heitler/Trident, tous déclenchés sous l'action du champ coulombien atomique. La transition entre ces différents régimes a toutefois été peu explorée, notamment au moyen de simulations cinétiques intégrées. Cette thèse vise précisément à étudier les processus mentionnés ci-dessus dans divers scénarios d'interaction laser-plasma relativiste. Ce travail a été réalisé à l'aide du code particle-in-cell (PIC) CALDER conçu au CEA/DAM, qui, au début de ce travail, modélisait déjà les mécanismes synchrotron et Breit-Wheeler.

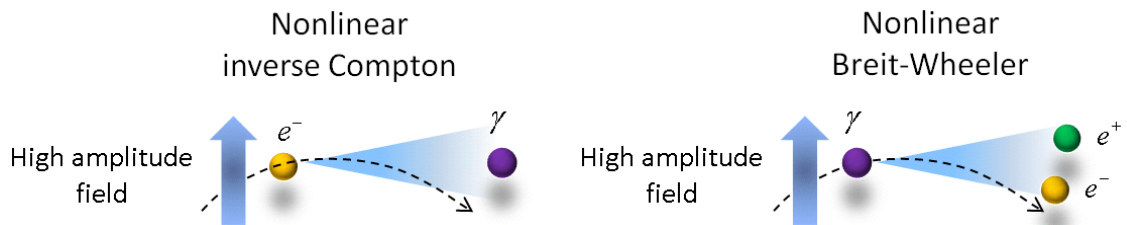


Figure 1: Processus radiatif de Compton inverse nonlinéaire (ou synchrotron) et création de paire électron-positron (e^-e^+) par effet Breit-Wheeler nonlinéaire. Ces deux effets sont induits dans un champ de forte amplitude.

Processus induits dans un champ coulombien atomique

La première étude a pour but d'étendre les capacités de simulation du code PIC aux mécanismes induits dans un champ coulombien. Plusieurs processus sont étudiés dans le cadre de cette thèse : les déflections angulaires élastiques, la génération de photons par Bremsstrahlung et de positrons par Bethe-Heitler/Trident. Ils sont schématiquement représentés sur la Fig. 2.

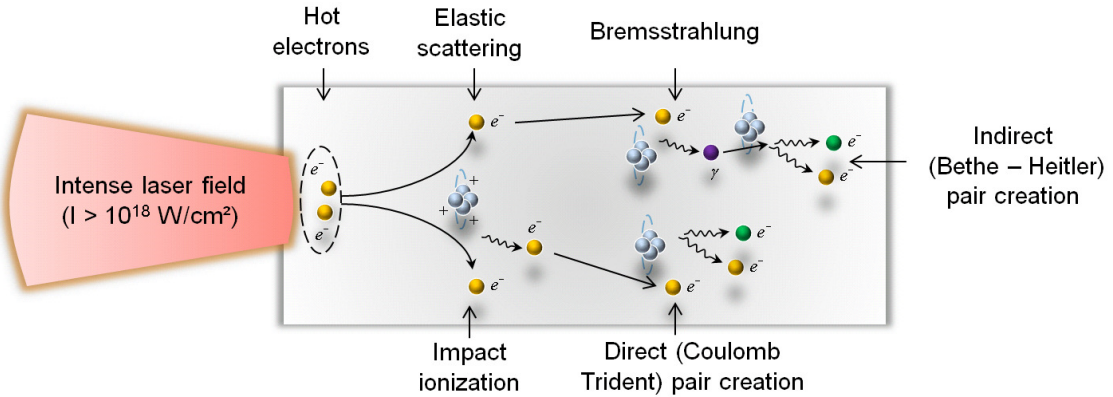


Figure 2: L’interaction d’un laser intense avec la matière génère des électrons rapides, qui peuvent subir divers processus induits lors de leur interaction avec un champ coulombien atomique.

Dans le Chap. 3, les sections efficaces des processus Bremsstrahlung (émission de photons) et Bethe-Heitler (création de paires électron-positron) sont dérivées par des méthodes classiques afin de tenir compte des variations de l’écrantage électronique selon le degré d’ionisation du milieu traversé par les électrons et les photons. L’implémentation des déflections angulaires est revue par des arguments heuristiques afin de prendre en compte ces effets d’écrantage lors des déflections électron-ion. De nouveaux modules associés à la création de photon et de paires ont été implémenté dans le code PIC CALDER et celui traitant des déflections angulaires a été mis à jour. Forte de ces implémentations, la partie Monte Carlo du code peut désormais reproduire le pouvoir d’arrêt d’électrons dans les solides, sur une large gamme d’énergies allant de 10 keV à 1 GeV.

Après cette étape de validation, nous avons mené une étude numérique de la génération de positrons par Bremsstrahlung / Bethe-Heitler et Trident lors du transport d’électrons relativistes dans une cible de cuivre. Comparées à un modèle théorique, nos simulations mettent en lumière l’impact des transferts d’énergie entre électrons et ions (via l’accélération de ceux-ci) sur la création de paires dans des cibles fines (5 – 15 μm). Pour les cibles les plus fines (5 μm), l’énergie perdue par les électrons au profit des ions devient non-négligeable et limite alors la production de positrons. Le modèle théorique 0D auquel sont confrontés nos résultats (Myatt *et al.*, 2009) ne propose pas cette vision auto-consistante de l’accélération d’ions et surestime donc la création de positrons.

Rayonnement de haute énergie dans l'interaction laser-matière relativiste

Nous nous intéressons ensuite à la compétition entre deux processus permettant de générer des photons de haute énergie lors de l'interaction laser-matière relativiste : le Bremsstrahlung et l'émission synchrotron. L'objectif consiste à caractériser leur efficacité relative, ainsi que leur propriétés spectrales, dans des feuilles de cuivre irradiées par un laser femtoseconde d'intensité 10^{22} W/cm^2 . Cette étude est motivée par le manque de résultats

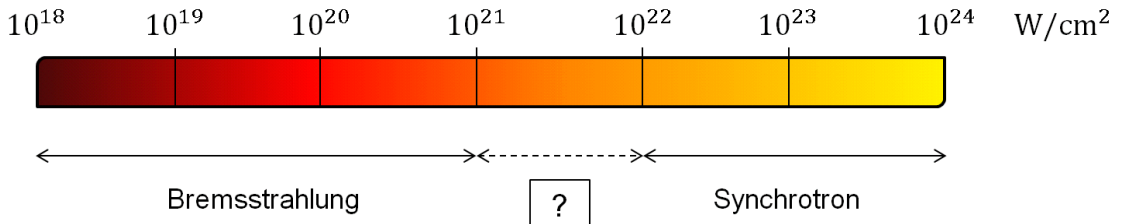


Figure 3: Compétition entre les processus de Bremsstrahlung et d'émission synchrotron lors de l'interaction laser-matière. L'intensité du laser varie de 10^{18} à 10^{24} W/cm^2 .

théoriques sur le sujet et l'anticipation des expériences sur les futures installations lasers.

Le Bremsstrahlung est bien caractérisé et observé régulièrement de façon expérimentale pour l'interaction laser-solide, notamment pour des matériaux de Z élevés et d'épaisseur de l'ordre de quelques mm. Il permet de générer des photons dont l'énergie est de l'ordre de quelques dizaines de MeV pour des intensités laser de l'ordre de $10^{20-21} \text{ W/cm}^2$. L'obtention de telles énergies photoniques via l'émission synchrotron stimulée par laser n'a été que très peu observée ([Poder et al., 2018](#); [Cole et al., 2018](#)), et uniquement lors de l'interaction laser-faisceau d'électron et non lors de l'interaction laser-solide. A l'aide de codes numériques particle-in-cell, largement exploités pour simuler l'interaction laser-matière relativiste, l'influence de l'intensité laser ([Pandit and Sentoku, 2012](#)) et du matériau ([Wan et al., 2017](#)) sur la compétition entre les deux processus radiatifs ont été mis en évidence. Il n'existe cependant pas de résultat clair sur l'impact d'une variation de l'épaisseur du matériau irradié par le laser. Nous étudions précisément cette question dans le Chap. 4.

Nous introduisons d'abord les bases de l'interaction laser-matière ultra-relativiste, en présentant les concepts de transparence induite, de génération d'électrons rapides et d'accélération d'ions. Nous abordons ensuite un problème simplifié, constitué de l'interaction d'un laser uniforme avec un plasma de densité uniforme (soit transparent soit opaque au laser). Un des points notables est que dans le cas d'un plasma transparent, nous mettons en évidence le processus plasma qui est à l'origine de l'émission synchrotron. Celui-ci se démarque notamment du résultat plus partiel et simplifié précédemment avancé par [Brady et al. \(2012\)](#). Enfin, nous examinons le scénario plus réaliste de l'interaction d'un laser court (femtoseconde) avec une feuille de cuivre dont l'épaisseur varie de $\sim 10 \text{ nm}$ à $\sim 10 \mu\text{m}$. La production de photons s'avère maximale dans des cibles de quelques dizaines de nanomètres devenant transparentes, par effet relativiste et expansion ultra-rapide, durant l'impulsion laser, et est alors imputable à l'émission synchrotron. Le Bremsstrahlung gagne en importance avec l'épaisseur de la cible, jusqu'à prendre le pas sur l'émission synchrotron au-delà de $2 \mu\text{m}$. Les propriétés spectrales des deux mécanismes sont analysées en détail et corrélées à l'évolution ultra-rapide de la cible.

Améliorer l'efficacité de l'émission synchrotron avec des réseaux de nanofils

Finalement, nous explorons le potentiel de cibles composées de nano-fils pour augmenter le rayonnement synchrotron produit lors de l'interaction laser-matière. L'objectif est de mettre en avant un potentiel schéma expérimental pour la première observation expérimentale du rayonnement synchrotron déclenché par interaction laser-solide relativiste.

Ce type de structure est déjà employée lors d'expériences d'interaction laser-matière relativiste comme illustré sur la Fig. 4 ([Jiang et al., 2016](#)). Cette nanostructure a été irradiée par un laser d'intensité 10^{21} W/cm^2 afin d'accélérer des électrons à des énergies relativistes $\sim 15 \text{ MeV}$. A des intensités plus modérées ($I = 10^{17} - 10^{20} \text{ W/cm}^2$) des

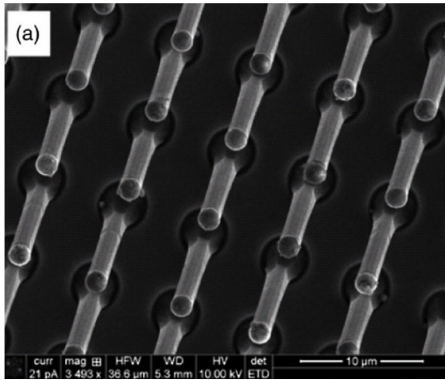


Figure 4: Exemple d'un réseau de nano-fils fabriqué pour une expérience d'interaction laser-matière relativiste (image de [Jiang et al. \(2016\)](#)).

expériences d'accélération d'ion ([Khaghani et al., 2017](#)), de radiographie X ([Samsonova et al., 2017](#)), ou de génération de hautes densités d'énergies ([Purvis et al., 2013](#)) ont déjà été réalisées à l'aide de réseaux de nano-fils.

Au cours du Chap. 5, nous envisageons le potentiel des réseaux de nano-fils dans le cadre des expériences de court et long terme, lors desquelles les intensités laser seront de l'ordre de $I = 10^{21}-10^{23} \text{ W/cm}^2$. Nous mettons en valeur plusieurs mécanismes de génération d'électrons rapides qui dépendent des paramètres du réseau tels que l'espacement des fils, leur diamètre ou leur matériau. Plusieurs régimes de rayonnement synchrotron sont mis en évidence selon ces mêmes grandeurs et en fonction du temps. Une étude paramétrique met en exergue la géométrie la plus efficace, s'illustrant, pour une intensité de 10^{22} W/cm^2 , par un taux de conversion radiatif de 10%. Cette configuration conduit à une détente rapide des nano-fils, produisant un plasma quasi uniforme et transparent à l'essentiel de l'impulsion laser. En outre, nous montrons que si des cibles uniformes de faible densité reproduisent les performances optimales des nano-fils pour des densités moyennes $\leq 5 \times 10^{22} / \text{cm}^3$, ceux-ci assurent un rayonnement élevé pour des densités supérieures à $5 \times 10^{22} / \text{cm}^3$. La robustesse de ce résultat est confirmée par la simulation d'un profil laser réaliste, présentant un profil transverse Gaussien et un angle d'incidence de 30° . Enfin, nous proposons une étude préliminaire d'accélération de protons lors de l'interaction d'un laser avec des nano-fils. Après un rappel des mécanismes d'accélération pour des cibles planes, celle-ci s'illustre par une mise en valeur de l'impact d'une variation de l'épaisseur du substrat et de la longueur des fils sur l'énergie maximale des protons.

Introduction

Scientific context

Plasmas physics

Plasma is the prevailing state of matter in the universe, exceeding in proportion the three other well-known solid, liquid and gaseous states. It is formed when matter is heated or compressed enough to ionize atoms, providing a bath of charged particles which dynamics is ruled by electromagnetic interactions. Stars are the first plasma one can think of. The core temperature of our sun is estimated to be 1.5 keV and is maintained by the continuous fusion of hydrogen isotopes. Other types of plasmas can be found in the magnetosphere surrounding the planet (at a few Earth radius altitude) or in the ionosphere (between 60 and 1000 km of altitude). On a daily basis, partially ionized plasmas are employed in discharge lamps to provide lights of different wavelengths (e.g. neon lamps).

Concise history of lasers

Lasers find many applications in our day to day life. For instance we routinely use them while we print documents, watch a movie, listen to music or as we scan barcodes at the supermarket. To emphasize their generalisation in our lives, one may think of the beauty sector where salons offer laser-assisted permanent hair or tattoo removal. However the main applications of lasers are industry or medicine. In industry they are operated to weld or cut materials. In the medical field they are daily employed for eye surgery, to treat some skin diseases, to fasten wound healing and even for periodontic disorders. One of their most striking features is their ability to estimate distances with an unprecedented accuracy, providing efficient tools for metrology.

Lasers consist in a powerful monochromatic light source. They rely on the fundamental mechanism of stimulated emission. During this process an excited atomic electron loses some energy as a result of its interaction with a photon of specific wavelength. The energy loss is radiated as a new photon which phase, wavelength and direction are identical to the initial photon. This process is maintained long enough in a gain medium located between two mirrors. The radiation emitted is therefore confined, amplified and eventually released, forming a laser beam. As an example, one of the first experimental realisation based on this principle was done almost 60 years ago by [Maiman \(1960\)](#). It consisted in a flash lamp providing photons of particular wavelength 5500Å, illuminating a 1 cm ruby cristal coated with two layers of silver. The output light consisted in a bi-chromatic laser of wavelengths 6929Å and 6943Å.

Further improvements were suggested over time to increase the energy and the power available in the laser beam. Only the most relevant are reported and briefly recalled in chronological order. The first one is the introduction by [Hellwarth \(1961\)](#) of switchs that can modify the quality factor Q of the amplification, known as Q-switchs. With

this process, a Pockels cell lowers the amplification during a certain time and enables to accumulate photons which are all suddenly delivered, bringing the possibility to generate short and pulsed laser beams. The second enhancement that can be noticed is mode locking as demonstrated by [Mocker and Collins \(1965\)](#). It permits to add the amplitude of all waves of the cavity (i.e. to get photons in phase) and therefore to both amplify and shorten the duration of the laser beam. This may be done, in particular, by changing the cavity length and be coupling with Q-switches.

One of the most significant evolution for intense lasers is Chirped Pulse Amplification (CPA) brought by [Strickland and Mourou \(1985\)](#), recently awarded by a Nobel Prize ([The Nobel Prize in Physics, 2018](#)). It is directly inspired from radar technology and is of particular interest to increase the intensity of a laser beam. Indeed the amplification in laser cavities is limited to a higher threshold over which adverse processes are induced. The principle of this technology relies on the following steps: the beam is temporally stretched, then amplified by several orders of magnitude, and is finally compressed back. The amplification exploits a serie of gratings or optical components which have the property to disperse light depending of its wavelength. The growth of the laser intensity thanks to the developement of CPA is substantial since it raised by five or six orders of magnitudes since 1985 (see Fig. 5). The final step toward achieving higher intensities is the Optical Parametric CPA (OPCPA). The process takes advantage of non-linear optical crystals which turn an input wave into two output waves that are phase-matched. Under the right conditions, the amplification is simplified as fewer passes are needed than the usual CPA technique. It is currently implemented at state-of-the-art laser facilities around the world indicating seemingly good prospects to improve available laser intensities. Some of those projects are recalled in the following subsection.

State of the art and forthcoming laser facilities

In the frame of this PhD, we are particularly interested in laser systems capable to deliver high powers ($\gtrsim 1 \text{ PW}$). In practice, such lasers are based on the CPA technology, with either Titanium Sapphire or Neodymium gain medium. They can also be formed using the OPCPA technique and cristals with non-linear optical properties (DKDP crystals). Laser systems reaching a power of 1 PW or higher are usually divided into two groups: high-energy and high power lasers.

The first group is made of lasers delivering 0.5 to 10 kJ in 0.5 to 10 ps. They are usually coupled to ns-TW-class lasers and employed for heating or backlighting in experiments related to Inertial Confinement Fusion (ICF). One can first think of the [ARC](#) laser which is exploited with the 192 [NIF](#) beams (1.8 MJ), and the [PETAL](#) laser, dedicated to realize diagnostics of experiments at the [LMJ](#) facility. Some of the beams of the [VULCAN](#) and [ORION](#) lasers can supply 0.5 kJ in 0.5 ps. One can also cite the [OMEGA-EP](#) and [LFEX](#) lasers ([Azechi et al., 2009](#)) who can both deliver 1 kJ in 1 ps. After the energy of those lasers is temporally compressed and spatially focused, it reaches on-target peak-intensities in the range $10^{18-20} \text{ W/cm}^2$.

The second group is made of lasers delivering less energy (20 to 40 J) but in a much shorter time (20 to 40 fs). To name a few, there is the [VEGA](#) laser (30 J delivered in 30 fs), the [BELL](#) laser (40 J delivered in 30 fs), the CoRels/GIST project (83 J delivered in 19.4 fs) ([Sung et al., 2017](#)), and the CAEP project (91.1 J delivered in 18.6 fs) ([Zeng et al., 2017](#)). The current record of 4.9 PW is hold by this latter Chinese laboratory. The maximum intensity reached, after spatial focussing of those lasers can be of the order of 10^{21} W/cm^2 and may reach 10^{22} W/cm^2 in short and mid-term experiments.

In the long term ($\simeq 5$ years), lasers reaching the 10 PW level are planned in different

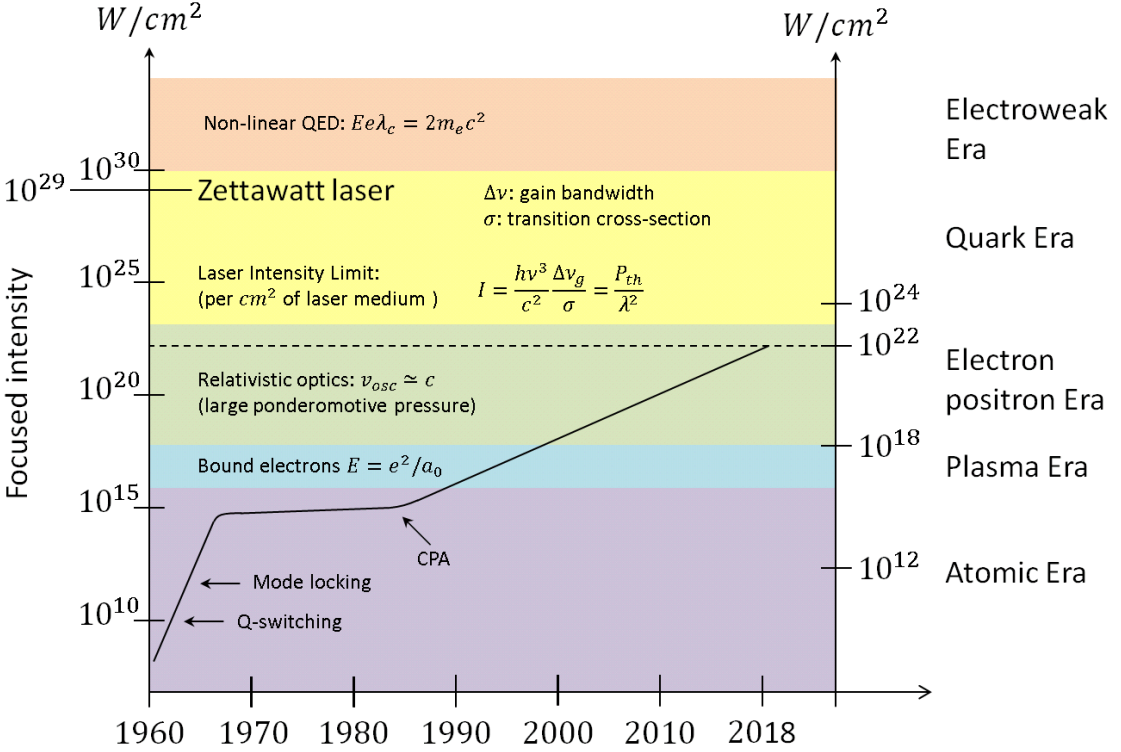


Figure 5: Evolution of the laser intensity available in laboratory since 1960. Image from ([Mourou et al., 2006](#)).

countries. Such power can be delivered by diminishing the laser duration to a few laser cycles, e.g. in France with the [APOLLON](#) laser aiming to deliver $\simeq 150$ J in $\simeq 15$ fs. Two laser systems with similar characteristics will also be developed and coherently added up in the framework of the [ELI-NP](#) project in Romania, enabling to reach a power as high as 20 PW power. In the United Kingdom an upgrade of the [VULCAN](#) laser is expected to deliver $\simeq 400$ J of energy in $\simeq 20$ fs, providing a single pulse of 20 PW. In order to manufacture a 10 PW laser system, it is also possible to rise the pulse energy. For example, the [ELI-BL](#) project, under development in Czech Republic, proposes to employ a pulse of $\simeq 130$ fs duration along with 1.3 kJ of energy. In the longer term ($\simeq 5 - 20$ years), the 100 PW level is expected to be reached by combining several 10 PW laser beams with the second step of the [ELI-BL](#) project or with the [XCELS](#) projects hosted in Russia.

Radiative and Quantum Electrodynamics (QED) processes

The recent advances achieved in terms of peak laser intensity in a growing number of laboratories has motivated theoretical and numerical studies involving laser intensities $\geq 10^{22} W/cm^2$. In particular, the production of γ -rays by the laser-induced synchrotron emission process and the electron-positron (e^-e^+) pair creation by the Breit-Wheeler process were shown to have a strong interplay with collective plasma processes. These two mechanisms are presented in Fig. 6. The synchrotron-like mechanism occurs for relativistic electrons which are accelerated by the strong laser field and therefore radiates high-energy photons (Fig. 6(a)). The Breit-Wheeler process is induced by the decay of γ -rays into e^-e^+ pairs as they travel in the strong laser field provided their energy is higher than twice the electron rest-mass energy (Fig. 6(b)). As these two processes are mediated

by the strong electromagnetic field of the laser pulse, they saturate on the pulse duration time-scale. Their numerical simulation is therefore computationally affordable for state-of-the-art super computers. Fig. 6(c) represents the electromagnetic Trident process during which an electron-positron pair is directly emitted by a relativistic electron. This latter process is less studied than the Breit-Wheeler mechanism in the literature as it is of lower efficiency. Among applications one can think of the study of quantum radiation reaction on laser-driven electrons (Blackburn *et al.*, 2014; Ji *et al.*, 2014b; Wang *et al.*, 2015b; Cole *et al.*, 2018; Poder *et al.*, 2018), the massive production of electron-positron pairs through the Breit-Wheeler process (Bell and Kirk, 2008; Nerush *et al.*, 2011; Ridgers *et al.*, 2012; Ji *et al.*, 2014c; Zhu *et al.*, 2016; Grismayer *et al.*, 2017; Jirka *et al.*, 2017), relativistic laboratory astrophysics (Liang, 2013; Chen *et al.*, 2015; Lobet *et al.*, 2015) and radiation pressure ion acceleration (Naumova *et al.*, 2009; Bulanov *et al.*, 2010; Tamburini *et al.*, 2012).

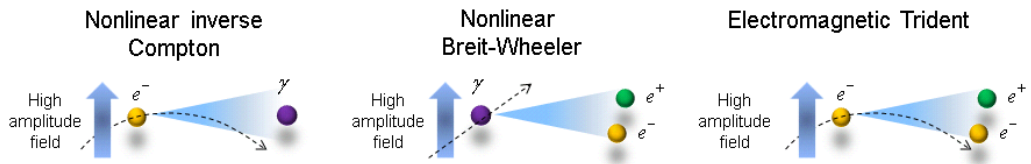


Figure 6: Nonlinear Inverse Compton (or synchrotron-like) radiative process, nonlinear Breit-Wheeler and electromagnetic Trident electron-positron ($e^- e^+$) pair creation mechanisms. All are mediated by a high amplitude field.

In practice, laser systems operate with on-target intensities of the order of 10^{19} - 10^{21} W/cm^2 . The major radiative process for this range of intensities is the Bremsstrahlung and the main $e^- e^+$ pair production mechanisms are the Bethe-Heitler and the Coulomb Trident. Contrary to synchrotron, Breit-Wheeler and electromagnetic Trident, they are mediated by the Coulomb field of atoms (see Fig. 7). A significant number of experiments involving the emission of γ -rays by the Bremsstrahlung process were conducted. Potential applications range from radiography of ultra-fast phenomena (Kmetec *et al.*, 1992; Schnürer *et al.*, 1995; Perry *et al.*, 1999; Cowan *et al.*, 2000; Santala *et al.*, 2000; Ledingham *et al.*, 2000; Glinec *et al.*, 2005; Galy *et al.*, 2007; Chen *et al.*, 2009; Westover *et al.*, 2010; Compant La Fontaine *et al.*, 2012; Courtois *et al.*, 2013) to the generation of $e^- e^+$ jets as the γ -rays interact with heavy ions (Cowan *et al.*, 1999; Gahn *et al.*, 2000; Chen *et al.*, 2009). The reproduction of laboratory-scaled astrophysical scenarios has motivated the experimental realisation of quasi-neutral $e^- e^+$ jets of record density ($10^{16} / \text{cm}^3$) employing mm-sized high- Z targets. The Bethe-Heitler process can be triggered either by direct irradiation of the material sample (Chen *et al.*, 2009, 2010; Chen *et al.*, 2015; Liang *et al.*, 2015), or by wakefield-driven electron beams originating from a laser-irradiated gas jet (Sarri *et al.*, 2013, 2015; Xu *et al.*, 2016). The quasi-neutrality of the $e^- e^+$ plasma produced is ensured by the second method, while the ratio of positrons to electrons is only 50% with the first one.

Goal and plan of the thesis

The main goal of this PhD consists in studying laser-matter interaction in the multi-PW regime which will involve the radiative and QED processes mentioned above. The simulation code employed is the Particle-In-Cell (PIC) code CALDER developed at CEA which was recently updated with modules accounting for the processes induced in a strong

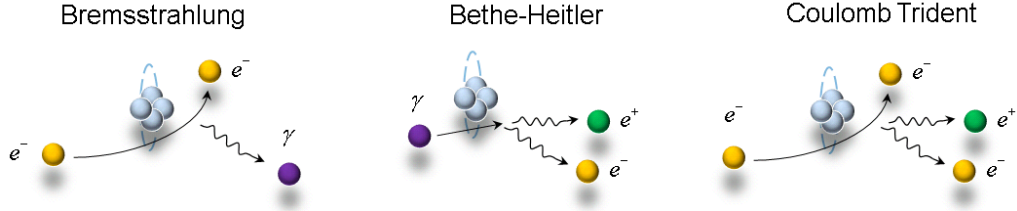


Figure 7: Bremsstrahlung radiative process, Bethe-Heitler and Coulomb Trident electron-positron (e^-e^+) pair creation mechanism. All are mediated by a Coulomb atomic field.

electromagnetic field (Lobet, 2015) (see Fig. 6). This work is presented through five chapters which are summarized below.

The first chapter of this manuscript is a state of the art of PIC codes. It recalls the essential numerical methods exploited in Particle-In-Cell codes and provides insights on the key steps of its time loop. Extensions of the PIC method, enabling to describe radiative and QED effects are also put forward.

The second chapter is a state of the art of the emission processes that can be triggered in a strong electromagnetic field. The modeling of the synchrotron and Breit-Wheeler processes is illustrated and their implementation in the PIC framework is recalled. In particular, the differences arising between the classical and quantum formula accounting for the synchrotron emission rate are underlined.

The third chapter aims to extend the simulation capabilities of PIC codes to all photon and positron generation mechanisms induced during relativistic laser-plasma interactions. Several processes triggered in an atomic Coulomb field are presented: elastic scattering, impact ionization, Bremsstrahlung, Bethe-Heitler as well as Coulomb Trident (direct emission of an e^-e^+ pair by a relativistic electron). For each mechanism, we give theoretical cross-sections and then describe their implementation in the PIC code CALDER. The cross-sections of elastic scattering, Bremsstrahlung and Bethe-Heitler are determined by taking into account the effects of electronic shielding in an arbitrarily ionized plasma. After validation on test cases, an analysis of the generation of photons and positrons during the transport of relativistic electrons in a thin copper foil is proposed. The legitimacy of these simulations is confirmed by a comparison with a theoretical model.

The fourth chapter focuses on the competition between Bremsstrahlung and synchrotron emission during relativistic laser-solid interaction. It is motivated by the lack of theoretical results concerning the competition between Bremsstrahlung and synchrotron radiation. Firstly, basics of relativistic laser-plasma interaction are recalled, especially fast electron generation and ion acceleration mechanisms. Secondly, the synchrotron process is characterized in a simple scenario where a laser interacts with uniform density plasmas of various densities. Thirdly, Bremsstrahlung and synchrotron prevailing regimes are inferred from 1D and 2D PIC simulations. In particular, it is demonstrated that the two processes can be of comparable efficiency for a thin foil (one micron) of average atomic number ($Z = 29$) stimulated by a laser of 10^{22} W/cm^2 intensity.

The fifth chapter is devoted to the interaction of an intense laser with nanowires. The aim is to understand how the effectiveness of synchrotron radiation can be altered, or even amplified, by the unique properties of such a plasma. A parametric study is conducted using PIC simulations. It highlights an optimal nanowire array geometry, allowing to convert up to 10% (resp. 6%) of the laser energy into photons with an energy greater than 10 keV (resp. 1 MeV) for an average plasma density $n_{e,av}/n_c \simeq 15 - 20$. A comparison of the synchrotron efficiency between nanowires and plasmas of uniform sub-solid density

is also proposed. Its outcome is that for low average densities ($n_e/n_c \leq 50n_c$) both kind of targets are equally efficient, whereas for higher average densities ($n_e/n_c \geq 50n_c$), nanowires are better. The high radiation yield of 10% achieved is confirmed by simulations in a more realistic scenario where the laser has a finite focal spot of $10\text{ }\mu\text{m}$ FWHM and a moderate incidence angle of 30° . The perspective to accelerate protons from a nanowire array is also considered in the last part of this chapter. PIC simulations were run in order to understand how the nanowire array structure can alter the classical ion acceleration mechanisms known for solid thin foils.

Part I

Theory and implementation of radiative and QED processes

Chapter 1

Particle-in-cell method

1.1 Introduction

A Particle-In-Cell code coherently simulates the evolution of a distribution of charged particles. It solves first principle equations that are presented below. The particles are differentiated depending on their species, denoted by α . Each species of particle is characterized by its distribution function denoted by $f_\alpha(\mathbf{x}, \mathbf{p}, t)$, which depends on 7 variables: 3 in space, 3 in momentum space and time. In the particle-in-cell method, charged particles are represented by a shape factor and their dynamic is accounted for by the Klimontovich equation

$$\frac{\partial}{\partial t} f_\alpha + \mathbf{v} \cdot \frac{\partial}{\partial \mathbf{x}} f_\alpha + q_\alpha e (\mathbf{E} + \mathbf{v} \times \mathbf{B}) \cdot \frac{\partial}{\partial \mathbf{p}} f_\alpha = 0. \quad (1.1)$$

The fields \mathbf{E} , \mathbf{B} are the electric and magnetic fields induced by interactions between particles. Collisions take place on a small scale length (the Fermi length L_F) and imposes a thin discretization, which is not computationally affordable. For this reason, the spatial step is set to a Debye length (L_D), the characteristic length above which collective plasma effects take place. The fields can be self-generated or come from an external source (a laser for example). In addition, one assumes that the plasma is dominated by kinetic effects rather than Coulomb interactions, which requires a high number of particles in a Debye sphere. If one denotes n the plasma density this condition reads $nL_D^3 \gg 1$. Collisional effects are usually added as an extension under the form of a Monte Carlo module.

The evolution of charged particles generates fluctuations in the electromagnetic fields which are consistently described by Maxwell's equations

$$\nabla \cdot \mathbf{E} = \frac{\rho}{\epsilon_0} \quad \nabla \cdot \mathbf{B} = 0 \quad (1.2)$$

$$\frac{\partial \mathbf{B}}{\partial t} = -\nabla \times \mathbf{E} \quad \frac{\partial \mathbf{E}}{\partial t} = c^2 (\nabla \times \mathbf{B} - \mu_0 \mathbf{j}) \quad (1.3)$$

where ρ denotes the charge and \mathbf{j} the current in the plasma. They are defined by $\rho(\mathbf{x}, t) = \sum_\alpha q_\alpha \int f_\alpha(\mathbf{x}, \mathbf{p}, t) d\mathbf{p}$ and $\mathbf{j}(\mathbf{x}, t) = \sum_\alpha q_\alpha \int \mathbf{v} f_\alpha(\mathbf{x}, \mathbf{p}, t) d\mathbf{p}$. In practice, the number of particles in a plasma of interest ($\gg 10^9$) is too high given the performance of modern supercomputers. It is possible to rewrite the Klimontovich equation by substituting (\mathbf{x}, \mathbf{p})

by (\mathbf{X}, \mathbf{Y}) such as

$$\frac{d\mathbf{X}}{dt} = \frac{\mathbf{Y}}{m\sqrt{1 - \frac{\mathbf{Y}^2}{m^2 c^2}}} \quad (1.4)$$

$$\frac{d\mathbf{Y}}{dt} = q_\alpha (\mathbf{E} + \mathbf{v} \times \mathbf{B}) \quad (1.5)$$

The Klimontovich equation can be written as

$$\frac{\partial f_\alpha}{\partial t} + \frac{d\mathbf{X}}{dt} \cdot \frac{\partial f_\alpha}{\partial \mathbf{X}} + \frac{d\mathbf{Y}}{dt} \cdot \frac{\partial f_\alpha}{\partial \mathbf{Y}} = 0 \rightarrow \frac{d}{dt} [f_\alpha(\mathbf{X}(t), \mathbf{Y}(t), t)] = 0 \quad (1.6)$$

One can note that f_α is conserved along the curves $(\mathbf{X}(t), \mathbf{Y}(t))$. PIC codes animate a reduced number of particles, known as macro-particles, according to equations (1.4) and (1.5) self-consistently with the field evolution provided by Maxwell's equations (1.2)-(1.3). Each of those macro-particles represent a group of real particles.

The code solves those equations every time steps following the loop represented in Fig. 1.1. Five steps are identified and referred by letters. They will all be presented in the following sections. We will first describe the interpolation stage in section 1.2 (steps a and c) and then move on to the resolution of Maxwell's equations (step b) in Sec. 1.3. The motion of particles will be treated in Sec. 1.4 (step d). We will finally recall different methods employed in the literature to implement collisional and radiative processes in Sec. 1.6 (step e).

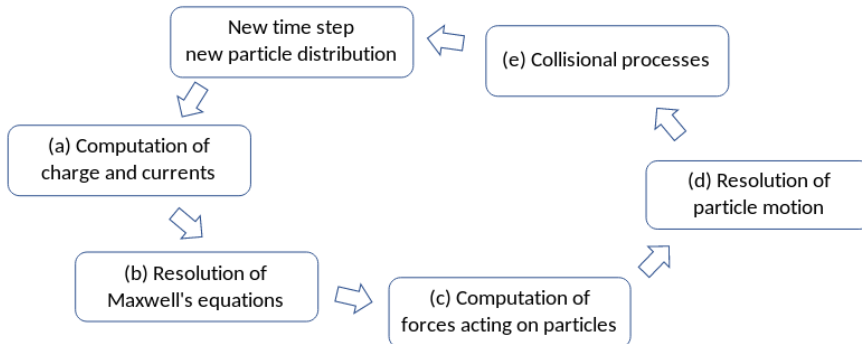


Figure 1.1: Time loop of a Particle-In-Cell code.

1.2 Interpolation steps

In the time loop of a PIC code, two steps require to interpolate data from the particles' position to the mesh points and vice versa. In order to solve Maxwell's equation, one first needs to interpolate the currents known at the particles' position to the mesh points (current assignation). Secondly, the Lorentz force experienced by a particle is obtained by the interpolation of the \mathbf{E} and \mathbf{B} fields from the mesh points to the particle's position.

Let us introduce some notations (see Fig. 1.2(a)), the coordinate of the i -th particle is denoted \mathbf{x}_i and the coordinate of the j -th mesh point by \mathbf{X}_j . The charge and current at

the mesh points are determined from the N_p particles present in the simulation

$$\rho(\mathbf{X}_j) = \sum_{\alpha} \sum_{i=1}^{N_p} q_{\alpha} S(\mathbf{X}_j - \mathbf{x}_i) \quad (1.7)$$

$$\mathbf{j}(\mathbf{X}_j) = \sum_{\alpha} \sum_{i=1}^{N_p} q_{\alpha} v_i S(\mathbf{X}_j - \mathbf{x}_i) \quad (1.8)$$

The function S introduced is a shape function that will be presented below. We first provide the interpolation step required to determine the force acting on each particles. This consists in projecting the fields from the N_m mesh points, located at coordinate \mathbf{X}_j , to the particle's position \mathbf{x}_i

$$\mathbf{E}(\mathbf{x}_i) = \sum_{j=1}^{N_m} \mathbf{E}(\mathbf{X}_j) S(\mathbf{X}_j - \mathbf{x}_i) \quad (1.9)$$

$$\mathbf{B}(\mathbf{x}_i) = \sum_{j=1}^{N_m} \mathbf{B}(\mathbf{X}_j) S(\mathbf{X}_j - \mathbf{x}_i) \quad (1.10)$$

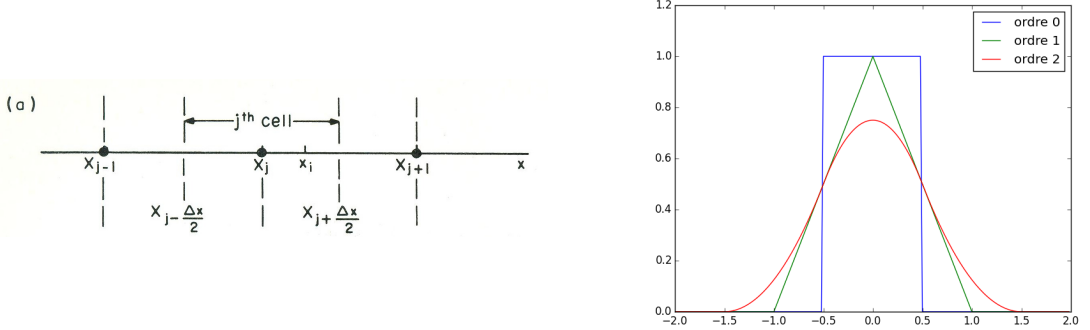


Figure 1.2: (a) Notations for a 1D domain, \mathbf{x}_i denotes a particle's coordinate and \mathbf{X}_j a mesh point coordinate (taken from [Birdsall and Langdon \(1991\)](#)); (b) shape functions of order 0, 1 and 2 plotted from formula (1.11).

Those interpolations mostly depend on the choice of the shape function S . We denote $H(x)$ the Heaviside function defined as $H(x) = 1 \forall x \geq 0$ and $\xi = x/\Delta x$. The shape functions, in one dimension, are defined for all $\xi \in \mathbb{R}$ and for all $n \in \mathbb{N}$ by

$$S^0(\xi) = H\left(\xi + \frac{1}{2}\right) H\left(\xi - \frac{1}{2}\right)$$

$$S^n(\xi) = \underbrace{(S^0 * S^0 * \dots * S^0)}_{\times(n+1)}(\xi) \quad (1.11)$$

Their expressions for $n = 0, 1$ and 2 are

$$S^0(\xi) = \begin{cases} 1 & \text{if } -\frac{1}{2} \leq \xi \leq \frac{1}{2} \\ 0 & \text{otherwise} \end{cases}$$

$$S^1(\xi) = \begin{cases} \xi + 1 & \text{if } -1 \leq \xi \leq 0 \\ 1 - \xi & \text{if } 0 \leq \xi \leq 1 \\ 0 & \text{otherwise} \end{cases}$$

$$S^2(\xi) = \begin{cases} \frac{3}{4} - |\xi|^2 & \text{if } |\xi| \leq \frac{1}{2} \\ \frac{1}{2} (\frac{3}{2} - |\xi|)^2 & \text{if } \frac{1}{2} \leq \xi \leq \frac{3}{2} \\ 0 & \text{otherwise} \end{cases}$$

We plot them in Fig. 1.2(b). Those functions respect the charge conservation condition $\int_{-L}^L S^n(x) = 1$ with $(-L, L)$ the set of definition of the function S^n . In two dimensions, this shape function (S^{2d}) is obtained with the tensor product of one dimensional shape functions

$$S^{2d}(x, y) = S(x) \otimes S(y)$$

$$S^{2d}(X_i - x^n, Y_j - y^n) = S(X_i - x^n) S(Y_j - y^n)$$

It is required to consistently employ the same shape function for all interpolations to prevent the rise of an undesirable numerical force ([Birdsall and Langdon \(1991\)](#)). One can see that a shape function of order 0 has a sharp edge, leading to abrupt discontinuities and numerical noise during simulations. For this reason, high order interpolation factors are introduced and enable to get rid of the discontinuity observed for order 0. In PIC simulations shape functions of order 2, 3 and 4 are commonly employed.

1.3 Resolution of Maxwell's equations

1.3.1 Explicit method from K. Yee

We report here the method developped by [Yee \(1966\)](#) to solve Maxwell's equations. It proved to be robust and is now employed in many PIC codes.

Let us consider a cell of the grid in a three dimensional simulation domain as represented by Fig. 1.3. The spatial steps along x , y and z are denoted by Δx , Δy and Δz , the time step is denoted by Δt . The Finite Difference Time Domain (FDTD) scheme is derived such as the spatial partial derivatives of the **E** and **B** fields are of first order and centered. The evolution of the magnetic and electric fields is then solved every half time steps according to

$$\left(\frac{\partial \mathbf{B}}{\partial t} \right)^n = -(\nabla \times \mathbf{E})^n \quad (1.12)$$

$$\left(\frac{\partial \mathbf{E}}{\partial t} \right)^{n+\frac{1}{2}} = c^2 (\nabla \times \mathbf{B} - \mu_0 \mathbf{j})^{n+\frac{1}{2}} \quad (1.13)$$

Fig. 1.3 shows a mesh cell and the points of the grid where quantities are evaluated.

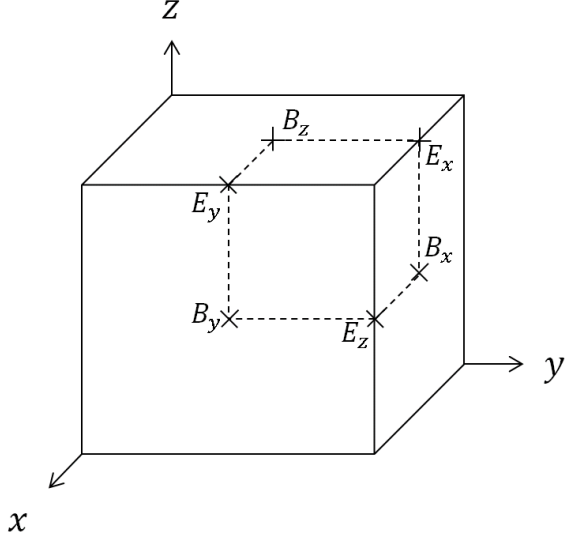


Figure 1.3: Discretization of \mathbf{E} and \mathbf{B} on a 3D grid cell. The components of the \mathbf{B} field are evaluated at the center of the cell's side and the components of the \mathbf{E} field are evaluated at the center of the cell's edge.

The discretized form of Eq. (1.12) projected in three dimensions is

$$\frac{(B_x)_{i,j+\frac{1}{2},k+\frac{1}{2}}^{n+\frac{1}{2}} - (B_x)_{i,j+\frac{1}{2},k+\frac{1}{2}}^{n-\frac{1}{2}}}{\Delta t} = - \frac{(E_z)_{i,j+1,k+\frac{1}{2}}^n - (E_z)_{i,j,k+\frac{1}{2}}^n}{\Delta y} + \frac{(E_y)_{i,j+\frac{1}{2},k+1}^n - (E_y)_{i,j+\frac{1}{2},k}^n}{\Delta z} \quad (1.14)$$

$$\frac{(B_y)_{i+\frac{1}{2},j,k+\frac{1}{2}}^{n+\frac{1}{2}} - (B_y)_{i+\frac{1}{2},j,k+\frac{1}{2}}^{n-\frac{1}{2}}}{\Delta t} = - \frac{(E_x)_{i+\frac{1}{2},j,k+1}^n - (E_x)_{i+\frac{1}{2},j,k}^n}{\Delta z} + \frac{(E_z)_{i+1,j,k+\frac{1}{2}}^n - (E_z)_{i,j,k+\frac{1}{2}}^n}{\Delta x} \quad (1.15)$$

$$\frac{(B_z)_{i+\frac{1}{2},j+\frac{1}{2},k}^{n+\frac{1}{2}} - (B_z)_{i+\frac{1}{2},j+\frac{1}{2},k}^{n-\frac{1}{2}}}{\Delta t} = - \frac{(E_y)_{i+1,j+\frac{1}{2},k}^n - (E_y)_{i,j+\frac{1}{2},k}^n}{\Delta x} + \frac{(E_x)_{i+\frac{1}{2},j+1,k}^n - (E_x)_{i+\frac{1}{2},j,k}^n}{\Delta y} \quad (1.16)$$

The discretized form of Eq. (1.13) projected in three dimensions reads

$$\begin{aligned} \frac{(E_x)_{i+\frac{1}{2},j,k}^{n+1} - (E_x)_{i+\frac{1}{2},j,k}^n}{c^2 \Delta t} &= \frac{(B_z)_{i+\frac{1}{2},j+\frac{1}{2},k}^{n+\frac{1}{2}} - (B_z)_{i+\frac{1}{2},j-\frac{1}{2},k}^{n+\frac{1}{2}}}{\Delta y} - \frac{(B_y)_{i+\frac{1}{2},j,k+\frac{1}{2}}^{n+\frac{1}{2}} - (B_y)_{i+\frac{1}{2},j,k-\frac{1}{2}}^{n+\frac{1}{2}}}{\Delta z} \\ &\quad - \mu_0 (J_x)_{i+\frac{1}{2},j,k}^{n+\frac{1}{2}} \\ \frac{(E_y)_{i,j+\frac{1}{2},k}^{n+1} - (E_y)_{i,j+\frac{1}{2},k}^n}{c^2 \Delta t} &= \frac{(B_x)_{i,j+\frac{1}{2},k+\frac{1}{2}}^{n+\frac{1}{2}} - (B_x)_{i,j+\frac{1}{2},k-\frac{1}{2}}^{n+\frac{1}{2}}}{\Delta z} - \frac{(B_z)_{i+\frac{1}{2},j+\frac{1}{2},k}^{n+\frac{1}{2}} - (B_z)_{i-\frac{1}{2},j+\frac{1}{2},k}^{n+\frac{1}{2}}}{\Delta x} \\ &\quad - \mu_0 (J_y)_{i,j+\frac{1}{2},k}^{n+\frac{1}{2}} \\ \frac{(E_z)_{i,j,k+\frac{1}{2}}^{n+1} - (E_z)_{i,j,k+\frac{1}{2}}^n}{c^2 \Delta t} &= \frac{(B_y)_{i+\frac{1}{2},j,k+\frac{1}{2}}^{n+\frac{1}{2}} - (B_y)_{i-\frac{1}{2},j,k+\frac{1}{2}}^{n+\frac{1}{2}}}{\Delta x} - \frac{(B_x)_{i,j+\frac{1}{2},k+\frac{1}{2}}^{n+\frac{1}{2}} - (B_x)_{i,j-\frac{1}{2},k+\frac{1}{2}}^{n+\frac{1}{2}}}{\Delta y} \\ &\quad - \mu_0 (J_z)_{i,j,k+\frac{1}{2}}^{n+\frac{1}{2}} \end{aligned}$$

As the derivatives are centered, the scheme is characterized by a precision of order 2. A stability analysis can be lead in the limit of a plane wave: $(\mathbf{E}, \mathbf{B})(\mathbf{x}, t) = (\mathbf{E}_0, \mathbf{B}_0) \exp[i(\mathbf{k} \cdot \mathbf{x} - \omega t)]$. The Courant Friedrichs Lewy (CFL) condition ensuring the convergence of the scheme reads

$$(c \Delta t)^2 \left(\frac{1}{\Delta x^2} + \frac{1}{\Delta y^2} + \frac{1}{\Delta z^2} \right) \leq 1 \quad (1.17)$$

Moreover, this scheme ensures that the discretized form of $\nabla \cdot \nabla \times \mathbf{A}$ and $\nabla \times \nabla \phi$ vanishes for all \mathbf{A} and ϕ . This result can be employed in equations (1.12) and (1.13) where taking the divergence in each terms leads to

$$\frac{\nabla \mathbf{B}^{n+1/2} - \nabla \mathbf{B}^{n-1/2}}{\Delta t} = 0 \quad (1.18)$$

$$\frac{\rho^{n+1} - \rho^n}{\Delta t} + \nabla \mathbf{j}^{n+1/2} = 0 \quad (1.19)$$

Assuming that the divergence of \mathbf{B} is 0 at the first time step, formula (1.18) ensures it remains conserved for all time steps. Formula (1.19) shows Maxwell-Gauss equation is respected as long as the continuity equation is fulfilled ([Esirkepov \(2001\); Barthélémy \(2005\)](#)).

1.3.2 Improved resolution of Maxwell's equations

The method of [Yee \(1966\)](#) presents one main limit. It appears for example in the numerical dispersion relation for a plane electromagnetic wave which is obtained by injecting the discretized form of $(\mathbf{E}, \mathbf{B})(\mathbf{x}, t) = (\mathbf{E}_0, \mathbf{B}_0) \exp[i(\mathbf{k} \cdot \mathbf{x} - \omega t)]$ in the discretized equations of the Yee scheme

$$\left(\frac{\sin \omega \Delta t / 2}{c \Delta t} \right)^2 = \left(\frac{\sin k_x \Delta x / 2}{\Delta x} \right)^2 + \left(\frac{\sin k_y \Delta y / 2}{\Delta y} \right)^2 + \left(\frac{\sin k_z \Delta z / 2}{\Delta z} \right)^2 \quad (1.20)$$

This numerical dispersion relation for a plane wave in vacuum is not the one physically expected, except along diagonal directions (such as $|k_x| = |k_y| = |k_z|$). It therefore introduces non-physical waves propagating with a phase velocity $v_\phi < c$. As particles

propagate with a velocity v such as $v_\phi \leq v \leq c$ Cherenkov radiation is emitted. We recall that this type of radiation takes place when a particle propagates faster than the phase velocity of light in a dielectric media. Three solutions exist in the literature to limit this numerical Cherenkov effect. Pukhov (1999) and Lehe *et al.* (2013) introduced coefficients on derivatives in the Yee scheme to cancel the dispersion along the propagation direction of an electron beam accelerated by a high intensity laser pulse in a low density plasma. This was done in order to reduce the unphysical growth of the beam emittance. Implicit methods were also developed by Zagorodnov *et al.* (2003), Drouin (2009) and effectively reduce the dispersion of the Yee scheme. The spectral method suggests to completely cancel numerical dispersion by a resolution of the Maxwell's equations in the Fourier domain (Gonoskov (2013)). All these schemes have a lower dispersion than the Yee method presented above, but demand more computational resources.

1.4 Resolution of particles' motion

The motion of particles is described by the relativistic Newton equation and is solved by the common method first reported by Boris *et al.* (1972). The Boris scheme is a leap frog scheme solving

$$\frac{d\mathbf{x}}{dt} = \mathbf{v} \quad \frac{d\mathbf{p}}{dt} = q_\alpha (\mathbf{E} + \mathbf{v} \times \mathbf{B}) \quad (1.21)$$

where α denotes a given species. It can be expressed under the following form (Boris *et al.* (1972))

$$\mathbf{x}^{n+1} = \mathbf{x}^n + \Delta t \mathbf{v}^{n+1/2} \quad (1.22)$$

$$p^{n+1/2} = m\gamma^{n+1/2} v^{n+1/2} \quad (1.23)$$

$$\frac{\mathbf{p}^{n+1/2} - \mathbf{p}^{n-1/2}}{\Delta t} = q_\alpha \left(\mathbf{E}^n + \frac{1}{c} \frac{\mathbf{p}^{n+1/2} + \mathbf{p}^{n-1/2}}{2\gamma^n m_\alpha} \times \mathbf{B}^n \right) \quad (1.24)$$

In Eq. (1.22), the position of particles is updated every integer time steps (n) from the velocity at half time steps ($n \pm 1/2$) by a first order Euler method. In Eq. (1.24), the momentum of particles are taken at half time step ($n \pm 1/2$) and are updated by a centered first order method. Even if the expression of $p^{n+1/2}$ as a function of $p^{n-1/2}$ looks implicit, it is positively explicit and can be, for example, derived by introducing two intermediate momenta \mathbf{p}^\pm and the normalized \mathbf{B} field $\mathbf{b} = q_\alpha \Delta t \mathbf{B}^n / 2m$

$$\mathbf{p}^- = \mathbf{p}^{n-1/2} + \Delta t \frac{q\mathbf{E}^n}{2m_\alpha} \quad (1.25)$$

$$\mathbf{p}^+ = \frac{2}{1+b^2} \begin{bmatrix} -b_y^2 - b_z^2 & b_z + b_x b_y & -b_y + b_x b_z \\ -b_z + b_x b_y & -b_x^2 - b_z^2 & b_x + b_y b_z \\ b_y + b_x b_z & -b_x + b_y b_z & -b_x^2 - b_y^2 \end{bmatrix} \mathbf{p}^- \quad (1.26)$$

$$\mathbf{p}^{n+1/2} = \mathbf{p}^+ + \Delta t \frac{q\mathbf{E}^n}{2m_\alpha} \quad (1.27)$$

The decomposition contains three steps. During the first step, the particle is accelerated by the electric field as shown in Eq. (1.25). The second step involves only the normalized magnetic field \mathbf{b} and consists in a rotation (see Eq. (1.26)). The particle is accelerated during the third step as seen from Eq. (1.27). This scheme remains simple but has proven its effectiveness and is widely adopted in state-of-the-art PIC codes.

1.5 Non-conservation of charge during interpolation

The scheme presented in Sec. 1.2 has one major limit. Indeed, the interpolation from the particles to the mesh points performed in formula (1.7) invalidates the expected charge conservation, leading to $\nabla \mathbf{j} + \partial \rho / \partial t \neq 0$. As a result, the \mathbf{E} field does not fulfill the Maxwell-Gauss equation which raised an issue about the numerical scheme of PIC codes. Several solutions were suggested, starting with [Boris et al. \(1972\)](#) to conserve the charge.

[Boris et al. \(1972\)](#) bring a correction to the \mathbf{E} field such that it respects Maxwell-Gauss equation. This corrected field is denoted by \mathbf{E}_{cor} and can be determined provided one can find an adequate potential ϕ defined by

$$\mathbf{E}_{cor} = \mathbf{E} - \nabla \phi \quad (1.28)$$

$$\Delta \phi = \nabla \mathbf{E} - \frac{\rho}{\epsilon_0} \quad (1.29)$$

According to the definition of ϕ , $\nabla \mathbf{E}_{cor} = \rho / \epsilon_0$. This correction requires to solve an additional equation involving a Laplace operator (Eq. (1.29)). This is computationally expensive and another method was suggested by [Esirkepov \(2001\)](#).

The work of [Esirkepov \(2001\)](#) is of particular interest since it provides a general formalism to conserve the charge whatever the order of the shape function S and the dimensionality of the simulation domain (1, 2, 3). It is a result derived from former works valid in certain limits and obtained by [Villasenor and Buneman \(1992\)](#). He seeked for a current assignation method that ensures that the following discretized equation is verified

$$\nabla \mathbf{j} + \frac{\partial \rho}{\partial t} = 0 \quad (1.30)$$

To this purpose, he introduced the density decomposition vector $\mathbf{W} = (W_x, W_y, W_z)$ defined at time $n + 1/2$ by

$$\frac{(J_x)_{i+\frac{1}{2},j,k}^{n+\frac{1}{2}} - (J_x)_{i-\frac{1}{2},j,k}^{n+\frac{1}{2}}}{\Delta x} = -\frac{q}{\Delta t} (W_x)_{i,j,k}^{n+\frac{1}{2}} \quad (1.31)$$

$$\frac{(J_y)_{i,j+\frac{1}{2},k}^{n+\frac{1}{2}} - (J_y)_{i,j-\frac{1}{2},k}^{n+\frac{1}{2}}}{\Delta y} = -\frac{q}{\Delta t} (W_y)_{i,j,k}^{n+\frac{1}{2}} \quad (1.32)$$

$$\frac{(J_z)_{i,j,k+\frac{1}{2}}^{n+\frac{1}{2}} - (J_z)_{i,j,k-\frac{1}{2}}^{n+\frac{1}{2}}}{\Delta z} = -\frac{q}{\Delta t} (W_z)_{i,j,k}^{n+\frac{1}{2}} \quad (1.33)$$

The charge conservation expressed in Eq. (1.30) can be recast in terms of the density decomposition vector

$$(W_x)_{i,j,k}^{n+\frac{1}{2}} + (W_y)_{i,j,k}^{n+\frac{1}{2}} + (W_z)_{i,j,k}^{n+\frac{1}{2}} = S_{i,j,k}(x^{n+1}, y^{n+1}, z^{n+1}) - S_{i,j,k}(x^n, y^n, z^n) \quad (1.34)$$

where $S_{i,j,k}(x, y, z) = S(X_i - x, Y_j - y, Z_k - z)$, (X_i, Y_j, Z_k) is the position of the mesh cell (i, j, k) , (x^n, y^n, z^n) the particle's position at time n and $(x^{n+1}, y^{n+1}, z^{n+1})$ the particle's position at time $n + 1$. Let us first simplify the notations by dropping the indexes: $(W_{x,y,z})_{i,j,k}^{n+\frac{1}{2}} \equiv W_{x,y,z}$, $S_{i,j,k} \equiv S$ and by dropping the superscripts: $(x^n, y^n, z^n) \equiv (x, y, z)$ and $(x^{n+1}, y^{n+1}, z^{n+1}) \equiv (x + \delta x, y + \delta y, z + \delta z)$. Let us introduce the following eight shape functions (one for each summit of the 3D cell) $(f_i)_{1 \leq i \leq 8}$ defined for all

$(x, y, z, \delta x, \delta y, \delta z) \in \mathbb{R}^6$ by

$$\begin{aligned} f_1(x, y, z, \delta x, \delta y, \delta z) &= S(x, y, z) ; f_2(x, y, z, \delta x, \delta y, \delta z) = S(x + \delta x, y + \delta y, z + \delta z) \\ f_3(x, y, z, \delta x, \delta y, \delta z) &= S(x + \delta x, y, z) ; f_4(x, y, z, \delta x, \delta y, \delta z) = S(x, y + \delta y, z) \\ f_5(x, y, z, \delta x, \delta y, \delta z) &= S(x, y, z + \delta z) ; f_6(x, y, z, \delta x, \delta y, \delta z) = S(x + \delta x, y + \delta y, z) \\ f_7(x, y, z, \delta x, \delta y, \delta z) &= S(x + \delta x, y, z + \delta z) ; f_8(x, y, z, \delta x, \delta y, \delta z) = S(x, y + \delta y, z + \delta z) \end{aligned}$$

Assuming the following four hypothesis:

1. W_x, W_y and W_z are linear combinations of the shape functions $(f_i)_{1 \leq i \leq 8}$
2. The sum of the three components of the vector \mathbf{W} verifies the charge conservation equation

$$W_x + W_y + W_z = f_2 - f_1$$

3. If one of the shifts is zero, then the corresponding component of \mathbf{W} is also zero

$$\delta x = 0 \rightarrow W_x = 0, \quad \delta y = 0 \rightarrow W_y = 0 \quad \text{and} \quad \delta z = 0 \rightarrow W_z = 0$$

4. If $\forall (x, y) \in \mathbb{R}^2 \quad S(x, y, z) = S(y, x, z)$ and $\delta x = \delta y$ then $W_x = W_y$. The same property is assumed for invariance with respect to permutations of pairs (x, z) and (y, z) .

Boris *et al.* (1972) build a linear system of equations that provides a unique solution for the vector \mathbf{W} as a function of the shape functions $(f_i)_{1 \leq i \leq 8}$. The closed-form solution of \mathbf{W} is

$$\begin{aligned} W_x &= \frac{1}{3}(f_2 + f_3 - f_1 - f_8) + \frac{1}{6}(f_6 + f_7 - f_4 - f_5) \\ W_y &= \frac{1}{3}(f_2 + f_8 - f_5 - f_7) + \frac{1}{6}(f_4 + f_6 - f_1 - f_3) \\ W_z &= \frac{1}{3}(f_2 + f_5 - f_1 - f_6) + \frac{1}{6}(f_7 + f_8 - f_3 - f_4) \end{aligned}$$

1.6 Photon transport for PIC codes

The PIC method self-consistently describes the physics of a collisionless plasma and the propagation of electromagnetic fields but lacks a lot of processes. In particular, they do not account for any kind of processes involving individual photons that can be created by the plasma such as Bremsstrahlung emission, photo-ionization, K- α emission, Compton effect, atomic transitions, etc. The basic PIC loop presented in Fig. 1.1 relies on the hypothesis of a fully ionized plasma. As such, it does not put forward any description of bound electrons and therefore of all the atomic physics taking place in a plasma. In this section we review the two ways existing to model those effects. Firstly, we report the method developped by Sentoku *et al.* (2014) and Royle *et al.* (2017) in the PIC code PICLS. It enables to analyse the interplay of plasma physics and photon transport by coupling a PIC code and a radiative transport code. Secondly, we examine the second method which consists in a Monte Carlo implementation of the missing effects. The latter method is more commonly employed in PIC codes and represents one of the bases of this PhD work. While an extensive analysis of this approach will be provided in Chap. 2 and Chap. 3 we only give its keys aspects to understand it in this section.

1.6.1 Radiative transport equation in the PIC framework

The photon transport equation can be rigorously derived based on the conservation of the energy through a volume element in a time interval (Mihalas, 1978). Another method to derive this equation is also reported by (Mihalas, 1978). It starts from the Boltzman equation

$$\frac{\partial f}{\partial t} + \mathbf{v} \cdot \frac{\partial}{\partial \mathbf{x}} f + \mathbf{F} \cdot \frac{\partial}{\partial \mathbf{p}} f = \left(\frac{Df}{Dt} \right)_{\text{coll}} \quad (1.35)$$

and adapts it to photons. Let us first introduce the specific intensity of radiation at position \mathbf{r} , travelling in direction \mathbf{n} , with frequency ν at a time t . It is defined such that the amount of energy $d\mathcal{E}$ transported by radiation of frequencies $(\nu, \nu + \Delta\nu)$ across an element of area dS into a solid angle $d\Omega$ in a time interval dt is

$$d\mathcal{E} = I(\mathbf{r}, \mathbf{n}, \nu, t) dS \cos \theta d\Omega d\nu dt \quad (1.36)$$

Without relativistic effects, the force $\mathbf{F} \equiv 0$ and the photon propagates on a straight line $\mathbf{v} = c\mathbf{n}$ and its frequency remains the same. We introduce a photon distribution function defined from the specific intensity as $I(\mathbf{r}, \mathbf{n}, \nu, t) = ch\nu f(\mathbf{r}, \mathbf{n}, \nu, t)$, where h is Planck's constant. The equivalent of 'collisions' for photons, contained in the right hand side term in Eq. (1.35), is interaction with the plasma volume, coming from its emissivity (μ_e) and opacity (μ_o). With those elements, one can suggest the following equation for the specific intensity

$$\frac{1}{ch\nu} \left(\frac{\partial I}{\partial t} + c\mathbf{n} \cdot \nabla I \right) = \frac{1}{h\nu} (\mu_e - \mu_o I) \quad (1.37)$$

One can mention that this formula assumes that at position r and time t the plasma volume is at the local thermodynamic equilibrium. This enables to locally define a temperature T and a density n on which the coefficients μ_e and μ_o depend.

At every time steps and in every mesh cells, the transport equation is solved for a large range of frequencies ν and all angles Ω . The frequencies ν are discretized inhomogeneously in order to catch the narrow bound-bound atomic transitions of interest. The angle Ω is discretized in the upper hemisphere and assumed to be symmetric in the lower one. The numerical resolution is performed with a constrained interpolation profile (CIP) technique from Yabe *et al.* (1991). This work puts forward a general solver for hyperbolic equations of the same form as Eq. (1.37). The numerical scheme is an explicit finite difference method that interpolates the solution as a third order polynomial within the mesh cells.

In practice, the numerical resolution of Eq. (1.37) at every time step (Δt_{PIC}), in every cells (Δx_{PIC}), for all frequencies and all angles requires too much computational time. For this reason, a larger spatial grid ($\Delta x_{rad} > \Delta x_{PIC}$) is employed for the resolution of the radiation transport equation as well as a larger time step ($\Delta t_{rad} > \Delta t_{PIC}$). However, the new time and spatial steps must be small enough to describe all the gradients present in the problem. As an example, Royle *et al.* (2017) employs $\Delta x_{rad} \simeq 5\Delta x_{PIC}$ and $\Delta t_{rad} \simeq 5\Delta t_{PIC}$ and successfully reproduces an experiment where an X-ray Free Electron Laser (XFEL) heats a solid-density aluminium foil.

The interplay between the PIC and radiation transport part of the code is illustrated in Fig. 1.4. Once the PIC code time loop is performed, the local density and local temperature of the bulk electrons is determined in every cells. Those variables are employed to determine the local emissivity and opacity of the plasma. Equation (1.37) is then solved for every frequency ν_i and angle Ω_j which provides the specific intensity $I_{ij}(\Delta x_{rad}, \Omega_j, \nu_i, \Delta t_{rad})$. The related energy transferred from bound to free bulk electrons

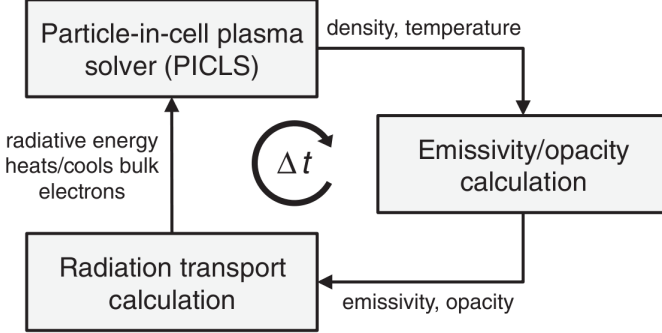


Figure 1.4: Coupling of a radiation transport code and the Particle-In-Cell code PICLS (image from [Royle et al. \(2017\)](#)).

is then deduced by integrating on all frequencies ν_i and angles Ω_j

$$dE_{ij} = \frac{1}{c} \int \int \frac{\partial I_{ij}}{\partial t} d\Omega d\nu \quad (1.38)$$

If the energy transfer is negative ($dE_{ij} < 0$), the free bulk electrons are uniformly heated, whereas if it is positive ($dE_{ij} > 0$) they are uniformly cooled. The determination of the emissivity and opacity coefficients is a key point of this scheme, as they are supposed to account for the energy transfers of the whole range of lacking physical effects. Ideally they depend on the local density and temperature of the plasma $\mu_e = \mu_e(n_i, T_e, h\nu)$ and $\mu_o = \mu_o(n_i, T_e, h\nu)$. In practice, they are pre-tabulated from the FLYCHK collisional radiative code assuming a cold material ([Chung et al. \(2005\)](#)).

The prior knowledge of the opacity and emissivity coefficients in arbitrary conditions of temperature and density is a constraint that can be overcome by describing the underlying processes by a Monte Carlo approach, as suggested by [Royle et al. \(2017\)](#). We explain the principle of this method in the next subsection and will detail the modeling, implementation and validation steps for various processes in Chap. 2 and Chap. 3.

1.6.2 Monte Carlo scheme for elastic and inelastic processes

The frame of this method is very general and can be applied to any process for which cross-sections are known. This method was first added in a PIC code by [Takizuka and Abe \(1977\)](#), enriched by [Nanbu \(1997\)](#); [Sentoku and Kemp \(2008\)](#) and [Pérez et al. \(2012\)](#). It consists in the addition of a Monte Carlo module inside the time loop of the PIC code. It is called before ending the time step, as indicated in fig. 1.1. The different steps of the Monte Carlo code are illustrated in Fig. 1.5.

In this scheme, macro-particles are paired at every time steps and in every cells. The scattering or energy loss/gain of macro-particles is determined from cross-sections that are sampled with the inversion of the cumulative distribution function which is an usual Monte Carlo sampling method. We introduce the term 'macro-collision' which denotes a simulated event between two macro-particles. The Monte Carlo scheme is based on assumptions which are the following. Firstly, events are cumulated on one PIC time step (Δt), as their typical time-scale is much lower compared to Δt . Secondly, the interaction conditions are provided by the local properties inside each cell (temperature $\langle T \rangle$ and density $\langle n \rangle$ are spatially averaged in the cell) and also depend on the two interacting particles momenta \mathbf{p}_1 and \mathbf{p}_2 . The heart of the method relies in the random pairing of

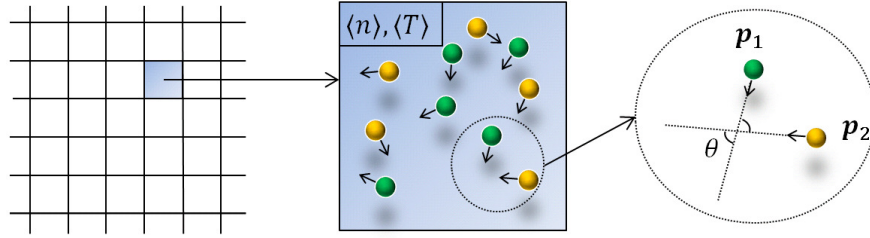


Figure 1.5: Macro-particle pairing Monte Carlo scheme. Events are treated in every cells at every time steps.

particles which is detailed in the next paragraph.

Macro-particles of similar or different species are paired randomly. For macro-collisions within a same species, macro-particles are simply paired with their neighbour. Let us now consider two species α and β within a cell with N_α and N_β macro-particles. We assume without loss of generality that $N_\alpha > N_\beta$. The goal is to randomly form $\max(N_\alpha, N_\beta) = N_\alpha$ pairs to perform the macro-collisions. Each macro-particle of species α is selected once, whereas some macro-particles of species β are selected several times (see below). In order to fairly and representatively select macro-particles from species β , [Takizuka and Abe \(1977\)](#) introduces two sub-groups of macro-particle pairs. They are abstract concepts, but ensure to not introduce any bias in the selection process. We introduce (i, ϵ) defined by $N_\alpha/N_\beta = i + \epsilon$ with $i \in \mathbb{N}$ and $\epsilon \in (0, 1)$. A first group is made of $(i+1)\epsilon N_\beta$ macro-particles of specie α and ϵN_β macro-particles of specie β . We emphasize that $\epsilon N_\beta = N_\alpha - i N_\beta \in \mathbb{N}$. In this group, each macro-particle of specie β is paired $i+1$ times with a macro-particle of specie α . A second group is made of $i(1-\epsilon)N_\beta$ macro-particles of specie α and $(1-\epsilon)N_\beta$ macro-particles of specie β . In this group, each macro-particle of specie β is paired i times with a macro-particle of specie α . We exemplify the grouping of macro-particles with an example in Fig. 1.6 in the simple case where the two species are electrons ($N_{e^-} = 9$) and ions ($N_i = 4$).

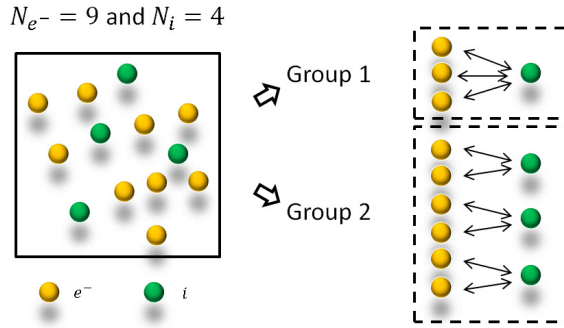


Figure 1.6: Example of macro-particle pairing in a mesh cell for $N_{e^-} = 9$ and $N_i = 4$. Two groups are formed and $\max(N_{e^-}, N_i) = 9$ macro-collisions are computed.

Once macro-particles are paired, relevant cross-sections can be sampled depending on the conditions in the cell (density, temperature, ionization degree of atoms) as well as the relative velocity of two macro-particles. In order to provide a practical example of how a radiative process can be implemented within this framework, we introduce the Bremsstrahlung process in Fig. 1.7, during which a relativistic electron experiencing an atomic Coulomb field is accelerated and radiates a fraction of its energy. The indexes 1

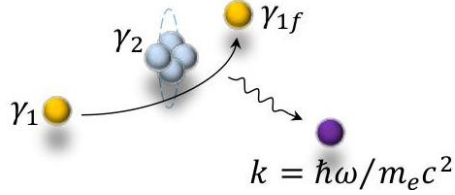


Figure 1.7: Generation of a macro-photon via the Bremsstrahlung process from a randomly sampled pair of macro-particles

and 2 denote a macro-electron and a macro-ion randomly selected according to the method illustrated in Figs. 1.5 and 1.6. The energy of the macro-photon created is determined from the cross-section of the Bremsstrahlung process which is extensively discussed in Chap. 3. This macro-photon is then introduced in the Particle-In-Cell code time loop and the energy of the incident electron, $(\gamma_1 - 1)mc^2$, is subsequently decreased.

This short introduction of the Monte Carlo module will be completed in Chap. 2 and Chap. 3 as it requires to introduce proper modeling for each process. This Monte Carlo macro-particle pairing scheme is computationally demanding but is implemented in a growing number of PIC codes such as CALDER, PICLS and SMILEI. Other PIC codes such as EPOCH and VLPL include a simpler, yet computationally less demanding, version of this Monte Carlo algorithm.

Conclusion

Overall, the main steps of a Particle-In-Cell code are recalled in this chapter. After presenting how field propagation and particle motion are resolved, we put forward two methods to include additional physical processes of interest. The first one (coupling of PIC and photon transport codes) is less developed than the second one (Monte Carlo) which is widely used in state of the art PIC codes, including CALDER, developed at CEA. It embodies one of the major points of this PhD work and is presented in Chap. 3. Before dealing with this issue, Chap. 2 first focuses on another radiative process of interest in the context of future multi-PW facilities which is laser-driven synchrotron emission.

Chapter 2

Processes induced in an electromagnetic field

As a relativistic electron experiences the strong field associated with a high laser intensity ($\geq 10^{22} \text{ W/cm}^2$) it can radiate a high number of photons through nonlinear inverse Compton scattering. This basic process is anticipated to have a strong back-reaction on the electron trajectory and offers new opportunities to develop ultra-fast energetic particle sources. Among potential applications are the impact of this radiative mechanism on the radiation pressure ion acceleration (Naumova *et al.*, 2009; Bulanov *et al.*, 2010; Tamburini *et al.*, 2012) and the study of quantum radiation reaction on laser-driven electrons (Blackburn *et al.*, 2014; Ji *et al.*, 2014b; Wang *et al.*, 2015b; Cole *et al.*, 2018; Poder *et al.*, 2018). The copious number of γ -rays produced can, when interacting with the strong laser field, decay into electron-positron pairs through the Breit-Wheeler process (Bell and Kirk, 2008; Nerush *et al.*, 2011; Ridgers *et al.*, 2012; Ji *et al.*, 2014c; Zhu *et al.*, 2016; Grismayer *et al.*, 2017; Jirka *et al.*, 2017). The electron-positron plasmas thus formed, characterized by a unique symmetry between positively and negatively charged particles, can be employed to reproduce laboratory-scaled astrophysics scenarios (Liang, 2013; Chen *et al.*, 2015; Lobet *et al.*, 2015).

The first section of this chapter presents the modelisation of the nonlinear inverse Compton scattering. The key hypotheses will be formulated and the resulting photon emission rates illustrated. The purpose is to implement an ad-hoc photon emission rate within the Particle-In-Cell framework. This goal is part of a general effort carried by several groups with state of the art Particle-In-Cell codes (Kirk *et al.*, 2009; Nerush *et al.*, 2011; Blackburn *et al.*, 2014; Ji *et al.*, 2014b; Wallin *et al.*, 2015; Vranic *et al.*, 2016). In a second section, we briefly introduce two pair generation processes induced by an intense electromagnetic field which are sparsely addressed in the frame of this PhD: the multi-photon Breit-Wheeler and the electromagnetic Trident.

2.1 Radiation of photons by nonlinear inverse Compton scattering

In this section, we firstly introduce the modeling of the nonlinear inverse Compton scattering and secondly describe its implementation in the Particle-In-Cell code CALDER.

2.1.1 Physical model

As a relativistic electron travels in an electromagnetic wave, it can be accelerated and can therefore radiate a fraction of its energy (Blumenthal and Gould, 1970). This process, known as nonlinear inverse Compton scattering, only depends on the quantum nonlinearity parameter (Ritus, 1985)

$$\chi_e = \frac{e\hbar}{m^3 c^3} |F_{\mu\nu} p^\nu| \quad (2.1)$$

where e denotes the electron charge, m its mass, c the light velocity and \hbar the reduced Planck constant. p^ν denotes the electron four-momentum and $F_{\mu\nu}$ the electromagnetic field tensor

$$F = \begin{pmatrix} 0 & E_x/c & E_y/c & E_z/c \\ -E_x/c & 0 & -B_z & B_y \\ -E_y/c & B_z & 0 & -B_x \\ -E_z/c & -B_y & B_x & 0 \end{pmatrix} \quad (2.2)$$

For an electron, the quantum parameter reads

$$\chi_e = \frac{\gamma_e}{E_S} \sqrt{-(\boldsymbol{\beta} \cdot \mathbf{E})^2 + (\mathbf{E} + \mathbf{v} \times \mathbf{B})^2} \quad (2.3)$$

One can project the \mathbf{E} field on the direction parallel (\mathbf{E}_{\parallel}) and perpendicular (\mathbf{E}_{\perp}) to the electron velocity vector, which leads, in the limit of a relativistic electron ($\gamma_e^2 \gg 1$), to

$$\chi_e = \frac{\gamma_e}{E_S} \sqrt{\frac{\mathbf{E}_{\parallel}^2}{\gamma_e^2} + (\mathbf{E}_{\perp} + \mathbf{v} \times \mathbf{B})^2} \simeq \frac{\gamma_e}{E_S} |\mathbf{E}_{\perp} + \mathbf{v} \times \mathbf{B}| \quad (2.4)$$

where E_S is the Schwinger field defined as $E_S = m^2 c^3 / e \hbar = 1.3 \times 10^{18} \text{ V/m}$ (Schwinger, 1951). This parameter represents the field amplitude in the electron rest-frame. In the particular case of a single electron of velocity $\mathbf{v}_e \parallel \mathbf{x}$, with \mathbf{x} the propagation direction of a plane wave of the form $\mathbf{A} = A_L \sin [\omega_0 (x - t/c)] \mathbf{y}$, the electron quantum parameter reads

$$\chi_e = \gamma_e \frac{\omega_0 A_L}{E_S} \cos(\omega_0 t) \times \begin{cases} (1 - |v_e|/c) & \text{if } \mathbf{v}_e = +|v_e| \mathbf{x} \\ (1 + |v_e|/c) & \text{if } \mathbf{v}_e = -|v_e| \mathbf{x} \end{cases} \quad (2.5)$$

In the first case displayed in Eq. (2.5), the electron and the wave are propagating in the same direction such that the quantum parameter χ_e reaches a minimum. In the second case, the electron and the wave are propagating in opposite directions such that the quantum parameter χ_e is maximized. This latter geometry is beneficial to enhance the radiation of an electron and will be referred to as counter-propagating geometry in this PhD work.

Similarly, the significance of quantum effects on a photon travelling in a strong external electromagnetic field is only accounted by the quantum nonlinearity parameter

$$\chi_\gamma = \frac{e\hbar^2}{m^3 c^3} |F_{\mu\nu} k^\nu| = \frac{\gamma_\gamma}{E_S} |\mathbf{E}_{\perp} + \mathbf{v} \times \mathbf{B}| \quad (2.6)$$

where $\hbar k^\nu$ is the photon four-momentum, and γ_γ is the normalized photon energy $\gamma_\gamma = \hbar\omega/mc^2$. One can deduce the following relation, valid for relativistic electrons or as $\mathbf{E}_{\parallel} \simeq \mathbf{0}$

$$\chi_e \gamma_\gamma \simeq \chi_\gamma \gamma_e \quad (2.7)$$

The derivation of the photon production rate of an electron propagating in an arbitrary electromagnetic field is too complex. However, it can be simplified, provided two assumptions are formulated.

1. The external field is uniform and quasistatic.
2. The external field is weak compared to the Schwinger field $E_S = 1.3 \times 10^{18} \text{ V/m}$.

For the first approximation, the coherence time of the emission process (t_{coh}) is assumed to be much smaller than the electromagnetic wave period $2\pi/\omega_0$. The coherence time is defined as the time required for the electron to be deflected by an angle $1/\gamma_e$ and is defined, in the classical regime, as

$$t_{coh} = \frac{r_L}{\gamma_e c} = \frac{m\beta_e}{eB_L} \quad (2.8)$$

where $\beta_e = v_e/c$ and r_L is the Larmor radius of the electron. In the quantum regime, the same expression remains valid for the coherence time. The first approximation therefore implies

$$\frac{m}{eB_L} \ll \frac{2\pi}{\omega_0} \rightarrow \frac{eB_L}{m\omega_0} = a_L \gg 1 \quad (2.9)$$

where the parameter a_L defines the normalized field amplitude of the external electromagnetic wave. The incoherent nature of the emission also requires that the distance between electrons is larger than the radiation wavelength. Let us assume a density n_e of electrons, this condition can be recast as $n_e^{-1/3} \geq 2\pi c/\omega$. In a solid density plasma ($n_e = 10^{30} / \text{m}^3$), incoherent emission will be limited to photons energies $\geq 10 \text{ keV}$ and for undercritical plasmas ($n_e = 10^{24} / \text{m}^3$) to photons energies $\geq 100 \text{ eV}$.

The second approximation is necessary as in an arbitrary electromagnetic field, the rate of photon emission depends on two other parameters

$$f = |\mathbf{E}^2 - \mathbf{B}^2| / E_S^2 \quad \text{and} \quad g = |\mathbf{E} \cdot \mathbf{B}| / E_S^2 \quad (2.10)$$

Assuming $f \ll 1$, $g \ll 1$ and $\chi_e \gg \max(f, g)$ enables though to reduce the dependence of the emission rate only on the quantum parameter χ_e (Kirk *et al.*, 2009)

Under the assumptions of weak, static and uniform field, the rate of photon emission is expressed as (Reiss (1962), Nikishov and Ritus (1964))

$$\frac{d^2 N_{Cs}}{dt d\gamma_\gamma} (\gamma_e, \gamma_\gamma) = \frac{P_{cl}}{\gamma_\gamma m c^2} S(\gamma_e, \gamma_\gamma) \quad (2.11)$$

where P_{cl} is the classical radiated power defined as

$$P_{cl} = \frac{2}{3} \frac{\alpha_f m c^2}{\tau_c} \chi_e^2 \quad (2.12)$$

where $\alpha_f = e^2/(4\pi\epsilon_0\hbar c)$ is the fine structure constant and $\tau_c = \hbar/mc^2$ the Compton time. The function S is defined by

$$S(\gamma_e, \gamma_\gamma) = -\frac{\sqrt{3}}{2\pi} \frac{\gamma_\gamma}{\gamma_e^2 \chi_e^2} \left[\int_{2y}^{+\infty} K_{1/3}(s) ds - (2 + 3\chi_\gamma y) K_{2/3}(2y) \right] \quad (2.13)$$

where $y = \gamma_\gamma/[3\chi_e(\gamma_e - \gamma_\gamma)]$ and K_ν are modified Bessel functions of order ν . Another

expression is suggested by [Erber \(1966\)](#)

$$S(\gamma_e, \gamma_\gamma) = \frac{1}{2\pi^2} \frac{\gamma_\gamma^2}{\gamma_e^3 \chi_e^3} \sum_{i=1}^3 m_i(x) J_i(y) \quad (2.14)$$

where $x = \gamma_\gamma/\gamma_e$ and

$$m_1 = 1 + (1-x)^{-2} \quad m_2(x) = 2(1-x)^{-1} \quad m_3(x) = x^2(1-x)^2 \quad (2.15)$$

$$J_1(y) = \frac{1}{3y^2} \int_y^\infty \frac{u}{[(u/y)^{2/3} - 1]^{1/2}} K_{2/3}^2(u) du \quad (2.16)$$

$$J_2(y) = \frac{1}{3y} \int_y^\infty \left(\frac{u}{y}\right)^{1/3} \left[(u/y)^{2/3} - 1\right]^{1/2} K_{1/3}^2(u) du \quad (2.17)$$

$$J_3(y) = \frac{1}{3y^2} \int_y^\infty \frac{u}{[(u/y)^{2/3} - 1]^{1/2}} K_{1/3}^2(u) du \quad (2.18)$$

The total emission rate (dN_{Cs}/dt) is simply obtained after an integration of Eq. (2.11) on γ_γ

$$\frac{dN_{Cs}}{dt} = \int_0^{\gamma_e-1} \frac{P_{cl}}{\gamma_\gamma mc^2} S(\gamma_e, \gamma_\gamma) d\gamma_\gamma \quad (2.19)$$

The total radiated power (P_{Cs}) is deduced from the photon emission rate

$$P_{Cs} = \int_0^{\gamma_e-1} \frac{dP_{Cs}}{d\gamma_\gamma} d\gamma_\gamma \quad (2.20)$$

$$= \int_0^{\gamma_e-1} \gamma_\gamma mc^2 \frac{d^2 N_{Cs}}{dt d\gamma_\gamma} d\gamma_\gamma \quad (2.21)$$

$$= P_{cl} \int_0^{\gamma_e-1} S(\gamma_e, \gamma_\gamma) d\gamma_\gamma \quad (2.22)$$

In the classical regime ($\chi_e \ll 1$), the function S has a simpler expression ([Blumenthal and Gould \(1970\)](#))

$$S(\omega) = \frac{\omega}{\omega_{cr}} \int_{\omega/\omega_{cr}} K_{5/3}(t) dt \quad (2.23)$$

where ω/ω_{cr} represents the frequency limit of the spectrum defined by $\tau_C \omega_{cr} = 3\gamma_e \chi_e / (2 + 3\chi_e)$.

The number of photons radiated by the synchrotron process $d^2N/dtd\gamma_\gamma$ with the quantum formula (Eq. (2.13)) or with the classical formula (Eq. (2.23)) are illustrated in Fig. 2.1(a) for different values of the electron quantum parameter $\chi_e = 0.01$, $\chi_e = 0.1$ and $\chi_e = 1$. We assumed that a single electron is travelling in a uniform external magnetic field of normalized amplitude $eB/m\omega = 100$. One can note that the number of low energy photons ($\gamma_\gamma/(\gamma_e - 1) \leq 10^{-2}$) emitted decreases as the quantum parameter rises. However, as χ_e goes from 10^{-2} to 1, the proportion of photons with an energy $\gamma_\gamma/(\gamma_e - 1) \simeq 1$ increases. The total rate of emission, integrated on the photon energy, is represented in Fig. 2.1(b). One can see a good agreement between the quantum and classical formulas for low electron quantum parameters ($\chi_e \leq 0.03$). However there is a significant discrepancy for $\chi_e \geq 0.1$, clearly showing the validity range of the classical formula. Even if the number $d^2N/dtd\gamma_\gamma$ of low-energy photons diverges (as $\gamma_\gamma \rightarrow 0$)

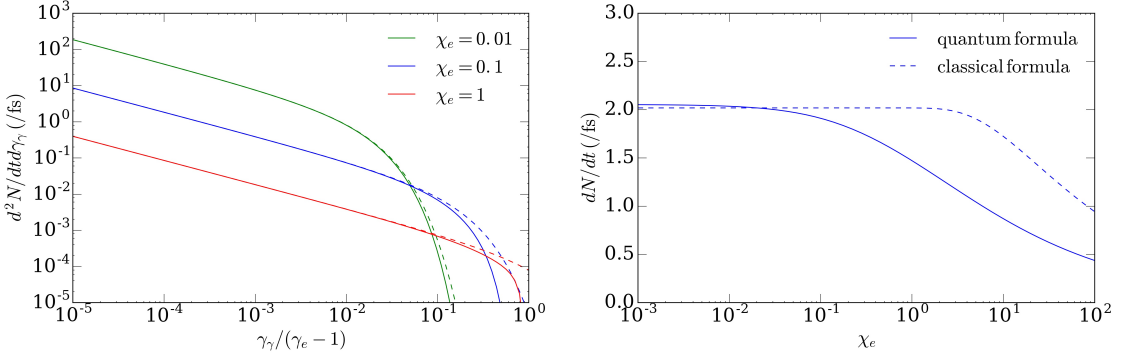


Figure 2.1: (a) $d^2N/dtd\gamma_\gamma$: number of photons emitted per time unit and photon energy unit illustrated for $\chi_e = 0.01, 0.1$ and 1 (see Eq. (2.11)) (b) dN/dt : total number of photons emitted per time unit as a function of the electron quantum parameter χ_e (see Eq. (2.19)). Solid lines represent the quantum formula and dashed lines the classical one.

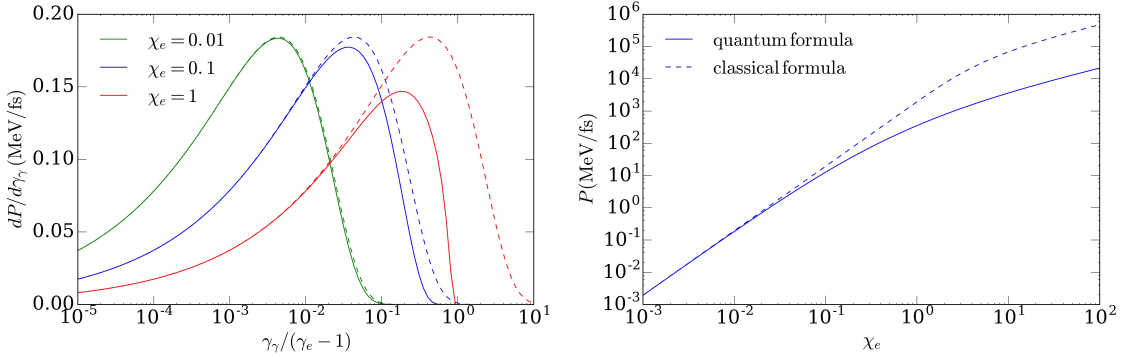


Figure 2.2: (a) $dP/d\gamma_\gamma$: power radiated per photon energy unit illustrated for $\chi_e = 0.01, 0.1$ and 1 (b) P : total power emitted as a function of the electron quantum parameter χ_e . Solid lines represent the quantum formula and dashed lines the classical one.

the radiated power, defined as $dP/d\gamma_\gamma = \gamma_\gamma m c^2 d^2 N/dtd\gamma_\gamma$, converges. We plotted the radiated power in Figs. 2.2(a-b) from its expression (Eqs. (2.20)-(2.22)). The difference between the classical and quantum formula is clearer in Fig. 2.2(a). We also see that the classical formula predicts the emission of photons with an energy higher than the electron kinetic one for a quantum parameter $\chi_e = 1$. The radiated power peaks at low photon energies for low χ_e : $\gamma_\gamma/(\gamma_e - 1) \simeq 0.005$ for $\chi_e = 0.01$ but at higher photon energies for higher χ_e : $\gamma_\gamma/(\gamma_e - 1) \simeq 0.2$ for $\chi_e = 1$. The total power, integrated on the photon energy, is displayed in Fig. 2.2(b) and the over-estimation characterizing the classical formula is even more visible on this figure.

The formula of the photon emission rate, expressed in Eqs. (2.11)-(2.13), depends on four parameters ($\gamma_e, \gamma_\gamma, \chi_e, \chi_\gamma$). It can be rewritten in order to only depend on the two parameters (χ_e, χ_γ) (Kirk *et al.*, 2009)

$$F(\chi_e, \chi_\gamma) = -\frac{2}{3} \frac{\chi_\gamma}{\chi_e^2} \left[\int_{2y}^{+\infty} K_{1/3}(s) ds - (2 + 3\chi_\gamma y) K_{2/3}(2y) \right] \quad (2.24)$$

$$= \frac{2\chi_\gamma^2}{3\sqrt{3}\pi\chi_e^4} \sum_{i=1}^3 m_i(x) J_i(y) \quad (2.25)$$

where $y = \chi_\gamma / [3\chi_e(\chi_e - \chi_\gamma)]$ (see Eq. 2.7). As a consequence, the expression of the emission rate can be written as

$$\frac{d^2 N_{Cs}}{dt d\chi_\gamma} (\chi_e, \chi_\gamma) = \frac{3\sqrt{3}}{4\pi} \frac{P_{cl}}{\gamma_\gamma m c^2} \frac{F(\chi_e, \chi_\gamma)}{\chi_e^2} \quad (2.26)$$

The differential radiated power can be deduced as

$$\frac{dP_{Cs}}{d\chi_\gamma} (\chi_e, \chi_\gamma) = \frac{\sqrt{3}}{2\pi} \alpha_f \frac{mc^2}{\tau_C} F(\chi_e, \chi_\gamma) \quad (2.27)$$

The total radiated power is obtained after the integration of Eq (2.27) on χ_γ

$$P_{Cs} = P_{cl} g(\chi_e) \quad (2.28)$$

where

$$g(\chi_e) = \frac{3\sqrt{3}}{4\pi \chi_e^2} \int_0^{\chi_e} F(\chi_e, \chi_\gamma) d\chi_\gamma \quad (2.29)$$

$$\simeq [1 + 4.8(1 + \chi_e) \log(1 + 1.7\chi_e) + 2.44\chi_e^2]^{-2/3} \quad (2.30)$$

In the classical regime ($\chi_e \ll 1$), the function $F(\chi_e, \chi_\gamma)$ can be deduced from the relation $\omega/\omega_{cr} = 2\chi_\gamma/(3\chi_e^2)$ and Eq. (2.23).

$$F(\chi_e, \chi_\gamma) = \frac{2\chi_\gamma}{3\chi_e^2} \int_{\frac{2\chi_\gamma}{3\chi_e^2}}^{\infty} K_{5/3}(t) dt \quad (2.31)$$

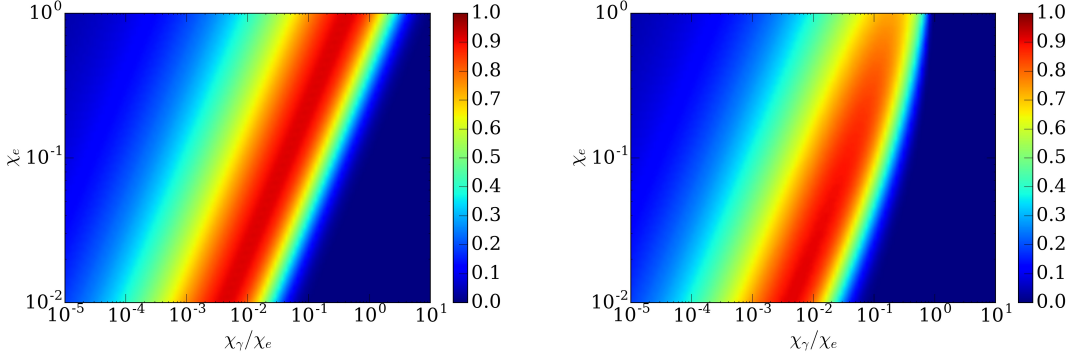


Figure 2.3: Evolution of the normalized radiated power ($F(\chi_e, \chi_\gamma)$) (a) in the classical regime and (b) in the quantum regime (see Eq. (2.27))

Fig. 2.3 illustrates the normalized radiated power $dP/d\chi_\gamma(\chi_e, \chi_\gamma)$ as a function of the electron (χ_e) and photon (χ_γ) quantum parameters. The first thing that can be noticed is in Fig. 2.3(a). In the limit $\chi_e \simeq 1$, the classical formula predicts photons with a quantum parameter higher than the electron quantum parameter ($\chi_\gamma/\chi_e > 1$) which is equivalent to photon energies higher than the electron kinetic energy since $\chi_\gamma/\chi_e \simeq \gamma_\gamma/\gamma_e$. It is therefore required to employ the formula derived in the quantum regime in order to not introduce this unphysical behavior. One can observe indeed that this error is corrected by the quantum formula in Fig. 2.3(b). The second feature of this radiated power is the location of the spectra peak. In the classical limit, the radiated power peaks for relatively

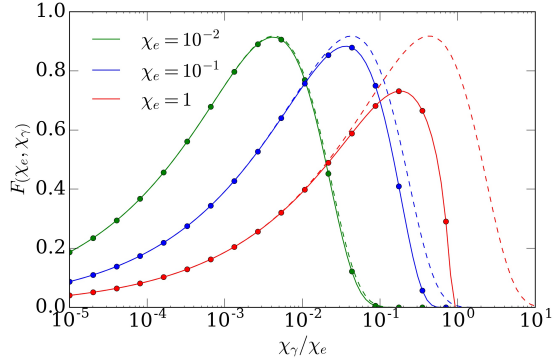


Figure 2.4: Evolution of the normalized radiated power ($F(\chi_e, \chi_\gamma)$) for different values of the electron quantum parameter $\chi_e = 10^{-2}, 10^{-1}$ and 1. In the quantum regime, the function is represented either by the dots (Eq. (2.24)) or by the solid lines (Eq. (2.25)). In the classical regime, it is represented by the dashed curves (Eq. (2.31))

low values of χ_γ/χ_e , e.g. 5×10^{-3} for $\chi_e = 10^{-2}$. In the quantum regime, the spectra peak is located near $\chi_\gamma/\chi_e \simeq 0.2$. This particularity is depicted in Fig. 2.4 where we represent the normalized power for three different values of the electron quantum parameter $\chi_e = 10^{-2}, 10^{-1}$ and 1. Using the relation $\chi_\gamma/\chi_e \simeq \gamma_\gamma/\gamma_e$ (valid for relativistic electrons), this means than in the classical regime, most photons have a low energy compared to the electrons whereas in the quantum one it is of the order of the electron kinetic energy.

2.1.2 Continuous radiation loss

The radiation emitted by an electron during its acceleration in a strong field affects its trajectory via a force known as the radiative friction force or radiation reaction. Obtaining the corrected motion equation accounting for this force is a problem tackled by Lorentz (1916) and latter by Abraham and Föppl (1918) and Dirac (1938). The equation accounting for this back reaction of radiation on the electron trajectory is usually named after those three authors and referred to as Lorentz-Abraham-Dirac (LAD) equation. This equation is plagued by non-physical behavior, as the non-respect of the principle of inertia (Spohn, 2000). In the frame of this PhD, we are interested by the corrected form from Sokolov *et al.* (2009) of the LAD equation

$$\frac{dp^\mu}{d\tau} = f_L^\mu + f_{rad}^\mu \quad (2.32)$$

$$\frac{dx^\mu}{d\tau} = \frac{p^\mu}{m} + \tau_0 \frac{P_{Cs}}{P_{cl}} \frac{f_L^\mu}{m} \quad (2.33)$$

where $f_L^\mu = \frac{e}{m} F_\nu^\mu p^\nu$ is the Lorentz force four-vector and $f_{rad}^\mu = \frac{I p^\mu}{mc^2}$ is the radiation friction force four-vector. τ is the proper time defined as $\gamma = dt/d\tau$ in the comoving Lorentz frame and $\tau_0 = \frac{2}{3} \frac{e^2}{4\pi\epsilon_0 mc^3}$. The power radiated (P_{Cs}) is already defined in Eq.(2.28) as the product of the classical radiated power $P_{cl} = 2\alpha_f mc^2 \chi_e^2 / 3\tau_c$ and a quantum correction term $g(\chi_e)$ defined in Eq. (2.30).

2.1.3 Implementation of the continuous model

In order to implement the system of Eqs. (2.32)-(2.33) in a PIC code, [Sokolov et al. \(2009\)](#) rewrote it in terms of three-vectors

$$\frac{d\mathbf{p}}{dt} = \mathbf{f}_L + e\delta\mathbf{v} \times \mathbf{B} - \frac{\gamma^2}{c^2}\mathbf{v}(\delta\mathbf{v} \cdot \mathbf{f}_L) \quad (2.34)$$

$$\frac{d\mathbf{x}}{dt} = \mathbf{v} + \delta\mathbf{v} \quad (2.35)$$

where \mathbf{f}_L and $\delta\mathbf{v}$ are defined by

$$f_L = e(\mathbf{E} + \mathbf{v} \times \mathbf{B}) \quad (2.36)$$

$$\delta\mathbf{v} = \frac{\tau_0}{m} \frac{\mathbf{f}_L - [(\mathbf{v} \cdot \mathbf{f}_L)/c^2]\mathbf{v}}{1 + \tau_0(\mathbf{v} \cdot \mathbf{f}_L)/mc^2} \quad (2.37)$$

and the classical radiated power $P_{cl} = \gamma^2(\delta\mathbf{v} \cdot \mathbf{f}_L)$. In the numerical scheme by [Sokolov et al. \(2009\)](#), the terms accounting for the radiation reaction, $e\delta\mathbf{v} \times \mathbf{B}$ and $\gamma^2\mathbf{v}(\delta\mathbf{v} \cdot \mathbf{f}_L)/c^2$, are evaluated at the n -th time step by

$$\mathbf{f}_L^n = \frac{e}{m}(\mathbf{E}^n + \mathbf{v}^n \times \mathbf{B}^n) \quad (2.38)$$

$$\delta\mathbf{v}^n = \frac{\tau_0}{m} \frac{\mathbf{f}_L^n - [(\mathbf{v}^n \cdot \mathbf{f}_L^n)/c^2]\mathbf{v}^n}{1 + \tau_0(\mathbf{v}^n \cdot \mathbf{f}_L^n)/mc^2} \quad (2.39)$$

The usual particle pusher (see Sec. 1.4) is first activated and provides a momentum $\tilde{p}^{n+1/2}$, that does not yet account for radiation loss. The radiation reaction term is added after the classical particle pusher and enables to update the particles' momentum, now accounting for radiation reaction

$$p^{n+1/2} = \tilde{p}^{n+1/2} + \Delta t [e\delta\mathbf{v}^n \times \mathbf{B}^n - \gamma^{n2}\mathbf{v}^n(\delta\mathbf{v}^n \cdot \mathbf{f}_L^n)/c^2] \quad (2.40)$$

The particle's velocity $v^{n+1/2}$ and position x^{n+1} are then updated

$$v^{n+1/2} = \frac{p^{n+1/2}}{m\sqrt{1 + \left(\frac{p^{n+1/2}}{mc}\right)^2}} \quad (2.41)$$

$$x^{n+1} = x^n + \Delta t v^{n+1/2} + \delta v^n \quad (2.42)$$

In the PIC code CALDER, a simplified version of this algorithm is employed. It is assumed that the term $e\delta\mathbf{v} \times \mathbf{B}$ in Eq. (2.34) is small enough to be neglected. This assumption is checked by [Lobet \(2015\)](#) for the interaction of a single electron with a counter-propagating circularly polarized electromagnetic pulse. The remaining term $\gamma^2\mathbf{v}(\delta\mathbf{v} \cdot \mathbf{f}_L)/c^2 = P_{rad}\mathbf{v}/c^2$ is evaluated from the expression derived in the quantum regime (Eq. 2.28). This simplification enables to have a smooth transition when we couple the continuous and discontinuous descriptions in Sec. 2.1.4. To summarize, firstly the electron quantum parameter is calculated

$$\chi^n = \frac{\gamma^n}{E_S} \sqrt{\left(\mathbf{E}_{\parallel}^n/\gamma^n\right)^2 + \left(\mathbf{E}_{\perp}^n + \mathbf{v}^n \times \mathbf{B}^n\right)^2} \quad (2.43)$$

Secondly, the radiation reaction is determined

$$f_{rad}^n = -\frac{P_{clg}(\chi^n) v^n}{c^2} \quad (2.44)$$

Thirdly, the electron velocity ($v^{n+1/2}$) is updated after the calculation by the classical particle pusher ($\tilde{v}^{n+1/2}$)

$$v^{n+1/2} = \tilde{v}^{n+1/2} - \frac{\Delta t f_{rad}^n}{m \gamma^{n+1/2}} \quad (2.45)$$

2.1.4 Implementation of the discontinuous model

When a relativistic electron travels through a strong field such that its quantum parameter $\chi_e \simeq 1$, the photon spectra significantly changes compared to the case $\chi_e \ll 1$ as shown in Sec 2.1.1. Those photons have an energy comparable to the electron kinetic energy and the recoil induced by each emission event must be accounted individually since it induces discontinuities of the electron trajectory. In practice, this is done with a Monte Carlo module that is added in the time loop of the PIC code. The implementation done in the code CALDER is similar to the one done by [Duclous et al. \(2011\)](#) and was done by [Lobet et al. \(2016\)](#). It follows the efforts carried out by other research groups such as [Kirk et al. \(2009\)](#); [Nerush et al. \(2011\)](#); [Blackburn et al. \(2014\)](#); [Ji et al. \(2014b\)](#); [Wallin et al. \(2015\)](#) and [Vranic et al. \(2016\)](#).

The emission of photons is described by an optical depth, denoted by τ_e . It is initially set to zero and grows according to Eq. (2.46) which relies on the emission rate in Eq. (2.11), rewritten as a function of the quantum parameter only

$$\frac{d\tau_e}{dt} = \int_0^{\chi_e} \frac{d^2 N_{Cs}}{d\chi_\gamma dt} d\chi_\gamma \quad (2.46)$$

A final optical depth $\tau_e^f = -\log(1 - \xi)$ is sampled from a random number in the interval $\xi \in (0, 1)$. In order to avoid numerical approximation issues when $\tau_e^f \rightarrow 0$, it is necessary to set a lower limit for it (10^{-100} in the code). When this final optical depth is reached, a photon is emitted, the macro-particle's optical depth is set to zero and the process can start again. Once a photon is emitted, its quantum parameter is sampled by the classical method of cumulative distribution function inversion. From a random number in the interval $\xi' \in (0, 1)$, the photon quantum parameter χ_γ is obtained by solving

$$\xi' = \frac{\int_0^{\chi_\gamma} F(\chi_e, \chi'_\gamma) d\chi'_\gamma}{\int_0^{\chi_e} F(\chi_e, \chi'_\gamma) d\chi'_\gamma} \quad (2.47)$$

where the expression of $F(\chi_e, \chi_\gamma)$ comes from Eq. (2.24). The photon energy is deduced as $\gamma_\gamma = \gamma_e \chi_\gamma / \chi_e$ (see Eq. 2.7, valid for relativistic electrons). The new macro-photon is initialized at the same position as the electron and with the same statistical weight. It is emitted parallel to the electron propagation direction. The electron momentum after emission (\mathbf{p}_f) is then deduced from its value before emission (\mathbf{p}_i) and the photon momentum: $\mathbf{p}_f = \mathbf{p}_i - \hbar \mathbf{k}$ with $\hbar \mathbf{k} = \gamma_\gamma m c \mathbf{p}_i / |\mathbf{p}_i|$. This algorithm enables momentum conservation but does not ensure energy conservation. The error done can be evaluated as $\delta E = (\gamma_f^2 - (\gamma_i - \gamma_\gamma)^2)^{1/2} \simeq (\gamma_\gamma / \gamma_i)^{1/2}$ for a relativistic electron ($\gamma_i \gg 1$).

This sampling method favors the emission of low-energy photons which weakly impact the simulation outcome, especially the production of electron-positron pairs. For this reason, the energy carried by photons with a low quantum parameter can be neglected.

In the PIC code CALDER, this lower limit χ_γ^{\min} is determined such that the energy carried by them is lower than $\epsilon = 10^{-9}$

$$\frac{\int_0^{\chi_\gamma^{\min}} F(\chi_e, \chi_\gamma) d\chi_\gamma}{\int_0^{\chi_e} F(\chi_e, \chi_\gamma) d\chi_\gamma} \leq \epsilon \quad (2.48)$$

The Monte Carlo time step is based on the duration of an emission event (τ_{em}) evaluated as

$$\frac{d\tau_e}{dt}(\chi_e) \simeq \frac{\tau_e^f}{\tau_{em}} \quad (2.49)$$

It can be lower than the PIC code time step, which implies to do subcycling. The increased number of events is computationally demanding but enables to treat them all.

The continuous and discontinuous photon emission can be coupled as suggested by [Duclos et al. \(2011\)](#). One can define a quantum parameter threshold χ_{th} above (resp. below) which photons are emitted by the discontinuous (resp. continuous) model. In practice this limit is set to $\chi_{th} = 10^{-3}$ in the PIC code CALDER. The function F is tabulated in advance as its calculation during the simulation is too time consuming.

2.2 Pair creation by the nonlinear Breit-Wheeler process

We now move on to the modeling and implementation of the Breit-Wheeler electron-positron pair generation process, believed to prevail for ultra-relativistic laser intensities $\geq 10^{23} \text{ W/cm}^2$. A brief paragraph is also devoted to the electromagnetic Trident electron-positron pair generation but it is not implemented in the Particle-In-Cell code CALDER. It is worth to mention that this latter process is induced by an electromagnetic field and is therefore different from the Coulomb Trident implemented in Chap. 3.

2.2.1 Physical Model

The nonlinear Breit-Wheeler process ($\gamma + n\omega \rightarrow e^- + e^+$) is also known as multi-photon Breit-Wheeler ([Breit and Wheeler, 1934](#)). It involves the decay of an energetic photon in an electron-positron pair as it travels in a strong electromagnetic field. The formalism required to derive emission rates accounting for this process are similar to the one presented for the nonlinear inverse Compton in Sec. 2.1. The importance of quantum effects affecting a photon depends on its quantum parameter χ_γ already defined in Eq. 2.6

$$\chi_\gamma = \frac{\gamma_\gamma}{E_S} |\mathbf{E}_\perp + \mathbf{v} \times \mathbf{B}| \quad (2.50)$$

Similarly to the modeling presented for the nonlinear inverse Compton scattering, it is required to formulate two hypothesis. Firstly, the external field triggering pair production is assumed to be quasistatic and uniform, implying that its normalized amplitude $a_L \gg 1$. Secondly, a_L is supposed to be negligible compared to the normalized Schwinger field $eE_s/m\omega_0 c \simeq 4 \times 10^5$. For a hard photon of quantum parameter χ_γ , the rate of emission of positrons with a quantum parameter χ_{e^+} is given by [Reiss \(1962\)](#) or by [Erber \(1966\)](#) as

$$\frac{d^2 N_{nBW}}{d\chi_{e^+} dt} = \frac{1}{\pi\sqrt{3}} \frac{\alpha_f mc^2}{\hbar\gamma\chi_\gamma} \left\{ \int_x^{+\infty} \sqrt{s} K_{1/3} \left(2s^{3/2}/3 \right) ds - \left[\left(2 - \chi_\gamma x^{3/2} \right) K_{2/3} \left(2x^{3/2}/3 \right) \right] \right\} \quad (2.51)$$

where $x = (\chi_\gamma/\chi_{e^+}\chi_{e^-})^{2/3}$ and χ_{e^\pm} denotes the quantum parameters of the created positron and electron. One can note that this expression is symmetric in χ_{e^+} and χ_{e^-} . The relation $\chi_\gamma = \chi_{e^+} + \chi_{e^-}$ enables to express the emission rate as a function of only one quantum parameter (χ_{e^+} or χ_{e^-}). The integration on χ_{e^+} of the differential emission rate in Eq. (2.51) provides the total emission rate of electron-positron pairs (Ritus, 1985)

$$\frac{dN_{nBW}}{dt} = \int_{\chi_{e^+}^{min}}^{\chi_{e^+}^{max}} \frac{d^2 N_{nBW}}{d\chi_{e^+} dt} d\chi_{e^+} \quad (2.52)$$

$$= \frac{\alpha_f mc^2}{\hbar} \frac{\chi_\gamma}{\gamma_\gamma} T_{nBW}(\gamma_\gamma, \chi_\gamma) \quad (2.53)$$

where the function $\chi_\gamma \rightarrow T_{nBW}(\chi_\gamma)$ is defined by

$$T_{nBW}(\gamma_\gamma, \chi_\gamma) = \frac{1}{\pi\sqrt{3}} \frac{1}{\chi_\gamma^2} \int_{\chi_{e^+}^{min}}^{\chi_{e^+}^{max}} \int_x^{+\infty} \sqrt{s} K_{1/3} \left(2s^{3/2}/3 \right) ds - \left[\left(2 - \chi_\gamma x^{3/2} \right) K_{2/3} \left(2x^{3/2}/3 \right) \right] d\chi_{e^+} \quad (2.54)$$

where K_ν denotes modified Bessel functions of order ν . $\chi_{e^+}^{min} = \chi_\gamma/\gamma_\gamma$ denotes the minimum quantum parameter of the positron (achieved for $\gamma_{e^+} \rightarrow 1$) and its maximum quantum parameter is $\chi_{e^+}^{max} = \chi_\gamma(1 - 1/\gamma_\gamma)$ (achieved for $\gamma_{e^-} \rightarrow 1$). An alternative expression of T_{nBW} is provided by Erber (1966)

$$T_{nBW}(\chi_\gamma) = \frac{0.16}{\chi_\gamma} K_{1/3}^2 \left(\frac{4}{3\chi_\gamma} \right) \quad (2.55)$$

These functions are plotted in Fig. 2.5(a,b) assuming a uniform external field of normalized amplitude $eB_L/m\omega_0 = 100$. The first striking feature of the emission rate in Fig. 2.5(a) is its symmetry with respect to $\chi_{e^+}/\chi_\gamma = 0.5$. The second thing to note is the position of the emission rate peak. It is located on the symmetry axis for $\chi_\gamma \leq 1$ and close to the two bounds of the spectra for $\chi_\gamma \geq 1$. The two formulas provided either by Erber (1966)

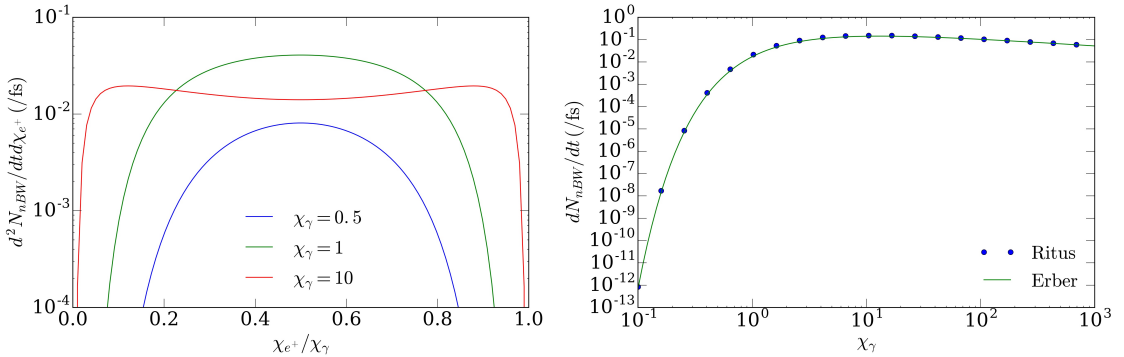


Figure 2.5: (a) Rate of positron emission as a function of the photon (χ_γ) and the positron (χ_{e^+}) quantum parameters (Eq. (2.51)); (b) Rate of emission integrated on χ_{e^+} as expressed in Eq. (2.51) (dots) and in Eq. (2.55) (solid curve). The external field is assumed to be uniform and of normalized amplitude $a_L = 100$.

and by Ritus (1985) are represented in Fig. 2.5(b). They agree very well on the interval $\chi_\gamma \in (10^{-1}, 10^3)$. The emission rate rises significantly for $\chi_\gamma \leq 1$, reaches a maximum for

$\chi_\gamma = 10$ and decreases slowly for $\chi_\gamma \geq 10$.

2.2.2 Monte Carlo implementation in the PIC code calder

The implementation of the nonlinear Breit-Wheeler process in the PIC code CALDER was performed by [Lobet et al. \(2016\)](#). Photons are treated as usual macro-particles and their quantum parameter is updated through a shape factor every time steps.

Following the same technique used for the emission of photons by nonlinear inverse Compton scattering and presented in Sec 2.1.4, the pair generation is associated with an optical depth τ_γ . It is initially set to zero and then grows according to the rate of emission recalled in the former subsection

$$\frac{d\tau_\gamma}{dt} = T_{nBW}(\chi_\gamma) \quad (2.56)$$

Once it reaches a final optical depth $\tau_\gamma^f = -\log(1 - \xi)$ sampled from a random number $\xi \in (0, 1)$ a pair is created and the photon is suppressed. The positron quantum parameter χ_{e^+} is determined by the common technique of cumulative distribution function inversion. From a random number $\xi' \in (0, 1)$, χ_{e^+} is obtained by solving

$$\xi' = \left(\int_{\chi_{e^+}^{min}}^{\chi_{e^+}} \frac{d^2 N_{nBW}}{d\chi'_{e^+} dt} d\chi'_{e^+} \right) / \left(\int_{\chi_{e^+}^{min}}^{\chi_{e^+}^{max}} \frac{d^2 N_{nBW}}{d\chi'_{e^+} dt} d\chi'_{e^+} \right) \quad (2.57)$$

The electron quantum parameter is deduced with the relation $\chi_{e^-} = \chi_\gamma - \chi_{e^+}$. The new electron and the new positron are initialized at the same position as the photon, with the same statistical weight. Their energy is deduced by the relation $\gamma_{e^\pm} = \gamma_\gamma \chi_{e^\pm} / \chi_\gamma$. They are assumed to have the same propagation direction as the photon $p_{e^\pm} = \sqrt{\gamma_{e^\pm}^2 - 1} \mathbf{k} / |\mathbf{k}|$. The Monte Carlo time step is based on the duration of an emission event (τ_{em}) evaluated as

$$\frac{d\tau_\gamma}{dt}(\chi_\gamma) \simeq \frac{\tau_\gamma^f}{\tau_{em}} \quad (2.58)$$

It is usually smaller than the PIC code time step and therefore requires to do subcycling, in order to describe all pair creation events. As for the implementation of the synchrotron emission, the function T is also pre-tabulated before the simulation to spare computational time.

2.3 Pair creation by the electromagnetic Trident process

Relativistic electrons travelling in a strong field can directly emit an electron positron pair by the electromagnetic Trident process. It is a second order process since it involves an intermediary virtual photon. The total emission rate is provided by [Erber \(1966\)](#)

$$\frac{dN_T}{dt}(\chi_e) = 0.32\alpha_f^2 \frac{2mc^2}{\hbar} \frac{a_L}{E_S} \Omega(\chi_e) \quad (2.59)$$

where $\Omega(\chi_e)$ is defined by

$$\Omega(\chi_e) = \int_0^{+\infty} u^{-2} W\left(\frac{u}{\chi_e}\right) K_{1/3}^2\left(\frac{4}{3u}\right) du \quad (2.60)$$

$$W(x) = xK_0(x)K_1(x) - \frac{x^2}{2} [K_1^2(x) - K_0^2(x)] \quad (2.61)$$

where K_ν are modified Bessel functions of order ν . The function $\chi_e \rightarrow \Omega(\chi_e)$ has a simpler expression in the limit $\chi_e \ll 1$ and $\chi_e \gg 1$ ([Erber, 1966](#))

$$\Omega(\chi_e) = \begin{cases} \frac{\pi^{5/2}}{16} (3\chi_e)^{1/4} \exp\left[-8(3\chi_e)^{-1/2}\right] & \text{if } \chi_e \ll 1 \\ \frac{\pi^2}{2} \ln \chi_e & \text{if } \chi_e \gg 1 \end{cases} \quad (2.62)$$

Fig. 2.6 displays the number of pairs created per time unit as a function of the incident

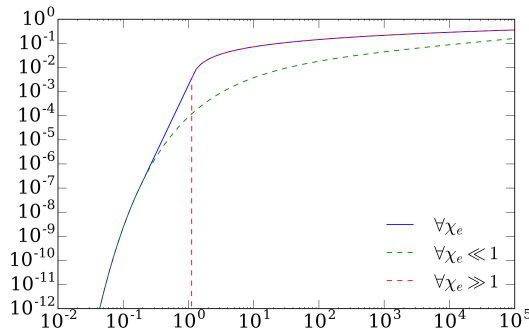


Figure 2.6: dN/dt : number of electron positron pairs created by the electromagnetic trident process as a function of the incident electron quantum parameter. The blue line illustrates Eq. (2.59) and the two others illustrate Eq. (2.62).

electron quantum parameter. It is assumed that the external field is uniform and of normalized amplitude $eB_L/m\omega_0 = 100$. Fig. 2.6 evidences that the formula (2.62) suggested in the limit $\chi_e \ll 1$ is a very good approximation to the more general formula ($\forall \chi_e$) in Eq. (2.59). In the limit $\chi_e \gg 1$, the rate of emission rises slowly ($\propto \log \chi_e$), such that it becomes negligible compared to the Breit-Wheeler ([Lobet \(2015\)](#)). This process is not implemented in the PIC code CALDER.

Conclusions

This chapter is dedicated to the modeling of radiative and QED processes induced in an electromagnetic field of strong amplitude and their implementation in the Particle-In-Cell code CALDER. Firstly, we deal with nonlinear inverse Compton scattering. We present the classical and quantum formula accounting for the photon emission rate and how they are introduced within the Particle-In-Cell framework. Secondly, we recall the theoretical formalism to include the Breit-Wheeler electron-positron pair generation mechanism.

As a perspective, it is worth to mention recent initiatives to question the key hypothesis formulated in the modeling of the aforementioned processes ([Di Piazza et al., 2018](#); [Ilderton et al., 2018](#); [Aleksandrov et al., 2018](#)). This assumption is formulated in Sec. 2.1.1 and is also known as Local Constant Field Approximation (LCFA). The goal of these studies is to improve the simulation capabilities of numerical codes employed to understand

experiments involving relativistic laser-plasma interaction.

Chapter 3

Processes induced in a Coulomb atomic field

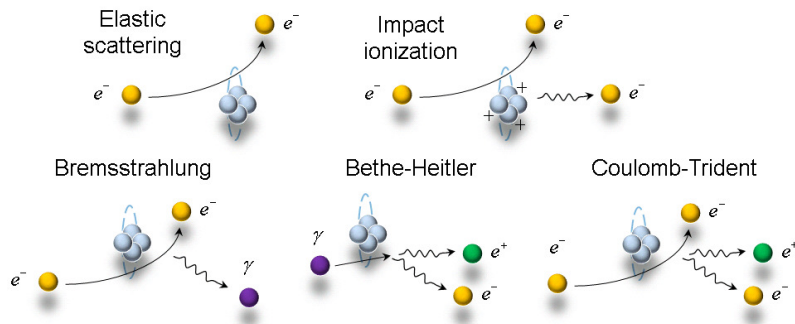


Figure 3.1: Processes triggered by the interaction of particles with a Coulomb atomic field.

The Particle-In-Cell (PIC) method has become the most widely used technique for simulating plasma physics ([Birdsall and Langdon, 1991](#)). Since it is based on first principle equations (Klimontovich and Maxwell), it can be employed in a variety of contexts. From an academical point of view, it embodies the ideal tool to consider different kind of plasma instabilities. From a practical point of view, it enables to interpret and plan ahead laser-plasma experiments involving the building of large and expensive infrastructures. Such experiments are related to applied research domains such as inertial confinement fusion ([Lindl, 1995](#)) and plasma-based particle accelerators ([Esarey *et al.*, 1996](#)). The continuous advances in laser intensity enable to tackle other topics such as the laboratory reproduction of astrophysical scenarios ([Blandford and McKee, 1977](#)), quantum electrodynamics, nuclear and particle physics ([Di Piazza *et al.*, 2012](#)).

The PIC approach, however, is computationally expensive such that the spatial resolution usually employed is a Debye length and does not allow to take into account binary Coulomb collisions between charged particles, let alone the generation of high-energy photons and positrons expected in high-Z materials driven at relativistic intensities ($\geq 10^{18} \text{ Wcm}^{-2}$). To cope with this issue it was suggested by [Takizuka and Abe \(1977\)](#) to implement those effects in PIC codes via a Monte Carlo macro-particle pairing scheme. Even though it requires further developments, *e.g.* to address relativistic plasmas or non-equally weighted macro-particles, it enables an accurate self-consistent description of the Coulomb collisions and photon/positron generation processes arising in laser-plasma interactions. The principle of this method is general and can be introduced at the end of Chap.2. It can be applied to any process provided it can be adequately modeled within the

PIC framework. Several enhancements of this Monte Carlo pairing scheme are proposed in the literature ([Nanbu, 1997](#); [Nanbu and Yonemura, 1998](#); [Sentoku and Kemp, 2008](#); [Peano et al., 2009](#); [Pérez et al., 2012](#)).

This chapter will deal with the numerical modeling of those processes (see Fig. 3.1) induced in a Coulomb atomic field and their implementation in the PIC code CALDER. One section is devoted to each mechanism. We are interested in elastic scattering between charged particles (Sec. 3.1), electron-ion impact ionization (Sec. 3.2), the Bremsstrahlung process where electrons generate photons (Sec. 3.3) which may decay into electron-positron (e^-e^+) pairs by the Bethe-Heitler process (Sec. 3.4) and the Coulomb Trident process involving the direct emission of an (e^-e^+) pair by an electron (Sec. 3.5). Sec. 3.6 is devoted to the competition of the two pair creation mechanisms in a solid target.

3.1 Elastic scattering

Collisions are taken into account by a Monte Carlo module inserted in a PIC code (see Sec. 1.6.2 for a general introduction). They are modeled as random events following a theoretical cross-section. Their sampling takes place every time steps in every mesh cell and involves a pair of macro-particles (electrons, ions or photons). It is considered representative of the desired distribution if one employs a large number of macro-particles. The model of Nanbu (1997) introduced hereafter describes the basic elastic scattering between two macro-particles which are assumed to be located in a given mesh cell at some time step.

3.1.1 Nanbu's theory for Debye's screening

Let us start by the definition of some notations denoting two macro-particles experiencing a simple scattering. The four momentum vector of the first (resp. second) particle is indexed with 1 (resp. 2) as precised in Tab. 3.1. The variables without exponent are those for the laboratory frame (K) whereas those with a * exponent denote the same variables in the center-of-mass frame (K^*). The same variables after the scattering are denoted with a index f whereas we leave no index before the scattering. The macro-particles' mass

Reference frame	Laboratory (K)	Center-of-mass (K^*)
incident first particle	$(\mathbf{p}_1, \gamma_1/c)$	$(\mathbf{p}_1^*, \gamma_1^*/c)$
deflected first particle	$(\mathbf{p}_{1f}, \gamma_{1f}/c)$	$(\mathbf{p}_{1f}^*, \gamma_{1f}^*/c)$
incident second particle	$(\mathbf{p}_2, \gamma_2/c)$	$(\mathbf{p}_2^*, \gamma_2^*/c)$
deflected second particle	$(\mathbf{p}_{2f}, \gamma_{2f}/c)$	$(\mathbf{p}_{2f}^*, \gamma_{2f}^*/c)$
polar-azimuthal angles	(θ, ϕ)	(θ^*, ϕ^*)
multiple scattering angle	χ	χ^*

Table 3.1: Notations for variables in the laboratory and center-of-mass frame

m_1 and m_2 are arbitrary, as well as their momenta p_1 and p_2 and charges q_1 and q_2 . The azimuthal and polar angles after a simple scattering are denoted by θ^* and ϕ^* . The multiple scattering angle is χ^* defined by $\cos \chi^* = \mathbf{p}_1^* \cdot \mathbf{p}_{1f}^* / |\mathbf{p}_1^*|^2$. The calculations are performed in the center-of-mass frame as it reduces the calculations. Indeed, both macro-particles have opposite initial momentum $\mathbf{p}_1^* = -\mathbf{p}_2^*$ and final momentum $\mathbf{p}_{1f}^* = -\mathbf{p}_{2f}^*$. The velocity of the frame (K^*) is defined as

$$\mathbf{v}_C = \frac{\mathbf{p}_1 + \mathbf{p}_2}{m_1 \gamma_1 + m_2 \gamma_2} \quad (3.1)$$

With a Lorentz transform, one can deduce the four momentum of the first macro-particle in the center-of-mass frame (K^*) (and therefore the second by the symmetry mentioned previously)

$$\mathbf{p}_1^* = \mathbf{p}_1 + \left[\frac{\gamma_C - 1}{v_C^2} (\mathbf{v}_C \cdot \mathbf{v}_1) - \gamma_C \right] m_1 \gamma_1 \mathbf{v}_C \quad \gamma_1^* = (1 - \mathbf{v}_C \cdot \mathbf{v}_1 / c^2) \gamma_C \gamma_1 \quad (3.2)$$

Usually the time and spatial steps of a PIC code are too large to account for every simple scattering events. Based on the previous work of Nanbu (1997); Nanbu and Yone-mura (1998) the model implemented accounts for the multiple scattering over one spatial and time step. In this work a probability density function of the multiple scattering angle

is fitted from Monte Carlo simulations of N successive and independent scatterings in a plasma. Let χ^* denote the scattering angle in the frame (K^*) this fitted function is defined as

$$f(\chi^*) = \frac{A}{4\pi \sinh A} \exp(A \cos \chi^*) \quad (3.3)$$

The variable A is the solution of equation $\coth A - A^{-1} = \exp(-s_{12})$. The factor s_{12} is related to the mean-squared scattering angle $\langle \theta^{*2} \rangle$ by the relation $s_{12} = N\langle \theta^{*2} \rangle / 2$. The function f is therefore a function of a unique parameter, s_{12} which is deduced from two equalities (3.4) and (3.5). The first one (3.4) comes from the adiabatic invariant $\sigma v_{rel} \gamma_1 \gamma_2$ (Landau and Lifshitz, 1975). It provides the number of collisions N during a time step Δt

$$N = \sigma^* v_{rel}^* \frac{\gamma_1^* \gamma_2^*}{\gamma_1 \gamma_2} n_2 \Delta t \quad (3.4)$$

The variable $v_{rel} = |\mathbf{v}_1 - \mathbf{v}_2|$ is a scalar that defines the relative velocity between the two macro-particles. The second equation that enables to derive the parameter s_{12} comes from the relativistic scattering cross section σ^* in the center-of-mass frame. It is taken from the work of Frankel *et al.* (1979) and follows a distribution denoted $d\sigma^*/d\Omega^*$ defined in the limit of small scattering angles $\theta \ll 1$

$$\frac{d\sigma^*}{d\Omega^*} = \left(\frac{2q_1 q_2}{4\pi\epsilon_0} \frac{1 + v_1^* v_2^*/c^2}{p_1^* v_{rel}^*} \right)^2 \frac{1}{\theta^{*4}} \quad (3.5)$$

Ω^* denotes the solid angle after a simple scattering. This expression is integrated from θ_{min} to $\theta_{max} = 2\text{ rad}$. We then deduce that $\langle \theta^{*2} \rangle \propto \ln(2/\theta_{min}) \equiv \ln(\Lambda)$. The minimum scattering angle θ_{min} is associated with the inverse of the maximum impact parameter, L_D the Debye length, accounting for a Debye screening prevailing in an ionized plasma. For this reason we switch the notation θ_{min} to θ_D . The expression for s_{12} is obtained from the integration of (3.5) and substitution of (3.4) in the expression of $s_{12} = N\langle \theta^{*2} \rangle / 2$

$$s_{12} = \frac{n_2 \Delta t \ln \Lambda (q_1 q_2)^2}{4\pi\epsilon_0^2} \frac{v_{rel}^* \gamma_1^* \gamma_2^*}{\gamma_1 \gamma_2} \left(\frac{1 + v_1^* v_2^*/c^2}{p_1^* v_{rel}^*} \right)^2 \quad (3.6)$$

It can be simplified and expressed only as a function of the initial parameters of the problem in the laboratory frame. Knowing the expression of p_1^* and γ_1^* which are defined by (3.2), $\gamma_2^* = (1 - v_C v_2/c^2) \gamma_C \gamma_2$ and the center-of-mass velocity is given by (3.1) one can derive the following expression for the parameter s_{12} controlling the multiple scattering function defined in (3.3)

$$s_{12} = \frac{n_2 \Delta t \ln \Lambda (q_1 q_2)^2}{4\pi\epsilon_0^2 c^4 m_1 \gamma_1 m_2 \gamma_2} \frac{\gamma_C p_1^*}{m_1 \gamma_1 + m_2 \gamma_2} \left(1 + c^2 \frac{m_1 \gamma_1^* m_2 \gamma_2^*}{p_1^{*2}} \right)^2 \quad (3.7)$$

In this model of Nanbu (1997), screening effects appear in the Coulomb logarithm ($\ln \Lambda$) in Eq. (3.7). This term is heuristically calculated according to the method adopted by Lee and More (1984)

$$\ln \Lambda = \max \left[2, \frac{1}{2} \ln \left(1 + \frac{b_{max}^2}{b_{min}^2} \right) \right] \quad (3.8)$$

where b_{min} and b_{max} are the lower and upper impact parameter cutoffs. The maximum impact parameter is taken equal to the Debye length $b_{max} = L_D$. The minimum impact

parameter b_{min} is obtained by the relation $b_{min} = \max(\hbar/2p^*, b_0)$ with b_0 the impact parameter for a 2 rad scattering

$$b_0 = \frac{q_1 q_2}{4\pi\epsilon_0 c^2} \frac{\gamma_C}{m_1 \gamma_1 + m_2 \gamma_2} \left(\frac{m_1 \gamma_1^* m_2 \gamma_2^*}{p_1^{*2}} c^2 + 1 \right)^2 \quad (3.9)$$

The maximum value 2 is fixed in order to fit numerical results (for more details see [Lee and More \(1984\)](#)). The Debye length L_D is calculated every time steps in every cells and takes into account all species $L_D^{-2} = \sum_\alpha 4\pi n_\alpha q_\alpha^2 / T_\alpha$.

Once the Coulomb logarithm and s_{12} are determined, one can sample the multiple angle of scattering χ^* . This is done by inverting the cumulative distribution function associated with the probability density function $f(\chi^*)$ defined in (3.3). The azimuthal angle ϕ^* is sampled randomly in $(0, 2\pi)$ and the momentum of the deflected macro-particles is deduced from a rotation as shown by [Sentoku and Kemp \(2008\)](#)

$$\mathbf{p}_{1f}^* = -\mathbf{p}_{2f}^* = \begin{bmatrix} \frac{p_{1x}^* p_{1z}^*}{p_{1\perp}^*} & -\frac{p_{1y}^* p_{1z}^*}{p_{1\perp}^*} & p_{1x}^* \\ \frac{p_{1y}^* p_{1z}^*}{p_{1\perp}^*} & \frac{p_{1x}^* p_{1z}^*}{p_{1\perp}^*} & p_{1y}^* \\ -p_{1\perp}^* & 0 & p_{1z}^* \end{bmatrix} \begin{pmatrix} \sin \chi^* \cos \phi^* \\ \sin \chi^* \sin \phi^* \\ \cos \chi^* \end{pmatrix} \quad (3.10)$$

A Lorentz transform back to the laboratory frame provides the deflected momentum of the first macro-particle (and the second by symmetry)

$$\mathbf{p}_{1f} = \mathbf{p}_{1f}^* + \left[\frac{\gamma_C - 1}{v_C^2} (\mathbf{v}_C \cdot \mathbf{p}_{1f}^*) + m_1 \gamma_1^* \gamma_C \right] \mathbf{v}_C \quad (3.11)$$

The model of [Nanbu \(1997\)](#) generally describes the multiple scattering between a pair of charged macro-particles over a typical time step of a PIC simulation, given the plasma state of a mesh cell. This process is induced in a Coulomb atomic field which is assumed to be screened by a Debye potential. We will see in the next subsection that a different potential can be employed, especially one taking into account the screening of bound electrons.

3.1.2 Description of bound electron screening

The existing model of binary Coulomb collisions implemented in CALDER only describes charged particles interactions and, in particular, elastic interactions between free electrons and ionized atoms. This is easily seen by considering the parameter s_{12} presented in formula (3.7). Now it is well-known that neutral atoms can cause elastic scattering of electrons. To include this effect in a simple manner within the framework of [Pérez et al. \(2012\)](#) we recall that in formula (3.7) q_1 and q_2 represent the effective charges of the interacting particles while the Coulomb logarithm involves the screening angle of the Coulomb potential $\ln(2/\theta_{min})$.

For a macro-collision between an electron and an atom, the parameter s_{12} cancels as it is proportional to the product of the macro-particles charges ($s_{12} \propto q_1 q_2 = 0$). The multiple scattering distribution becomes

$$f(\chi^*) \simeq \exp [-(1 - \cos \chi^*) / s_{12}] / s_{12} \text{ as } s_{12} \rightarrow 0 \quad (3.12)$$

Since $s_{12} \rightarrow 0$, the function f is cancelled for all χ^* , except for three blow up points ($\chi^* = 0, \pi, 2\pi$). Numerically speaking, macro-particles are thus not deflected when they

are paired with neutral atoms and this raises a major issue.

There are therefore two refinements to operate in order to increase the range of validity of Nanbu (1997)'s model to arbitrary ionized atoms. The first one is to adapt the numerical scheme and overcome the nonexistent (and unphysical) scattering of particles when they are paired with neutral atoms. This can be quickly addressed by avoiding the cancellation of the parameter s_{12} and of the scattering distribution. We suggest to modify the charge q_2 of an ion in this formula: we simply replace it by the nucleus charge Z . With this refinement the scattering by a neutral atom is now taken into account but the information on the ion charge Z^* is lost. We will see however that it can be recovered in the next paragraph.

The second refinement consists in suggesting a consistent model accounting for bound electron screening. In Nanbu's model, screening effects only appear in the Coulomb logarithm $\ln \Lambda$ expressed in Eq. (3.8) in the form of a maximum impact parameter b_{max} equal to the Debye length L_D and proportional to the inverse of the Debye screening angle θ_D ($b_{max} \propto \theta_D^{-1}$). In order to get a screening angle consistently accounting for an arbitrary ionization degree, we refer to the work of Molière (1947) (written in German). He developed a mathematical theory on the multiple scattering of electrons by atoms which was later rephrased by Bethe (1953) (written in English).

Firstly, we describe how Molière determines a screening angle in the limit of electron scattering on a nucleus (he uses a Thomas-Fermi potential). Secondly we suggest to extend his result to a mixed Thomas-Fermi-Debye potential expressed as (Nardi and Zinamon, 1978)

$$V_{TFD} = \frac{Ze}{4\pi\epsilon_0 r} \left[\left(1 - \frac{Z^*}{Z}\right) \exp\left(-\frac{r}{L_{TF}}\right) + \frac{Z^*}{Z} \exp\left(-\frac{r}{L_D}\right) \right] \quad (3.13)$$

The parameters L_{TF} and L_D respectively denote the Thomas-Fermi and Debye lengths. In the limit of a neutral solid, this potential is reduced to the usual Thomas-Fermi one whereas in the limit of a fully ionized plasma, it is equivalent to the classical Debye one. For an arbitrary degree of ionization the potential V_{TFD} is an interpolation between both limits, depending on the ionization rate Z^*/Z . While this expression is purely heuristic, it enables to have a continuous description between the screened potential of a neutral and fully ionized atom.

Molière's theory for simple scattering

Let us first introduce notations. We are now working in the ion-rest frame where all variables are denoted with a ' as shown in Table 3.2. In order to keep consistent notations with the formalism of Nanbu, the electron variables are denoted by a subscript 1 and the ion variables are denoted by a subscript 2. The azimuthal and polar angles after a simple scattering are denoted by θ' and ϕ' . The multiple scattering angle (χ') is defined by $\cos \chi' = \mathbf{p}'_1 \cdot \mathbf{p}'_{1f} / |\mathbf{p}'_1|^2$. We denote by \mathbf{k}'_i and \mathbf{k}'_d the incident and deflected wave vectors. The screened differential scattering cross section derived in the first Born approximation for an arbitrary potential V reads (Molière, 1947)

$$\sigma(\theta') = \left(\frac{m_1 e}{2\pi\hbar^2} \right)^2 \left| \int e^{-i(\mathbf{k}'_d - \mathbf{k}'_i) \cdot \mathbf{r}} V(\mathbf{r}) d\mathbf{r} \right|^2 \quad (3.14)$$

Let us consider the case of a Thomas-Fermi potential defined by

$$V_{TF}(r) = \frac{Ze}{4\pi\epsilon_0 r} e^{-r/L_{TF}} \quad (3.15)$$

Reference frame	Laboratory (K)	Ion-rest (K')
incident first particle	$(\mathbf{p}_1, \gamma_1/c)$	$(\mathbf{p}'_1, \gamma'_1/c)$
deflected first particle	$(\mathbf{p}'_{1f}, \gamma'_{1f}/c)$	$(\mathbf{p}'_{1f}, \gamma'_{1f}/c)$
incident second particle	$(\mathbf{p}_2, \gamma_2/c)$	$(\mathbf{p}'_2, \gamma'_2/c)$
deflected second particle	$(\mathbf{p}'_{2f}, \gamma'_{2f}/c)$	$(\mathbf{p}'_{2f}, \gamma'_{2f}/c)$
polar-azimuthal angles	(θ, ϕ)	(θ', ϕ')
multiple scattering angle	χ	χ'

Table 3.2: Notations for variables in the laboratory and center-of-mass frame

The screened differential scattering cross section can be obtained from Eq. (3.14) and has the following closed-form for the Thomas-Fermi potential

$$\sigma_{TF}(\theta') = \sigma_{Ru}(\theta') K_{rel}(\theta') K_{scr,TF}(\theta') \quad (3.16)$$

with σ_{Ru} the Rutherford scattering cross-section, $K_{scr,TF}$ and K_{rel} are respectively screening and relativistic factors introduced by [Zeitler and Olsen \(1964\)](#) defined by

$$\begin{aligned} \sigma_{Ru}(\theta') &= \frac{4Z^2e^4}{4\pi\epsilon_0 m_1^2 v_1'^4} \frac{1}{(4\sin^2 \frac{\theta'}{2})^2}, \quad K_{rel}(\theta') = 1 - \beta_1'^2 \sin^2 \frac{\theta'}{2} \\ K_{scr,TF}(\theta') &= \frac{\left(4\sin^2 \frac{\theta'}{2}\right)^2}{\left(4\sin^2 \frac{\theta'}{2} + \theta_{TF}'^2\right)^2} \end{aligned} \quad (3.17)$$

The angle $\theta_{TF}' = \hbar/(p'_1 L_{TF})$ is defined as the Thomas-Fermi screening angle. It can also be defined from a first order partial wave expansion ([Molière, 1947](#))

$$\ln \theta_{TF}' = -\frac{1}{2} - \lim_{\theta_{TF}' \rightarrow \infty} \left\{ \int_0^{\theta_{TF}'} \frac{K_{scr,TF}(\theta')}{\theta'} d\theta' - \ln \theta_{TF}' \right\} \quad (3.18)$$

where the dependence of the term $K_{scr,TF}$ on the potential V_{TF} is provided by the formula

$$K_{scr,TF}(\theta') = \frac{(k\theta')^4}{4\alpha_f^2} \left| \int_0^\infty J_0(k\theta'r) [e^{i\Phi(r)} - 1]^2 \right|^2 \quad (3.19)$$

$$\Phi(r) = -\frac{2}{\hbar v_1'} \int_r^\infty \frac{V_{TF}(\rho)}{(\rho^2 - r^2)^{1/2}} \rho d\rho \quad (3.20)$$

where $k = \hbar/p'_1$ and J_0 is a notation for the first kind Bessel function of order 0.

Having in mind the method used by Molière to define a screening angle θ_{TF}' from a given potential V_{TF} , we are eager to reproduce the calculations with the mixed Thomas-Fermi-Debye potential $V_{TFD} = (1-q)V_{TF} + qV_D$ with $q = Z^*/Z$ and V_D the Debye potential. This was already done by [Gremillet \(2001\)](#). In the limit of small angle scatterings, the

screening factor reads

$$K_{scr,TFD}(\theta') = (1 - q^2) \frac{\theta'^4}{(\theta'^2 + \theta'^2_{TF})^2} + q^2 \frac{\theta'^4}{(\theta'^2 + \theta'^2_D)^2} + 2q(1 - q) \frac{\theta'^4}{(\theta'^2 + \theta'^2_{TF})(\theta'^2 + \theta'^2_D)} \quad (3.21)$$

The screening angle θ'_{TFD} is derived employing formula (3.18) and provides ([Gremillet, 2001](#))

$$\theta'_{TFD} = \theta'^{\xi_{TF}}_{TF} \theta'^{\xi_D}_D \quad \text{with} \quad \begin{cases} \xi_{TF} = (1 - q)^2 - 2q(1 - q) / (\theta'^2_{TF}/\theta'^2_D - 1) \\ \xi_D = q^2 + 2q(1 - q) / (1 - \theta'^2_{TF}/\theta'^2_D) \end{cases} \quad (3.22)$$

From the theory of Molière we have a screening angle θ'_{TFD} accounting for a mixed Thomas-Fermi-Debye potential and therefore arbitrary ionized plasmas and solids. We choose to employ this screening angle θ'_{TFD} to improve the screening description in the theory of Nanbu. We replace in the Coulomb logarithm (formula (3.8)) the Debye screening angle θ_D by the Thomas-Fermi-Debye one θ_{TFD} .

Molière's theory for multiple scattering

The contribution of Molière is not limited to simple scatterings. He also built a theory describing multiple scattering of an electron beam in a solid. His work is a good benchmark for PIC simulated scattering in solids. Since we already introduced Molière's formalism, we present the main formulas he provides to describe multiple scattering in a solid. We are still working in the ion-rest frame where variables are marked with a ' superscript. The initial distribution of electrons is assumed to be mono-energetic forming a Dirac delta function $f(\chi', 0) = \delta(\chi')$ and obeys the transport equation for a cylindrical beam.

$$\frac{\partial f(\chi', s')}{\partial s'} = -n'_i f(\chi', s') \int \sigma(\theta') 2\pi \theta' d\theta' + n'_i \int f(\chi' - \theta', s') \sigma(\theta') d\theta' \quad (3.23)$$

The goal is to determine the probability $f(\chi', s')$ that after a distance s' , an electron is deflected by an angle χ' . The variable s' (without index) is the distance travelled by a particle of the beam and should not be confused with the parameter s_{12} introduced in the frame of Nanbu's framework. The result is derived in the limit of weak scatterings and irrespective of the cross-section expression. The full calculation was rephrased by [Bethe \(1953\)](#) and involves Bessel transforms. The analytical derivation is valid for a number of collisions ranging from ~ 5 to ~ 20 . It is expressed as an expansion that reads

$$f_M(\chi', s') \chi' d\chi' = \Theta' d\Theta' \left(f^{(0)}(\Theta') + \frac{1}{B} f^{(1)}(\Theta') + \frac{1}{B^2} f^{(2)}(\Theta') + \dots \right) \quad (3.24)$$

$$f^n(\Theta') = \frac{1}{n!} \int_0^\infty u J_0(u\Theta') \exp\left(-\frac{u^2}{4}\right) \left[\frac{u^2}{4} \ln \frac{u^2}{4}\right]^n du \quad \forall n \geq 0$$

Several parameters are introduced during the derivation. J_0 denotes a Bessel function of the first kind and of order 0. Θ' is a reduced angle defined by $\Theta' = B^{-1/2} \chi' / \theta'_c$ where B is the implicit solution of equation $B - \ln B = b$ with b a parameter defined as $b = \ln(1 - 2C + \theta'_c/\theta'_M)$. C is the Euler constant, θ'_M the Molière screening angle obtained after numerical integration of Eq. (3.18) for Molière's potential. θ'_c is defined such that

the probability of one scattering event at a higher angle is equal to 1. The momentum of the incident particle, its velocity and Lorentz factor have the usual notation p' , β' and γ' and the expression of θ'_M and θ'_c are

$$\theta'^2_M = \frac{\hbar^2}{(1.13p'L_{TF})^2} (1.13 + 3.76\alpha^2) \quad \theta'^2_c = \frac{4\pi_i s' Z (Z+1) e^4}{m^2 c^4 \beta'^4 \gamma'^2} \quad (3.25)$$

In practice we limit the expansion of (3.24) to the first terms f^0 , f^1 and f^2 . Indeed [Bethe \(1953\)](#) demonstrated that this approximation is enough to keep an accurate result in all cases (below 1%). For $n = 0$ the distribution f^0 is a Gaussian function with a variance $\theta'^2_c B$. The $n - th$ term of the sum, which is $B^{-n} f^n$, appears as a correction of decreasing significance as n increases.

The theoretical framework to implement and benchmark multiple scattering in a PIC code was presented in this subsection. The underlying modeling stands out from former results. Indeed, it provides a consistent way to describe screening effects from both free and bound electrons through the use of a mixed Thomas-Fermi-Debye potential. The theory of Molière for multiple scattering summarised here will be employed as a benchmark with PIC-simulated scattering of electron beams in Sec. 3.1.4. Before this, we report in the next subsection (3.1.3) how to perform the numerical implementation of those scattering events in a PIC code.

3.1.3 Monte Carlo implementation

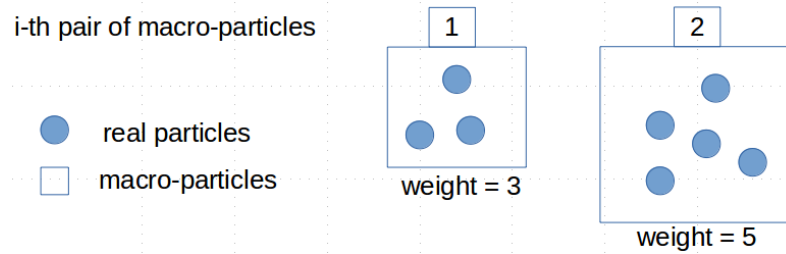


Figure 3.2: Monte Carlo pairing of macro-particles with different numerical weight.

The Monte Carlo module is called every time steps in every cells to compute the scattering of particles, pair by pair. In practice, macro-particles with different numerical weight can be paired and a sampling issue appears as stated first by [Nanbu and Yonemura \(1998\)](#). Let us introduce some notations from [Pérez et al. \(2012\)](#) and consider N_1 and N_2 macro-particles from species 1 and 2 within a mesh cell. Each macro-particle is indexed by i and its individual weight is denoted by W_{i1} for specie 1 or W_{i2} for specie 2. $N_{12} = \max(N_1, N_2)$ denotes the total number of pairs as described by [Nanbu and Yonemura \(1998\)](#). The weight is defined as the number of real particles represented by a macro-particle. From this definition, we deduce the local number densities for the two species: $n_1 = \sum_{i=1}^{N_1} W_{i1}$ and $n_2 = \sum_{i=1}^{N_2} W_{i2}$. The problem is illustrated in Fig. 3.2. For the sake of clarity, we consider two macro-particles with simple numerical weights (3 and 5), meaning they respectively represent 3 and 5 real particles. Physically speaking, there are three scattering events during this time step Δt . If one does not specify anything, the Monte Carlo module scatters both macro-particles. As a consequence it scatters 5 real particles of the second specie instead of 3 during the time step Δt . This over-estimation is compensated by a simple refinement. For each macro-particle of the pair, a scattering

probability is introduced to compensate for the weight difference

$$P_{i1} = \frac{W_{i2}}{\max(W_{i1}, W_{i2})} \quad P_{i2} = \frac{W_{i1}}{\max(W_{i1}, W_{i2})} \quad (3.26)$$

In the simplified case in Fig. 3.2, those probabilities are respectively $P_{i1} = 1$ and $P_{i2} = 3/5$. The addition of a probability changes the average time step of the macro-particles $\delta t_{i1} = P_{i1}\Delta t$ and $\delta t_{i2} = P_{i2}\Delta t$. The average time step for macro-particle number 1 is

$$\overline{\Delta t_1} = \frac{\sum_{i=1}^{N_{12}} W_{i1} \delta t_{i1}}{\sum_{i=1}^{N_1} W_{i1}} = \Delta t_1 \frac{n_{12}}{n_1} \quad \text{with} \quad n_{12} = \sum_{i=1}^{N_{12}} \min(W_{i1}, W_{i2}) \quad (3.27)$$

Symmetrically we get the average time step for macro-particle number 2: $\overline{\Delta t_2} = \Delta t_2 n_{12}/n_2$. Since we want to conserve energy and momentum on a large number of collisions, we impose $\overline{\Delta t_1} = \overline{\Delta t_2} = \Delta t$, the simulation time step. This modification restores symmetry between the two species 1 and 2 having different numerical weights. This can be seen in the new expression of the parameter s_{12} characterising the multiple scattering distribution. We have $s_{12} = s_{12}(\Delta t_1) = s_{21}(\Delta t_2)$ with

$$s_{12} = \frac{n_1 n_2}{n_{12}} \frac{\Delta t \ln \Lambda(q_1 q_2)^2}{4\pi\epsilon_0^2 c^4 m_1 \gamma_1 m_2 \gamma_2} \frac{\gamma_C p_1^*}{m_1 \gamma_1 + m_2 \gamma_2} \left(1 + c^2 \frac{m_1 \gamma_1^* m_2 \gamma_2^*}{p_1^{*2}}\right)^2 \quad (3.28)$$

All the elements to numerically implement multiple scattering in a PIC code were presented. They rely on a Monte Carlo algorithm added in the time loop of the PIC code. This module samples the cross-sections every time steps in every cells. It ensures, on average, to remain representative of the initial distribution even with macro-particles of different numerical weight.

3.1.4 Numerical tests with arbitrary ionized atoms

In this subsection, we are eager to illustrate the new models and implementations brought in the PIC code CALDER. Firstly we compare the scattering of electrons in a solid according to the model of Nanbu and the theory of Molière and find a resonable agreement. Secondly we study the influence of the plasma ionization state on particle scattering. To this purpose, we depict the scattering of electrons in plasmas with varying ionization rates and point out the relative influence of bound and free electron screening.

We compute the angle distribution of a mono-energetic electron beam (100 keV) propagating in copper of density 8.96 g.cm^{-3} in Fig. 3.3. The PIC simulations (blue curves) are compared to the multiple scattering theory of Molière (green curves plotted from formula (3.24)) and a Monte Carlo sampling of the angle-differential cross-section including Molière's screening (red histogram based on Eq. (3.21)). We recall that we are working in the ion-rest frame and that all quantities are denoted by a'. In the PIC simulations we propagate a mono-energetic electron beam along the x axis over a distance $s' = 0.5, 1$ and $26 \mu\text{m}$ and report its angle-resolved distribution. According to the theory of Molière, this corresponds to $N'_c = 10.1, 20.2$ and 505 collisions for the incident electrons. We observe that the PIC simulations tend to agree with the Monte Carlo sampling only for a large number of collisions. The difference observed for small number of collisions between Nanbu's model and Molière's theory comes from their different validity domains. We illustrate those validity domains in Fig. 3.4. Nanbu determined the multiple scattering distribution for a number of collisions $N'_c = 100 \rightarrow 3000$, which is much higher than for

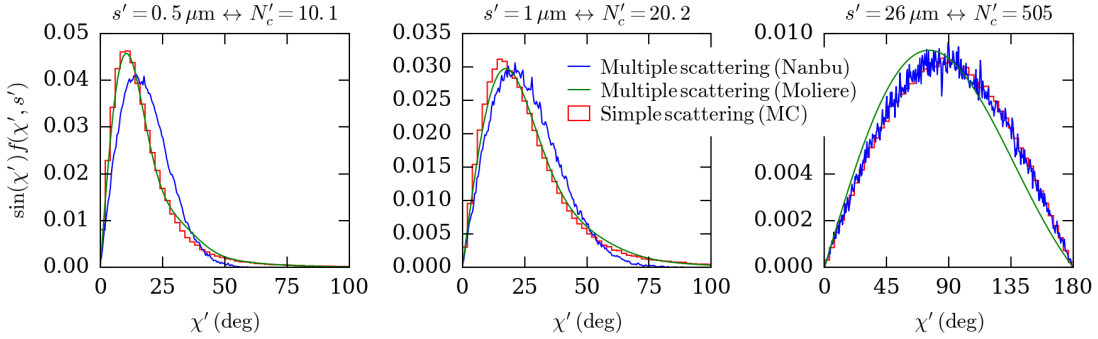


Figure 3.3: Angle distribution for a 100 keV electron beam in copper ($Z = 29$) with density $\rho = 8.96 \text{ g/cm}^3$ after (a) 10.01 (b) 20.2 and (c) 505 collisions. Comparison of the multiple scattering model of Nanbu (blue curves), of Molière (green curves) and the Monte Carlo sampling of Molière's formula for simple scattering (red histograms)

Molière ($N'_c = 5 \rightarrow 20$).

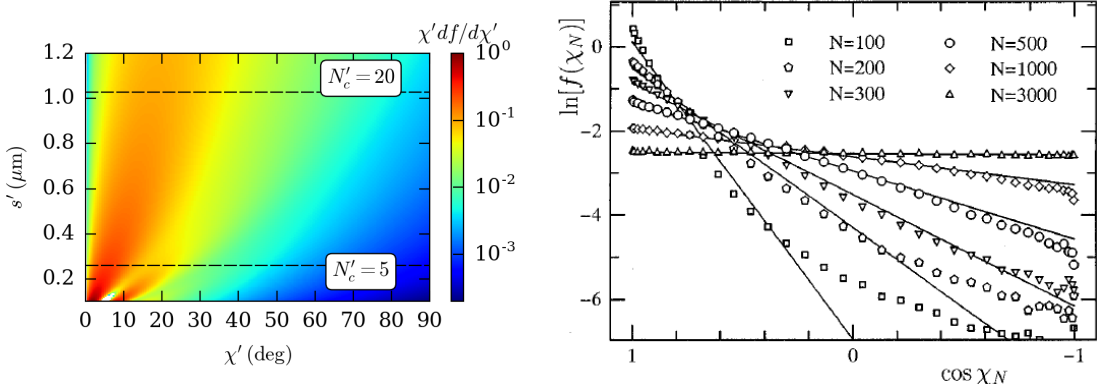


Figure 3.4: (a) Angle-distribution predicted by the theory of Molière with its range of validity ($5 \leq N'_c \leq 20$) (b) Fit employed in the PIC code (solid lines), based on Monte Carlo simulations (circles) and first determined by Nanbu (1997). In his formalism N denotes the number of collisions and χ_N the multiple angle of scattering after N collisions during a time step Δt .

We benchmarked the multiple scattering of an electron beam in a solid by comparing numerical PIC simulations with the theory of Molière. We are now eager to study the electron beam scattering in partially ionized plasmas. This illustrates the role of the screening angle θ_{TFD} we introduced in Sec. 3.1.2 to account for a consistent description of the free and bound electrons in the model of Nanbu.

The influence of the ionization degree is illustrated in Fig. 3.5. A mono-energetic (100 keV) electron beam propagates in copper of solid density (8.96 g.cm^{-3}). We choose rather short distances of propagation ($s = 0.25 \rightarrow 1 \mu\text{m}$) to remain in the validity range of Molière's multiple scattering theory. The number of collisions is defined by $N'_c = n_{is} \int 2\pi \sin \theta' \sigma' d\theta'$. In Fig. 3.5 it is determined for $Z^* = 0$. The different ionization degrees selected $Z^* = 0, 10, 20$ and 29 are chosen such that the screening angle of the mixed Thomas-Fermi-Debye potential varies significantly: $\theta_{TFD} = 3, 2, 1$ and $0.4 \times 10^{-8} \text{ rad}$. This corresponds to a screening length increasing from 21 to 140 pm. This raise of the

potential scale length allows collisions with a higher impact parameter to take place and we therefore observe that the scattering of the beam is more effective for a same distance travelled.

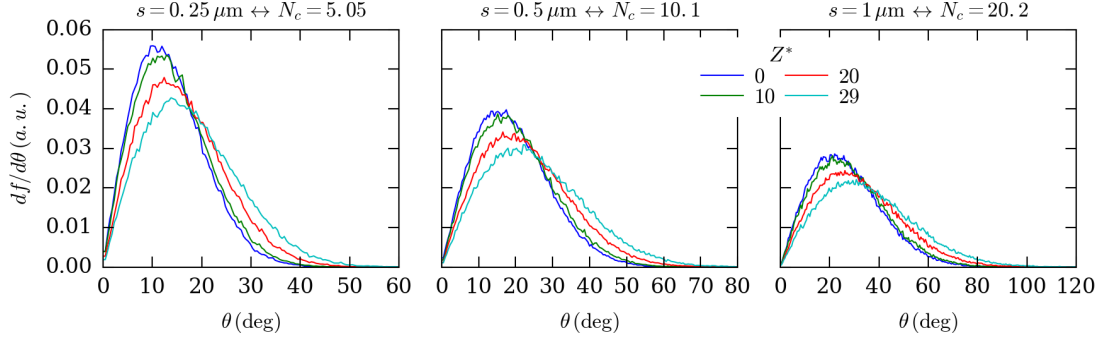


Figure 3.5: Angle distribution for a 100 keV electron beam in copper ($Z = 29$) with density $\rho = 8.96 \text{ g/cm}^3$ after (a) 5.05 (b) 10.1 and (c) 20.2 collisions. The degree of ionization is gradually raised $Z^* = 0, 10, 20$ and 29 and consequently modifies the screening angle θ_{TFD} defined in formula (3.22).

Conclusion This section summarises the theory, implementation and provides numerical tests to assess the validity of elastic scattering in a PIC code. The theory relies on the work of Nanbu (1997). It is based on an adequate multiple scattering distribution that is sampled by a Monte Carlo module added in the PIC code time loop. We benchmarked it with the theory of Molière on a test scenario of electron beam scattering into a solid. We also demonstrated that the scattering of an electron beam in a partially ionized plasma rises with its ionization degree. This is inferred with PIC simulations where we introduced screening effects in the Monte Carlo module sampling the scattering events. More precisely we employed the theory of Molière to get a consistent description of screening effects and introduced it in the PIC code CALDER.

3.2 Impact ionization

3.2.1 Model for impact ionization

The electron-ion impact ionization cross-sections for an atom of number Z are functions of all the atomic orbitals. The energy transfers are quantified through binding energies which depend on the ionization degree Z^* and all the orbital levels $k \in (1, Z - Z^*)$. We denote $B_Z^{Z^*}(k)$ the binding energy of the k -th orbital. The values of $B_Z^0(k)$ are determined by Bearden and Burr (1967); Vaughan (1986) as well as $B_Z^{Z^*}(Z - Z^*)$ (Carlson *et al.*, 1970). The others can be obtained employing the following relation

$$B_Z^{Z^*}(k) = B_Z^{Z^*}(Z - Z^*) - B_Z^0(Z - Z^*) + B_Z^0(k) \quad (3.29)$$

We denote W the secondary electron energy, the energy-differential cross-section of the secondary electron generated given a binding energy $B_Z^{Z^*}(k) = B_k$ during impact ionization is $d\sigma_k/dW$. It depends on the incident electron energy E , the occupation number N_k , the mean kinetic energy U_k . We introduce the following normalisation and

notations: $\epsilon = E/B_k$, $w = W/B_k$, $\epsilon' = E/(mc^2)$, $b' = B_k/(mc^2)$, $u' = U_k/(mc^2)$, $\beta_\epsilon = 1 - (1 + \epsilon)^{-2}$, $\beta_b = 1 - (1 + b')^{-2}$ and $\beta_u = 1 - (1 + u')^{-2}$. The cross-section is given by [Kim et al. \(2000\)](#)

$$\frac{d\sigma_k}{dw} = \sigma_k^0 \left[A_3 f_3(w) + f_2(w) + \frac{2A_2}{\epsilon - 1} - A_1 f_1(w) \right] \quad (3.30)$$

with

$$\begin{aligned} \sigma_k^0 &= 2\pi r_e^2 N / [b' (\beta_\epsilon^2 + \beta_b^2 + \beta_u^2)] \quad f_n(w) = (w+1)^{-n} + (\epsilon-w)^{-n} \\ A_1 &= \frac{1}{1+\epsilon} \frac{1+2\epsilon'}{(1+\epsilon'/2)^2} \quad A_2 = \frac{\epsilon-1}{2} \frac{b'^2}{(1+\epsilon'/2)^2} \quad A_3 = \ln \left(\frac{\beta_\epsilon^2}{1-\beta_\epsilon^2} \right) - \beta_\epsilon^2 - \ln(2b') \end{aligned}$$

The analytical integration of Eq. (3.30) leads to the total cross-section for the orbital number k

$$\sigma_k = \int_0^{(\epsilon-1)/2} \frac{d\sigma_k}{dw} dw = \sigma_k^0 \left[\frac{A_3}{2} \left(1 - \frac{1}{\epsilon^2} \right) + 1 - \frac{1}{\epsilon} + A_2 - A_1 \ln \epsilon \right] \quad (3.31)$$

The average energy transferred to the secondary electron can also be evaluated from Eq. (3.30)

$$\begin{aligned} \langle w_k \rangle &= \frac{1}{\sigma_k} \int_0^{(\epsilon-1)/2} w \frac{d\sigma_k}{dw} dw = \frac{\sigma_k^0}{\sigma_k} \left\{ \frac{A_3}{2} \frac{(\epsilon-1)^2}{\epsilon(\epsilon+1)} + 2 \ln \left(\frac{\epsilon+1}{2} \right) \right. \\ &\quad \left. - \ln \epsilon + A_2 \frac{\epsilon-1}{4} - A_1 \left[\ln \epsilon - (\epsilon+1) \ln \left(\frac{\epsilon+1}{2} \right) \right] \right\} \end{aligned}$$

Physically speaking the evaluation of the phenomena requires to sample the cross-section of all atomic orbitals k . Numerically speaking it is time consuming and we choose to simplify things before the implementation. We sum the ionization cross-section over all orbitals to get only one total cross-section of impact ionization for Z and Z^* given: $\bar{\sigma} = \sum_k \sigma_k$. Similarly for the secondary electron energy, we sum it on all atomic orbitals $\bar{w} = \sum_k \langle w_k \rangle B_k \sigma_k / \bar{\sigma}$. The energy loss by the incident electron is calculated through the same approximation as $\bar{\epsilon} = \sum_k (\langle w_k \rangle + 1) B_k \sigma_k / \bar{\sigma}$.

3.2.2 Monte Carlo implementation

Having in mind the assumptions formulated to model electron-ion impact ionization, we now report how the implementation is made. The scattering algorithm described in Sec. 3.1 can be adapted to implement impact ionization in a PIC code.

Before the calculation starts, the total cross-section $\bar{\sigma}$, the energy of the secondary electron \bar{w} and the energy loss of the incident electron $\bar{\epsilon}$ are tabulated for all ionization degrees Z^* of all species present in the simulation and for various incident electron energies E . Each time step in every cells, electron-ion pairs of macro-particles are formed in a similar way than for elastic scattering. A probability for impact ionization (P_{io}) is determined from the ionization frequency $\nu_i = |v_{rel}| n_e \bar{\sigma}$ where v_{rel} is the relative velocity between the electron and ion and n_e the electron density in the cell

$$P_{io} = 1 - \exp(-|v_{rel}| n_e \bar{\sigma} \Delta t) \quad (3.32)$$

The probability is sampled with a random variable of uniform distribution on the interval $(0, 1)$ denoted by U . If $P_{io} < U$ a secondary electron with energy \bar{w} is generated, the incident electron energy loses an energy $\bar{\epsilon}$ and the ion charge is raised. When both macro-particles have a different numerical weight, the probability is modified as in Eq. (3.26)

$$P_{io} = 1 - \exp\left(-v_{rel} \frac{n_e n_i}{n_{ei}} \bar{\sigma} \Delta t\right) \quad (3.33)$$

the variable n_{ei} has the same meaning than previously and is defined by $n_{ei} = \sum \min(W_e, W_i)$. In the code, we take into account this additional probability in the following way. If $W_e \geq W_i$, the incident electron loses the energy $\bar{\epsilon}$ with a probability W_i/W_e . The ion charge is always incremented and a secondary electron is generated. If $W_e < W_i$, the incident electron loses energy with a probability 1, the ionization occurs with a probability W_e/W_i and is followed by the ionization degree increment and the creation of a secondary electron.

We described the implementation of impact ionization in a PIC code. It is based on the same algorithm than for multiple scattering and includes the same management of arbitrary weighted macro-particles. There are however two major differences. Firstly, the ionization cross-sections are provided in the ion-rest frame and not the center-of-mass frame. Secondly, we now employ tabulated data to evaluate impact ionization probability and the energy transfers.

3.2.3 Calculation of the electron collisional stopping power

The validation of the impact ionization module has already been done by Pérez *et al.* (2012). He selected a simple scenario where a monoenergetic electron beam propagates in a medium triggering impact ionization. The ionization rate as well as the secondary electron density were successfully compared to theoretical expectations. The collisional stopping power of those electrons in Aluminum is also simulated and a good agreement is found with the ESTAR database from the National Institute of Standards and Technology (NIST).

Those results are promising but the implementation of impact ionization presents one limit. For the sake of simplicity and to save computational time, the impact ionization is carried out in the same reference frame as for multiple scattering, which is the center-of-mass (c.o.m.) frame of the two macro-particles. This represents an approximation since the impact ionization cross-sections are given in the ion-rest frame. An assumption is thus made which is most of the time true: both frames are alike since ions are much heavier than electrons. We questioned this hypothesis by comparing the collisional stopping power calculated in the c.o.m. and the ion-rest frames. One may expect that as electrons have a greater energy and as the ions get lighter, the discrepancy between the two calculations will grow. We quantified the relative difference between the collisional stopping power calculated in those two frames and present it in Fig 3.6 for incident electron energies $E = 10 \text{ keV} \rightarrow 1 \text{ GeV}$. The relative difference does grow with the electron energy and as the ion atomic number decreases and eventually reaches 20 % for 1 GeV electrons propagating in carbon. This great gap emphasizes the need to take into account those different frames in the Monte Carlo module. Our description therefore stands out of usual PIC codes and provides a unique degree of precision on the underlying physics of those phenomena.

Conclusion In this section we described the model, the implementation and the numerical validation of the electron-ion impact ionization in the PIC code CALDER. The

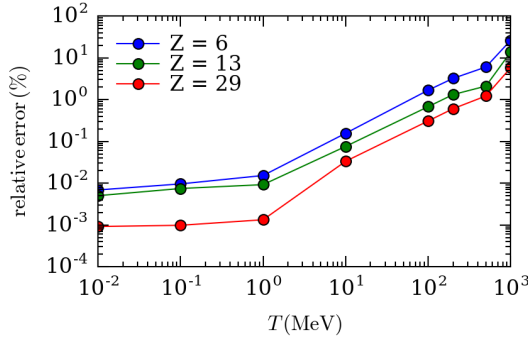


Figure 3.6: Relative error between the collisional stopping power determined in the c.o.m. and the ion-rest frames. Incident electron energies vary in the range $T_1 = 10 \text{ keV} \rightarrow 1 \text{ GeV}$ and several ion species are considered: carbon, aluminum and copper

model is based on the cross-section of [Kim et al. \(2000\)](#). It is implemented with the same algorithm than multiple scattering and adapted to enable secondary electron generation. The validation was already done but we evidenced and quantified its limit in the case of energetic electrons impacting light ions.

3.3 Bremsstrahlung emission of photons

3.3.1 Cross-sections accounting for free and bound electron screening

In this subsection, we derive analytical cross-sections for the Bremsstrahlung process that take into account Thomas-Fermi and Debye-type screening effects in a unified fashion depending on the plasma parameters. For this purpose, we will follow the prescriptions of [Koch and Motz \(1959\)](#); [Motz et al. \(1969\)](#) for the various electron energy ranges under consideration. The calculations are done in the ion-rest frame where variables are denoted by ' according to the convention defined in Sec. 3.1.2. For the sake of simplicity, we drop this notation for this whole section.

Simple atomic potential model

The Coulomb interaction between a high-energy electron and an ion's nucleus is modified by the screening due to bound and/or free electrons, depending on the ionization state of the medium. For neutral atoms of atomic number Z , the Coulomb potential around the nuclear charge can be assumed of the Yukawa type:

$$V_{\text{TF}}(r) = \frac{Ze}{4\pi\epsilon_0 r} \exp(-r/L_{\text{TF}}) \quad (3.34)$$

$$L_{\text{TF}} = 4\pi\epsilon_0 \frac{\hbar^2}{me^2} Z^{-1/3} \quad (3.35)$$

where the Thomas-Fermi length, L_{TF} , accounts for the shielding by the bound electrons. We have introduced ϵ_0 the permittivity of free space, m_e the electron mass and e the elementary charge and $\hbar \equiv h/2\pi$ the Planck constant. More precise multi-exponential fits of the Thomas-Fermi potential could be used ([Molière, 1947](#)), but we will limit ourselves to the above simple approximation. While L_{TF} applies, in principle, to an isolated neutral atom (where charge neutrality is fulfilled at infinity), we assume that it also holds in a

cold neutral medium, where charge neutrality is fulfilled at the ion-sphere radius ([March, 1957](#)).

In a highly ionized plasma, the Coulomb potential can be modeled in a similar form:

$$V_D(r) = \frac{Ze}{4\pi\epsilon_0 r} \exp(-r/L_D) \quad (3.36)$$

$$L_D = \sqrt{\frac{\epsilon_0 k_B T}{e^2 n_i Z^* (Z^* + 1)}} \quad (3.37)$$

where L_D is the Debye length that describes the screening by the free electrons and plasma ions, Z^* is the ionization degree, k_B is the Boltzmann constant and n_i is the ion density. We have supposed a globally neutral plasma ($n_e = Z^* n_i$) and equal electron and ion temperatures ($T_e = T_i = T$). To address coupled plasma regimes, we impose a lower bound on L_D , equal to the interatomic distance: $r_i = (3/4\pi n_i)^{1/3}$ ([Lee and More, 1984](#)). In practice, the ionization degree is evaluated using a numerical fit to the Thomas-Fermi model for a finite-radius atom ([More, 1985](#)).

In the general case of a partially ionized plasma, following [Nardi and Zinamon \(1978\)](#); [Nardi et al. \(2007\)](#); [Rozsnyai \(1979\)](#), we assume for simplicity that the Coulomb potential can be described as a weighted sum of the above Thomas-Fermi and Debye screened potentials:

$$V_{TFD}(r) = \left(1 - \frac{Z^*}{Z}\right) V_{TF}(r) + \frac{Z^*}{Z} V_D(r). \quad (3.38)$$

In a cold neutral medium ($Z^* \rightarrow 0$), we have $V_{TFD} \rightarrow V_{TF}$, whereas, in a fully ionized plasma, $V_{TFD} \rightarrow V_D$, as expected. Also, $V_{TFD} \rightarrow Ze/4\pi\epsilon_0 r$ when $r \rightarrow 0$ as it should. More accurate screening models could be used ([Das et al., 2016](#)) but at the expense of analytical simplicity.

Screening effects

Let us consider an electron of total energy γ_1 (normalized to m_ec^2) and absolute momentum $p_1/mc = \sqrt{\gamma_1^2 - 1}$, both measured in the ion rest frame. After emitting a photon of energy $k = \hbar\omega/m_ec^2$ in the screened atomic field, the electron's normalized energy and momentum become $\gamma_2 = \gamma_1 - k$ and $p_2/mc = \sqrt{\gamma_2^2 - 1}$, respectively. For given electron and ion parameters, the importance of screening effects on the Bremsstrahlung process can be assessed by comparing the maximum impact parameter, $r_{\max} = \hbar/(p_1 - p_2 - kmc)$ with the Thomas-Fermi or Debye screening length ([Koch and Motz, 1959](#)). If r_{\max} is much smaller than L_{TF} or L_D , then the corresponding screening process can be neglected. Figure 3.7 plots r_{\max} as a function of the normalized electron kinetic energy, $\gamma_1 - 1$, for various relative photon energies $k/(\gamma_1 - 1) \in (0.1, 0.5, 0.9)$. Overlaid are plots of L_{TF} and L_D in an almost solid-density ($\sim 8 \times 10^{21} \text{ cm}^{-3}$) Cu plasma of temperature equal to 10 keV and 100 keV. The Thomas-Fermi shielding due to bound electrons is expected to have sizeable effects for both low and very high electron energies, which are enhanced with decreasing photon energy. For the quasi-solid plasma density chosen, the Debye length becomes larger than the interatomic distance r_i for plasma temperatures higher than 12 keV. As a consequence the Debye screening due to free electrons is predicted to be stronger as the photon energy decreases. It is expected to be pronounced for low (1 keV) and high (100 MeV) energy electrons but to remain weak for intermediate electrons (1 MeV).

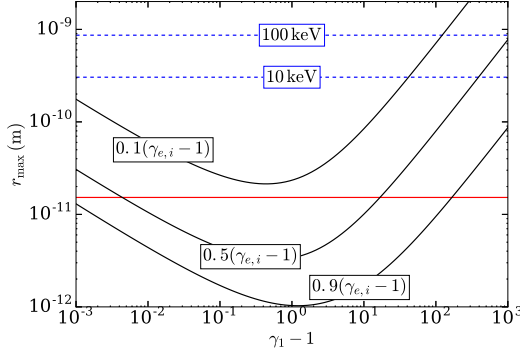


Figure 3.7: Maximum impact parameter r_{\max} (solid black curves) vs normalized electron energy for photon energies $\in (0.1, 0.5, 0.9) \times (\gamma_1 - 1)$. Debye screening lengths (dashed blue lines) are plotted for a Cu plasma of temperatures equal to 10 and 100 keV. The Thomas-Fermi screening length is plotted as a red line.

In the following paragraphs, cross-section formulas will be derived based on both Thomas-Fermi and Debye-type shieldings. As to our knowledge there is no general analytical Bremsstrahlung cross section for electron energies varying from the keV to the GeV ranges, we will draw upon the results of Koch and Motz (1959), and make use of three distinct formulas, respectively valid for (i) non-relativistic ($1 < \gamma_1 \leq 2$); (ii) moderately relativistic ($2 \leq \gamma_1 \leq 100$) and (iii) ultra-relativistic ($\gamma_1 > 100$) electron energies.

Non-relativistic regime

The nonrelativistic (NR) electron ($1 < \gamma_1 \leq 2$) Bremsstrahlung cross section, differential in the photon energy, reads in the Born approximation (Heitler, 1954)

$$\frac{d\sigma_{\text{NR}}}{dk} = \frac{64\pi^4 r_e^2 \alpha_f}{3kp_1^2} \int_{\delta p_-}^{\delta p_+} |\tilde{V}_{\text{TFD}}(u)|^2 u^3 du \quad (3.39)$$

where $\alpha_f = e^2/(4\pi\epsilon_0\hbar c)$ denotes the fine structure constant, $r_e = e^2/(4\pi\epsilon_0 m_e c^2)$ is the classical electron radius, and $\delta p_+ = p_1 + p_2$ and $\delta p_- = p_1 - p_2$ are, respectively, the maximum and minimum momentum transfers in the collision. Moreover, we have introduced \tilde{V}_{TFD} the Fourier transform of the screened atomic potential V_{TFD}

$$\bar{V}_{\text{TFD}}(u) = \frac{1}{(2\pi)^3} \int_{\Omega} V_{\text{TFD}}(\mathbf{r}) \exp(i\mathbf{u} \cdot \mathbf{r}) d^3 r \quad (3.40)$$

After substituting Eqs. (3.38) and (3.40) into Eq. (3.39), one obtains

$$\frac{d\sigma_{\text{NR}}}{dk} = \frac{16r_e^2 Z^2 \alpha_f}{3kp_1^2} [g(\delta p_+, \delta p_-, \zeta_F, L_F) + g(\delta p_+, \delta p_-, \zeta_D, L_D) + \Gamma_c] \quad (3.41)$$

where we have introduced the function g

$$g(\delta p_+, \delta p_-, \zeta, l) = \frac{\zeta^2}{2} \left[\ln \left(\frac{\delta p_+^2 l^2 + 1}{\delta p_-^2 l^2 + 1} \right) + \frac{1}{\delta p_+^2 l^2 + 1} - \frac{1}{\delta p_-^2 l^2 + 1} \right] \quad (3.42)$$

and the coupling term Γ_c

$$\Gamma_c = \frac{\zeta_F \zeta_D}{L_D^2 - L_F^2} \left[L_F^2 \ln \left(\frac{\delta p_-^2 L_D^2 + 1}{\delta p_+^2 L_D^2 + 1} \right) + L_D^2 \ln \left(\frac{\delta p_+^2 L_F^2 + 1}{\delta p_-^2 L_F^2 + 1} \right) \right] \quad (3.43)$$

We introduced the effective Thomas-Fermi charge $\zeta_{TF} = 1 - Z^*/Z$ and the effective Debye charge $\zeta_D = Z^*/Z$ which identifies with the ionization degree. The lengths l , L_F and L_D are normalized by the classical electron radius r_e .

As is well known (Elwert, 1939), the accuracy of the Born approximation can be improved in the nonrelativistic regime by applying the Elwert multiplicative factor to Eq. (3.41), in the limit $Z\alpha(1/\beta_2 - 1/\beta_1) \ll 1$

$$f_E = \frac{\beta_1}{\beta_2} \frac{1 - \exp(-2\pi Z\alpha_f/\beta_1)}{1 - \exp(-2\pi Z\alpha_f/\beta_2)}. \quad (3.44)$$

Figure 3.8 displays the Elwert-corrected cross section $kd\sigma_{NR}/dk$ (red curve) as a function of the normalized photon energy $k/(\gamma_1 - 1)$ for a 1 and 100 keV electron interacting with neutral Cu atoms (where the Debye shielding vanishes). On the same graph are plotted the reference tabulated data of Seltzer and Berger (1986), $kd\sigma_{SB}/dk$ (black curve), and the nonscreened cross section for a point Coulomb potential (formula 3BN in Koch and Motz (1959)), $kd\sigma_{3BN}/dk$ (light blue curve). The difference between $kd\sigma_{SB}/dk$ and $kd\sigma_{3BN}/dk$ highlights the need to take into account screening effects in the full photon energy range. Furthermore, we observe that our analytical formula satisfactorily reproduces Seltzer and Berger's data. We have checked, in the energy ranges $1 < \gamma_1 \leq 2$ the relative error, averaged over $0 < k/(\gamma_1 - 1) \leq 1$, between $kd\sigma_{NR}/dk$ and the tabulated data $kd\sigma_{SB}/dk$. It rises up to $\sim 80\%$ for 1 keV electrons, then decreases as low as $\sim 8\%$ for 50 keV electrons and rises again to 27 % for 500 keV electrons. For higher Z material of interest like gold, this difference rises since the validity of the Born approximation is even worst than for copper ($2\pi Z/137\beta_1 \ll 1$).

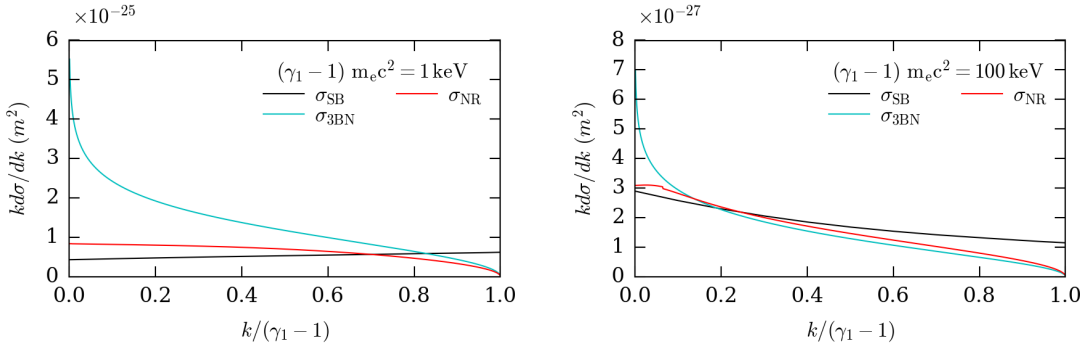


Figure 3.8: Nonrelativistic Bremsstrahlung cross section ($kd\sigma/dk$) vs photon energy ($k = \hbar\omega/mc^2$) normalized by the electron kinetic energy $(\gamma_1 - 1)$ for a 1 keV and a 100 keV electron interacting with neutral Cu atoms. Comparison of the Elwert-corrected analytical formula (σ_{NR} , red curve), Seltzer and Berger (1986)'s data (σ_{SB} , black curve) and the nonscreened formula 3BN from Koch and Motz (1959) (σ_{3BN} , blue curve).

Figure 3.9 quantifies the effect of the Debye shielding on $kd\sigma_{NR}/dk$ as a function of the target ionization. In practice, this ionization degree is evaluated from the plasma temperature, density and atomic number using a numerical fit to the Thomas-Fermi model

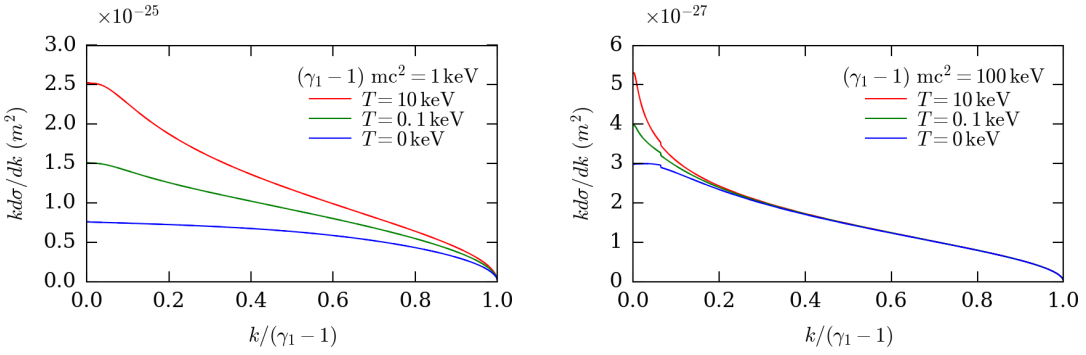


Figure 3.9: Nonrelativistic Bremsstrahlung cross section ($kd\sigma/dk$) vs photon energy ($k = \hbar\omega/mc^2$) normalized by the electron kinetic energy ($\gamma_1 - 1$) for a 1 keV and a 100 keV electron in a solid-density Cu plasma of temperature ranging from $T = 0$ to 10 keV.

for a finite-radius atom (More, 1985). The electron kinetic energy is still set to 1 and 100 keV, while the temperature of the solid-density Cu target is varied in the range $0 \leq T \leq 10$ keV. One can notice that we observe the behavior expected from the analysis of Figure 3.7. While all curves tend to coincide at large photon energies, the cross section at low photon energies ($k/(\gamma_1 - 1) \lesssim 0.1$) rises (up to $\sim 60\%$ for $k \rightarrow 0$) with the target temperature. The screening effects are all the more pronounced that the plasma temperature rises for a fixed incoming electron energy. Moreover we note a decrease of the Debye screening influence as the electron energy rises from 1 keV to 100 keV. However, the thermal dependence of the total radiative stopping power remains modest: a mere 4% increase is found when the plasma temperature is raised from 0 to 10 keV. The slight discontinuity seen in Fig. 3.9(b) for a 100 keV incident electron marks the limit of the Elwert factor application ($Z\alpha_f(1/\beta_2 - 1/\beta_1) \ll 1$). We took an upper value of 10^{-2} for this condition.

Moderately relativistic regime

For moderately relativistic electrons ($2 \leq \gamma_1 \leq 100$), the energy-differential Bremsstrahlung cross section is given by Bethe and Mott (1934); Koch and Motz (1959) and is valid for arbitrary screening

$$\frac{d\sigma_R}{dk} = \frac{4Z^2 r_e^2 \alpha_f}{k} \left\{ \left[1 + \left(\frac{\gamma_1 - k}{\gamma_1} \right)^2 \right] [I_1(\delta) + 1] - \frac{2}{3} \frac{\gamma_1 - k}{\gamma_1} \left[I_2(\delta) + \frac{5}{6} \right] \right\} \quad (3.45)$$

where $k = \hbar\omega/mc^2$ denotes the normalized photon energy and the terms I_1 and I_2 account for screening effects

$$I_1(\delta) = \int_{\delta}^1 \frac{du}{u^3} (u - \delta)^2 [1 - F_e(u)]^2 \quad (3.46)$$

$$I_2(\delta) = \int_{\delta}^1 \frac{du}{u^4} [u^3 - 6\delta^2 u \ln(u/\delta) + 3\delta^2 u - 4\delta^3] \times [1 - F_e(u)]^2 \quad (3.47)$$

The argument $\delta = k/2\gamma_1(\gamma_1 - k)$ approximately quantifies the minimum momentum transfer to the atom in the limit $\gamma_1, \gamma_2 \gg 1$. The above functions involve the electron form

factor

$$F_e(u) = 1 - u^2 \tilde{V}(u) \quad (3.48)$$

For a simple single-exponential potential, $V(r) = (q/4\pi\epsilon_0 r) \exp(-r/l)$, I_1 and I_2 have the following closed-form expression

$$I_1 = q^2 \left[l\delta (\arctan \delta l - \arctan l) - \frac{l^2}{2} \frac{(1-\delta)^2}{1+l^2} + \frac{1}{2} \ln \left(\frac{1+l^2}{1+(l\delta)^2} \right) \right] \quad (3.49)$$

$$I_2 = \frac{q^2}{2} \left[4l^3\delta^3 (\arctan \delta l - \arctan l) + (1+3l^2\delta^2) \ln \left(\frac{1+l^2}{1+l^2\delta^2} \right) + \frac{6^4\delta^2}{1+l^2} \ln \delta + \frac{l^2(\delta-1)(\delta+1-4l^2\delta^2)}{1+l^2} \right] \quad (3.50)$$

where we recall that lengths l are normalized by r_e . However, for the more general potential $V(r) = V_{\text{TFD}}(r)$, no exact analytical solution can be found for I_2 contrary to I_1 . Drawing upon the work by Tsai (1974), an approximate analytical expression can be derived by matching the asymptotic expressions of Eq. (3.45) obtained in the limit $\delta \rightarrow 0$ using the double-exponential potential $V_{\text{TFD}}(r)$ and a single-exponential potential (hereafter referred to as the “reduced potential”), $V_R(r)$. To this goal, we make use of the asymptotic expression

$$I = \lim_{\delta \rightarrow 0} I_1 = \lim_{\delta \rightarrow 0} I_2 = \int_0^1 u^3 \left(\frac{1-F_e(u)}{u^2} \right)^2 du \quad (3.51)$$

This integral can be analytically evaluated for V_{TFD} . Let I_{TFD} denote its solution

$$I_{\text{TFD}} = \frac{\zeta_{\text{TF}}^2 (1+L_{\text{TF}}^2) \ln(1+L_{\text{TF}}^2) - L_{\text{TF}}^2}{1+L_{\text{TF}}^2} + \frac{\zeta_{\text{D}}^2 (1+L_{\text{D}}^2) \ln(1+L_{\text{D}}^2) - L_{\text{D}}^2}{1+L_{\text{D}}^2} + \frac{\zeta_{\text{TF}}\zeta_{\text{D}} [L_{\text{D}}^2 \ln(1+L_{\text{TF}}^2) - L_{\text{TF}}^2 \ln(1+L_{\text{D}}^2)]}{L_{\text{D}}^2 - L_{\text{TF}}^2} \quad (3.52)$$

For the reduced potential $V_R(r) = (q_R/4\pi\epsilon_0 r) \exp(-r/L_R)$, where $q_R = Ze$ and L_R is the sought-for reduced screening length, the solution of the above integral is

$$I_R = \frac{q_R^2}{2} \frac{(1+L_R^2) \ln(1+L_R^2)}{1+L_R^2} \quad (3.53)$$

The asymptotic equality $\lim_{\delta \rightarrow 0} d\sigma_{\text{TFD}}/dk = \lim_{\delta \rightarrow 0} d\sigma_R/dk$ implies $\lim_{\delta \rightarrow 0} I_{\text{TFD}} = \lim_{\delta \rightarrow 0} I_R$, which defines the equation solved by L_R . Setting $a = 2I_{\text{TFD}}/q_R^2$ and $x = L_R^2$, this equation can be recast

$$a(x+1) = (x+1) \ln(x+1) - x \quad (3.54)$$

The solution involves the Lambert W -function

$$L_R \equiv \sqrt{x} = \left\{ \exp [W(-e^{-1-2a}) + 1 + 2a] - 1 \right\}^{1/2} \quad (3.55)$$

As the coefficient a is positive, W varies over the interval $[-1/e, 0]$, so that L_R is well defined. Combining Eqs. (3.55) with Eqs. (3.45) and (3.53) gives a closed-form analytical expression for the cross section $d\sigma_R/dk$.

In Fig. 3.10, we represent the screened Bremsstrahlung cross section using the Thomas-Fermi-Debye potential obtained by numerical integration ($kd\sigma_{\text{TFD}}/dk$, red triangles) and the Reduced potential determined by an analytical derivation ($kd\sigma_R/dk$, plain red curve).

In this limit case of a cold unionized plasma $Z^* = 0$, both formulations are equal since the Debye screening vanishes. The cross section for a 5 and 40 MeV kinetic electron energy incident on neutral Cu atoms is considered. Overall good agreement is also found with the reference data of [Seltzer and Berger \(1986\)](#) ($k\sigma_{\text{SB}}/dk$, black curve), except near $k/(\gamma_1 - 1) = 1$, where a factor of ~ 2 discrepancy is observed. Comparison with the nonscreened relativistic formula 3BN cross section ($k\sigma_{\text{3BN}}/dk$, blue curve) shows that electron shielding is mostly influent at low and very high relative photon energies. In the relativistic regime ($2 < \gamma_1 \leq 100$), the relative error, averaged over $0 < k/(\gamma_1 - 1) < 1$, between $k\sigma_{\text{R}}/dk$ and the tabulated data $k\sigma_{\text{SB}}/dk$ is $\sim 40\%$ for 1 MeV electrons and then steadily decreases to $\sim 10\%$ for 50 MeV electrons.

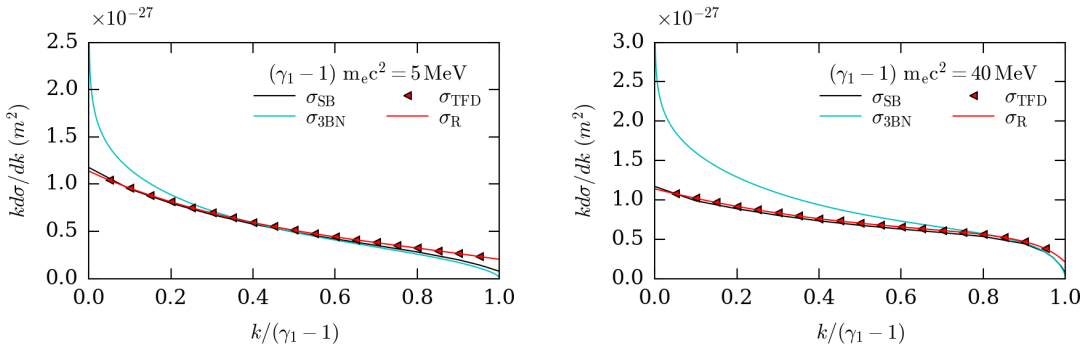


Figure 3.10: Moderately relativistic Bremsstrahlung cross section ($kd\sigma/dk$) vs photon energy ($k = \hbar\omega/mc^2$) normalized by the electron kinetic energy ($\gamma_1 - 1$) for a 5 and a 40 MeV electron interacting with neutral Cu atoms. Comparison of the numerically computed cross section using the Thomas-Fermi-Debye potential ($kd\sigma_{TFD}/dk$, red triangles), the reduced analytical formula ($kd\sigma_R/dk$, red curve), Seltzer and Berger (1986)'s data ($kd\sigma_{SB}/dk$, black curve) and the nonscreened 3BN formula from Koch and Motz (1959) ($kd\sigma_{3BN}/dk$, light blue curve).

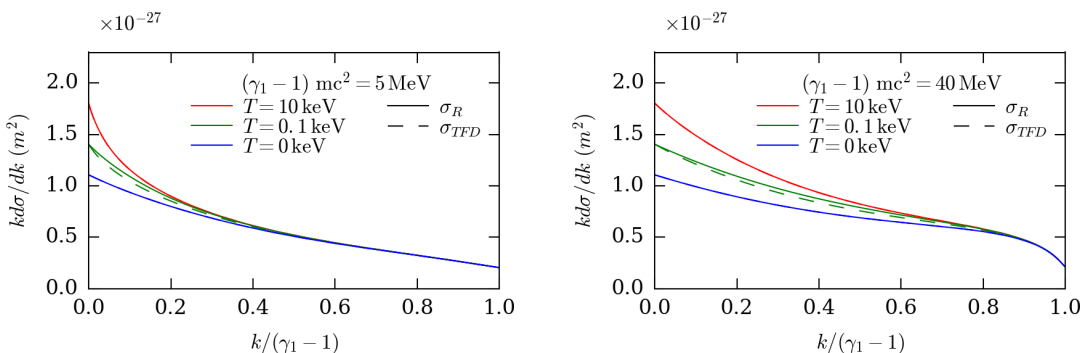


Figure 3.11: Moderately relativistic Bremsstrahlung cross section ($kd\sigma/dk$) vs photon energy ($k = \hbar\omega/mc^2$) normalized by the electron kinetic energy ($\gamma_1 - 1$) for a 5 MeV and a 40 MeV electron in a solid-density Cu plasma of temperature ranging from $T = 0$ to 10 keV. Comparison of the numerically computed cross section using the Thomas-Fermi-Debye potential ($kd\sigma_{TFD}/dk$, dashed lines) with the reduced analytical formula ($kd\sigma_R/dk$, solid lines).

The dependence of the Bremsstrahlung cross section upon the plasma temperature

is illustrated in Fig. 3.11. The incident electron energies are of 5 and 40 MeV and the Cu plasma temperature varies in the range $0 \leq T \leq 10$ keV. The cross section derived analytically from the Reduced potential (solid lines, $kd\sigma_R/dk$) closely reproduces the cross section numerically integrated from the Thomas Fermi Debye potential (dashed lines, $kd\sigma_{TFD}/dk$) in the limit $\delta \rightarrow 0$ as expected and shows little differences for any δ . As in the nonrelativistic regime illustrated in Fig. 3.9, the Debye screening proves mainly significant at low electron-to-photon energy transfers. Even if it leads to a $\sim 50\%$ increase in the cross section for $k/(\gamma_1 - 1) \rightarrow 0$ as the plasma temperature rises from 0 to 10 keV, this only corresponds to a 10% increase of the radiative stopping power. Overall, in the relativistic regime ($2 \leq \gamma_1 \leq 100$), we remark that screening effects slightly rises with the incident electron energy.

Ultra-relativistic regime

For ultrarelativistic electron energies ($\gamma_1 > 100$), the accuracy of the Born-approximation formula (3.45) is improved by adding the Coulomb correction term $f_C(Z)$ (Koch and Motz, 1959)

$$\frac{d\sigma_R}{dk} = \frac{4Z^2 r_e^2 \alpha_f}{k} \left\{ \left[1 + \left(\frac{\gamma_1 - k}{\gamma_1} \right)^2 \right] [I_1(\delta) + 1 - f_C(Z)] - \frac{2}{3} \frac{\gamma_1 - k}{\gamma_1} \left[I_2(\delta) + \frac{5}{6} - f_C(Z) \right] \right\} \quad (3.56)$$

where $k = \hbar\omega/mc^2$ denotes the normalized photon energy. Introducing ζ the Riemann function, the correction factor is defined by Koch and Motz (1959)

$$f_C(Z) = \frac{\alpha_f^2 Z^2}{1 + \alpha_f^2 Z^2} \sum_{n=0}^{\infty} (-\alpha_f^2 Z^2)^n [\zeta(2n+1) - 1] \quad (3.57)$$

In practice, keeping the first four terms is sufficient for an accurate computation of f_C even for high Z values.

In the case of a 100 and a 500 MeV incident electron interacting with neutral Cu atoms, Fig. 3.12 compares the Bremsstrahlung cross section, $kd\sigma/dk$, computed numerically with the Thomas-Fermi-Debye potential ($kd\sigma_{TFD}/dk$, red triangles) with the analytical expression obtained using the reduced potential ($kd\sigma_R/dk$, plain red curve). The two curves fit since in the limit of cold unionized plasma they are both based on the sole Thomas-Fermi screening. Also plotted are the data from Seltzer and Berger (1986) ($kd\sigma_{SB}/dk$, black curve) and, to highlight the importance of shielding effects, the nonscreened formula 3BN from Koch and Motz (1959) ($kd\sigma_{3BN}/dk$, light blue curve). The analytic cross section is in good agreement with $kd\sigma_{SB}/dk$, while $kd\sigma_{3BN}/dk$ overestimates the latter by a factor > 1.5 at photon energies $k/(\gamma_1 - 1) < 0.1$. In the ultra-relativistic regime ($\gamma_1 \geq 100$), the relative error, averaged on $0 < k/(\gamma_1 - 1) < 1$, between our analytical cross-section ($kd\sigma_R/dk$) and the tabulated data from Seltzer and Berger ($kd\sigma_{SB}/dk$) is $\sim 10\%$ for 60 MeV electrons and decreases to reach a plateau of 2% for electron energies lying in the range $0.5 \rightarrow 10$ GeV.

Still for a 100 or 500 MeV incident electron, the thermal variations of the Bremsstrahlung cross section are illustrated in Fig. 3.13 when raising the temperature of the solid-density Cu target from 0 to 10 keV. As in the moderately relativistic case, the analytic cross section based on the reduced potential ($kd\sigma_R/dk$) closely matches the numerically

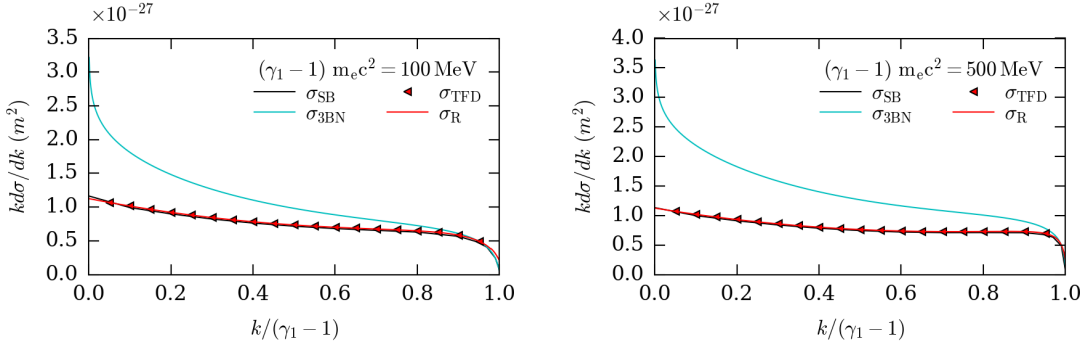


Figure 3.12: Ultra-relativistic Bremsstrahlung cross section ($kd\sigma/dk$) vs photon energy ($k = \hbar\omega/mc^2$) normalized by the electron kinetic energy ($\gamma_1 - 1$) for a 100 and a 500 MeV electron interacting with neutral Cu atoms. Comparison of the numerically computed Coulomb-corrected cross section using the Thomas-Fermi-Debye potential ($kd\sigma_{\text{TFD}}/dk$, red triangles), the reduced analytical formula ($kd\sigma_R/dk$, red curve), Seltzer and Berger (1986)'s data ($kd\sigma_{\text{SB}}/dk$, black curve) and the nonscreened formula 3BN from Koch and Motz (1959) ($kd\sigma_{3\text{BN}}/dk$, light blue curve).

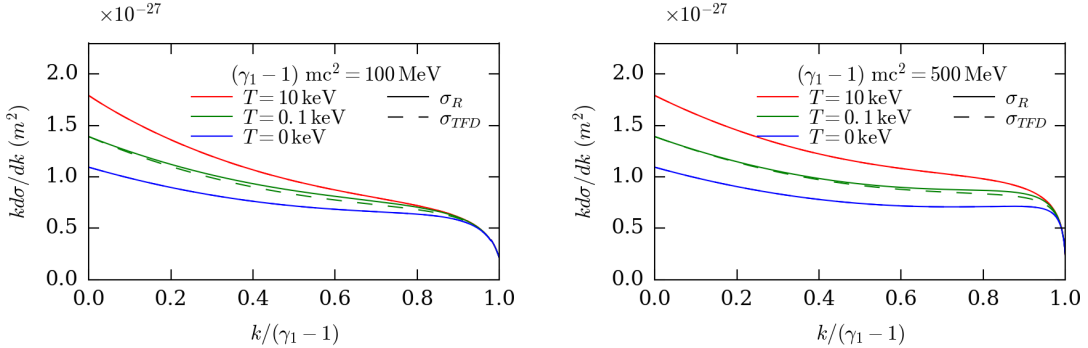


Figure 3.13: Ultra-relativistic Bremsstrahlung cross section ($kd\sigma/dk$) vs photon energy ($k = \hbar\omega/mc^2$) normalized by the electron kinetic energy ($\gamma_1 - 1$) for 100 and 500 MeV electron in a solid-density Cu plasma of temperature ranging from $T = 0$ to 10 keV. Comparison of the numerically computed Coulomb-corrected cross section using the Thomas-Fermi-Debye potential ($kd\sigma_{\text{TFD}}/dk$, dashed curves) with the reduced analytical formula ($kd\sigma_R/dk$, solid curves).

evaluated cross section ($kd\sigma_{\text{TFD}}/dk$) as $\delta \rightarrow 0$ and shows little discrepancies for any δ . Compared to the moderately relativistic regime where the Debye screening only affects low energy photons ($k/(\gamma_1 - 1) \leq 20\%$), it now significantly modifies the cross section for a larger range of photon energies up to $k/(\gamma_1 - 1) \leq 70\%$. This has sizeable effects on the radiative stopping power since it increases of 30 % as the plasma temperature rises from 0 to 10 keV in the ultra-relativistic regime.

We presented a systematic derivation of the energy-differential Bremsstrahlung cross-section accounting for bound and free electron screening in a large range of incident electron energies. We compared quantitatively this model to the unscreened description in Koch and Motz (1959) and the reference data of Seltzer and Berger (1986). The Debye potential prevailing in a fully ionized plasma tends to rise the Bremsstrahlung cross-section for low electron to photon energy transfers, especially for incident electron energies below 1 keV

and above 1 GeV.

3.3.2 Implementation of Bremsstrahlung emission

Minimum cutoff for photon energy

The Bremsstrahlung cross-section $d\sigma/dk$ diverges as $k \rightarrow 0$ since $d\sigma/dk \simeq 1/k$. When the cross-section is numerically evaluated, the interval of photon emission must be reduced from $(0, 1)$ to $(10^{-n}, 1)$, $n \geq 1$ in order to avoid the singularity. We therefore neglect all the energy radiated in the range $(0, 10^{-n})$. We suggest to define n large enough such that this total becomes negligible compared to the energy radiated in the range $(10^{-n}, 1)$. The criterion reads

$$\left(\int_0^{10^{-n}} k \frac{d\sigma}{dk} dk \right) \leq \epsilon \left(\int_0^1 k \frac{d\sigma}{dk} dk \right) \quad (3.58)$$

We choose $n = 7$ which ensure that the value of ϵ is $\leq 10^{-5}$.

Tabulation for ab initio Particle-In-Cell simulations

In practice we enable the PIC code user to choose between the sole Thomas-Fermi and the Thomas-Fermi-Debye screened cross-sections. They are tabulated before the simulation starts as follows.

For a sole Thomas-Fermi screening, we have one table per atomic number Z . The electron kinetic energy T_1 is discretized between 1 eV and 10 GeV, with a logarithmic step and 10^4 points. The normalized photon energy $k/(\gamma_1 - 1)$ is discretized between 10^{-7} and 1, with a logarithmic step and 10^2 points. This adds up to 10^6 32-bit reals stored per atomic number (thus, per file).

For a Thomas-Fermi-Debye screening, we have one table per ionization degree (thus 30 files for copper). In each of those files, the electron kinetic energy T_1 is discretized between 1 eV and 10 GeV, with a logarithmic step and 10^2 points, the photon energy $k/(\gamma_1 - 1)$ is discretized between 10^{-7} and 1, with a logarithmic step and 10^2 points. The Debye length L_D is discretized between the atomic radius r_a ($= 135$ pm for copper) and ~ 1 mm, with a logarithmic step and 10^2 points. The upper value correspond to the most extreme case we could expect to occur in a simulation of a plasma with a density $10^{-6} n_c$ and a temperature of 10 GeV. Those files also contains 10^6 32-bit reals. The tables are composed of 32-bit reals in order to remain consistent with the PIC code CALDER. However, we emphasize the need to compute the tables with 64-bit reals. Indeed some calculations fall below the 32-bit real limit (10^{-8}) and this leads to abberations as shown in Fig. 3.14. We plotted the differential cross-section for a 5 MeV incident electron on a fully ionized carbon ($Z^* = 6$) and a Debye length $L_D = 0.5$ mm. As one can see, the cross-section becomes negative and the cumulative distribution function, becomes higher than 1. This effect is enhanced as the Debye length rises and depends, of course, on the way each computer system/compiler rounds operations.

Whatever the model, the interpolation in the tables is very simple. Let x denotes the sampled value and $(x_i)_{1 \leq i \leq n}$ the table discretization. x is a general notation denoting either the incident electron energy, the photon energy or the Debye length. Let us assume that the value x falls in the interval (x_{i_0}, x_{i_0+1}) . We simply choose x_{i_0} as the interpolation of x . When a value falls out the table range it is taken equal to the nearest point (x_1 or x_n).

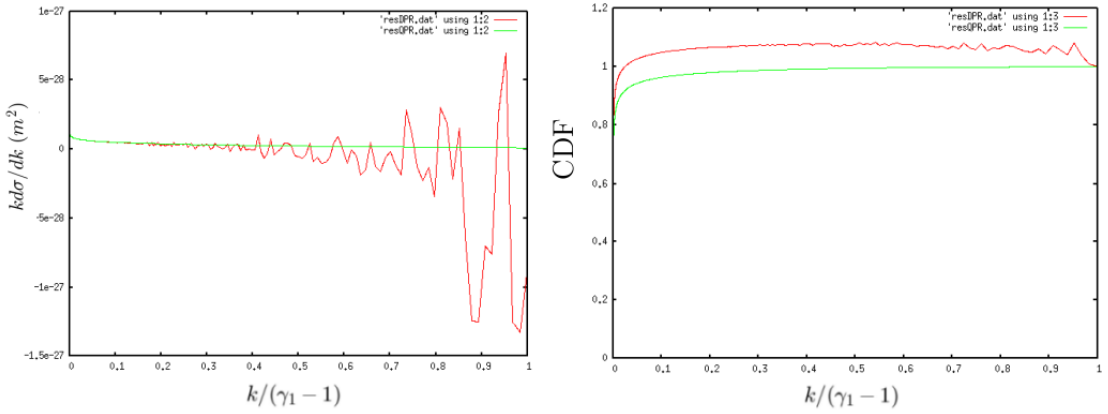


Figure 3.14: (a) Bremsstrahlung energy differential cross-section ($kd\sigma/dk$) vs photon energy ($k = \hbar\omega/mc^2$) normalized by the electron kinetic energy ($\gamma_1 - 1$) computed from Eq. (3.45) and (b) corresponding cumulative distribution functions tabulated in the PIC code. The calculations performed with 32 bits reals (labeled resDPR.dat) are represented by the red curves and with 64-bit reals (labeled resQPR.dat) by the green curves.

Exact simulation of photon number and spectra

We now illustrate the numerical validation of the Bremsstrahlung module. A test scenario is employed in order to compare the output with a theoretical result. In practice, we enable the user to choose between two models of screening for the Bremsstrahlung cross-sections. The first one is the simple Thomas-Fermi screening, validated in Fig. 3.15 and the second one is the Thomas-Fermi-Debye one, validated in Fig. 3.16.

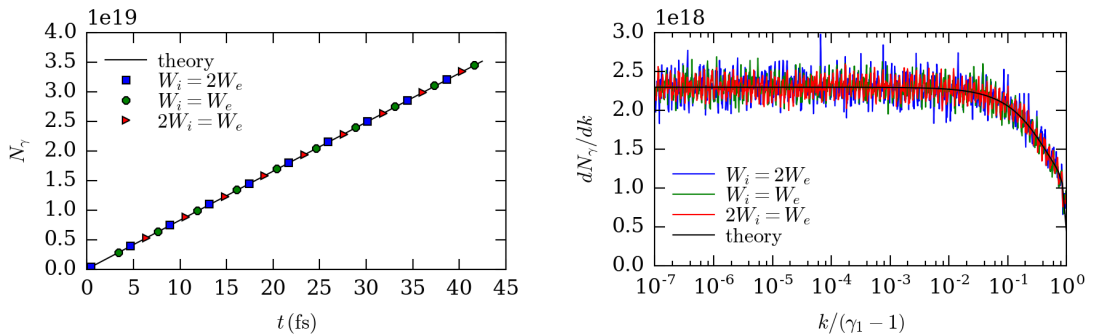


Figure 3.15: Validation of the Bremsstrahlung module for arbitrarily weighted macro-particles and the Thomas-Fermi screening model. (a) Number and (b) energy-resolved spectra of photons generated by 40 MeV electrons incident on neutral copper atoms. The theoretical result is represented with black lines. Three different weight ratios are employed $W_i/W_e = 2, 1$ and $1/2$.

We performed 1D simulations with periodic conditions along the x axis. Only the Monte Carlo module is activated, the electromagnetic solver is turned off. The macro-collisions are treated in the ion-rest frame. We consider the propagation of a monoenergetic electron beam with an energy of 40 MeV, density $n_e/n_c = 1$ and length $l = 10c/\omega_0$ through a solid copper target of density $n_i/n_c = 80$. Given the simple system we investigate, the

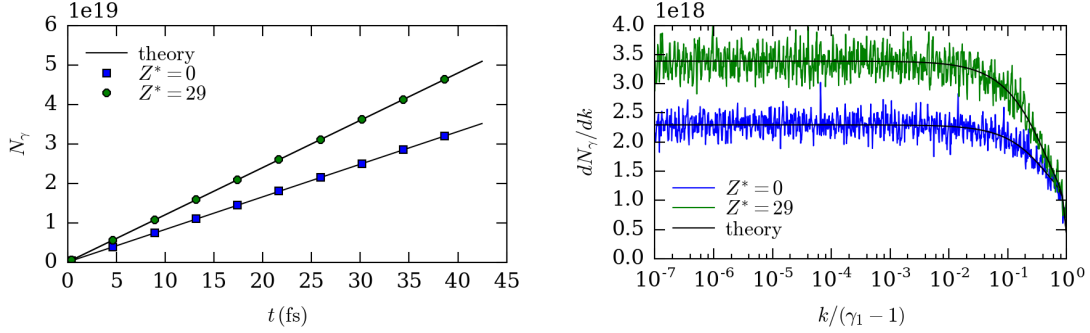


Figure 3.16: Validation of the Bremsstrahlung module for the Thomas-Fermi-Debye screening model. (a) Number and (b) energy-resolved spectra of photons generated by 40 MeV electrons incident on neutral copper atoms (blue curves) and fully ionized copper (green curves). The theoretical result is represented with black lines.

theoretical number of photons is provided by the following formula

$$\frac{dN_\gamma}{dt} = n_e l \times \sigma_{Br} n_i v_{rel} \quad (3.59)$$

where $n_e l$ is the number of electrons, and $\sigma_{Br} n_i v_{rel}$ the frequency of photon emission for one electron. The expected photon spectra is obtained from the derivation of Eq. (3.59) against k the photon energy.

In Fig. 3.15(a) we check the management of arbitrarily weighted macro-particles for the Bremsstrahlung module. The number of macro-ions is varied and the number of macro-electrons is kept constant. This implies different numerical weights for the macro-particles which are handled with the method described in Sec. 3.1.3. For three different ratios of macro-particle weights ($W_i/W_e = 2, 1$ and $1/2$) we obtain the exact same number of macro-photons as expected. This number matches the theoretical expectation of Eq. (3.59). The energy-resolved photon spectra obtained for the three simulations is displayed in Fig. 3.15(b). They all fit perfectly together and with the theory. The photon energy is normalized by the incident electron kinetic energy $\gamma_1 - 1$ and varies between the minimum bound mentioned above $10^{-7} \times (\gamma_1 - 1)$ and $(\gamma_1 - 1)$.

The Thomas-Fermi-Debye screening model is validated in Fig. 3.16. We compare the photon production for the same monoenergetic electron beam (40 MeV, $n_e/n_c = 1$ and length $l = 10c/\omega_0$) propagating either through a neutral copper target (blue curves) or a fully ionized one (green curves). The theoretical result is well reproduced by the simulations. We can also visualize the influence of the ionization degree on the Bremsstrahlung production of photons. As stated previously in Sec. 3.3, the Debye screening prevails for highly ionized material and increases the photon number and overall radiated energy.

The validation of the Bremsstrahlung module was done for the two screening models available to the PIC code user. The output of this module (photon number and their energy-resolved spectra) are illustrated on a test-case.

3.3.3 Validation of the simulated electron radiative stopping power

Benefiting from the possibility to couple within the same simulation particle scattering, impact ionization and Bremsstrahlung radiation, one can now simulate the electron stopping power into solids. In this subsection, we successfully confront the PIC-simulated

collisional, radiative and total stopping power to the ESTAR database of the NIST.

Simulations of electrons propagating through solid copper and experiencing either impact ionization or Bremsstrahlung losses were run. With this kind of computation we can measure both the collisional and the radiative stopping powers. The total stopping power is obtained by adding both. The electron energy is assumed to decrease linearly with time. Let us consider a one dimensional infinite neutral copper target with temperature $T = 0$ and density $n_i = 60n_c$. The electron beam is monoenergetic with $T_1 = 10\text{ keV} \rightarrow 1\text{ GeV}$ denoting the kinetic energy at time $t = 0$. The density of the beam is $n_1 = n_c$. On a numerical point of view, particle scattering is treated in the center-of-mass frame and impact ionization and Bremsstrahlung are computed in the ion-rest frame.

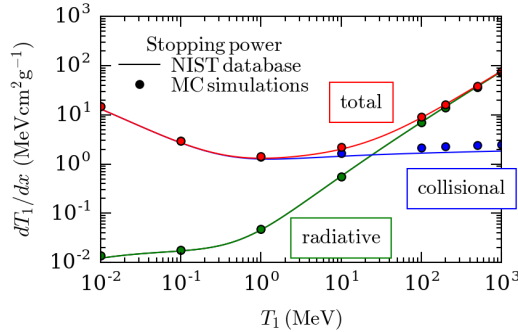


Figure 3.17: Stopping power in copper for incident electrons with energies $T_1 \in (10\text{ keV}, 1\text{ GeV})$. The formula from the NIST is represented by the solid line and the Monte Carlo CALDER simulations by the dots.

Fig 3.17 displays the comparison between simulations and the theoretical formula from the NIST. The radiative stopping power is accurately reproduced whatever the incident electron energy. The collisional stopping power is very close to the NIST database for $T_1 = 10\text{ keV} \rightarrow 1\text{ MeV}$ and a slight difference rises above $T_1 = 1\text{ MeV}$. This slight discrepancy comes from the density effect. It represents the influence of the fields generated as the electron propagates faster in the material.

The impact ionization and the Bremsstrahlung modules implemented in CALDER accurately reproduce the collisional and radiative stopping powers as predicted by the ESTAR database from the NIST. This agreement was checked for copper and in a large range of incident electron energies ($10\text{ keV} \rightarrow 1\text{ GeV}$).

3.4 Bethe-Heitler pair creation

We now move on to the Bethe-Heitler process which accounts for the decay of γ -rays, potentially emitted by the Bremsstrahlung process, into electron-positron pairs.

3.4.1 Cross-sections accounting for free and bound electron screening

The cross-section of pair production by a photon of normalized energy ($k = \hbar\omega/mc^2 \gg 1$) differential in the positron normalized energy ($\gamma_+ = E_+/mc^2$) is given (in the ion-rest frame) by Formula 3D-1003 of Motz *et al.* (1969)

$$\frac{d\sigma_{\text{BH}}}{d\gamma_+} = \frac{4Z^2 r_e^2}{137} \frac{dk}{k^3} \left\{ (\gamma_+^2 + \gamma_-^2) [I_1(\delta) + 1] + \frac{2}{3} \gamma_+ \gamma_- \left[I_2(\delta) + \frac{5}{6} \right] \right\} \quad (3.60)$$

where $\delta = k/(2\gamma_+\gamma_-)$. This formula assumes large electron and positron energies ($\gamma_+, \gamma_- \gg 1$) and negligible nucleus recoil. It turns out to be very similar to the Bremsstrahlung cross-section, Eq. (3.45), and, in particular, involves the same screening functions $I_{1,2}$ defined by Eq. (3.46) and (3.47).

As for the Bremsstrahlung, one can study the screening effects on the Bethe-Heitler energy cross section (see Fig. 3.18). Different photon energies, 100 MeV and 1 GeV, and several plasma temperatures, $T = 0, 0.1, 0.5, 1.$ and 10 keV, are considered. The curves have a symmetry axis for $2\gamma_+ = k$. The lower and upper thresholds for the positron Lorentz factor are respectively 1 and $k - 1$. The cross-section has a flat shape centered on $2\gamma_+ = k$. The Debye screening effects become more significant as the incident photon energy rises from 100 MeV to 1 GeV. Indeed the gap between the cross section in a cold plasma (0 keV) and in a hot plasma (10 keV) is less than 10 % for incident photon energies $\hbar\omega \leq 100$ MeV and monotonously increases to sizeable differences up to 50 % for $\hbar\omega = 1$ GeV. In a practical context of laser-solid interaction, Debye screening effects have a weak impact since photon energies barely reach 100 MeV. In the context of electron beams accelerated by Laser Wakefield Acceleration, which energy can reach $\sim 1, 2$ GeV, interacting with high Z targets this may have a noticeable impact. Such experiments were conducted recently

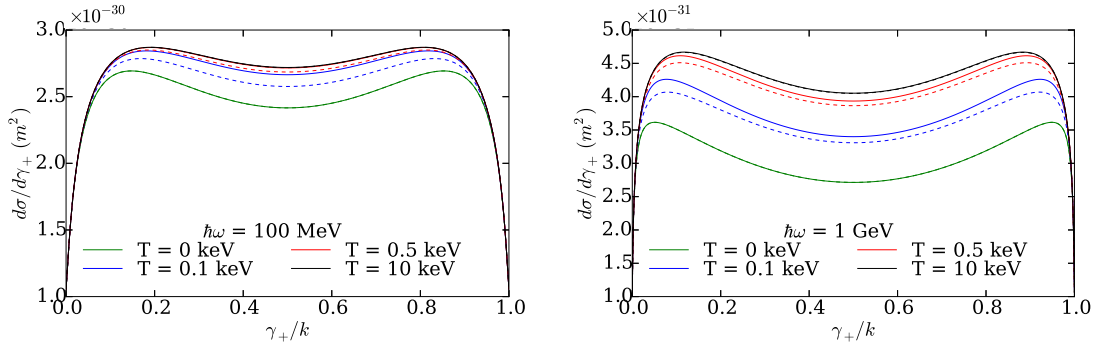


Figure 3.18: Bethe Heitler cross section ($d\sigma/d\gamma_+$) for 100 MeV and 1 GeV incident photons in a solid-density Cu plasma of temperature ranging from $T = 0$ to 10 keV. k denotes the normalized photon energy $k = \hbar\omega/mc^2$. Comparison of the numerically computed cross section using the Thomas-Fermi-Debye potential ($d\sigma_{TFD}/d\gamma_+$, dashed curves) with the reduced analytical formula ($d\sigma_R/d\gamma_+$, solid curves).

We extended the work done for the Bremsstrahlung process in order to derive energy-differential cross-sections for the Bethe-Heitler pair creation. They account for weak and strong ionization degree of the atom and therefore stands out of usual descriptions limited to neutral atoms. In a highly ionized plasma, the Debye screening has a larger spatial extent than the Thomas-Fermi one. This allows collisions with a higher impact parameter and therefore increases the Bethe-Heitler cross-section.

3.4.2 Implementation of the Bethe-Heitler pair creation

Tabulation for ab initio Particle-In-Cell simulations

As for the Bremsstrahlung module, the user can choose between the simple Thomas-Fermi or the mixed Thomas-Fermi-Debye screening model fro the cross-sections. We briefly report the choices made to build the tables that are sampled in the PIC code.

For the simple Thomas-Fermi screening model, we have one table per atomic number. The incident photon energy is tabulated in the range $\hbar\omega \in (2mc^2, 10 \text{ GeV})$ with a logarithmic step and 10^4 points. The positron energy is sampled in 10^2 points in the range $(mc^2, \hbar\omega - mc^2)$ with a linear step. This adds up to 10^6 32-bit reals per table.

For the mixed Thomas-Fermi-Debye screening model, we have one file per ionization degree. For each of them, the incident photon energy is tabulated in the range $\hbar\omega \in (2mc^2, 10 \text{ GeV})$ with a logarithmic step and 10^2 points. The positron energy is sampled in 10^2 points in the range $(mc^2, \hbar\omega - mc^2)$ with a linear step. The Debye length L_D is discretized between the atomic radius r_a ($= 135 \text{ pm}$ for copper) and $\simeq 1 \text{ mm}$, with a logarithmic step and 10^2 points. This adds up to 10^6 32-bit reals per table.

Since the Bethe-Heitler cross-sections are very similar to the Bremsstrahlung ones, the same numerical issue as in Sec. 3.3.2 is observed. It requires the same solution which is the use of 64-bit reals. Whatever the model, the interpolation in the tables is very simple and exactly the same that for the Bremsstrahlung tables (see Sec. 3.3.2).

Exact simulation of positron number and spectra

The implementation of this module is very similar to the Bremsstrahlung one. It is still based on the same Monte Carlo macro-particle pairing scheme described in Sec. 3.1. We consider a 1D mono-energetic ($\hbar\omega = 1 \text{ GeV}$) photon beam ($n_\gamma/n_c = 1$ and length $l = 10c/\omega_0$) propagating in solid copper. In this simple scenario, the number of positron can be easily derived

$$\frac{dN_{e^+}}{dt} = n_{el} \times \sigma_{BH} n_i v_{rel} \quad (3.61)$$

The energy-resolved spectra of the positrons is obtained by derivation of Eq. (3.61) against

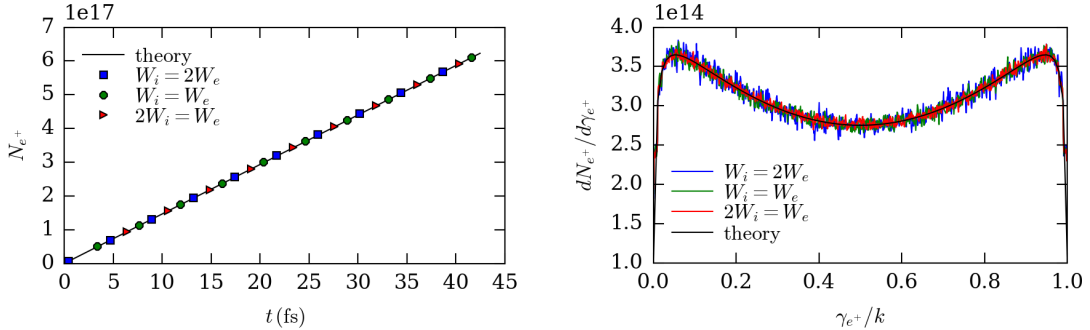


Figure 3.19: Validation of the Bethe-Heitler module for arbitrarily weighted macro-particles and the Thomas-Fermi screening model. (a) Number and (b) energy-resolved spectra of positrons generated by 1 GeV photons incident on neutral copper atoms. The theoretical result is represented with black lines. Three different weight ratios are employed $W_i/W_e = 2, 1$ and $1/2$

γ_{e^+} . We illustrate in Fig. 3.19 the validation of the Bethe-Heitler module in the PIC code for the Thomas-Fermi screening model and in Fig. 3.20 the Thomas-Fermi-Debye model. In Fig. 3.19 we show that arbitrarily weighted macro-particles are handled carefully. To this purpose, we change the initial numerical weight of the macro-ions by increasing their initial number per cell. We observe a rigorous reproduction of the theoretical number (Fig. 3.19(a)) and energy-resolved spectra (Fig. 3.19(b)) of positrons, whatever the ion-to-electron numerical weight ratio ($W_i/W_e = 2, 1$ and $1/2$). This result is obtained for

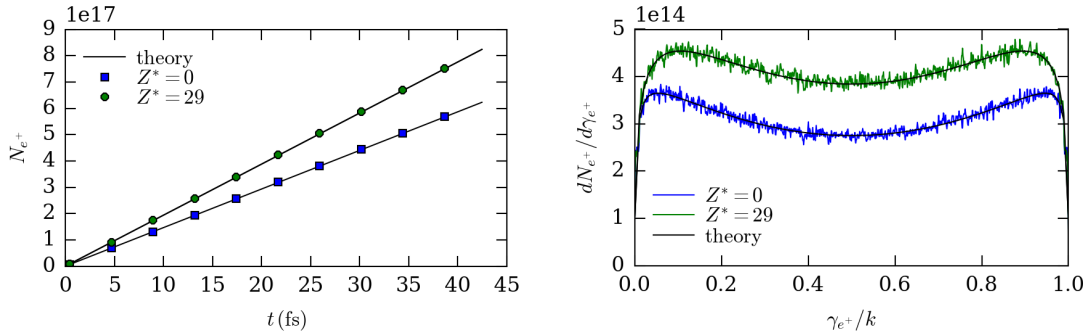


Figure 3.20: Validation of the Bethe-Heitler module for the Thomas-Fermi-Debye screening model. (a) Number and (b) energy-resolved spectra of positrons generated by 1 GeV photons incident on neutral copper atoms (blue curves) and fully ionized copper (green curves). The theoretical result is represented with black lines

the Thomas-Fermi screened cross-sections of the Bethe-Heitler process. For the Thomas-Fermi-Debye screened cross-sections (Fig. 3.20), we propagate the photon beam in neutral copper (blue curves) and fully ionized copper (green curves). We observe once again the reproduction of the expected number of positron and of their energy-resolved spectra respectively in Fig. 3.20(a) and (b). The number of positrons significantly increases between the case of weak ($Z^* = 0$) and strong ionization ($Z^* = Z$). This tendency is also observed for the Bremsstrahlung process (see Sec. 3.3.2) and has the same physical origin. It comes from the larger scale length of the Debye potential, prevailing in a plasma, compared to the Thomas-Fermi potential, prevailing in a solid. This enables higher impact parameter events to occur and therefore increases the cross-section.

We provided the evidence that we can handle arbitrary weighted macro-particles and reproduce the number and energy-resolved spectra of positrons generated by the Bethe-Heitler process in the PIC code CALDER. Overall the modeling of this process is very similar to the Bremsstrahlung.

3.5 Coulomb-Trident pair creation

We now consider the Coulomb Trident process, during which a relativistic electron directly radiates an electron-positron pair, without any intermediary photon.

3.5.1 Non-screened cross-sections

Let us first introduce some notations. The Coulomb Trident process involves an incident electron of energy E_1 creating an electron-positron pair of energy E_p that can be expressed as a function of the new electron (E_-) and positron (E_+) energies: $E_p = E_- + E_+$. The initial electron of energy E_1 has a final energy $E_{1f} = E_1 - E_p$. E denotes the total energy of a particle whereas the notation T , adopted in previous sections, denotes its kinetic energy. In order to sample this process in the Monte Carlo module of a PIC code, we provide the total cross-section (σ_{CT}), the pair-energy differential cross-section ($d\sigma_{CT}/dE_p$) and the pair-and-positron-energy differential cross-section ($d^2\sigma_{CT}/dE_p dE_-$) of the Coulomb-Trident process. As there are less theoretical results on this process (Murota *et al.*, 1956) than for the Bethe-Heitler, we do not take into account any screening of the cross-sections. In the following of this subsection, all cross-sections are unscreened.

The total cross-section, valid in the range $(2mc^2, 100 \text{ MeV})$, was obtained by [Gryaznykh et al. \(1998\)](#)

$$\sigma_{CT} = 5.22Z^2 \ln^3 \left(\frac{2.30 + T_0(\text{MeV})}{3.52} \right) \times 10^{-34} \text{ m}^2 \quad (3.62)$$

This formula is a fit between two theoretical formulas. The first one is valid near the threshold of pair production and comes from [Baier and Katkov \(2008\)](#)

$$(\sigma_{CT})_{E_1 \approx 2mc^2} = \frac{7Z^2 r_e^2 \alpha^2}{2304} \frac{(E_1 - 2mc^2)^3}{(mc^2)^3} \quad (3.63)$$

The second one ([Landau and Lifshitz, 1975](#)) is valid at high incident electron energies

$$(\sigma_{CT})_{E_1 \gg mc^2} = \frac{28\pi Z^2 r_e^2 \alpha^2}{27} \ln^3 (mc^2) \quad (3.64)$$

This total cross-section is plotted in Fig. 3.21 for different atomic numbers ($Z = 13, 29, 47$ and 79) and incident electron energies $E_1 \in (2mc^2, 100 \text{ MeV})$. It is worth to mention that this formula is believed to overestimate the positron production by a factor of $\simeq 4$ as recently stated by [Embréus et al. \(2018\)](#).

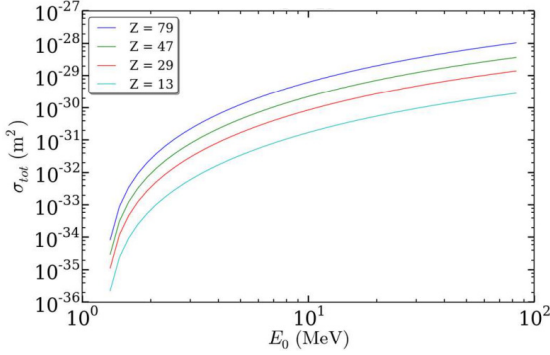


Figure 3.21: Total Coulomb-Trident cross-section for different Z numbers, plotted from formula (3.62)

and 79) and incident electron energies $E_1 \in (2mc^2, 100 \text{ MeV})$. It is worth to mention that this formula is believed to overestimate the positron production by a factor of $\simeq 4$ as recently stated by [Embréus et al. \(2018\)](#).

We determine the pair energy differential cross-section $d\sigma_{CT}/dE_p$ with an approach similar to [Vodopiyanov et al. \(2015\)](#). An interpolation is performed between two cases which are $p_+, p_- \ll m_e c$ and $p_+, p_- \gg m_e c$. The formulas involved were first derived by [Bhabha \(1935\)](#) (formulas 30 and 34)

$$\left(\frac{d\sigma_{CT}}{dE_p} \right)_{p_+, p_- \ll mc} = \frac{(Zr_e \alpha_f)^2}{32} \left[\log \gamma_1^2 - \frac{161}{60} + C + C_r + C_z \right] \frac{E_p^3}{(mc^2)^4} \quad (3.65)$$

$$\left(\frac{d\sigma_{CT}}{dE_p} \right)_{p_+, p_- \gg mc} = \frac{56}{9\pi} (Zr_e \alpha_f)^2 \ln \left(\frac{C_1 E_p}{mc^2} \right) \ln \left(\frac{C_2 mc^2 \gamma_1}{E_p} \right) \frac{1}{E_p} \quad (3.66)$$

k and k_p are constants of order 1, the coefficients C, C_r and C_z only depend on the incident

electron Lorentz factor γ_1 . Let $x = 1/\gamma_1$ the coefficients are

$$\begin{aligned} C_1 &= C_2 = 1 \\ C &= 4 \frac{x^2}{1-x^2} \log \frac{1}{x^2} - \frac{4}{3}x^2 + \frac{1}{6}x^4 \\ C_z &= 3 \frac{x^2}{1-x^2} \left(1 - \frac{x^2}{1-x^2} \log \frac{1}{x^2} \right) - \frac{13}{5}x^2 + \frac{7}{4}x^4 - \frac{9}{10}x^6 + \frac{1}{5}x^8 \\ C_r &= -\frac{3}{2} \frac{x^2}{1-x^2} \left(1 - \frac{x^2}{1-x^2} \log \frac{1}{x^2} \right) + \frac{4}{5}x^2 - \frac{1}{8}x^4 - \frac{1}{20}x^6 + \frac{1}{40}x^8 \end{aligned} \quad (3.67)$$

In order to account for any momentum p_-, p_+ of the electron-positron pair, we take the harmonic mean of formulas (3.65) and (3.66) following the idea of [Vodopiyarov et al. \(2015\)](#)

$$\frac{d\sigma_{CT}}{dE_p} = \frac{\left(\frac{d\sigma_{CT}}{dE_p} \right)_{p_+, p_- \ll mc} \times \left(\frac{d\sigma_{CT}}{dE_p} \right)_{p_+, p_- \gg mc}}{\left(\frac{d\sigma_{CT}}{dE_p} \right)_{p_+, p_- \ll mc} + \left(\frac{d\sigma_{CT}}{dE_p} \right)_{p_+, p_- \gg mc}} \quad (3.68)$$

This cross-section is illustrated for electrons incident on copper in Fig. 3.22. Their energies are respectively $E_1 = 5, 20$ and 100 MeV.

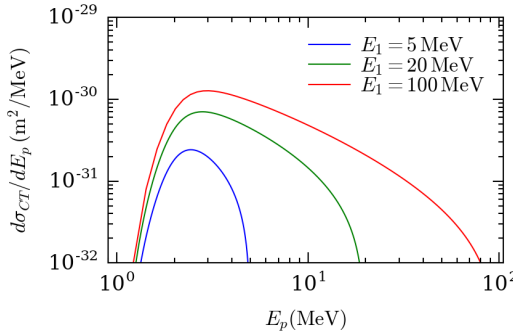


Figure 3.22: Pair-energy differential cross-section of the Coulomb-Trident process for different incident electron energies $E_1 = 5, 20$ and 100 MeV in copper. The curves are plotted from formula (3.68).

The double energy-differential cross section is also taken directly from [Bhabha \(1935\)](#) (formula 32). It is derived in the limit $E_1 \gg E_-, E_+ \gg mc^2$ and reads

$$\frac{d^2\sigma_{CT}}{dE_- dE_+} = \frac{8}{\pi} (Zr_e\alpha_f)^2 \frac{E_+^2 + E_-^2 + 2E_-E_+/3}{(E_- + E_+)^4} \log \left[\frac{C_1 E_- E_+}{(E_- + E_+) mc^2} \right] \log \left[\frac{C_2 E_1}{(E_- + E_+)} \right] \quad (3.69)$$

This cross-section is plotted in Fig. 3.23 for an incident electron energy of 40 MeV and pair energies equal to 28 and 35 MeV. For a given pair energy, we note that the double-differential cross-section is symmetrical with respect to the axis $2E_+ = E_p$.

We recalled the Coulomb-Trident differential and total cross-sections from [Bhabha \(1935\)](#) and [Gryaznykh et al. \(1998\)](#). They are derived in the approximation of an un-screened nucleus field. Further improvements may be done to take into account for a simple-exponential screened potential as done by [Murota et al. \(1956\)](#).

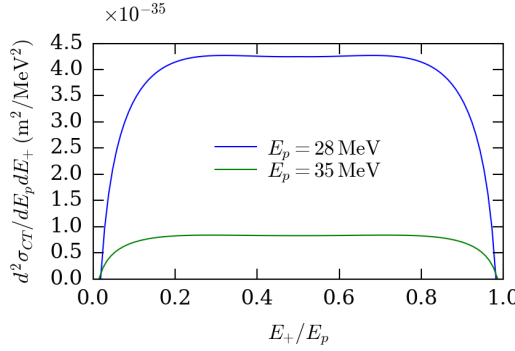


Figure 3.23: Double-differential cross-section of the Coulomb-Trident process for an incident electron energy $E_1 = 40$ MeV and pair energies of 28 and 35 MeV in copper. The curves are plotted from formula (3.69).

3.5.2 Implementation of the Coulomb-Trident pair creation

Tabulation for ab initio Particle-In-Cell simulations

The simulation of the Coulomb Trident electron-positron pair creation requires two tables per atomic number Z . The first one contains the pair-energy differential cross-section $d\sigma_{CT}/dE_p$ and the second one the double-differential cross-section $d^2\sigma_{CT}/dE_-dE_+$.

For the first table, the incident electron energy varies in the range $(2mc^2, 100 \text{ MeV})$ with a linear step and 10^2 points. The pair energy is sampled in 10^2 points in the range $(2mc^2, E_1 - mc^2)$ with a linear step. Once the pair energy E_p is sampled from the first table, the second table is used to sample the electron energy E_- . The positron energy is then deduced by $E_+ = E_p - E_-$. For this, we tabulate the double-differential cross-section for pair energy in the range $(2mc^2, 100 \text{ MeV})$ with a linear step and 10^2 points. The energy of the created electron is sampled in the range $(mc^2, E_p - mc^2)$ with a linear step and 10^2 points.

The interpolation is done as for the Bremsstrahlung and Bethe-Heitler tables (see Secs. 3.3.2 and 3.4.2). There is no need to increase the number of points in the table since it is limited to a small range of incident electron energies.

Exact simulation of positron number and spectra

We now validate the implementation of the Coulomb Trident pair production in the PIC code CALDER. We consider a simple scenario with a 1D, monoenergetic (40 MeV) electron beam (density $n_e/n_c = 1$) of length $l = 10c/\omega_0$ propagating in copper of solid density $n_i/n_c = 80$. We employ periodic boundary conditions along the x axis. The field solver is switched off and only the Monte Carlo module is activated. In this simple problem, the rate of positron emission over time is simply modeled by the product of the pair-production frequency for one electron $\sim \sigma_{CT} n_i v_{rel}$, multiplied by the total number of electrons n_{el}

$$\frac{dN_{e^+}}{dt} = \sigma_{CT} n_i v_{rel} \times n_{el} \quad (3.70)$$

The energy-resolved spectra of the pairs created is obtained by the derivation of Eq. (3.70) against E_p . We first check the handling of arbitrary weighted macro-particles in Figure 3.24. One can see that for different initial macro-particles numerical weight, the number of positrons created remains unchanged and agrees perfectly with the theoretical result from

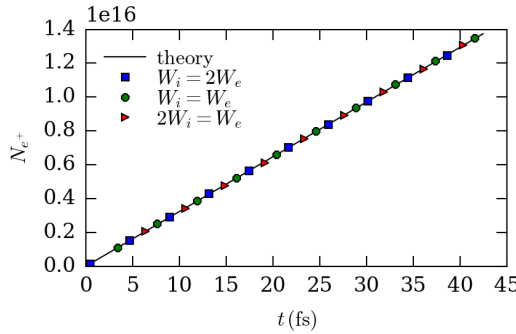


Figure 3.24: Number of positrons created by the Coulomb-Trident process for 40 MeV electrons incident on copper. Three simulations were done with varying initial statistical weights for macro-ions and macro-electrons $W_i/W_e = 2, 1$ and $1/2$. The theoretical result is plotted as a black line from Eq. (3.70).

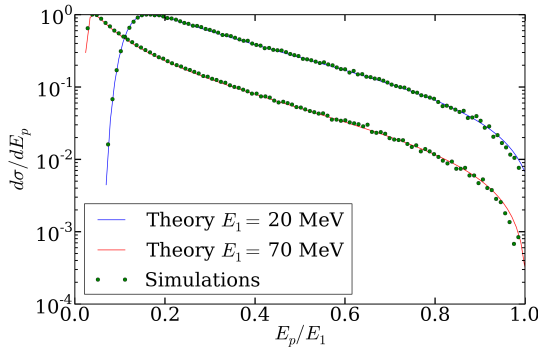


Figure 3.25

Eq. (3.70). We also confirm that the pair-energy differential cross-section is well-sampled in Fig. 3.25. We illustrate the good agreement with the theory for two different incident electron energies $E_1 = 20$ MeV.

In this section, we validated the electron-positron pair creation via the Coulomb-Trident process in the PIC code CALDER. It is done in two steps. Firstly we evidenced that we can reproduce the expected rate of pair creation for arbitrarily weighted macroparticles. Secondly we showed pair-energy resolved energy spectra matching the cross-section given in the literature ([Bhabha, 1935](#)).

3.6 Application to fast electron relaxation in a solid target

3.6.1 Theoretical 0D model on positron creation

This model from [Myatt et al. \(2009\)](#) was published with the main goal of optimising the laser-driven pair production on the OMEGA EP laser system ([Waxer et al., 2005](#)). This model was found to be consistent with the experimental results of [Chen et al. \(2015\)](#).

In this model, the indirect (Bremsstrahlung + Bethe-Heitler) and the direct (Trident) pair creation processes are both treated. The main result we are interested in is the comparison between the two processes efficiency. The starting point of the model simplifies the reality. It describes the relaxation of a relativistic electron distribution in a solid target.

They are assumed to be heated by an energetic laser ($\simeq 1kJ$) and generate photons and electron-positron pairs. In the following on this subsection, we recall how the number of pairs can be evaluated thanks to the formalism developped by [Myatt et al. \(2009\)](#).

The calculation of the positron yield through the Bethe-Heitler process requires to first evaluate the Bremsstrahlung spectra of photons. In the article of [Myatt et al. \(2009\)](#) this is done by taking the energy-differential Bremsstrahlung cross-section from [Seltzer and Berger \(1986\)](#). However we will employ the expression we implemented in the PIC code CALDER presented in Sec. 3.3.1. The number of photons with energy between k and $k + dk$, denoted by $N_\gamma(k)dk$, can be expressed as a function of the energy-differential Bremsstrahlung cross-section denoted by $d\sigma_{Br}/dk$. It is assumed that an electron of kinetic energy T_1 is continuously slowed down at a pace given by the stopping power denoted dT_1/ds ([Berger et al., 1984](#))

$$N_\gamma(k)dk = \int_0^\infty dT_1 f_1(T_1) \int_0^{T_1} dT n_i \frac{d\sigma_{Br}}{dk}(T, k) \left| \frac{dT}{ds} \right|^{-1} \quad (3.71)$$

where $k = \hbar\omega/mc^2$ is the normalized photon energy. The total energy contained into photons is denoted by $\epsilon_{\gamma,0}$ and the total energy contained into photons above the $2mc^2$ pair generation threshold is denoted by $\epsilon_{\gamma,2mc^2}$. It is deduced by multiplying (3.71) by the photon energy k and integrating over k . After inversion of the integral signs, one obtains

$$\begin{aligned} \epsilon_{\gamma,0} &= \int_0^\infty dT_1 f_1(T_1) T_1 \eta_0(T_1) \\ \epsilon_{\gamma,2mc^2} &= \int_{2mc^2}^\infty dT_1 f_1(T_1) T_1 \eta_{2mc^2}(T_1) \end{aligned}$$

with η_0 (resp. η_{2mc^2}) denoting the radiation yield for all photons (resp. above $2mc^2$) as defined by the ICRU report by [Berger et al. \(1984\)](#)

$$\eta_0(T_1) = \frac{n_i}{T_1} \int_0^{T_1} dT \left| \frac{dT}{ds} \right|^{-1} \int_0^T dk k \frac{d\sigma_{Br}}{dk}(T, k) \quad (3.72)$$

$$\eta_{2mc^2}(T_1) = \frac{n_i}{T_1} \int_{2mc^2}^{T_1} dT \left| \frac{dT}{ds} \right|^{-1} \int_{2mc^2}^T dk k \frac{d\sigma_{Br}}{dk}(T, k) \quad (3.73)$$

An example is illustrated in Fig 3.26. We took the case of an electron of kinetic energy T_1 experiencing Bremsstrahlung losses in gold. The Bremsstrahlung yield of photons is a rising function of the incident electron energy T_1 . At low electron energies $T_1 \leq 5$ MeV the relative difference between the two yields (for all photons or $\forall \hbar\omega \geq 1.022$ MeV) remains significant ($\geq 20\%$). For higher electron energies, both are very similar. This illustrates that most of the photons are likely to produce pairs in the latter case.

Once the photon spectra is calculated with formula (3.71) one can estimate the number of positrons emitted by the Bethe-Heitler process. Two main physical issues are taken into account while deriving this number. The first deals with the effective photon propagation depth as it propagates through the target. The attenuation of a photon of energy k can be taken into account with an attenuation coefficient of the form $\mu(k) = n_i \sigma_{tot}$. The cross-section σ_{tot} accounts for the main processes that may alter the photon transport such as coherent and incoherent Compton scattering, photoelectric absorption, photonuclear absorption in addition to pair creation. It was measured for all $Z = 1, 100$ $k = 1$ MeV, 100 GeV and tabulated by [Hubbell et al. \(1980\)](#). The second effect emerges as photons only cross the target once and therefore have a limited propagation length in

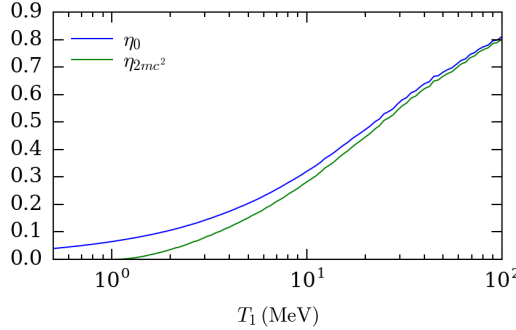


Figure 3.26: Bremsstrahlung energy yield of an electron propagating in gold as a function of its kinetic energy T_1 , for all photons (η_0) and above the $2mc^2$ threshold (η_{2mc^2}). The curves represent formula (3.72) and (3.73).

the material, contrary to electrons which are assumed to experience refluxing and lose all their energy in the target. The longitudinal (d) and transverse (r) dimensions of the target as well as the solid angle Ω of the photon emission are introduced. The following effective propagation depth (in g/cm²) denoted by $\langle \rho L \rangle_\Omega$ takes into account both effects mentioned above and is defined by

$$\langle \rho L \rangle_\Omega = \frac{1}{4\pi} \int d\Omega \frac{\rho d}{2|\cos \theta|} C\left(\frac{\mu(k)d}{|\cos \theta|}\right) \quad (3.74)$$

This coefficient is homogeneous to g/cm². It can be interpreted as the average of the product of the density ρ times L , the distance travelled by the photon. It is approximated and averaged assuming a homogeneous and isotropic repartition of photons in the target. It depends on the photon emission angle θ , the target length d and the linear attenuation coefficient $\mu(k)$ for a photon of energy k . The function C is defined as $C(w) = 2[\exp(-w) - (1-w)]/w^2$. This correction coefficient ranges from unity ($w \rightarrow 0$) to $2|\cos \theta|/\mu(k)d$ for large w . We simplify the notation $\mu(k) = \mu$ and change the variable $x = |\cos \theta|$, this integral can then be expressed as

$$\langle \rho L \rangle_\Omega = \rho d \int_0^1 dx \min \left\{ \frac{1}{2x} C\left(\frac{\mu d}{x}\right), \frac{r}{d} \right\} \quad (3.75)$$

The effect of the finite transverse size of the target r is taken into account by the minimum in Eq. (3.75). It is set to 1 mm. The above integral has the closed-form solution

$$\begin{aligned} \langle \rho L \rangle_\Omega = & \frac{1}{2} \frac{\rho}{\mu} \left[1 + \left(1 - \frac{1}{\mu d} \right) \left(1 - e^{-\mu d} \right) - \mu d Ei(-\mu d) \right] \\ & - \frac{x^* \rho}{2} \left[1 + \left(1 - \frac{x^*}{\mu d} \right) \left(1 - e^{-\mu d/x^*} \right) - \frac{\mu d}{x^*} Ei\left(-\frac{\mu d}{x^*}\right) \right] \\ & + x^* \rho r \end{aligned} \quad (3.76)$$

where $Ei(x) = \int_{-x}^{\infty} dt e^{-t}/t$ and x^* the solution of equation $x^* (1 - e^{-\mu d/x^*}) / (\mu d) = 1 - \mu$. Once this coefficient is fully explicit, the following expression for the number of Bethe-

Heitler positrons of energy between E_+ and $E_+ + dE_+$ can be obtained

$$N_{+,BH}(E_+) dE_+ = \frac{n_i}{\rho} \int_0^\infty dk N_\gamma(k) \frac{d\sigma_{BH}}{dE_+}(k, E_+) \langle \rho L \rangle_\Omega \quad (3.77)$$

where $d\sigma_{BH}/dE_+$ is the Bethe-Heitler energy-differential cross-section. The total positron yield via the Bethe-Heitler process is

$$Y_{+,BH} = \frac{N_A}{A} \int_{2mc^2}^\infty dE_+ N(E_+) \quad (3.78)$$

where N_A denotes the Avogadro constant and A the atomic weight. Interchanging the integral signs enables to get an expression depending only on the total Bethe-Heitler cross section, rather than the energy-differential one

$$Y_{+,BH} = \frac{n_i}{\rho} \int_0^\infty dk N_\gamma(k) \sigma_{BH}(k) \langle \rho L \rangle_\Omega \quad (3.79)$$

We recall that the dependence with respect to the target length and width is contained in the effective photon propagation depth $\langle \rho L \rangle_\Omega$ as expressed in formula (3.76). In the model of [Myatt et al. \(2009\)](#) the total Bethe-Heitler cross-section as well as the linear mass attenuation coefficient $\mu(k)$ are interpolated directly from the tables of [Hubbell et al. \(1980\)](#). In our case we keep the attenuation coefficient from [Hubbell et al. \(1980\)](#) but employ the cross-sections implemented in CALDER (see Sec. 3.4).

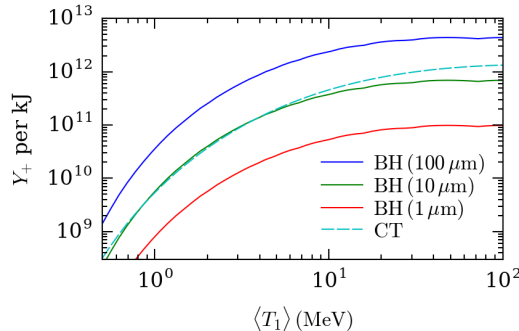


Figure 3.27: Positron yield as a function of fast electron average kinetic energy $\langle T_1 \rangle$ (MeV) in gold. The abbreviation BH stands for the Bethe-Heitler process and CT for the Coulomb Trident mechanism. The yields of positrons are determined via the formulas (3.79) and (3.80).

The result is represented in Fig 3.27 for thin ($1 \mu\text{m}$) and thicker ($100 \mu\text{m}$) gold targets. The number of positrons is given as a function of the energy contained in the fast electron distribution. We chose an exponential electron distribution $f_1(T_1) = \exp(-T_1/\langle T_1 \rangle)/T_1$ as it propagates in a gold target ($Z = 79$). The number of positrons created by the Bethe-Heitler process rises as a function of the target thickness and the fast electron distribution temperature. For a kJ class laser it is expected to reach values of 10^{11} or 10^{12} .

The Coulomb-Trident pair yield is more straightforward to derive. Let us consider any electron distribution given by $f_1(T_1)$ propagating in a uniform target and experiencing only collisional and radiative losses. We denote by $Y_{+,CT}$ the Coulomb Trident yield. The

number of positrons emitted by this one-step process is

$$Y_{+,CT} = \int_{2mc^2}^{\infty} dT_1 f_1(T_1) \int_{2mc^2}^{T_1} dT n_i \sigma_{CT}(T) \left| \frac{dT}{ds} \right|^{-1} \quad (3.80)$$

where $\sigma_{CT}(T)$ is the Coulomb-Trident total cross-section from [Gryaznykh et al. \(1998\)](#). The expression (3.80) is straightforward to implement and illustrated in Fig 3.27 where the abbreviation CT stands for Coulomb Trident and BH stands for Bethe-Heitler. In this model the direct pair production (by Coulomb-Trident) does not depend on the target longitudinal dimension. In order to derive the analytical expression (3.80) for $Y_{+,CT}$, the model assumes that all electrons remain in the target (whatever its thickness) until their energy goes below the $2mc^2$ pair generation threshold.

We note that above a threshold of $10\text{ }\mu\text{m}$ the Bethe-Heitler (indirect) pair production dominates the Coulomb-Trident (direct) one in gold. For thinner targets ($\simeq 1\text{ }\mu\text{m}$) the direct pair production prevails and leads to the generation of more positrons than the indirect mechanism. This behavior can be explained as for very thin targets, photons do not travel in enough matter to efficiently decay into an electron-positron pair, thus reducing the efficiency of the Bethe-Heitler process. With Fig. 3.27 this threshold is observed for a $10\text{ }\mu\text{m}$ target.

In this subsection, we recalled the theoretical model from [Myatt et al. \(2009\)](#) which provides convenient formulas to calculate the number of positrons generated during the relaxation of a fast electron distribution in a solid gold target. Both processes are taken into account (Bethe-Heitler and Coulomb-Trident) and their efficiency is compared. It is found that in practical laser-target experiments involving kJ-class lasers the Bethe-Heitler process prevails if the target thickness is higher than $10\text{ }\mu\text{m}$ and the Coulomb-Trident dominates for thinner targets (thickness lower than $10\text{ }\mu\text{m}$).

3.6.2 Self-consistent Particle-In-Cell simulations

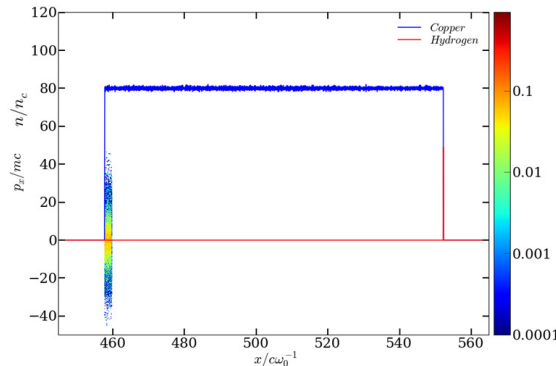


Figure 3.28: 1D PIC setup: relaxation of an initially localized fast electron distribution (colormap) in a $15\text{ }\mu\text{m}$ copper target. The copper density is represented by the blue curve and is uniform ($n_{Cu}/n_c = 80$) and the thin (6.25 nm) contaminant proton layer is illustrated by the red curve, at the rear side of the target.

We now compare the above model to self-consistent PIC-simulations describing plasma effects along with particle scattering, impact ionization, radiative and pair generation processes. As an application we compute the positron yield produced by a hot electron population in a solid Cu target of varying thickness ($5\text{ }\mu\text{m} \leq l \leq 15\text{ }\mu\text{m}$). Their energy is

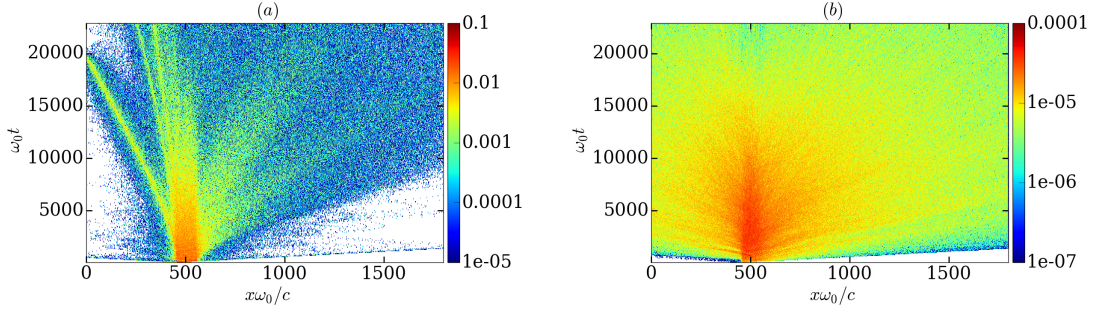


Figure 3.29: Spatio-temporal evolution (x, t) of the density (normalized to $n_c = 1.1 \times 10^{21} \text{ cm}^{-3}$) of (a) fast electrons from the initial Maxwell-Jüttner distribution and (b) Bremsstrahlung photons. For both electrons and photons, low energy cutoff of 1 MeV is applied. The target thickness is $15 \mu\text{m}$ and the initial average kinetic energy of electrons is $\langle T_1 \rangle = 10 \text{ MeV}$.

distributed according to a relativistic isotropic Maxwell-Jüttner distribution of temperature T_g

$$f_\theta(T_1) dT_1 = \frac{\exp\left[-\sqrt{1+T_1^2}/\theta\right]}{\theta K_2(1/\theta)} T_1^2 dT_1 \quad \text{with} \quad \theta = \frac{k_B T_g}{mc^2} \quad (3.81)$$

K_2 denotes the first kind Bessel function of order 2. The average kinetic energy is denoted by $\langle T_1 \rangle = \int T f_\theta(T) dT$. For $\theta \ll 1$, $\langle T_1 \rangle \rightarrow 3\theta/2$ and for $\theta \gg 1$, $\langle T_1 \rangle \rightarrow 3\theta$. The PIC simulation setup is depicted by Fig. 3.28. The $x - p_x$ electron distribution is plotted on the colormap and its integral is normalized to 1. The initial electron density is $n_e/n_c = 1$ and it is initially contained in a 320 nm layer located at the front side of the target. The copper target has an initial uniform density profile with $n_{Cu}/n_c = 80$ (blue curve). We also model a thin (6.25 nm) contaminant proton layer at the rear side of the target with density $n_H/n_c = 60$ (red curve).

In order to confront PIC simulations with the model of Myatt *et al.* (2009), we need to calculate a steady-state number of pairs which is typically reached after several ps for the thin targets at stake in this study. Those durations are quite large and can only be simulated in a simplified $1Dx \times 3Dv$ geometry. Depending on target thickness, we observed that 1 to 2.5 million iterations are needed to capture the steady-state number of positrons generated by the Bethe-Heitler and Coulomb-Trident processes. We chose to decrease the spatial step down to $\lambda_0/420$ in order to reduce numerical heating ($\lambda_0 = 1 \mu\text{m}$). As an example we noted a very low (3%) relative error on the energy balance at final time for a $5 \mu\text{m}$ target and a fast electron distribution with a 5 MeV average kinetic energy. The simulation domain counts 120.000 cells ($\leftrightarrow 286 \mu\text{m}$ long). This enables to catch the full dynamic of the rear side TNSA expansion of the contaminant layer. The plasma center is initially located at abscissa $x\omega_0/c = 500$ ($\leftrightarrow 80 \mu\text{m}$). The multiple scattering, impact ionization, Bremsstrahlung, Bethe-Heitler and Coulomb-Trident modules are activated. We treat those processes in the appropriate frame (c.o.m. frame or ion-rest frame) since we demonstrated it can lead to significant errors (see Sec. 3.2.3). The Bremsstrahlung, Bethe-Heitler and Coulomb-Trident processes are only simulated for the copper ions and are neglected for the thin contaminant proton layer.

The space-time evolutions of the electron, photon, proton, copper and positron densities are displayed in Fig. 3.29(a-b), Fig. 3.30(a-b) and Fig. 3.31(a-b) in the case $\langle T_1 \rangle = 10 \text{ MeV}$ and $l = 15 \mu\text{m}$. In Fig. 3.29(a) electrons are seen to expand towards vacuum from

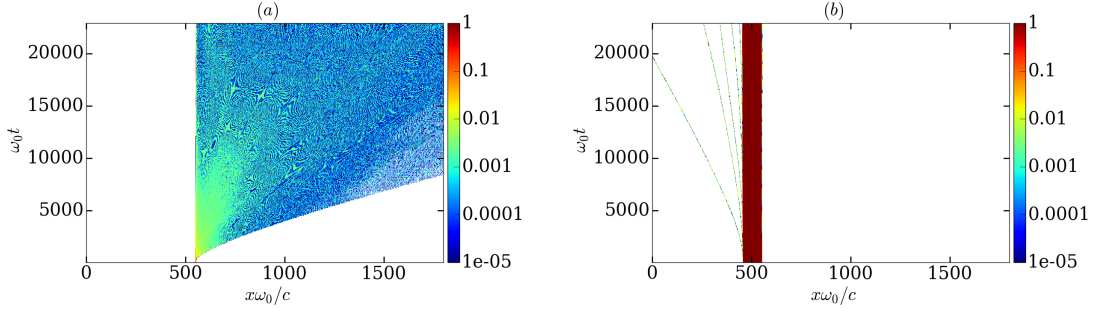


Figure 3.30: Spatio-temporal evolution (x, t) of the density (normalized to $n_c = 1.1 \times 10^{21} \text{ cm}^{-3}$) of (a) rear side protons (b) copper ions. No energy selection is applied, contrary to Fig 3.29. The target thickness is $15 \mu\text{m}$ and the initial average kinetic energy of electrons is $\langle T_1 \rangle = 10 \text{ MeV}$.

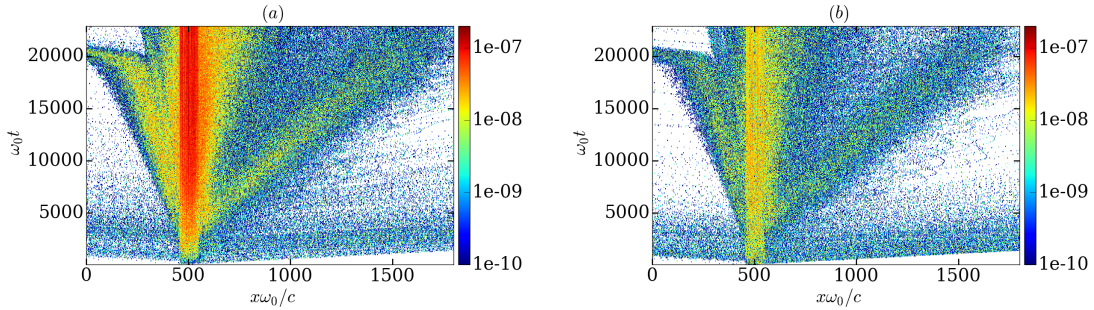


Figure 3.31: Spatio-temporal evolution (x, t) of the density (normalized to $n_c = 1.1 \times 10^{21} \text{ cm}^{-3}$) of (a) the Bethe-Heitler and (b) the Coulomb-Trident positrons. No energy selection is applied, contrary to Fig 3.29. The target thickness is $15 \mu\text{m}$ and the initial average kinetic energy of electrons is $\langle T_1 \rangle = 10 \text{ MeV}$.

both sides of the target. The expansion in the $x > 0$ direction (rear side) occurs faster due to the lighter protons. The proton and copper expansion are respectively displayed in Fig. 3.30(a) and (b). Protons located in the thin contaminant layer overall absorb a significant fraction of the initial hot electron energy (30% after $12.2 \text{ ps} \leftrightarrow 23000\omega_0^{-1}$) as witnessed on the red curve in Fig. 3.32 (it is analyzed and interpreted below).

The Coulomb Trident process saturates at $\omega_0 t \simeq 10^4 \leftrightarrow 5.3 \text{ ps}$ and the Bethe-Heitler at $\omega_0 t \simeq 2.3 \times 10^4 \leftrightarrow 12.2 \text{ ps}$. Both positron densities in Fig. 3.31(a-b) exhibit four distinct structures. The first one comes from positrons generated early ($\omega_0 t \leq 3000$) forming a jet-structure and leaving the simulation domain before instant $\omega_0 t \simeq 3 \times 10^3$. The second one is accompanied by fast electrons and both species form a bunch moving at a speed of $\simeq 0.06c$. Those positrons are generated at early times ($\omega_0 t \leq 6 \times 10^3$) by the hot electrons and then leave the target, overlapping with the expanding protons as seen in Fig. 3.30(a). The third and highest peak of emission is located at the core of the copper target ($450 \leq x\omega_0/c \leq 550$). The density of positrons remains higher in this area as they have a perpendicular momentum. Indeed, because of the 1D geometry, photons created with a near grazing birth angle ($\theta \rightarrow 90^\circ$) will remain a time $l/(c \cos \theta) \rightarrow \infty$ in the target. The fourth and last structure is located at the front side of the target and is backward-directed. Thanks to Figs 3.30(b) we note that it follows the copper ion expansion with a

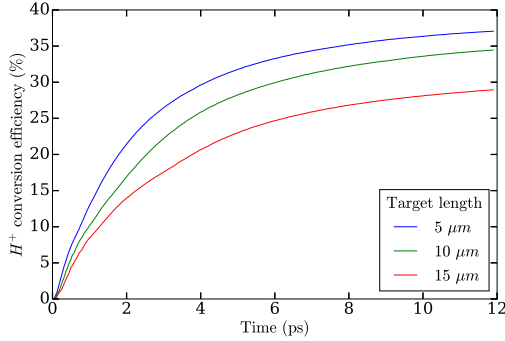


Figure 3.32: Evolution of the electron to proton conversion efficiency for three target thicknesses: 5, 10, 15 μm . The electrons are initially distributed according to a relativistic Maxwell-Juttner law of average kinetic energy $\langle T_1 \rangle$.

speed of $\simeq 0.02c$. A discontinuity in the velocity of this electron-positron jet is observed at late times $\omega_0 t \simeq 2 \times 10^4$. It is probably a numerical effect due to the energetic copper macro-particles leaving the simulation domain at this time (see Fig. 3.30(b)).

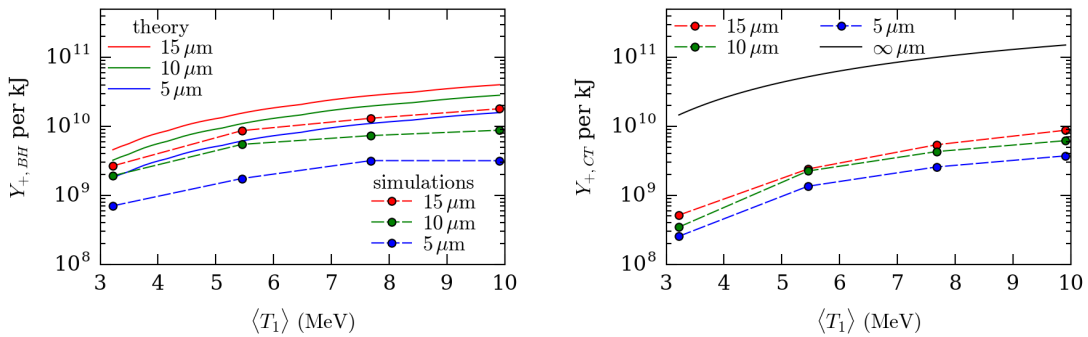


Figure 3.33: (a) Generation of positrons by Bethe-Heitler and (b) by Coulomb Trident mechanisms as a function of target thickness and fast electron average kinetic energy. The $1Dx \times 3Dv$ PIC simulations are represented by dashed lines and the Monte Carlo 0D model of Myatt *et al.* (2009) by solid lines.

We now compare in Fig 3.33 the steady-state number of positrons emitted by the Coulomb-Trident and Bethe-Heitler processes as a function of the target thickness (5 – 15 μm) and the electron average kinetic energy ($\langle T_1 \rangle = 3 - 10 \text{ MeV}$). The first thing to be noticed is that the PIC simulations reproduce the trend of the theoretical model. Indeed both indicate that the higher the electron temperature or the target thickness, the higher the number of positrons. However the theoretical model overestimates this number of positrons. There is a noticeable gap that grows as the target gets thinner: the relative difference for the Bethe-Heitler process is 44 % in a 15 μm target and 68 % in a 5 μm one. This overestimation of the theoretical model comes from its assumption on electrons that cannot accelerate ions via the TNSA mechanism. In Fig 3.32 we depict the evolution of the conversion efficiency of hot-electron energy into protons for the three target thicknesses. Unidimensional PIC simulations does not properly describe the hot-electron dilution during the plasma expansion (thus over-estimating the hot-electron density), resulting in rather high values (30 – 35 %). However they demonstrate why the

gap between the PIC simulations and the theoretical model increases for thinner targets. All the energy lost by electrons to the benefit of the ions is not available for pair production anymore. The theoretical model ignores this particular phenomenon as described in the former subsection.

In this section we compared the efficiency of the direct (Coulomb Trident) and indirect (Bethe-Heitler) electron-positron pair production. To this purpose, we confronted the theoretical 0D model of [Myatt *et al.* \(2009\)](#) to self-consistent 1D PIC simulations. The comparison emphasizes the over-estimation of the positron number in the model. It comes from the neglect of one particular plasma process which is the target normal sheath acceleration.

Conclusions

The Particle-In-Cell code CALDER now accounts for various processes such as multiple scattering, impact ionization, Bremsstrahlung radiation of photons, Bethe-Heitler and Coulomb-Trident electron-positron pair creation. They are modeled by a macro-particle pairing scheme included in a Monte Carlo module called every time step of a PIC simulation. We emphasize the improvements done in order to give a coherent description of the screened potential mediating all those effects. Indeed we introduced models accounting for both the low and high ionization limits for scattering, Bremsstrahlung emission and Bethe-Heitler pair production. Overall we observed that in the limit of high ionization, the efficiency of those effects are enhanced compared to the limit of low ionization. This comes from the larger screening length of the Debye potential used to describe the potential screening in a plasma compared to the Fermi potential in a neutral medium. The numerical implementation was validated through comparisons with theoretical models. We compared the numerical simulations to the multiple deflection theory of [Molière \(1947\)](#), to the NIST stopping-power database and to a theoretical model on pair creation from [Myatt *et al.* \(2009\)](#).

Part II

Radiative processes induced by laser solid interaction

Chapter 4

High-energy radiation in ultra-relativistic laser-solid interactions

During the interaction of an intense laser pulse ($I_0 \geq 10^{18} \text{ Wcm}^{-2}$) with an initially solid material sample, a significant fraction of the laser energy (from a few % to $\sim 50\%$) is converted into fast electrons, accelerated up to relativistic energies (Wilks *et al.*, 1992; Lefebvre and Bonnaud, 1997; Davies, 2009; Kemp *et al.*, 2014). While propagating through the dense inner region of the illuminated target (or through a secondary convertor target), those electrons can radiate part of their kinetic energy, either directly through Bremsstrahlung (Kmetec *et al.*, 1992; Gahn *et al.*, 1998; Perry *et al.*, 1999; Hatchett *et al.*, 2000; Edwards *et al.*, 2002; Galy *et al.*, 2007; Compart La Fontaine *et al.*, 2012), or indirectly through radiative relaxation of excited atomic states (Yasuike *et al.*, 2001; Stephens *et al.*, 2004; Sefkow *et al.*, 2011). The former process leads to continuous broadband photon spectra that extend up to the maximum fast electron energy, whereas the latter one yields discrete spectra determined by atomic line transitions. Both types of fast electron-induced radiation can serve for high-resolution flash radiography of dense objects (Glinec *et al.*, 2005; Ravasio *et al.*, 2008; Park *et al.*, 2008; Brambrink *et al.*, 2009; Westover *et al.*, 2010; Courtois *et al.*, 2011; Jarrott *et al.*, 2014; Antonelli *et al.*, 2017), absorption spectroscopy of heated plasmas (Audebert *et al.*, 2005; Lecherbourg *et al.*, 2007), or characterization of the fast-electron distribution (Pisani *et al.*, 2000; Santala *et al.*, 2000; Martinolli *et al.*, 2006; Chen *et al.*, 2009; Meadowcroft and Edwards, 2012; Zulick *et al.*, 2013). In addition, laser-driven high-energy Bremsstrahlung photon sources have been exploited to trigger photonuclear reactions (Cowan *et al.*, 2000; Ledingham *et al.*, 2003; Schwoerer *et al.*, 2003; Wang *et al.*, 2017), as well as to generate unprecedented dense electron-positron pair beams through the Bethe-Heitler process in high- Z thick targets (Liang *et al.*, 1998; Gahn *et al.*, 2000; Chen *et al.*, 2009; Sarri *et al.*, 2015; Williams *et al.*, 2016).

At the extreme laser intensities ($I_0 \gtrsim 10^{22} \text{ Wcm}^{-2}$) mainly addressed in this thesis, copious emission of energetic photons can also originate from direct laser-electron interaction, that is, through nonlinear inverse Compton scattering of the laser light by relativistic electrons (Zhidkov *et al.*, 2002; Koga, 2004). In the strong-field limit ($a_L \gg 1$) where the quasi-stationary field approximation holds, this mechanism is analogous to synchrotron emission (Erber, 1966; Kirk *et al.*, 2009; Di Piazza *et al.*, 2012), and hence can also be mediated by the intense quasistatic fields possibly induced during the laser-plasma interaction (Stark *et al.*, 2016) or even by the fields generated during the interaction of high-density e^-e^+ and e^-e^- beam (Del Gaudio *et al.*, 2018). The first all-optical generation of γ -ray

photons (with $\sim 0.1 - 10$ MeV energies) through nonlinear inverse Compton scattering was achieved by making collide a relativistic (> 100 MeV) electron beam issued from a plasma wakefield accelerator with a moderately relativistic ($I \sim 10^{19}$ Wcm $^{-2}$) femtosecond laser pulse (Phuoc *et al.*, 2012; Sarri *et al.*, 2014). Such conditions, however, led to a low quantum nonlinearity parameter ($\chi_e \lesssim 0.01$) so that the radiation negligently affected the electron dynamics. Only recently, by means of more intense lasers ($I_0 \sim 4 \times 10^{20}$ Wcm $^{-2}$) and higher-energy (~ 2 GeV) wakefield-driven electron beams, have the first measurements of inverse Compton scattering in the radiation reaction regime ($\chi_e \gtrsim 0.2$) been carried out, providing evidence for substantial (up to $\sim 30\%$) radiation-induced electron energy losses (Cole *et al.*, 2018; Poder *et al.*, 2018).

Although of major interest for maximizing the χ_e parameter at fixed laser intensity (Blackburn *et al.*, 2014; Vranic *et al.*, 2014; Ridgers *et al.*, 2017), and thus testing models for quantum radiation reaction (Sokolov *et al.*, 2009; Bulanov *et al.*, 2011; Mackenroth *et al.*, 2013; Di Piazza *et al.*, 2018) under well-controlled conditions, the above laser-electron-beam collision scenarios do not allow a significant fraction of the laser pulse energy to be converted into synchrotron photons. With a peak laser intensity of 10^{22} W/cm 2 , significant ($\gtrsim 1\%$) radiation conversion efficiency, the laser pulse must rather interact with dense and/or extended enough plasma targets (Brady *et al.*, 2014; Nerush *et al.*, 2014; Wang *et al.*, 2015a; Chang *et al.*, 2017). In this context, it is important to determine the interaction conditions leading to synchrotron emission prevailing over Bremsstrahlung, and therefore the scaling of the two competing radiation processes with the target parameters. This problem has as yet only been touched upon, mainly because there are still very few PIC codes including modules for synchrotron and Bremsstrahlung radiations (Pandit and Sentoku, 2012; Ward and Sircombe, 2014). Notably, Pandit and Sentoku (2012) found that synchrotron emission dominates in $5\text{ }\mu\text{m}$ thick Cu targets irradiated at intensities exceeding $\sim 10^{22}$ Wcm $^{-2}$. More recently, Wan *et al.* (2017) showed dominance of synchrotron emission at $I_0 \geq 10^{21}$ Wcm $^{-2}$ (resp. $\geq 10^{22}$ Wcm $^{-2}$) in $1\text{ }\mu\text{m}$ thick Al (resp. Au) targets. Yet, none of these studies examined the influence of the target thickness on the radiation. Vyskočil *et al.* (2018) looked into the variations of the Bremsstrahlung spectrum from solid foils of various materials driven in the $3 \times 10^{21} - 10^{23}$ Wcm $^{-2}$ intensity range; their investigation, however, was restricted to micrometric thicknesses and, while apparently included in their simulations, synchrotron emission was not commented upon. These previous works motivate us to further examine the synchrotron/Bremsstrahlung competition as a function of the ultrafast target dynamics, which will be the main objective of this chapter. To this purpose, we will consider the case of a short-pulse ($\tau_0 = 50$ fs) laser of not-so-extreme intensity ($I_0 = 10^{22}$ Wcm $^{-2}$), relevant to ELI-class facilities during their first years of operation (Le Garrec *et al.*, 2014; Balabanski *et al.*, 2017).

This chapter will be structured as follows. Firstly, we will recall the basic processes involved in relativistic laser-solid interaction, from relativistic self-induced transparency to fast electron generation and ion acceleration. Secondly, we will present a series of somewhat idealized PIC simulations serving to characterize the synchrotron emission from plasmas of different density and thickness. Finally, we will perform integrated simulations, run both in 1D and 2D geometries, of the laser-induced high-energy radiation in Cu targets of thicknesses ranging from a few tens of nm to a few μm . The Bremsstrahlung and synchrotron radiation properties will be analyzed in detail, and shown to strongly depend on the transparency-opacity of the target.

4.1 Fundamentals of relativistic laser-plasma interaction

In this section, we briefly present the major phenomena underpinning the interaction of an ultra-intense laser wave with a plasma. Our purpose is to acquaint the reader with the basic mechanisms and scaling laws at stake in the following PIC simulation study. Starting from the motion of a single electron in vacuum, we recall the concept of relativistic self-induced transparency in classically opaque (overcritical) plasmas, and describe how electron acceleration operates in undercritical and overcritical plasmas. Finally, we present the main mechanisms of ion acceleration in overcritical plasmas. As will be shown in the following sections, ion acceleration in targets driven at ultrahigh intensities may occur fast enough to alter the dynamics of the radiating electrons. For a more comprehensive review, the reader is referred to dedicated textbooks ([Gibbon, 2005](#); [Mulser and Bauer, 2010](#)).

4.1.1 Dynamics of a single electron in an intense electromagnetic field

Let us first consider an electron interacting in vacuum with an electromagnetic (EM) planar wave of vector potential $\mathbf{A}(x, t)$, propagating at c along the x -axis. The electron motion is described by the following equations:

$$\frac{dp_x}{dt} = -\frac{e^2}{2m_e\gamma} \frac{\partial|\mathbf{A}|^2}{\partial x}, \quad (4.1)$$

$$\mathbf{p}_\perp = e\mathbf{A}, \quad (4.2)$$

$$\frac{d\gamma}{dt} = \frac{e^2}{2m_e\gamma} \frac{\partial|\mathbf{A}|^2}{\partial t}, \quad (4.3)$$

where $\gamma = \sqrt{1 + |\mathbf{p}|^2}$ is the electron Lorentz factor. The right-hand side of Eq. (4.1) represents the ponderomotive force \mathbf{F}_p exerted by the laser wave. For a linearly polarized (LP) wave ($\mathbf{A} = A_y \hat{\mathbf{y}}$), \mathbf{F}_p contains a dc component (associated with the slowly-varying wave envelope) and a fast-oscillating (at multiples of the second wave harmonic, $2\omega_0$) component. For a circularly polarized (CP) wave, by contrast, the high-frequency component vanishes. Equation (4.2) expresses the conservation of the transverse canonical momentum $\mathbf{P}_\perp = \mathbf{p}_\perp - e\mathbf{A}$. Exploiting the fact that, for a propagating EM wave, $\mathbf{A}(x, t)$ only depends on the phase $\xi = t - x/c$, one readily obtains the well-known relations ([Landau and Lifshitz, 1975](#))

$$\gamma - p_x/m_ec = \gamma_0 - p_{x0}, \quad (4.4)$$

$$\mathbf{p}_\perp = \mathbf{a} + \mathbf{p}_{\perp 0}, \quad (4.5)$$

where γ_0 and \mathbf{p}_0 are, respectively, the electron's initial Lorentz factor and momentum, and $\mathbf{a} = e\mathbf{A}/m_ec$ denotes the normalized vector potential. A practical expression of the latter is

$$a \approx 0.85 \times 10^{-9} \lambda_0 \sqrt{I}, \quad (4.6)$$

as a function of the laser's intensity I (in Wcm^{-2}) and wavelength $\lambda_0 = 2\pi c/\omega_0$ (in μm). For an electron initially at rest ($\gamma_0 = 1$, $\mathbf{p} = \mathbf{0}$), one obtains

$$p_x/m_ec = \gamma - 1 = a^2/2, \quad (4.7)$$

$$\mathbf{p}_\perp/m_ec = \mathbf{a}, \quad (4.8)$$

It follows that for $a > 1$, or equivalently $I\lambda_0^2 \gtrsim 10^{18} \text{ Wcm}^{-2}\mu\text{m}^2$, the electron is accelerated to relativistic energies, preferentially in the forward direction ($p_\perp/p_x = 2/a \ll 1$). Because its velocity remains lower than the velocity of light, however, it is gradually slipping relative to the wavefront (at a velocity $c - p_x/m_e\gamma \approx 2c/a^2$), which tends to limit its acceleration. This dephasing is further increased in a plasma where the wave phase velocity exceeds the velocity of light, causing the longitudinal electron momentum to scale as $p_x \propto a$ instead of $p_x \propto a^2$ (Robinson *et al.*, 2015).

Equations (4.7) and (4.8) predict that the electron will return to rest when being overtaken by the laser pulse. This behavior results from the idealized assumption of a propagating planar wave. In realistic settings, however, the laser has a typical transverse width of a few μm , allowing the electron to escape transversely with a finite energy gain. An approximate generalized expression for the dc component of the 3D ponderomotive force is (Bauer *et al.*, 1995; Quesnel and Mora, 1998)

$$\mathbf{F}_p = -\frac{e^2}{2m_e\langle\gamma\rangle} \nabla \langle |\mathbf{A}^2| \rangle, \quad (4.9)$$

where $\langle\gamma\rangle = \sqrt{1 + \langle|\mathbf{p}|^2/(m_ec)^2 + e^2\langle|\mathbf{A}^2|\rangle/(m_ec)^2}$ and $\langle\dots\rangle$ denotes an average over the laser period. Yet, even in a multidimensional geometry, there remains the issue of injecting the electron near the laser peak in order to maximize its acceleration prior to dephasing or transverse expulsion from the strong-field region. A possibility (Yu *et al.*, 1998) is to make the EM wave reflect off an overcritical (opaque) plasma: some of the electrons accelerated at the dense plasma boundary (or in the dilute plasma possibly formed in front of it) can be injected into the reflected wave and further accelerated up to $p_x/m_ec = [1 + |\mathbf{a}^2| - (\gamma_0 - p_{x0})^2]/[2(\gamma_0 - p_{x0})] \approx \gamma_0 a^2$ (assuming $1 \ll \gamma_0 \ll a^2$ and $\mathbf{p}_{\perp 0} = 0$). Such vacuum laser acceleration has been achieved experimentally only recently (Thévenet *et al.*, 2015). Note, though, that for relatively long laser pulses, the electron motion may be altered by the (quasi) standing wave formed by the overlapping incident and reflected waves. In this configuration, the notion of a dc ponderomotive force breaks down, and efficient stochastic heating of the electrons can be triggered (Bauer *et al.*, 1995; Sheng *et al.*, 2002; Bourdier *et al.*, 2005).

4.1.2 Relativistic self-induced transparency

Let us now consider the propagation of an intense EM wave in a uniform, infinitely long, cold plasma. The electron fluid motion then obeys the general equation (Sudan, 1993)

$$\frac{\partial}{\partial t}(\mathbf{p} - e\mathbf{A}) = \nabla(e\phi - m_ec^2\gamma), \quad (4.10)$$

where ϕ is the electrostatic potential due to charge separation induced by the EM wave. In the right-hand side of the above equation, the $-\nabla(m_ec^2\gamma)$ term corresponds to the ponderomotive force acting on the electron fluid. Assuming immobile ions, the above relation combined with Maxwell's equations yields a dispersion relation for the EM wave of the form (Barr *et al.*, 2000)

$$\omega_0^2 = k_0^2 c^2 + \frac{\omega_p^2}{\langle\gamma\rangle}, \quad (4.11)$$

where $\omega_p = \sqrt{n_{e0}e^2/m_e\epsilon_0}$ is the electron plasma frequency, n_{e0} is the unperturbed electron density, and $\langle\gamma\rangle = \langle\sqrt{1 + |\mathbf{p}|^2/(m_ec)^2}\rangle$ is the laser-cycle averaged Lorentz factor of the oscillating electrons. In a 1D geometry, conservation of the transverse electron canonical

momentum implies $\gamma = \sqrt{1 + p_x^2/(m_e c)^2 + |\mathbf{a}|^2}$. For uniform CP plane waves, $|\mathbf{a}^2| = a_L^2$ is a constant, yielding the exact expression $\langle \gamma \rangle = \sqrt{1 + a_L^2}$. Since $\nabla \gamma = 0$, the electron motion is then purely transverse ($p_x = 0$) and no charge separation builds up ($\phi = 0$). For LP plane waves, γ presents both a dc component and an anharmonic oscillation, and hence these waves are generally coupled to longitudinal oscillations. Assuming $p_\perp = eA \gg p_x$, one has the approximate expression $\langle \gamma \rangle \approx \sqrt{1 + a_L^2/2}$. According to Eq. (4.11), however, both polarizations allow the plasma to become transparent to the EM wave (*i.e.* $k_0^2 > 0$) when its vector potential is high enough that $\omega_0^2 > \omega_p^2/\langle \gamma \rangle$ is fulfilled. Introducing the nonrelativistic critical density $n_c = \epsilon_0 m_e \omega_0^2/e^2$ and the relativistically corrected critical density $n_{cr} = \langle \gamma \rangle n_c$, this condition can be recast as $n_e < n_{cr}$. It follows that laser propagation is enabled in the density range $n_c < n_e < n_{cr}$, contrary to what is expected from linear theory. This mechanism is referred to as relativistic self-induced transparency (RSIT) (Kaw and Dawson, 1970; Lefebvre and Bonnaud, 1995).

The above criterion should be considered as a rough estimate of the effective threshold in realistic settings since it neglects plasma and laser inhomogeneities as well as kinetic effects. The former are inevitable when a laser wave impinges onto a sharp-interface plasma, and prove to be particularly important for circular polarization. This is caused by the associated weak electron heating (due to the slowly-varying γ), which favors the ponderomotively induced compression of the electron plasma boundary, thus opposing the relativistic decrease in the plasma frequency. This problem was analytically solved by Cattani *et al.* (2000) in the cold-fluid limit, yielding the following condition for the onset of RSIT:

$$a_L > a_{th} = \begin{cases} 2n_{e0}(n_{e0} - 1) & \text{if } n_{e0}/n_c < 3/2 \\ n_{e0}(1 + a_B^2) \left(\sqrt{1 + a_B^2} - 1 \right) - a_B^4 & \text{if } n_{e0}/n_c \geq 3/2 \end{cases} \quad (4.12)$$

with $a_B^2 = n_{e0}[\frac{9}{8}n_0 - 1 + \frac{3}{2}(\frac{9}{16}n_{e0}^2 - n_{e0} + 1)^{1/2}]$ being the electromagnetic field strength at the compressed electron plasma boundary. The above threshold was confirmed through 1D PIC simulations by Eremin *et al.* (2010), who interpreted the onset of transparency as the consequence of the periodic escape of some energized electrons into vacuum. As a consequence, the radiative pressure can exceed the electrostatic one, thus allowing the laser to gradually move into the plasma. Siminos *et al.* (2012) further showed that those electron ‘leaks’ are enhanced for shorter laser rise time, resulting in RSIT at field strengths much below the cold-fluid threshold (4.12). Yet it was subsequently found (Siminos *et al.*, 2017) that this kinetic effect is mitigated when allowing the ions to respond to the electrostatic field set up at the compressed plasma boundary. The ion motion, which sets in over a time-scale of the order of ω_0^{-1} and is enhanced at large charge-to-mass ratios, tends to prevent the heated electrons from escaping into vacuum; electron compression is thus maintained at the irradiated side, and so the target may remain opaque beyond the theoretical threshold (4.12). For LP pulses, the strong electron heating at the plasma boundary tends to weaken the surface electron compression so that the effective RSIT threshold approaches the prediction of (4.11) (Lefebvre and Bonnaud, 1995).

A complementary study of RSIT was performed by Weng *et al.* (2012a), who inferred from PIC simulations an approximate formula for n_{cr} , valid in smooth density profiles

with fixed ion background, and in a broad parameter range ($10 \leq a_L \leq 200$):

$$n_{cr}/n_c = (1 + 0.48a_L^2)^{1/2} \text{ for CP pulses, in the limit } n_{e0}/n_c \leq 0.5\sqrt{1 + a_L^2}, \quad (4.13)$$

$$n_{cr}/n_c = (1 + 0.79a_L^2)^{1/2} \text{ for LP pulses, in the limit } n_{e0}/n_c \leq 0.8\sqrt{1 + a_L^2}. \quad (4.14)$$

In addition, these authors obtained a simple expression for the propagation velocity of the laser front in a transparent plasma:

$$v_f/c = \exp(-n_p/n_{cr}) (1 - n_{e0}/n_{cr})^{1/2}, \quad (4.15)$$

where $n_p = 2n_{e0}$ and $n_p = 4n_{e0}$ for LP and CP waves, respectively. This formula, which accurately matches simulation results, is weakly sensitive to the laser rise time since the pulse rapidly develops a steep gradient at its front (of length scale $\ll \lambda_0$) due to electron compression (measured by n_p , enhanced for a CP wave). This and the associated laser reflection lead to an effective laser propagation velocity that can be much lower than the relativistic group velocity $v_g/c = (1 - n_{e0}/n_{cr})^{1/2}$.

4.1.3 Fast electron generation in undercritical plasmas

Plasma wave induced acceleration

As previously mentioned, phase slippage due to superluminal EM wave propagation in a plasma ($\omega_0/k_0 > c$) is not favorable to efficient electron acceleration via direct interaction in the laser field (Robinson *et al.*, 2015). Yet, under appropriate conditions, however, an undercritical plasma is capable of converting the strong transverse laser field into a large longitudinal electrostatic field, associated with an electron wave of phase velocity equating the laser's group velocity, $v_p = v_g < c$, and of typical wavelength $\lambda_p \approx 2\pi c/\omega_p \gg \lambda_0$ (Tajima and Dawson, 1979). The maximum energy attainable by an electron trapped in such a wave is (in 1D geometry) $\gamma_{\max} \approx 2\gamma_p^2(eE_p/m_e\omega_p c)^2$, where $\gamma_p = (1 - v_p^2/c^2)^{-1/2}$ and $eE_p/m_e\omega_p c > 1$ is the normalized amplitude of the nonlinear plasma wave (Esarey *et al.*, 2009). In a 1D cold plasma, E_p is bounded by the relativistic wave breaking field (Teychenné *et al.*, 1993), $E_{\text{wb}} \approx \sqrt{2\gamma_p} m_e\omega_p c/e$, so that $\gamma_{\max} \leq 4\gamma_p^3$. This maximum energy is gained when the electron has traveled a dephasing length $L_d = m_e c^2 \gamma_{\max} / eE_p \approx (\gamma_p^2/\pi)(eE_p/m_e\omega_p c)\lambda_p$.

Two main regimes of plasma wave generation arise in tenuous plasmas driven by intense lasers depending on whether the pulse length (L) is smaller or larger than the plasma wavelength. For $L \lesssim \lambda_p$, the plasma wave (or wake) is driven resonantly by ponderomotive force of the laser in its rising and descending ramps. This corresponds to the standard regime of laser wakefield acceleration (Tajima and Dawson, 1979), extensively studied and largely improved in past decades (Esarey *et al.*, 1996; Malka *et al.*, 2002; Faure *et al.*, 2004; Geddes *et al.*, 2004; Mangles *et al.*, 2004; Leemans *et al.*, 2006; Joshi, 2007; Esarey *et al.*, 2009; Pak *et al.*, 2010; Lundh *et al.*, 2011; Thaury *et al.*, 2015). Currently, the most actively explored configuration is when the focused laser intensity is high enough to expel all the electrons from the vicinity of the laser axis. In this 3D blow-out regime (Pukhov and Meyer-ter-Vehn, 2002; Lu *et al.*, 2007), a fraction of the plasma electrons can be self-trapped in the plasma wave and accelerated up to GeV-range energies (Leemans *et al.*, 2014).

In the opposite limit, $L \gg \lambda_p$, the plasma wave can be generated through a variant of the near-forward stimulated Raman instability, namely the self-modulation instability (Antonsen and Mora, 1992). By producing plasma density modulations that are alter-

natively focusing and defocusing, this instability causes the laser pulse to fragment into a train of $\sim \lambda_p$ long pulses. Since this mechanism usually operates in plasmas denser ($> 0.01n_c$) than for the standard wakefield acceleration, electron dephasing occurs faster, allowing the trapped electrons to phase mix in the separatrix and to develop broad electron energy spectra (Modena *et al.*, 1995).

The number of trapped electrons in the fast plasma wave rises with increasing plasma wave amplitude and decreasing plasma wave phase velocity (Esarey *et al.*, 2009). Besides, their interaction with the untrapped bulk electrons induces a wakefield out of phase with that excited by the laser pulse. For an intense laser pulse propagating in a ‘dense’ yet transparent plasma, this secondary wakefield can disrupt the laser-induced one, a phenomenon known as beam loading (Lu *et al.*, 2007). This scenario was further examined numerically in Debayle *et al.* (2017) in the parameter range $5 \leq a_L \leq 100$ and $0.1 \leq n_{e0} \leq 2n_c$. Efficient thermalization of the plasma electrons was observed due to a two-stream-type interaction between the accelerated electron beam and the plasma electrons backward-accelerated at the laser head. In particular, thermal energies exceeding the ponderomotive scaling ($\langle \gamma \rangle \sim \sqrt{1 + a_L^2/2}$) was evidenced at laser field strengths $a_L \sim 50\text{--}100$ and plasma densities $\sim 0.1\text{--}0.2n_c$.

Direct laser acceleration

The transverse ponderomotive force of an intense laser propagating in an undercritical plasma causes radial expulsion of the plasma electrons. When $L \gg \lambda_p$, a positively charged channel is formed inside the laser pulse, resulting in a radial electrostatic field (evolving on the ion time scale). Moreover, an azimuthal magnetic field is induced by the accelerated electrons current. Both these quasistatic fields vary linearly with the radius, causing a relativistic electron of energy γ to oscillate transversely at the so-called betatron frequency $\omega_\beta \approx \omega_p/\sqrt{2\gamma}$. Efficient acceleration can occur when the betatron oscillation frequency equates the laser frequency experienced by the electron, $\omega_\beta \approx \omega_0 - v_x k_0$. This condition means that each transverse oscillation corresponds to the electron’s slipping exactly by one period in the laser wave (of wave phase velocity $\omega_0/k_0 > c$). The electron can thus be continually accelerated until detuning occurs due to the relativistic decrease in ω_β at high energy. This mechanism is called Direct laser acceleration (DLA), although it involves a combination of laser and quasistatic fields. It was first evidenced in PIC simulations (Pukhov *et al.*, 1999), predicting quasi-thermal electron distributions with effective temperature $T_h \approx 1.5 \times 10^{-9} a_L$ MeV. It was observed experimentally in $\sim 0.1n_c$ plasmas (Gahn *et al.*, 1999) and, more recently, in microwire arrays (Jiang *et al.*, 2016) and near-critical plasmas (Bin *et al.*, 2018).

4.1.4 Fast electron generation in overcritical plasmas

The generation of fast electrons in overcritical targets driven at relativistic laser intensities was first studied numerically by Wilks *et al.* (1992), showing Boltzmann-like energy spectra obeying the ponderomotive scaling $T_h \sim m_e c^2 \sqrt{1 + a_L^2/2}$. This problem has since been the subject of many theoretical investigations which revealed a wealth of competing acceleration processes, depending on the laser and plasma parameters (Gibbon, 1994; Lefebvre and Bonnaud, 1997; Mulser *et al.*, 2008; Kemp *et al.*, 2009; Mishra *et al.*, 2009; Baeva *et al.*, 2011; Paradkar *et al.*, 2011; Kemp *et al.*, 2014; Sheng *et al.*, 2015; Sorokovikova *et al.*, 2016). In particular, for a laser pulse with a finite prepulse or a duration sufficient to allow for significant ion expansion, an extended undercritical plasma can form in front

of the dense plasma region, in which some of the aforementioned acceleration mechanisms can arise. In the following, however, we will focus on the direct interaction of an ultraintense, short-pulse laser wave with a steep-gradient opaque plasma, as it will be the scenario mainly addressed in the subsequent PIC simulations.

Vacuum heating

Compared to undercritical plasmas, a specific feature of overcritical plasmas (of density $n_e \gg n_{cr}$) is to cause significant reflection of the incoming laser wave. The superimposition of the incoming and reflected waves yields the following standing wave in front of the plasma ($x < 0$),

$$a = 2a_L \cos(\omega_0 t) \sin(\omega_0 x/c), \quad (4.16)$$

$$\frac{eE_y}{m_e\omega_0 c} = 2a_L \sin(\omega_0 t) \sin(\omega_0 x/c), \quad (4.17)$$

$$\frac{eB_z}{m_e\omega_0} = 2a_L \cos(\omega_0 t) \cos(\omega_0 x/c), \quad (4.18)$$

where perfect reflection is assumed for simplicity. All fields vanish in the plasma ($x > 0$), *i.e.*, we neglect the finite size of the skin layer ($\sim c/\omega_p \ll \lambda_0$), where the laser field decays exponentially, as well as the electron-depleted layer induced by the laser ponderomotive force (Sanz *et al.*, 2012). The above relations express the well-known result that the laser electric field is zero at the surface of a perfect conductor, whereas the laser magnetic field is locally maximized, up to twice its vacuum value $\propto 2a_L$. The dynamics of test plasma electrons injected with a finite momentum \mathbf{p}_0 into this standing wave (including the skin layer) was investigated by Bauer and Mulser (2007). In the 1D geometry under consideration, the electron motion is ruled by Eq. (4.1), which can be recast as

$$\frac{dp_x}{dt} = m_e c \omega_0 \frac{a_L^2}{\gamma} \begin{cases} \sin(2\omega_0 x/c) [1 - \cos(2\omega_0 t)] & \text{if } x < 0 \\ 0 & \text{if } x > 0 \end{cases} \quad (4.19)$$

where $\gamma = \sqrt{1 + (p_x/m_e c)^2 + a^2}$ and assuming $p_{\perp 0} = 0$. It was found that low-energy electrons (with initial longitudinal velocity $|v_x/c| \lesssim \sqrt{a_L n_c/n_{e0}}$) are ponderomotively reflected in the skin layer. Their non-adiabatic interaction with the evanescent oscillating laser field gives rise to the so-called skin-depth heating, related to the $j \times B$ heating mechanism of Kruer and Estabrook (1985). Most notably, the largest energy gain occurs in vacuum, provided the electron is fast enough to overcome the ponderomotive potential barrier at the plasma boundary, and approaches the E_y antinode at $x = -\lambda_0/4$. The electron can thus be efficiently accelerated, before being rotated back into the plasma by the magnetic field. Such vacuum heating lasts about half a laser period, resulting in the injection of high-energy electron jets into the plasma at twice the laser frequency. When the initial longitudinal electron momentum is such that $|p_x| \gtrsim m_e c a_L$, the electron can move beyond the first E_y maximum, and thus interacts stochastically with the standing wave over an extended duration. This mechanism, though, becomes significant only for relatively long interactions (Kemp *et al.*, 2014).

The vacuum heating induced at laser intensities $> 10^{20} \text{ W cm}^{-2}$ was further examined by May *et al.* (2011). They showed that in order to experience the E_y antinode in its maximum phase, the electron (moving at $\sim c$) must leave the plasma at a time when the surface B_z field is still significant (albeit decreasing in absolute value). If the electron has a low transverse momentum, it will be rotated over a Larmor radius $r_L \sim p/(a_L m_e \omega_0) \ll$

$\lambda_0/4$, and will gain little energy. If, by contrast, it has a large transverse momentum, then it can be deflected normal to the surface, and make a ‘large’ excursion in vacuum. After being accelerated by E_y (with a transverse momentum gain $\delta p_y \simeq 2m_e c a_L$), it is rotated back to the plasma by B_z , whose sign has reversed meanwhile, with a longitudinal momentum $p_x \lesssim \delta p_y \simeq 2m_e c a_L$.

To illustrate this mechanism, we have performed a 2D PIC simulation under conditions similar to those in [May et al. \(2011\)](#). We have considered a LP laser wave with a flat temporal profile of field strength $a_L = 10$, reached after a rise time of two laser cycles. The overcritical plasma has a sharp interface, an initial density of $100n_c$ and an initial temperature of 75 keV. Figs. 4.1(a-d) evidence this mechanism with a zoom on the electron phase space 4.2 fs after the pulse maximum has hit the target. The accelerated bunches of electrons can be seen in Fig. 4.1(a) and (c) in the $x - p_x$ phase space of electrons. They have a $2\omega_0$ spacing, similarly to what is observed in the ponderomotive heating. One note, however, that this heating takes place in the vacuum in front of the plasma (vacuum heating [Bauer and Mulser \(2007\)](#)) and not in the plasma, contrary to the ponderomotive heating. Another difference with the ponderomotive heating is that we assumed that the fields are perfectly reflected on the surface whereas for ponderomotive heating, it is evanescent in the plasma skin depth. The two instants selected to depict this mechanism show its dynamic. At time $t = 4.2$ fs, the electric field E_y on the plasma surface is high whereas the magnetic field B_z is rather weak. In this first phase, electrons are accelerated by E_y and weakly deflected by B_z , as observed in their $p_x - p_y$ phase space displayed in Fig. 4.1(b). At time $t = 4.2 + 0.5$ fs the B_z field is now higher contrary to the E_y field which amplitude decreased. Electrons are therefore strongly deflected by B_z and experience a weak acceleration by E_y such that they are directed from the vacuum back toward the plasma surface, as seen in the $p_x - p_y$ phase space displayed in Fig. 4.1(d).

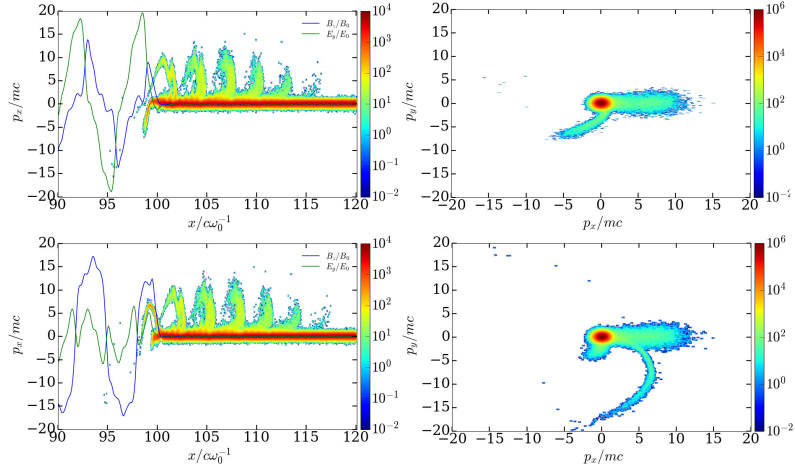


Figure 4.1: Top row: illustration at time $t = 4.2$ fs of the electron phase space (a) (x, p_x) and (b) (p_x, p_y). Bottom row: illustration at time $t = 4.2 + 0.5$ fs of the electron phase space (c) (x, p_x) and (d) (p_x, p_y). The y -averaged magnetic and electric fields forming the standing wave are superimposed (resp. blue and green curves). The laser amplitude is $a_L = 10$, the plasma has an initial thermal distribution of 75 keV and its density is $n_{e0}/n_c = 100$.

Electron preheating and injection

The above vacuum heating requires some level of electron preheating for efficient injection into the standing wave. It also requires non-exact conservation of the transverse canonical momentum; otherwise the electrons would keep their initial (low) thermal $\mathbf{p}_{\perp 0}$, and vacuum heating would be greatly weakened at high field strengths.

Among the possible preheating mechanisms are the aforementioned skin layer (or $\mathbf{J} \times \mathbf{B}$) heating ([Kruer and Estabrook, 1985](#); [Bauer and Mulser, 2007](#)) or, more importantly, the laser-driven $2\omega_0$ oscillation of the plasma electron boundary. This piston-type motion results from the interplay of the oscillating laser ponderomotive force and the charge-separation longitudinal electric field ([Gonoskov et al., 2011](#); [Sanz et al., 2012](#)). At laser intensities high enough that the oscillation amplitude of the plasma boundary is of the order of the plasma skin depth, the electrostatic field is capable of injecting electron bunches into the standing wave with longitudinal momenta well in excess of the thermal level. Further plasma heating can proceed through wave breaking in the skin layer and multi-stream instabilities between the vacuum-accelerated jets and the plasma return current ([Debayle et al., 2013](#); [Kemp and Divol, 2016](#)).

The interaction geometry ceases to be transversely invariant as soon as a focused laser wave is considered. The transverse intensity gradient induces a curvature of the plasma electron boundary; as a result, the laser electric field develops a component normal to the boundary, which can directly pull the surface electrons into the vacuum ([Brunel, 1987](#)). More importantly, a variety of processes, ranging from the electron Weibel filamentation instability ([Adam et al., 2006](#)) to the Rayleigh-Taylor instability ([Eliasson, 2015](#)) and the oscillating two-stream instability ([Wan et al., 2016](#)), can rapidly (over a few laser periods) trigger short-scale ($\gtrsim 1 \mu\text{m}$) transverse modulations of the plasma surface. Not only does this ‘rippling’ of the plasma surface greatly affect, through strong quasistatic electric and magnetic fields, the trajectories of the accelerated electrons—thus accounting for the effective large divergence of the hot electron distribution ([Adam et al., 2006](#); [Debayle et al., 2010](#))—, it also results in a strong isotropic heating (up to 10–100s of keV) of the bulk plasma ([May et al., 2011](#); [Kemp et al., 2014](#)), thus providing the desired hot reservoir for further acceleration in vacuum. Note that the target surface can also get rapidly modulated under the action of a CP pulse, hence enhancing the subsequent electron heating, in a manner essentially independent of the laser polarization ([Kemp et al., 2014](#)).

4.1.5 Ion acceleration in overcritical plasmas

The laser acceleration of high-energy electrons naturally gives rise to charge separation fields at the target boundaries. For not-so-intense ($\lesssim 10^{20} \text{ Wcm}^{-2}$), relatively long duration ($\sim 1 \text{ ps}$) laser pulses, the strongest electrostatic fields are generally produced at the target backside following the fast electrons’ breakout into vacuum. By contrast, for ultraintense ($> 10^{20} \text{ Wcm}^{-2}$), short pulse ($\lesssim 100 \text{ fs}$) lasers, the electrostatic field ponderomotively induced at the irradiated side is the dominant one. Both fields lead to acceleration of the local ions, the efficiency of which depends on the fields’ distribution and duration as well as on the target geometry. The properties of the main ion acceleration mechanisms, based on either the fast-electron-induced sheath field or the laser ponderomotive force, are presented in the following section. More thorough reviews can be found in [Daido et al. \(2012\)](#) and [Macchi et al. \(2013\)](#).

Target Normal Sheath Acceleration

The high-energy electrons generated by intense laser pulses in dense targets can propagate over large distances ($> 100 \mu\text{m}$) compared to the usual μm (or less) scale target thickness. When breaking out through the target boundaries, they induce a charge separation field, normal to the surface and of typical strength $E_x \approx T_h/e\lambda_{Dh} \approx \sqrt{T_h n_h/\epsilon_0}$ (where $T_h \sim m_e c^2 a_L$ is the typical temperature of the fast electrons, $\lambda_{Dh} = \sqrt{\epsilon_0 T_h / e^2 n_h}$ is their Debye length and n_h their density). This sheath field reflects the fast electrons over a distance $\sim \lambda_{Dh}$, causing them to recirculate across the target. Importantly, it is capable of ionizing the surface ions (if located on the non-illuminated backside) and accelerating them to MeV-range energies, a process known as target normal sheath acceleration (TNSA) (Wilks *et al.*, 2001). Due to their high Z/A ratio, the protons (initially contained in the target bulk or in the form of contaminants on the target surfaces) react fastest to the sheath field and acquire the highest velocities.

TNSA can be modeled similarly to the expansion of a hot plasma. This classical problem is usually formulated using standard fluid equations for the ions (of mass m_i and charge Z), and assuming that fast electrons obey a Boltzmann distribution (Gurevich *et al.*, 1966):

$$n_h = n_{h0} \exp(e\Phi/T_h), \quad (4.20)$$

$$\epsilon_0 \frac{\partial^2 \Phi}{\partial x^2} = e(n_e - Zn_i), \quad (4.21)$$

$$\left(\frac{\partial}{\partial t} + v_i \frac{\partial}{\partial x} \right) n_i = -n_i \frac{\partial v_i}{\partial x}, \quad (4.22)$$

$$\left(\frac{\partial}{\partial t} + v_i \frac{\partial}{\partial x} \right) v_i = -\frac{Ze}{m_i} \frac{\partial \Phi}{\partial x}. \quad (4.23)$$

For simplicity, we have considered that the system comprises a single (hot) electron species, whereas in most situations only a limited fraction of the plasma electrons are laser-accelerated, so that the contribution of the thermal bulk electrons should also be taken into account (Diaw and Mora, 2011; Diaw and Mora, 2012; Lécz *et al.*, 2013). If one assumes that quasineutrality ($n_h \approx Zn_i$) holds everywhere, the following self-similar solution can be derived:

$$n_h \approx Zn_i = n_{h0} \exp(-x/c_s t - 1), \quad (4.24)$$

$$v_i = c_s + x/t, \quad (4.25)$$

$$E_{ss} = -\partial \Phi / \partial x = T_h / ec_s t, \quad (4.26)$$

with $c_s = \sqrt{ZT_h/m_i}$ denoting the ion sound velocity. This solution is represented in Fig. 4.2.

Yet, the quasineutrality approximation at the heart of the self-similar solution breaks down around the ion front where the density gradient scale-length ($\sim c_s t$) becomes shorter than the Debye length. This problem was tackled by Mora (2003) who numerically solved the equations of motion for the ions, coupled with the nonlinear Poisson equation (4.21) assuming isothermal electrons. He found that the electric field presents a local maximum at the ion front, which is well described by the best-fitting formula

$$E_x = \frac{2(T_h n_h / \epsilon_0)^{1/2}}{[2e^1 + (\omega_{pi} t)^2]^{1/2}}, \quad (4.27)$$

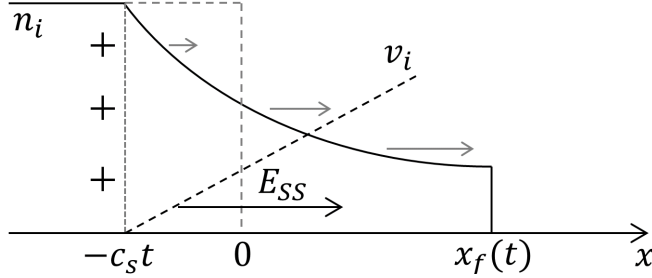


Figure 4.2: Ion density and velocity profiles as predicted by the self-similar solution of Eqs. (4.20)-(4.23). The plasma initially extends in the $x < 0$ half-space. The locations of the rarefaction wave ($x = -c_s t$) and of the ion front ($x = x_f$) are indicated. Note that the latter, where quasineutrality is not fulfilled, is not properly described by the self-similar solution (Mora, 2003). Due to quasineutrality, the self-similar electric field (E_{ss}) is uniform in the region $-c_s t \leq x \leq x_f(t)$.

resulting into the following ion front velocity

$$v_{f,is} = 2c_s \ln \left[\omega_{pi} t / \sqrt{2e^1} + \sqrt{1 + (\omega_{pi} t)^2 / 2e^1} \right]. \quad (4.28)$$

The nonphysical logarithmic divergence of $v_{f,is}$ stems from a number of assumptions, including that (i) of a 1D geometry, valid insofar as the ion front displacement is shorter than the transverse width of the electric field distribution (Brantov *et al.*, 2015), and (ii) that of a constant electron temperature (despite the continuous energy transfer from the electrons to the ions). The latter hypothesis involves either an idealized semi-infinite plasma or, in a more realistic scenario, that, after laser extinction, the rarefaction wave launched inward at the sound velocity has not swept through the entire target thickness (l). This implies an acceleration time $t_{acc} \lesssim l/2c_s$; later on, the electrons start cooling down adiabatically, with $T_h \sim t^{-2}$ (resp. t^{-1}) in the relativistic (resp. ultrarelativistic) case. The problem of 1D TNSA in a finite size target has been addressed in Mora (2005) (and in Grismayer *et al.* (2008) using a more elaborate kinetic description for the electrons). The main difference with the isothermal expansion regime is that, due to the bounded electron energy, the ion front velocity saturates at the approximate value

$$v_{f,ad} = 2c_s \ln (0.32l/\lambda_{Dh} + 4.2), \quad (4.29)$$

where the sound velocity c_s and Debye length λ_{Dh} are now determined by the initial electron temperature T_{h0} and density n_{h0} . This formula also applies in the case of two (hot and cold) electron plasma species. Acceleration models interpolating between the isothermal and adiabatic regimes and including a simple description of multidimensional effects have been recently proposed in Brantov *et al.* (2015) and Ferri *et al.* (2018).

It should be remarked that both Eqs. (4.28) and (4.29) predict a T_h scaling of the maximum proton energy. Assuming that the hot electron distribution obeys the ponderomotive law, one expects a $\sim I_0^{1/2}$ dependence of the maximum proton energy, as observed experimentally (Fuchs *et al.*, 2006; Robson *et al.*, 2007). Note also that TNSA generates broad ion energy spectra, typically exponentially decaying (Macchi *et al.*, 2013). Finally, as shown in Mishra *et al.* (2018), TNSA can be maximized in targets that turn transparent (as a result of TNSA in the rising phase of the laser) near the laser peak: the electrons are then volumetrically re-heated, thus enhancing the sheath field and the final ion energies.

Radiative pressure acceleration

At the ultrahigh laser intensities considered in this work, ion acceleration can also, and often preferentially, take place in the charge separation layer ponderomotively induced at the target front side. Although this so-called radiation pressure acceleration (RPA) works best for CP pulses at given laser intensity (Macchi *et al.*, 2005; Robinson *et al.*, 2008; Klimo *et al.*, 2008), as the associated weak electron pressure does not oppose the radiation pressure (this holds before the target surface becomes rippled and differences in laser polarization level off), it also operates with LP pulses, in which case it can dominate TNSA at ultrahigh intensities (Esirkepov *et al.*, 2006) and/or nanometric targets (Qiao *et al.*, 2012; Kim *et al.*, 2013).

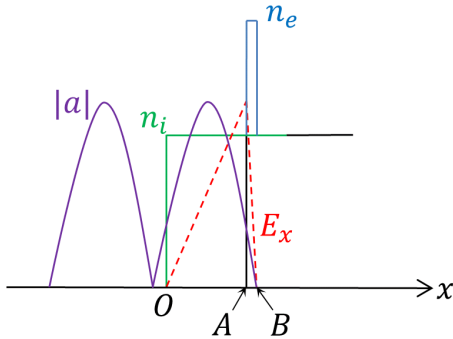


Figure 4.3: Schematic of RPA before ion motion. The ion density (green), electron density (blue), longitudinal electric field (red) and absolute value of the laser’s potential vector are plotted at the initial stage. The origin O corresponds to the initial ion boundary, while labels A and B indicate the boundaries of compressed electron layer

Figure 4.3 shows a sketch of the plasma density and field profiles at the target front side leading to RPA at the target front side (Macchi *et al.*, 2005). At normal incidence the laser’s ponderomotive force pushes the surface electrons to form a thin compressed layer of thickness close to the skin layer $l_s = c/\omega_p$ (segment AB), leaving behind an ion layer (segment OA) of thickness l_i , embedded in a linearly increasing electrostatic field $E_x = E_{x0}x/l_i$. The thickness l_i can be estimated assuming quasi-equilibrium between the radiation pressure, $P_{\text{rad}} = 2I_0/c$ (provided the laser reflection $R \sim 1$), and the electrostatic pressure $P_{\text{elec}} = \epsilon_0 E_{x0}^2/2 = (en_{e0}l_i)^2/2\epsilon_0$, and hence $l_i \simeq 2(\epsilon_0 I_0/c)^{1/2}/en_0 \propto a_L/n_{e0}$. Here complete electron depletion is considered in the ion layer, which is well verified for CP pulses, but less so for LP pulses due to hot electrons escaping into vacuum. Since, to first approximation, the electrostatic field is constant over each ion trajectory, the density of this front layer progressively drop, forming a dilute ‘tail’ of trailing ions. For LP pulses, hot electrons flowing from the dense plasma into this region will further trigger TNSA towards vacuum (Macchi *et al.*, 2005).

By contrast, the ions located in the compressed electron layer (AB) see a linearly decreasing electrostatic field, which accelerates them so that they all reach point B at the same time $t = (2m_il_s/ZE_{x0})^{1/2}$, with a mean velocity (Macchi *et al.*, 2005)

$$v_p = (ZeE_{x0}l_s/2m_i)^{1/2} \approx (ZI_0/m_i n_{e0}c)^{1/2}. \quad (4.30)$$

There follows an ion bunch injected at twice the above velocity into the inner plasma region, through which, thanks to charge neutralization by the ambient electrons, it subsequently propagates ballistically. This process repeats itself as long as the laser irradiation

is maintained, resulting, on average, in a pistonlike push of the plasma boundary at the constant velocity $v_p \propto a_L(Z/m_i n_{e0})^{1/2}$.

The above microscopic picture (Macchi *et al.*, 2005) can be given a simple macroscopic description by expressing the balance between the radiation pressure and the particle momentum flux in the rest frame of the laser piston (Wilks *et al.*, 1992). In a general relativistic framework (Robinson *et al.*, 2009), this condition reads

$$2I'_0/c = \frac{1 - \beta_p}{1 + \beta_p} I_0 = 2c\beta_p (n'_i p'_i + n'_e p'_e) = 2\rho c^2 \beta_p^2 \gamma_p^2, \quad (4.31)$$

where primed quantities are measured in the piston frame of normalized velocity $\beta_p = v_p/c$ and Lorentz factor γ_p . The second expression above represents the relativistically Doppler-shifted radiation pressure. The expression of the particle momentum flux on the right-hand side assumes charge neutrality in the unperturbed upstream plasma ($n'_e = Zn'_i = Z\gamma_p n_i$), and we have introduced the mass density $\rho = m_i n_i$. The piston velocity can be readily solved as (Robinson *et al.*, 2009)

$$\beta_p = \frac{B}{1 + B}, \quad (4.32)$$

with $B = \sqrt{I_0/\rho c^3} = a_L \sqrt{\alpha (n_c/n_i) (m_e/m_i)}$ ($\alpha = 1/2$ or 1 depending on the linear or circular polarisation of the laser). In the nonrelativistic regime, one recovers the above relation (4.30). The ions specularly reflected off the piston reach the maximum velocity

$$\beta_i = \frac{2\beta_p}{1 + \beta_p^2}, \quad (4.33)$$

corresponding to a kinetic energy

$$\epsilon_i = m_i c^2 \left(\frac{1 + \beta_p^2}{1 - \beta_p^2} - 1 \right) = m_i c^2 \frac{2B^2}{1 + 2B}. \quad (4.34)$$

The nonrelativistic RPA mechanism is therefore characterized by a $\propto I_0/n_i$ scaling of the ion energy, which makes it possibly more efficient than TNSA ($\propto \sqrt{I_0}$) provided the target density is sufficiently low (yet still overcritical) and the electron thermal pressure is superseded by the radiation pressure. For CP pulses, RPA leads to peaked ion energy spectra, which are strongly broadened when using LP pulses due to TNSA effects and laser-induced oscillations of the piston (Schlegel *et al.*, 2009). At ultrahigh laser intensities, electron cooling around the target front due to synchrotron-type radiation tends to decrease the dispersion of the ion spectrum but also its maximum energy (Tamburini *et al.*, 2010). Finally, it should be noted that, in a multidimensional geometry and for a finite laser spot, the laser-driven piston acquires a curvature due to the transverse intensity gradient, leading to hole boring (HB) of the surface ions. As a result, the notions of HB and RPA are often employed interchangeably.

Light sail acceleration

If the target subject to RPA is thin enough that the laser piston reaches its backside before the end of the laser pulse (*i.e.*, $v_p \tau_0 > l$), then the target as a whole gets accelerated in the so-called light sail acceleration (LSA) regime (Esirkepov *et al.*, 2004; Robinson *et al.*, 2008; Macchi *et al.*, 2009). In the case of LP pulses, this process implies that the piston overtakes the backside ions expanding through TNSA, *i.e.*, $v_p > v_{f,is}(l/v_p)$, where $v_{f,is}$ is given by

Eq. (4.28) (Qiao *et al.*, 2012). For typical values $I_0 \approx 10^{22} \text{ Wcm}^{-2}$ and $n_{e0} = 100\text{--}1000n_c$, this necessitates target foils of a few 10 nm thick.

In the LSA regime, the equation of motion of the coherently accelerated target ions obeys the following equation Marx (1966)

$$\frac{d}{dt}(\gamma_i \beta_i) = \frac{2}{\sigma c^2} I(t - x_i/c) \frac{1 - \beta_i}{1 + \beta_i}, \quad (4.35)$$

$$\frac{d}{dt}x_i = \beta_i c, \quad (4.36)$$

where $\sigma = m_i n_i l$ is the areal mass density. The right-hand side term in Eq. (4.35) is the force deriving from the EM radiative pressure. An analytical solution can be derived for a constant intensity profile $I(x, t) = I_0$ (Simmons and McInnes, 1993), which presents the following limiting expressions:

$$\gamma_i(t) \approx \begin{cases} 1 + 4(\Omega t)^2 & \text{if } \Omega t \ll 1 \\ (3\Omega t/4)^{1/3} & \text{if } \Omega t \gg 1 \end{cases} \quad (4.37)$$

where $\Omega = 2I_0/\sigma c^2$. Therefore, contrary to RPA, the ion energy increases with time in the LSA regime. This feature renders this mechanism very appealing provided the integrity of the target is maintained until the laser peak, which implies stringent conditions on the laser temporal contrast. In addition, the electron density should be sufficiently high to ensure opacity (Vshivkov *et al.*, 1998):

$$\frac{n_{e0}}{n_c} \frac{l}{\lambda_0} \gtrsim a_L/\pi, \quad (4.38)$$

This criterion is easily understood by realizing that, in order to reflect the incoming light, the maximum transverse electric field that can be induced by the relativistic target electrons ($\propto n_{e0}l$) should exceed the laser field strength ($\propto a_L$). A number of simulation studies (Esirkepov *et al.*, 2006; Macchi *et al.*, 2009; Brantov *et al.*, 2015) suggest that the condition $(n_{e0}l)/(n_c \lambda_0) \approx a_L/\pi$ is optimal in terms of ion acceleration, although, in the case of LP pulses, it may then proceed through a mix of LSA and TNSA, rather than through pure LSA. Furthermore, LSA is susceptible to fast-growing, Rayleigh-Taylor-like corrugation instabilities that may destroy the foil and precipitate the onset of relativistic transparency (Yan *et al.*, 2008; Eliasson, 2015). Using a sharp-rise laser pulse can help stabilize the foil acceleration (Pegoraro and Bulanov, 2007). Recent efforts in modeling and improving LSA have been reviewed in Macchi (2014) and Macchi *et al.* (2017).

4.2 Laser-induced synchrotron radiation in uniform plasmas of varying density

In this section, we report on a series of 2D CALDER PIC simulations of synchrotron radiation from uniform plasmas driven at ultrahigh laser intensity. Our main purpose is to identify distinct, density-dependent regimes of synchrotron emission, in light of which the integrated synchrotron/Bremsstrahlung simulations of Sec. 4.3 will be analyzed. Our results will also be confronted to previously published studies (Ridgers *et al.*, 2012; Brady *et al.*, 2012, 2014; Chang *et al.*, 2017).

The laser pulse is modeled as an EM plane wave of peak intensity $I_0 = 10^{22} \text{ Wcm}^{-2}$ ($a_L = 85$) and wavelength $\lambda_0 = 1 \mu\text{m}$, propagating in the $+x$ direction and linearly

Section	Plasma density	Plasma length	Temporal profile of the plane wave
Sec. 4.2.1 (3 simulations)	$n_e/n_c = 16$	$l = \infty \mu\text{m}$	2-cycles linear rise + infinite-plateau
		$l = \infty \mu\text{m}$	Gaussian with a 30 fs FWHM
		$l = 1 \mu\text{m}$	Gaussian with a 30 fs FWHM
Sec. 4.2.2 (3 simulations)	$n_e/n_c = 40$	$l = \infty \mu\text{m}$	2-cycles linear rise + infinite-plateau
		$l = \infty \mu\text{m}$	Gaussian with a 30 fs FWHM
		$l = 1 \mu\text{m}$	Gaussian with a 30 fs FWHM
Sec. 4.2.2 (3 simulations)	$n_e/n_c = 100$	$l = \infty \mu\text{m}$	2-cycles linear rise + infinite-plateau
		$l = \infty \mu\text{m}$	Gaussian with a 30 fs FWHM
		$l = 1 \mu\text{m}$	Gaussian with a 30 fs FWHM

Table 4.1: List of parameters changed in the simulations performed in this section. All other parameters are detailed in the text

polarized along the y axis. Unless otherwise stated, it has a constant temporal profile, preceded by a two-cycle-long (6.6 fs) linear ramp. The irradiated plasma is made of fully ionized carbon ions and electrons of uniform density varying in the range $17 \leq n_{e0} \leq 100n_c$. The steep-gradient front plasma boundary is located at $x = 16 \mu\text{m}$. The time at which the laser peak hits the target boundary is taken to be the time origin $t = 0$. The simulations are run over a time scale ($t \simeq 100 - 200$ fs) too short for the laser to reach the rear plasma boundary, so that the target can be considered as semi-infinite. The 2D domain comprises 4800×400 cells, with mesh size $\Delta x = \Delta y = \lambda_0/60$ and time step $\Delta t = 0.6\Delta x$. Each cell initially contains 10 particle per plasma species. Modules describing (classical and quantum) synchrotron radiation and Coulomb collisions are activated. Boundary conditions for both fields and particles are taken to be absorbing in the x direction and periodic in the y direction.

Since we run 2D simulations, all quantities describing the spectral properties of the photons are obtained per unit length of the third dimension z (m) but are normalized per μm of transverse direction. This choice is convenient since the usual focal spots of such lasers have a few microns length. For example in Fig. 4.4(a), the ordinate axis is in J/fs but corresponds to J/fs/ μm of transverse direction. Similarly in Fig. 4.4(b), the ordinate axis is in J/MeV/rad but corresponds to J/MeV/rad/ μm of transverse direction. In Fig. 4.6(b), the ordinate axis is in J/rad but corresponds to J/rad/ μm . The same rule applies for all figures representing spectral properties of the photons in the following sections of this chapter.

4.2.1 Synchrotron emission in relativistically undercritical plasmas

Let us first address the case of a relativistically undercritical plasma of density $n_{e0} = 17n_c$ (*i.e.*, $n_{e0}/a_L n_c = 0.2$). The temporal evolution of the total radiated power is plotted in Fig. 4.4(a). The overall trend is that of an approximately linear increase with time, as expected from the increasing plasma area covered by the laser wave (see below). Also visible are fluctuations of typical time scale $\sim 5 - 10$ fs. The associated angle-energy spectrum of the radiated energy is displayed in Fig. 4.4(b). The photon energy distribution is characterized by a quasiplateau extending up to a few MeV energies and cutoff energies of ~ 100 MeV. The photon angular distribution is broad and mainly concentrated in the backward direction ($\theta_\gamma > \pi/2$), but a weaker local maximum (about twice lower than the backward maximum) is also visible in the forward direction ($\theta_\gamma \approx 0.3$).

In order to shed light on the emission mechanism, we superimpose in Figs. 4.5(a,b)

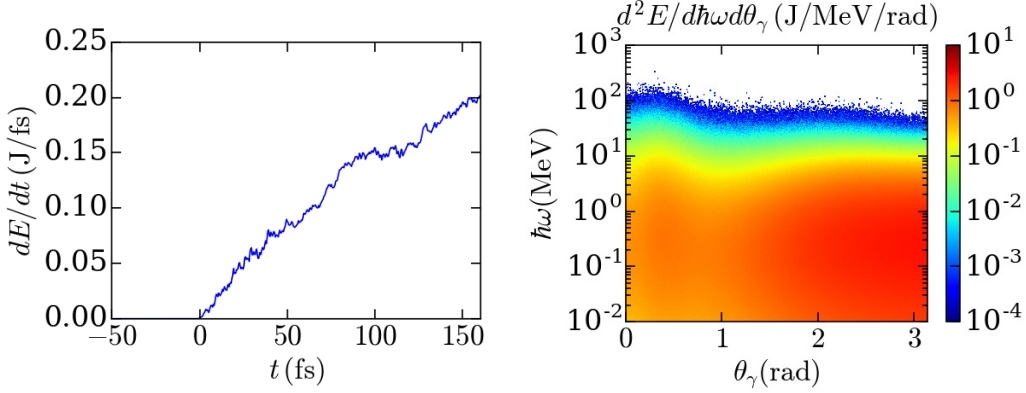


Figure 4.4: Simulation with a semi-infinite, $n_{e0} = 17n_c$ density plasma and a uniform laser wave. (a) Time history of the total radiated power; (b) Angle-energy spectrum of the radiated energy.

the $x - p_x$ (a) and $x - p_y$ (b) electron phase spaces (integrated along y) and a lineout of the radiated power density (P_γ) at $t = 36$ fs. Moreover, we plot in Fig. 4.5(c) lineouts of the transverse electric field (E_y), of the longitudinal electrostatic field ($\langle E_x \rangle$) and of the electron (n_e) charge density. The emission is seen to take place over the whole irradiated plasma region, in which the electrons have been accelerated to ultrarelativistic (both longitudinal and transverse) momenta. The $x - p_x$ phase space exhibits the usual forward-moving, high-energy (up to $p_x/m_ec \approx 500$) electron jets spatially modulated at $\lambda_0/2$, but also a denser, electron return current accelerated at $|p_x|/m_ec \approx 100 - 200$. Those counterstreaming electrons are first pushed forward in the rising edge of the laser before getting pulled back by the charge separation field, as observed in [Debayle et al. \(2017\)](#). The laser front moves at a velocity $v_f/c \sim 0.47$; This value is consistent, yet smaller than formula (4.15), probably as a result of mobile ions that favor electron compression (up to $n_e \sim 40n_c$) at the laser head. Transverse electron momenta as high as $|p_y/m_ec| \approx 300$ are observed in Fig. 4.5(b), which may seem surprising since one expects $|p_y| \leq a_L$ for an EM planar wave. In the present case, however, the EM profile is subject to transverse modulations (not shown), leading to local field maxima $|B_z| \approx 120m_e\omega_0/e$, so that the transverse canonical momentum is no longer conserved.

Interestingly, the return-current p_x profile presents anharmonic oscillations at $\lambda_{\text{mod}} \approx 1.5\lambda_0$, resulting in strong density modulations ($n_e \gtrsim 30n_c$) inside the laser pulse. The related maxima in $|p_x|$, when coinciding with E_y extrema, yield peaks in the radiated power density, which correspond to the ~ 5 fs time scale fluctuations seen in Fig. 4.4(a) around $t = 36$ fs. This is expected as those high-energy counterstreaming electrons are those optimizing the quantum parameter $\chi_e = \gamma(1 - v_x/c)a\hbar\omega_0/m_ec^2 \approx 2\gamma a\hbar\omega_0/m_ec^2$ (for purely counterstreaming electrons), resulting in a backward-directed radiated power $P_{\text{rad}} = (2/3)\alpha(m_ec^2)^2\chi_e^2/\hbar \approx (8/3)(r_e\omega_0/c)\omega_0 m_ec^2(\gamma a)^2$, with r_e being the classical electron radius, and assuming negligible quantum corrections [Kirk et al. \(2009\)](#). The large p_y momenta of the counterstreaming electrons account for the extended emission lobe seen in Fig. 4.4(b). This emission scenario, hinging on the electrons injected back into the EM wave at the laser front, was first investigated by [Brady et al. \(2012, 2014\)](#), where it was termed re-injected electron synchrotron emission (RESE), and found to yield the largest radiation yield at $I_0 \gtrsim 10^{22} \text{ Wcm}^{-2}$. The overall description provided in those works is consistent with our results, except regarding the quantitative estimate of the radiation burst time scale. This time was interpreted as that needed for the compressed

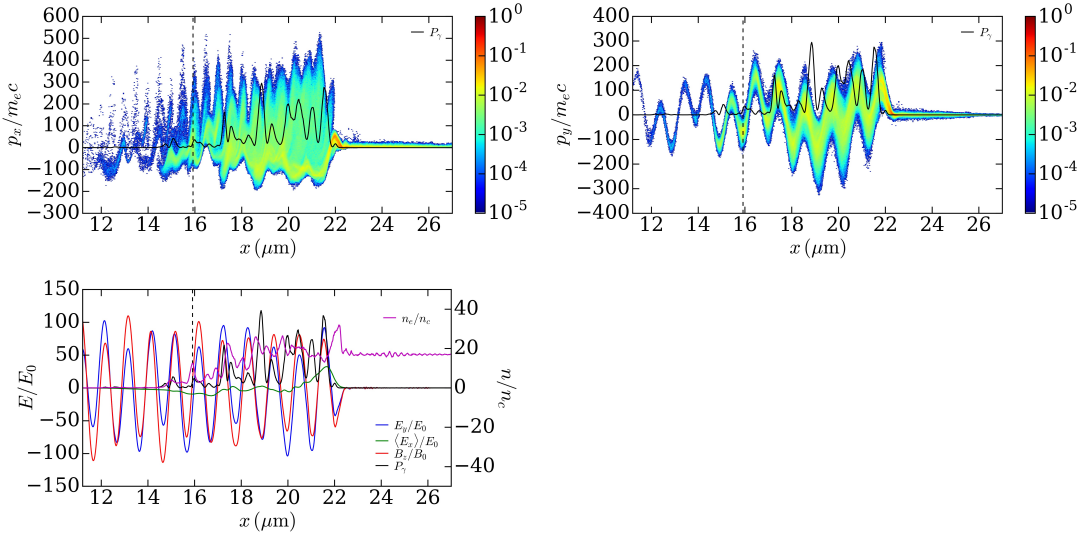


Figure 4.5: Simulation with a semi-infinite, $n_{e0} = 17n_c$ density plasma and a uniform laser wave. (a) $x - p_x$ and (b) $x - p_y$ electron phase spaces integrated in the y direction. A lineout at $y = 0$ of the radiation power density P_γ is overlaid in black. (c) Lineouts at $y = 0$ of the E_y electric field (blue), of the laser cycle-averaged E_x electric field (green), of the electron density n_e (purple) and of the radiated power density P_γ (black). The vertical dashed line locates the front plasma boundary. (d) $p_x - p_y$ electron distribution integrated over the whole box. All quantities are recorded at $t = 36$ fs after the on-target laser peak. P_γ is plotted in arbitrary units in the three figures.

electrons at the laser front to build up an electrostatic field ($E_x \approx en_{e0}ct/\epsilon_0$) exceeding the $\mathbf{v} \times \mathbf{B} \propto a_L$ force, thus reflecting them toward the laser source. This reasoning yields a ‘breakdown time’, $\tau_{bd} = aL(n_c/n_{e0})\omega_0^{-1}$. Under the present conditions we have $c\tau_{bd} \approx 0.8 \mu\text{m}$, significantly smaller than the observed spacing of the P_γ bursts in Fig. 4.4(a). Rather, we propose the following simple explanation for the modulations affecting the $p_x < 0$ hot electrons. Let us consider their motion in the rest frame of the laser front, in which the Doppler-shifted laser frequency is $\omega'_0 = \omega_0\sqrt{(1 - v_f/c)/(1 + v_f/c)}$ (assuming $k_0 \approx \omega_0/c$). The electrons impinging on the laser front from the unperturbed plasma experience the $2\omega'_0$ -oscillating component of the ponderomotive force while being successively slowed down and injected downstream at $v_x \approx -c$. As a result, a current modulation is induced with wavenumber $k'_{\text{mod}} = -2\omega'_0/c$. In the laboratory frame, this wavenumber becomes $k_{\text{mod}} = -2\gamma_f(1 - v_f/c)\omega'_0/c = -2[(1 - v_f/c)/(1 + v_f/c)]\omega_0/c$, corresponding to a wavelength

$$\lambda_{\text{mod}} = [(1 + v_f/c)/(1 - v_f/c)]\lambda_0/2. \quad (4.39)$$

In the present case, where $v_f/c = 0.47$, one expects $\lambda_{\text{mod}} \approx 1.4 \mu\text{m}$, in good agreement with the simulation.

The observation that the radiation is mainly backward directed and emitted as bursts throughout the irradiated region allows for a rough estimate of the total radiation yield:

$$\eta_\gamma = \xi \frac{P_\gamma n_{h<} v_f t}{I_0} = \frac{16}{3} \frac{e^2}{4\pi m_e c^2} \xi \left(\frac{\omega_0}{c}\right)^2 \frac{n_{h<}}{n_c} \langle\gamma\rangle^2 v_f t, \quad (4.40)$$

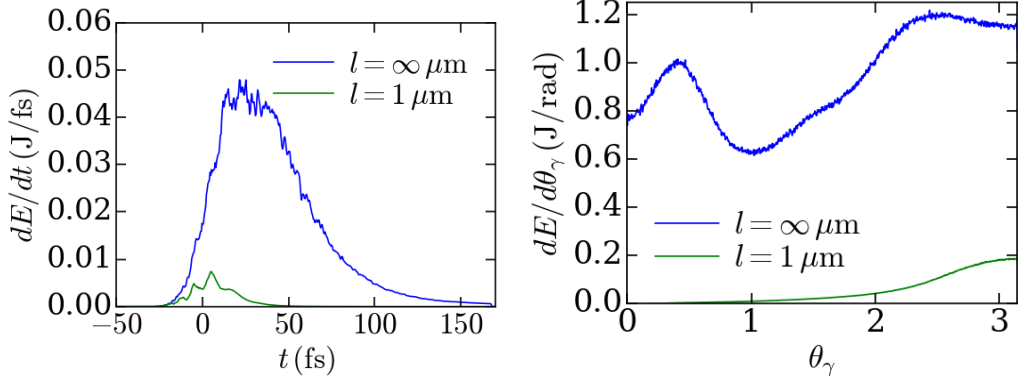


Figure 4.6: Simulations with a $n_{e0} = 17n_c$ density plasma and a $\tau_0 = 30$ fs Gaussian laser pulse. (a) Time history of the radiated power; (b) angular distribution of the radiated energy. The blue (resp. green) curves correspond to a semi-infinite (resp. $1 \mu\text{m}$ thick) plasma.

where we have introduced $n_{h<}$ the density of the $p_x < 0$ hot electrons, and ξ the ratio of the burst length to its spacing λ . Further assuming a mean electron energy $\langle \gamma \rangle \approx a_L$ gives

$$\eta_\gamma \approx \kappa \xi \frac{\omega_0}{c} \frac{n_{h<}}{n_c} a_L^2 v_f t, \quad (4.41)$$

with $\kappa = (16/3)(e^2/m_e c^2)(\omega_0/c) = 9.44 \times 10^{-8}$. Taking $v_f \approx 0.5c$, $n_{h<} = n_{e0}/2$ and $\xi = 0.1$ leads to $\eta_\gamma \approx 0.08$ at $t = 150$ fs. This value is consistent, yet about half lower than the PIC-predicted value $\eta_\gamma \approx 0.17$. This difference is attributed to uncertainties in the estimation of $\langle \gamma \rangle^2$ and to nonnegligible radiation from the high-energy p_x electrons interacting with the light reflected off the laser front.

We have repeated the same simulation with a Gaussian laser pulse of FWHM duration $\tau_0 = 30$ fs, impinging onto either a semi-infinite or $1 \mu\text{m}$ thick C⁶⁺ plasma of electron density $n_{e0} = 17n_c$. The results obtained are displayed in Figs. 4.6-4.8.

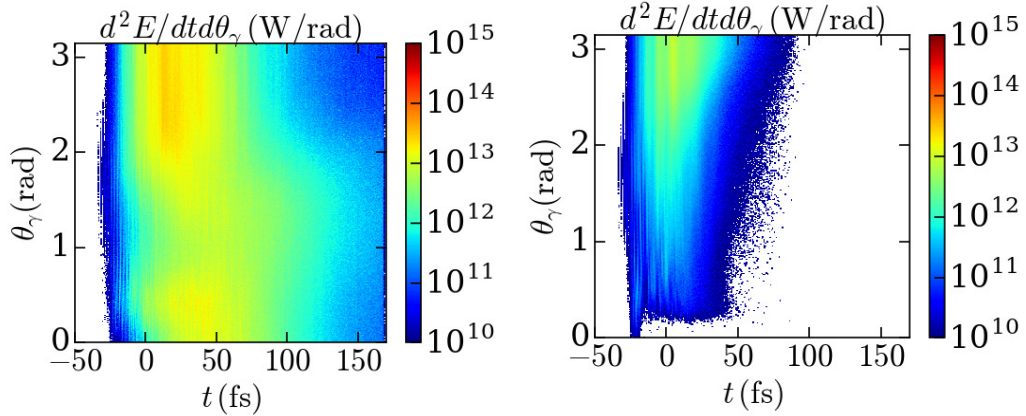


Figure 4.7: Simulations with a $n_{e0} = 17n_c$ density plasma and a 30 fs laser pulse. Time history of the angle-resolved spectrum of the synchrotron radiated energy for (a) a semi-infinite plasma and (b) a $1 \mu\text{m}$ thick plasma.

The case of a semi-infinite plasma yields a radiation spectrum consistent with that observed at early times with a constant laser drive. The radiated power at the pulse

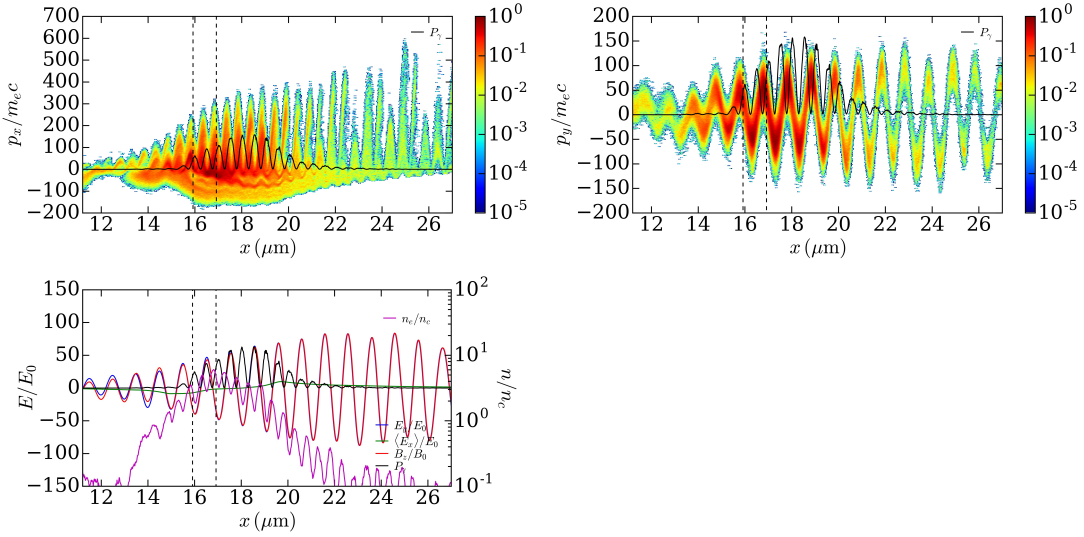


Figure 4.8: Simulation with a $1 \mu\text{m}$ thick, $n_{e0} = 17n_c$ density plasma and a 30 fs Gaussian laser pulse. (a) $x - p_x$ and (b) $x - p_y$ electron phase spaces integrated in the y direction. A lineout at $y = 0$ of the radiation power density P_γ is overlaid in black. (c) Lineouts at $y = 0$ of the E_y electric field (blue), of the laser cycle-averaged E_x electric field (green), of the electron density n_e (purple) and of the radiated power density P_γ (black). The vertical dashed lines locates the plasma boundaries. All quantities are recorded at $t = 24$ fs after the on-target laser peak. P_γ is plotted in arbitrary units in the three figures.

maximum [Fig. 4.6(a)] is close to that measured at $t \approx 30$ fs in Fig. 4.4(a), and the angular spectrum similarly features a dominant, backward-directed broad emission lobe, alongside a narrower and weaker forward-directed component [Fig. 4.6(b)]. The radiated power, however, happens to rapidly drop after $t \approx 40$ fs, as also evidenced by the time evolution of the angle-resolved power spectrum [Fig. 4.7(a)]. One can see that, at late times ($t \gtrsim 50$ fs), the angular spectrum develops a single maximum in the transverse direction ($\theta_\gamma \approx \pi/2$). This behavior is ascribed to the energy depletion of the laser pulse as it propagates through the plasma, which leads to near-transparency interaction conditions and enhances transverse emission (see below).

When considering a plasma of thickness $l = 1 \mu\text{m}$, the radiated power is reduced by a factor of ~ 6.5 . Such a drop is consistent with the scaling expected by substituting l for $v_f t$ into Eq. (4.41), $v_f \tau_0 / l \approx 5$. The main difference with the previous cases concerns the angular distribution, which presents a much narrower emission lobe centered at $\theta_\gamma = \pi$ [see Figs. 4.6(b) and 4.7(b)]. The reason for this is the rapid expansion of the heated plasma: Figure 4.8(c) shows that, by $t = 24$ fs, the electron distribution is already extending over a length $> 10 \mu\text{m}$. Besides, $\lambda_0/2$ -periodic density modulations are driven by the laser ponderomotive force, yielding density peaks where the ponderomotive force vanishes, *i.e.*, where $\partial_x A \sim B_z = 0$. The radiation is localized in the $\sim 5 \mu\text{m}$ -long denser plasma region, of average density $n_e \sim 1 - 5n_c$. The radiated power density shows a regular pattern with a periodicity of $\lambda_0/2$. The radiation peaks are correlated with the maxima of $|E_y|$ (or, equivalently $|B_z|$ as, due to very weak laser reflection, the approximation of an EM propagating wave applies). To a larger extent than in the previous simulations, the emission is caused by the high-energy $p_x < 0$ electrons refluxing across the expanding plasma, for which $\chi_e \sim 2\gamma|E_y|$. The higher-energy $p_x > 0$ electrons hardly contribute to

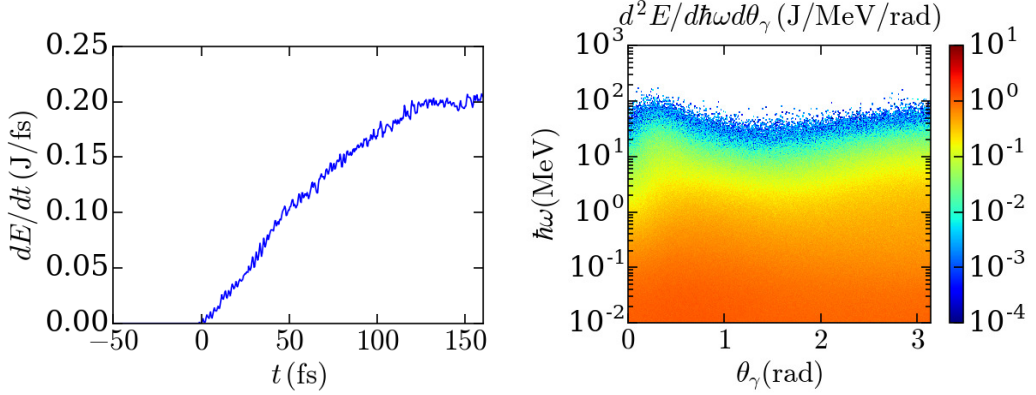


Figure 4.9: Simulation with a semi-infinite $n_{e0} = 40n_c$ density plasma and a uniform laser wave. (a) Time history of the total synchrotron radiated power; (b) Angle-energy spectrum of the synchrotron radiated energy.

the radiation because there is no significant laser reflection; this explains the vanishing forward directed spectrum in 4.7(b).

4.2.2 Synchrotron emission in overcritical plasmas

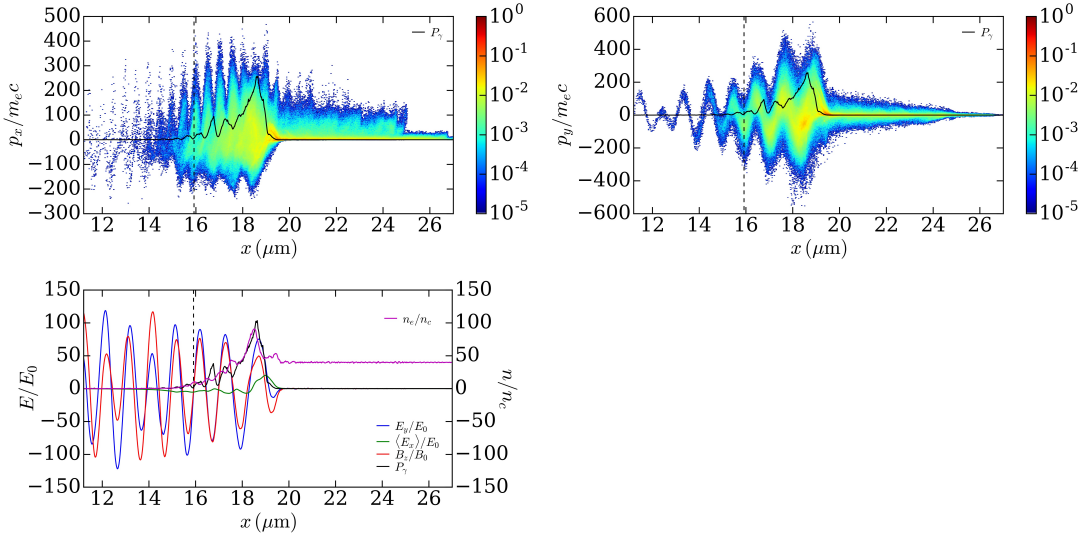


Figure 4.10: Simulation with a semi-infinite, $n_{e0} = 40n_c$ density plasma and a uniform laser wave. (a) $x - p_x$ and (b) $x - p_y$ electron phase spaces integrated in the y direction. A lineout at $y = 0$ of the radiation power density P_γ is overlaid in black. (c) Lineouts at $y = 0$ of the E_y electric field (blue), of the laser cycle-averaged E_x electric field (green), of the electron density n_e (purple) and of the radiated power density P_γ (black). The vertical dashed lines locates the plasma boundaries. All quantities are recorded at $t = 36$ fs after the on-target laser peak. P_γ is plotted in arbitrary units in the three figures.

We now address the photon emission in plasmas close or beyond the RSIT threshold. As a first illustration, we consider a semi-infinite plasma of near-critical density $n_{e0} = 40n_c$ ($n_{e0}/a_L n_c = 0.5$). Figure 4.9(a) shows that the total radiated power increases with time

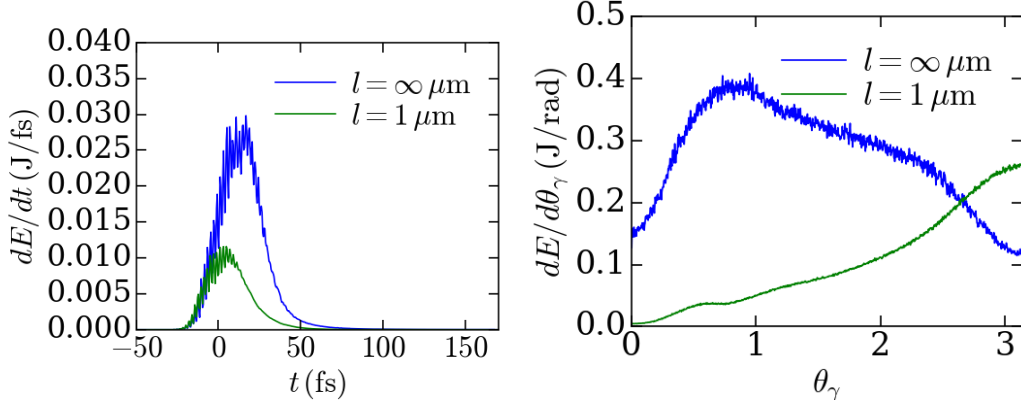


Figure 4.11: Simulations with a $n_{e0} = 40n_c$ density plasma and a $\tau_0 = 30$ fs Gaussian laser pulse. (a) Time history of the synchrotron radiated power; (b) angular distribution of the synchrotron radiated energy. The blue (resp. green) curves correspond to a semi-infinite (resp. $1\mu\text{m}$ thick) plasma.

at essentially the same rate as for $n_{e0} = 17n_c$ [Fig. 4.4(a)]. The photon energy spectrum remains relatively flat both in energy (up to a few MeV) and angle, yet now features a broad angular maximum around $\theta_\gamma \sim 1$ [4.9(b)]. This emission regime corresponds to the so-called transverse oscillating electron emission (TOEE) identified in Chang *et al.* (2017). It should be remarked that this study considered a $2\mu\text{m}$ laser focal spot and only reported on photon number spectra, which turn out to be more transversely directed than the present energy spectra. This radiative behavior can be understood from the electron phase spaces and field-density profiles displayed in Figs. 4.10(a)-(c) at $t = 36$ fs. The laser front is then located at $x \approx 19\mu\text{m}$, which corresponds to an effective propagation speed $v_f/c \approx 0.15$. This value closely matches the laser piston velocity (4.32), suggesting that the interaction has transitioned to a RPA-type regime. Figure 4.10(c), however, shows that the laser piston remains largely porous to hot electrons, as clearly seen by the relatively dense ($n_e \lesssim 30 - 40n_c$) electron population standing on the left of the compressed layer ($n_e \approx 100n_c$). This interaction regime corresponds to the incomplete HB identified in Weng *et al.* (2012b) (neglecting radiation). The latter electron population experiences the highest EM field, and presents a transverse momentum spread somewhat exceeding the longitudinal one [compare Figs. 4.10(a) and (b)]. The $\lambda_{\text{mod}} \approx 0.8\mu\text{m}$ wavelength of the $p_x < 0$ electron modulations is consistent with formula (4.39). The radiated power density peaks just in front of the laser piston, where the oscillating electrons attain the largest p_y momenta. The observed marginally forward emission points to the slightly dominant interaction of the $p_x > 0$ electrons with the reflected light.

We now examine the changes brought about by employing a 30 fs duration pulse or a $1\mu\text{m}$ thick plasma. As in the previous undercritical case, the radiated power curve essentially follows the temporal profile of the pulse and is reduced (albeit less than at $n_{e0} = 17n_c$) when using a $1\mu\text{m}$ thick plasma. Also, while the semi-infinite plasma leads to a broad angular spectrum [Fig. 4.12(a)], the thin plasma foil produces a more narrow, backward ($\theta_\gamma \approx \pi$) emission lobe [Figs. 4.11(b) and 4.12(b)]. Again, this stems from the rapid drop in the electron plasma density, allowing the laser pulse to shine through the plasma slab [Fig. 4.13(c)]. This breakout results both from front-side RPA and back-side TNSA, both processes being characterized by typical (laser piston or ion acoustic) velocities $v_p \approx c_s \approx 0.15c$, leading to the onset of RSIT at $t \approx l/2v_p \approx 10$ fs. Synchrotron emission is then predominantly due to recirculating (at $p_x \approx -100m_ec$) electrons in the

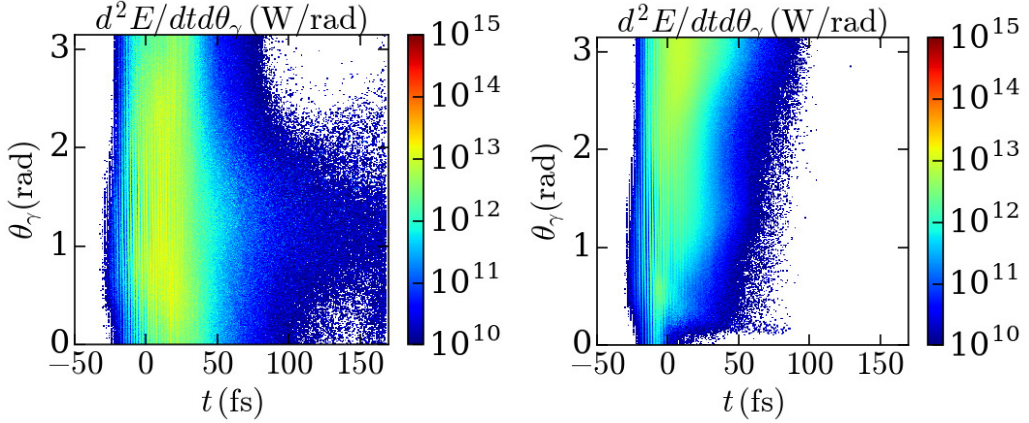


Figure 4.12: Simulations with a $n_{e0} = 40n_c$ density plasma and a 30 fs laser pulse. Time history of the angle-resolved spectrum of the synchrotron radiated energy for (a) a semi-infinite plasma and (b) a $1\text{ }\mu\text{m}$ thick plasma.

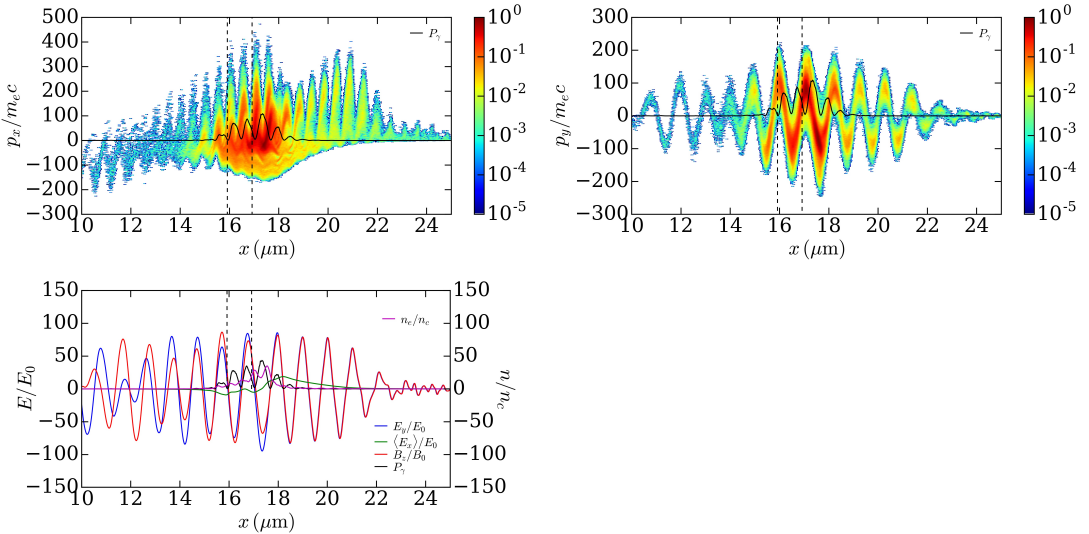


Figure 4.13: Simulation with a $1\text{ }\mu\text{m}$ thick, $n_{e0} = 40n_c$ density plasma and a 30 fs Gaussian laser pulse. (a) $x - p_x$ and (b) $x - p_y$ electron phase spaces integrated in the y direction. A lineout at $y = 0$ of the radiation power density is overlaid in black. (c) Lineouts at $y = 0$ of the E_y electric field (blue), of the laser cycle-averaged E_x electric field (green), of the electron density n_e (blue) and of the radiated power density P_γ (black). The vertical dashed lines locates the plasma boundaries. All quantities are recorded at $t = 11\text{ fs}$ after the on-target laser peak. P_γ is plotted in arbitrary units in the three figures.

central part ($n_e \approx 10 - 30n_c$) of the volumetrically heated plasma. The resulting radiated power density therefore still exhibits $\lambda_0/2$ -spaced modulations, correlated with the E_y (or B_z) extrema of the incoming EM wave.

We now consider a plasma of electron density $n_{e0}/n_c = 100$ (*i.e.* $n_e/a_L n_c = 1.2$). Figure 4.14(a) shows that the total radiated power increases about linearly with time while oscillating at $2\omega_0$. As before, these oscillations are caused by the periodic expulsion of energetic electrons from the (compressed) plasma boundary of electrons into the laser field. At early times, the laser-electron interaction is ruled by vacuum heating, as described

in Sec. 4.1.4. The electron phase spaces of Figs. 4.15(a,b,d) capture the instant ($t = 4\text{ fs}$) when the electrons accelerated by the E_y component of the standing wave set up in vacuum have acquired their maximum transverse momenta, and are being rotated by the B_z field toward the plasma [as clearly seen in (d)]. The peak radiated power density is located just in front of the steep plasma boundary [Fig. 4.15(c)], where B_z is at its highest and the accelerated electrons are characterized by $p_y \approx 150m_e c \gg p_x \gtrsim 0$, leading to marginally forward emission. The distorted E_y and B_z field profiles in vacuum are due to high-order harmonic generation from the oscillating plasma surface (Gonoskov *et al.*, 2011). Also, note that the fluid model for synchrotron emission presented in Serebryakov *et al.* (2015) under the present $n_e/a_L n_c \approx 1$ conditions assumes coherent motion of the compressed electron layer, and so misses the essentially kinetic character of the electron vacuum heating.

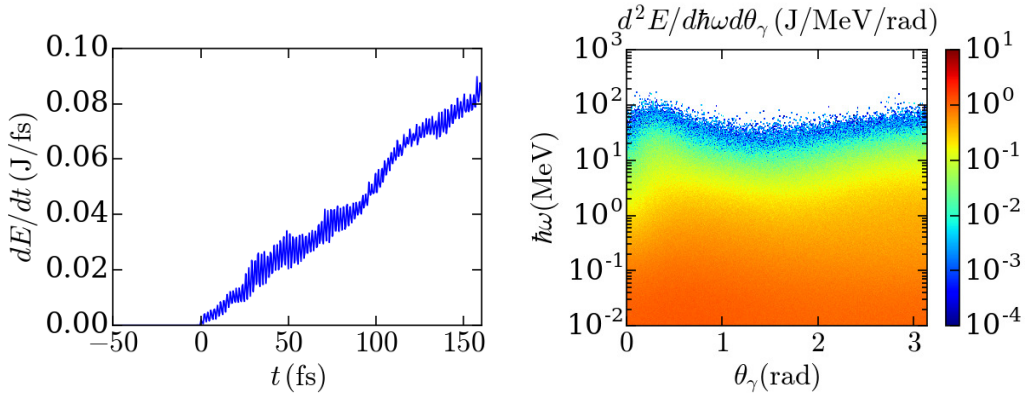


Figure 4.14: Simulation with a semi-infinite, $n_{e0} = 100n_c$ density plasma and a uniform laser wave. (a) Time history of the synchrotron radiated power; (b) angular distribution of the synchrotron radiated energy.

At a later time ($t = 36\text{ fs}$), as the plasma temperature has strongly increased and the plasma boundary (accelerated through RPA) has developed a longer scale-length density profile, the $2\omega_0$ structuring of the high-energy electron phase space is still observed [Figs. 4.16(a,b)]. The radiation, mainly due to $p_x > 0$ electrons, occurs in an enlarged ($\simeq 0.3\lambda_0$ thick) region that encompasses part of the skin layer and the moderate-density ($n_e \approx 10n_c$) underdense plasma formed in front of it. The time-increasing length of the effectively emitting plasma accounts for the observed linear rise in the radiated power [Fig. 4.14(a)]. The overall emission is mainly contained in a broad forward cone extending to backward angles [Fig. 4.14(b)].

Figures 4.17(a,b) and 4.18(a,b) display the time evolution of the radiated power and of the angular radiation spectrum, obtained for a 30 fs laser pulse interacting with a semi-infinite or $1\mu\text{m}$ thick plasma of $100n_c$ density. In contrast to the previously discussed undercritical or near-critical plasmas, the use of a thin plasma slab now leads to an increased radiated energy. In addition, the associated angular spectrum shows two forward and backward maxima, about symmetric relative to the transverse direction. The electron phase space and field profiles around the emission peak ($t = 11\text{ fs}$) are plotted in Figs. 4.19(a)-(c). Contrary to the $n_{e0} = 40n_c$ plasma which, by then, has turned transparent to the laser light, the target here remains essentially opaque, resulting in a $\sim 200n_c$ peak density at the boundary of its compressed skin layer ($x \approx 17\mu\text{m}$). The emission therefore takes place in the $\sim 5 - 100n_c$ density plasma shelf preceding the laser-driven piston, where the quasi-standing EM wave is established. There it is caused, with similar efficiencies, both by the forward- and backward-moving energetic electrons which, due to

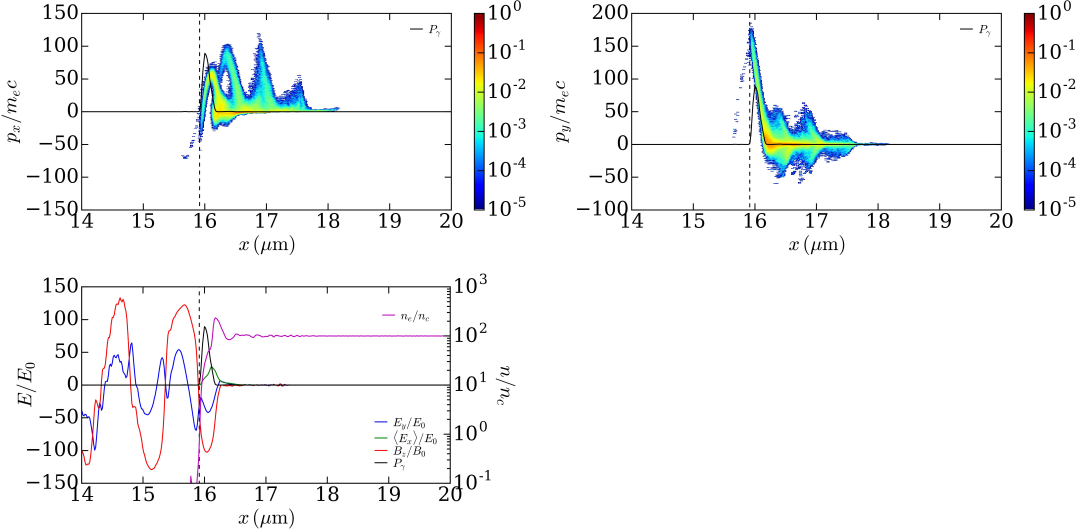


Figure 4.15: Simulation with a semi-infinite, $n_{e0} = 100n_c$ density plasma and a uniform laser wave. a) $x - p_x$ and (b) $x - p_y$ electron phase spaces integrated in the y direction. A lineout at $y = 0$ of the radiation power density P_γ is overlaid in black. (c) Lineouts at $y = 0$ of the E_y electric field (blue), of the laser cycle-averaged E_x electric field (green), of the electron density n_e (purple) and of the radiated power density P_γ (black). The vertical dashed lines locates the plasma boundaries. (d) $p_x - p_y$ electron distribution. All quantities are recorded at $t = 4$ fs after the on-target laser peak. P_γ is plotted in arbitrary units in the three figures.

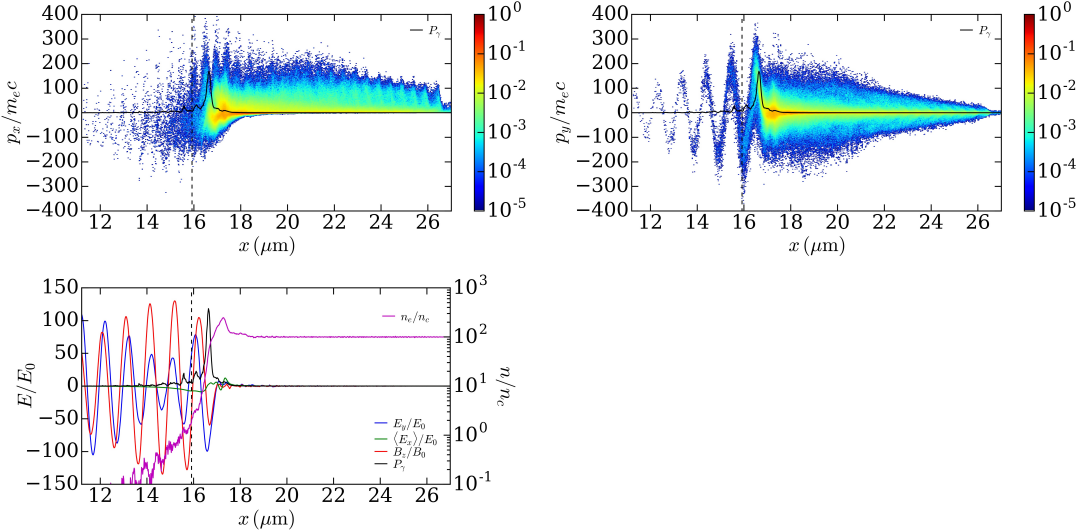


Figure 4.16: Same as Fig. 4.15 but at $t = 36$ fs after the on-target laser peak.

electrostatic confinement, recirculate across the expanding target. Owing to nonexistent hot-electron recirculation (and hence to a reduced electron kinetic pressure), the case of a semi-infinite plasma leads to a steeper-gradient, denser plasma boundary ($n_e \approx 400n_c$, not shown), inside which the electrons are driven to lower energies ($|p_x|/m_ec \lesssim 250$ vs. $|p_x|/m_ec \lesssim 400$). Synchrotron emission is then maximized at forward angles [Figs. 4.17(b)]

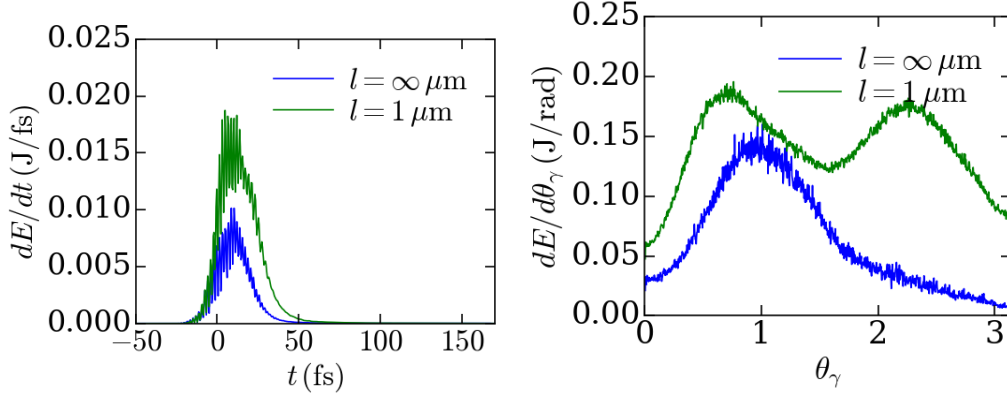


Figure 4.17: Simulations with a $n_{e0} = 100n_c$ density plasma and a $\tau_0 = 30$ fs Gaussian laser pulse. (a) Time history of the radiated power; (b) angular distribution of the radiated energy. The blue (resp. green) curves correspond to a semi-infinite (resp. 1 μm thick) plasma.

and 4.18(a)].

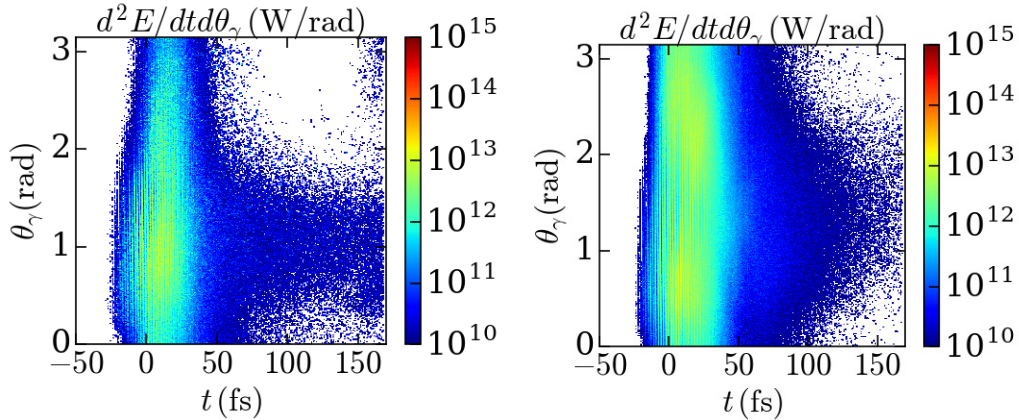


Figure 4.18: Simulations with a $n_{e0} = 100n_c$ density plasma and a 30 fs laser pulse. Time history of the angle-resolved spectrum of the synchrotron radiated energy for (a) a semi-infinite plasma and (b) a 1 μm thick plasma.

4.2.3 Conclusions

Our 2D PIC simulations, run at a laser intensity $I_0 = 10^{22} \text{ Wcm}^{-2}$, have shown the existence of distinct synchrotron emission regimes depending on the density, and therefore the transparency or opacity, of the irradiated plasma. Our results complement and refine several previously published studies (Ridgers *et al.*, 2012; Brady *et al.*, 2014; Chang *et al.*, 2017). At relativistically undercritical density ($n_{e0} = 17n_c$), the emission is mainly caused by energetic electrons counterstreaming against the laser wave. Those electrons are injected at high energies toward the laser source across the laser front, in a time-modulated way due to relativistic Doppler effects. As a result, backward-directed radiation bursts are produced throughout the whole laser-filled volume. While forward emission is also significant in semi-infinite plasmas due to nonnegligible reflected light (interacting with forward-moving electrons), it almost completely vanishes in rapidly expanding, 1 μm thick

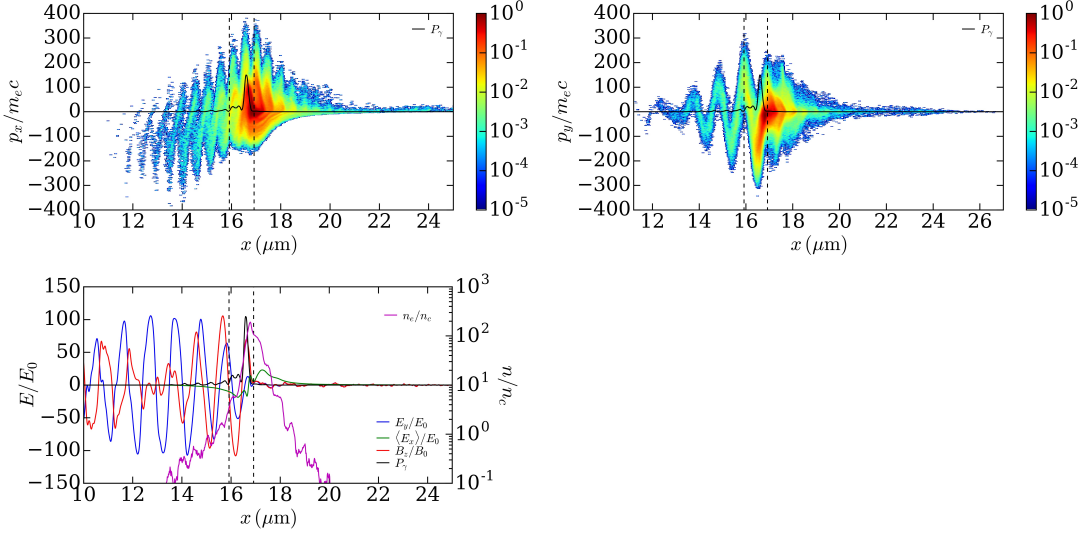


Figure 4.19: Simulation with a $1 \mu\text{m}$ thick, $n_{e0} = 100n_c$ density plasma and a 30 fs Gaussian laser pulse. (a) $x - p_x$ and (b) $x - p_y$ electron phase spaces integrated in the y direction. A lineout at $y = 0$ of the radiation power density P_γ is overlaid in black. (c) Lineouts at $y = 0$ of the E_y electric field (blue), of the laser cycle-averaged E_x electric field (green), of the electron density n_e (blue) and of the radiated power density P_γ (black). The vertical dashed lines locates the plasma boundaries. All quantities are recorded at $t = 11$ fs after the on-target laser peak. P_γ is plotted in arbitrary units in the three figures.

targets. At overcritical density ($n_{e0} = 100n_c$), the emission initially occurs in the narrow vacuum region where the electrons are energized, and, at later times, in a more extended region encompassing the skin layer and a fraction of the expanding pre-plasma. In semi-infinite targets, the radiation is dominated by electrons being rotated back to the target, and thus exhibits a broad maximum at forward angles (around $\theta_\gamma \approx 1$). In $1 \mu\text{m}$ targets, the radiation is enhanced with two forward and backward lobes owing to recirculating electrons. In plasmas just above the opacity threshold ($n_{e0} = 40n_c$), the emission is more isotropic, although still maximized in the forward direction. If the target is thin enough to become transparent to the laser pulse, the emission shifts to the purely backward direction.

4.3 Competition between Bremsstrahlung and Synchrotron radiation in foils of varying thickness

We now address the relative contributions of Bremsstrahlung and synchrotron emission to the total high-energy radiation from a laser-driven thin solid foil. In contrast to the few previous studies on this subject ([Pandit and Sentoku, 2012](#); [Wan et al., 2017](#); [Vyskočil et al., 2018](#)), which focused on the laser intensity dependence of those two processes, we will consider fixed laser parameters (namely, a laser intensity of 10^{22} Wcm^{-2} and a pulse duration of 50 fs) and a single target material (Cu), and will investigate, through 1D and 2D simulations, the influence of the target thickness, varied from a few nm to a few μm . We will show that both 1D and 2D simulations predict a $\sim 2 \mu\text{m}$ threshold thickness between the synchrotron- and Bremsstrahlung-ruled regimes, but also that 1D simulations inaccurately describe the radiation spectrum and efficiency at larger thicknesses.

4.3.1 Numerical setup

All simulations reported below consider a laser pulse propagating in the $+x$ direction, linearly polarized along y , with a wavelength $\lambda_0 = 1 \mu\text{m}$ and a maximum intensity $I_0 = 10^{22} \text{ Wcm}^{-2}$. It has a Gaussian temporal profile of 50 fs FWHM and, in 2D simulations, a Gaussian transverse profile of $w_0 = 5 \mu\text{m}$ FWHM. The target consists of a solid-density copper plasma slab initialized with 200 eV temperature, $Z^* = 25$ ionization rate and $n_{e0} = 2000n_c$ electron density. Its front and rear sides are coated with 3.2 nm thick hydrogen layers of $n_H = 50n_c$ atomic density, which model the hydrogen-rich surface contaminants usually responsible for proton beam generation in laser experiments ([Macchi et al., 2013](#)). Note that the presence of a thin hydrogen layer on the target front side implies an ultra-high intensity contrast ([Ceccotti et al., 2007](#)).

Dimension	Plasma length
1Dx×3Dv	$l = 10, 13, 16, 32, 51 \text{ nm}$ and $l = 0.1, 0.2, 0.4, 0.5, 0.6, 0.8, 1, 2, 5, 10 \mu\text{m}$
2Dx×3Dv	$l = 16, 32, 51 \text{ nm}$ and $l = 0.1, 0.5, 1, 5 \mu\text{m}$

Table 4.2: Summary of the parametric scan performed in this section, for 1D and 2D simulations. All other parameters are detailed in the text

The 1D domain has a length $L_x = 127 \mu\text{m}$ and a spatial step $\Delta x = 0.8 \text{ nm}$ (for target thicknesses $10 \leq l \leq 100 \text{ nm}$) or $\Delta x = 1.6 \text{ nm}$ (for $0.1 < l \leq 10 \mu\text{m}$). Each 1D cell contains between 300 and 1000 particles per cell for each species. Simulations are run over 450 fs (resp. 900 fs) after the on-target pulse peak for target thicknesses $10 \leq l \leq 100 \text{ nm}$ (resp. $100 < l \leq 10 \mu\text{m}$). Such durations are sufficient to capture the synchrotron emission (which mainly takes place over the pulse duration) and the beginning of the Bremsstrahlung saturation in the thickest targets.

In 2D, the domain dimensions are $L_x \times L_y = 127 \times 40 \mu\text{m}^2$ with a mesh size $\Delta x = \Delta y = 3.2 \text{ nm}$ (marginally resolving the plasma skin depth $c/\omega_p = 3.2 \text{ nm}$). The number of particles per cell and species is varied from 2000 to 1000 for $l \in (16, 32, 51) \text{ nm}$, and from 40 to 10 for $l \in (0.5, 1, 5) \mu\text{m}$. The simulations are run over durations ranging from 270 fs ($l = 16 \text{ nm}$) to $\approx 800 \text{ fs}$ ($l = 5 \mu\text{m}$).

In addition to Bremsstrahlung and synchrotron emission, all simulations self-consistently describe elastic Coulomb collisions, as well as impact and field induced ionization. Absorbing boundary conditions for particles and fields are employed in both x and y directions.

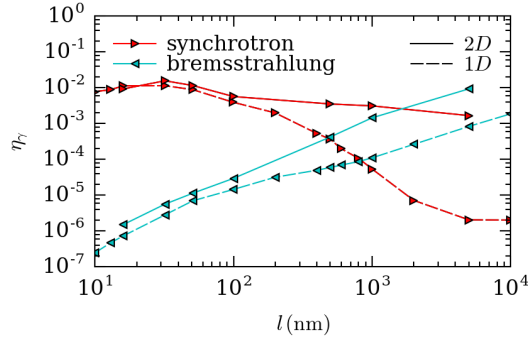


Figure 4.20: Radiation conversion efficiency through synchrotron emission (red triangles) and Bremsstrahlung (light blue triangles) as a function of target thickness. Solid (resp. dashed) curves represent 2D (resp. 1D) simulation results.

4.3.2 Target thickness dependence of the radiation yield

The energy conversion efficiencies of Bremsstrahlung (red) and synchrotron emission (light blue) are plotted in Fig. 4.20 as a function of the target thickness. The synchrotron yield (into > 10 keV photons) initially grows from $\eta_\gamma \approx 8 \times 10^{-3}$ at $l = 10$ nm to a maximum of ~ 0.015 in 2D (resp. ~ 0.01 in 1D) at $l = 32$ nm. Actually, in 1D, the synchrotron yield is unchanged between $l = 17$ nm and $l = 32$ nm. At larger thicknesses, it rapidly drops away in 1D (down to $\eta_\gamma \approx 2 \times 10^{-3}$ at $l = 200$ nm and $\eta_\gamma \leq 4 \times 10^{-5}$ at $l \geq 1 \mu\text{m}$) but more slowly in 2D ($\eta_\gamma = 2 \times 10^{-3}$ at $l = 5 \mu\text{m}$).

By contrast, the Bremsstrahlung curve exhibits a steady rise with thicker targets: from $\eta_\gamma \approx 2 \times 10^{-7}$ at $= 10$ nm to $\sim 2 \times 10^{-3}$ at $l = 10 \mu\text{m}$ in 1D, and from $\eta_\gamma \approx 2 \times 10^{-6}$ at $= 17$ nm to ~ 0.01 at $l = 5 \mu\text{m}$ in 2D. These variations obey a power-law dependence, $\eta_b \propto l^{1.8}$ in 1D (in the $10 \leq l \leq 100$ nm range) $\eta_b \propto l^{1.5}$ in 2D (in the $17 \text{ nm} \leq l \leq 5 \mu\text{m}$ range) and . Overall, though, the 1D Bremsstrahlung values underestimate the 2D values by a factor of a few, and this discrepancy tends to increase with $l \gtrsim 0.5 \mu\text{m}$ (this trend, however, may result from simulation times too short compared to the hot-electron relaxation time). In spite of these differences at large l , the two simulation geometries lead to comparable threshold thicknesses (l_{th}) above which Bremsstrahlung is the dominant radiation process, namely, $l_{\text{th}} \approx 1 - 2 \mu\text{m}$ in 2D and $l_{\text{th}} \lesssim 1 \mu\text{m}$ in 1D.

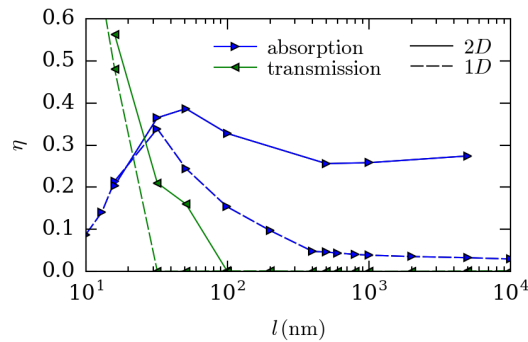


Figure 4.21: Laser absorption (blue triangles) and transmission (green triangles) rates as a function of target thickness. Solid (resp. dashed) curves represent 2D (resp. 1D) simulation results.

It is interesting to confront those results to the variations of the laser reflection and transmission rates, displayed in Fig. 4.21. The laser absorption attains a maximum value $\eta \approx 0.33$ (resp. 0.38) at $l = 32$ nm (resp. 50 nm) in 1D (resp. 2D), close to the synchrotron-optimizing thickness. Similarly to synchrotron emission, the 1D and 2D absorption curves greatly differ at larger thicknesses: While 1D simulations predict a fast decrease (down to $\eta \approx 0.05$ at $l = 400$ nm), 2D simulations show a modest drop (from ~ 0.38 to ~ 0.28) in the range $50 \leq l \leq 500$ nm), followed by quasi-saturation. Such variations of the laser absorption between 1D and 2D simulations are ascribed to transverse modulations of the laser-irradiated surface, resulting in laser interaction at non-strictly normal incidence and increased degrees of freedom due to non-conserved transverse canonical momentum ([Adam et al., 2006](#); [Kemp et al., 2014](#); [Kemp and Divol, 2016](#); [Wan et al., 2016](#)). In parallel, as expected, the transmission rate exhibits a continuous decreasing trend, more pronounced in 1D where it drops from $T \approx 0.48$ at $l = 17$ nm down to $T < 0.01$ at $l = 32$ nm. In 2D, it remains significant ($T \approx 0.2$) at $l = 32$ nm, and essentially vanishes at $l = 500$ nm. The comparison of Fig. 4.20 with Fig. 4.21 reveals that strong synchrotron efficiency requires both strong laser absorption and significant laser transmission, the only exception being the 32-nm-thick 1D foil that optimizes the synchrotron yield while lying just above the opacity threshold. Such conditions are also known to optimize ion acceleration in thin target foils ([d'Humières et al., 2005](#); [Esirkepov et al., 2006](#); [Brantov et al., 2015](#)).

In the following, we will examine a few cases in order to illustrate distinct target and radiation dynamics, and will pinpoint, when relevant, major differences between 1D and 2D simulations.

4.3.3 Influence of the target dynamics on the radiation processes

Transparent and near-transparent targets

Let us first consider a 16 nm target thickness, which is close to the theoretical transparency threshold (neglecting ion motion), $l \approx (\lambda_L/\pi)a_L(n_c/n_{e0}) \approx 12$ nm [Eq. (4.38)]. The spatio-temporal evolution of the foil predicted by a 1D simulation is shown in Figs. 4.22(a,b). It can be seen that the target is expanding while being accelerated forward in the rising edge of the laser, and becomes transparent near the pulse peak ($t = 0$). The temporal evolution of the total particle and photon energies is displayed in Fig. 4.23. The fraction ($\sim 20\%$) of absorbed laser energy mainly goes into Cu ions, whose kinetic energy exceeds that of the electrons as early as $t \approx -30$ fs. The electron kinetic energy reaches its maximum around the laser peak ($t = 0$) and slowly decreases at later times (by a factor ~ 8 over ~ 300 fs), mainly to the benefit of ions.

The initial interaction phase (before transparency) is illustrated in Figs. 4.24(a,b) at $t = -15$ fs. The electrons have then been accelerated to $|p_x/m_ec| \sim 100 \sim a_L$ and are streaming back and forth over a spatial extent $\sim 1 \mu\text{m}$, inducing a quasistatic sheath field $\langle E_x \rangle \approx 20m_ec/\omega_0$. This field causes outward acceleration of the front and back-side protons, which have already fully detached from the Cu ions [Fig. 4.24(b)]. The latter have also started expanding, yet most of them are still confined within a high-density ($Z^*n_{\text{Cu}} = 1000n_c$, i.e., about half their initial density) spike, in which the electrons attain a similar peak density. At this instant, the incoming laser field strength is $a \sim 50$, too low to trigger transparency. Synchrotron emission then mainly occurs in the foot of the density spike, where $10 \leq n_e \leq 100n_c$. From Fig. 4.22(c), this early-time emission has a broad angular distribution, with a moderate maximum at backward angles.

The onset of transparency is illustrated in Fig. 4.25 at $t = +3$ fs. The peak electron and Cu charge densities have dropped to $n_e \approx 100n_c$ and $Z^*n_{\text{Cu}} \approx 200n_c$, mostly as a

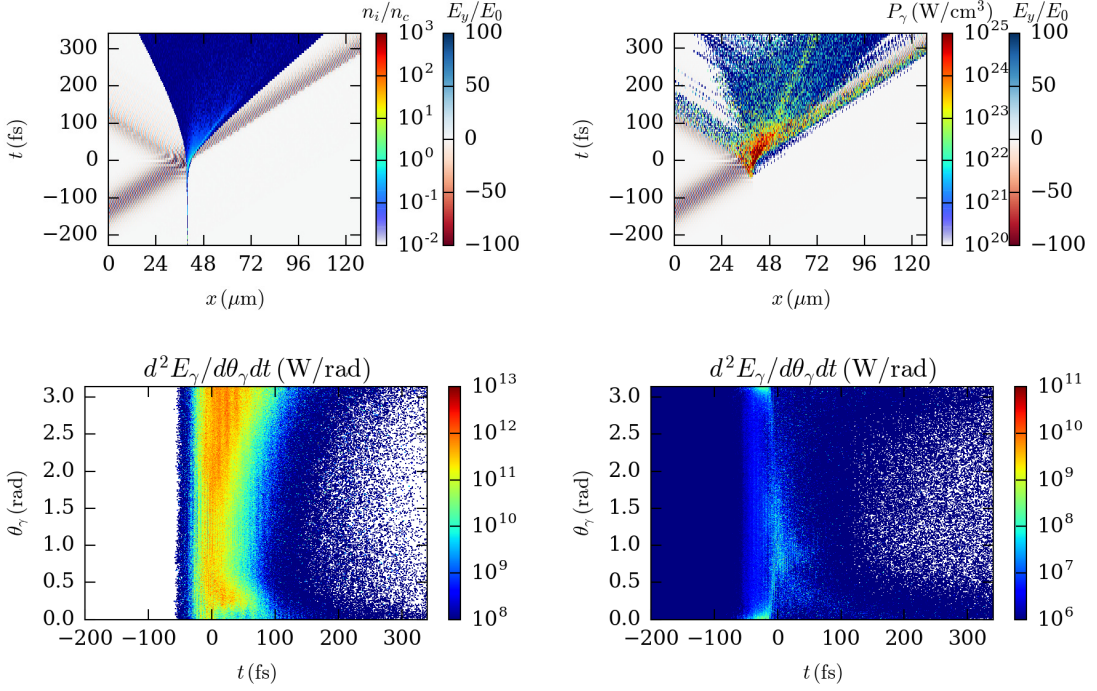


Figure 4.22: 1D simulation of a $l = 16$ nm target. (a) Space-time evolution of the ion density and E_y field. (b) Space-time evolution of the synchrotron radiated power density. Time evolutions of the angle-resolved (c) synchrotron and (d) Bremsstrahlung energy spectra.

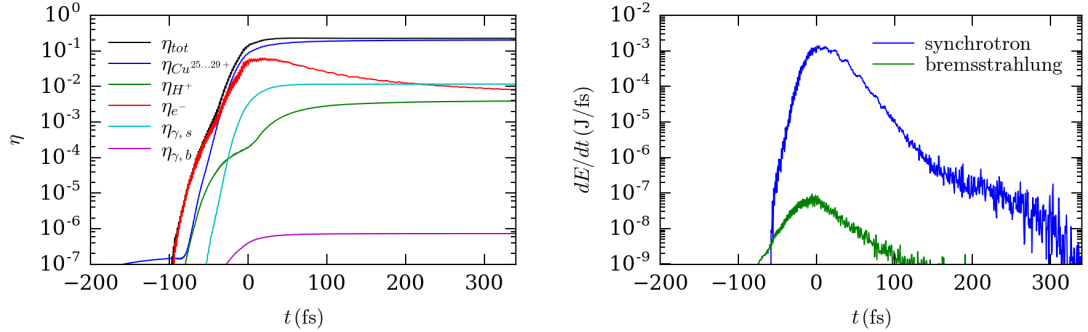


Figure 4.23: 1D simulation of a $l = 16$ nm target. (a) Time evolution of the total kinetic and photon energies normalized to the total injected laser energy, (b) Time evolution of the radiated power.

result of plasma expansion toward the laser source. This density decrease is lower than that expected from 1D target expansion, $n_{Cu}(t) \approx n_{Cu}(0)l_0/\sqrt{l_0^2 + c_{sh}^2 t^2}$ (Dorozhkina and Semenov, 1998), where l_0 is the initial target thickness and $c_{sh} \approx \sqrt{Za_L/m_{Cu}} \approx 0.14c$ is the sound velocity. Between $t = -15$ fs and $t = +3$ fs, this formula predicts a density drop by a factor ~ 26 instead of the measured value ~ 5 . We attribute this difference to the laser-induced compression of the Cu ions during their light-sail-type acceleration (which stops once the target turns fully transparent), as seen in Fig. 4.22. Despite being overcritical ($n_e/n_c > a_L$), the electron density spike is thin enough ($l < (1/\pi)a_L n_c/n_e$) to

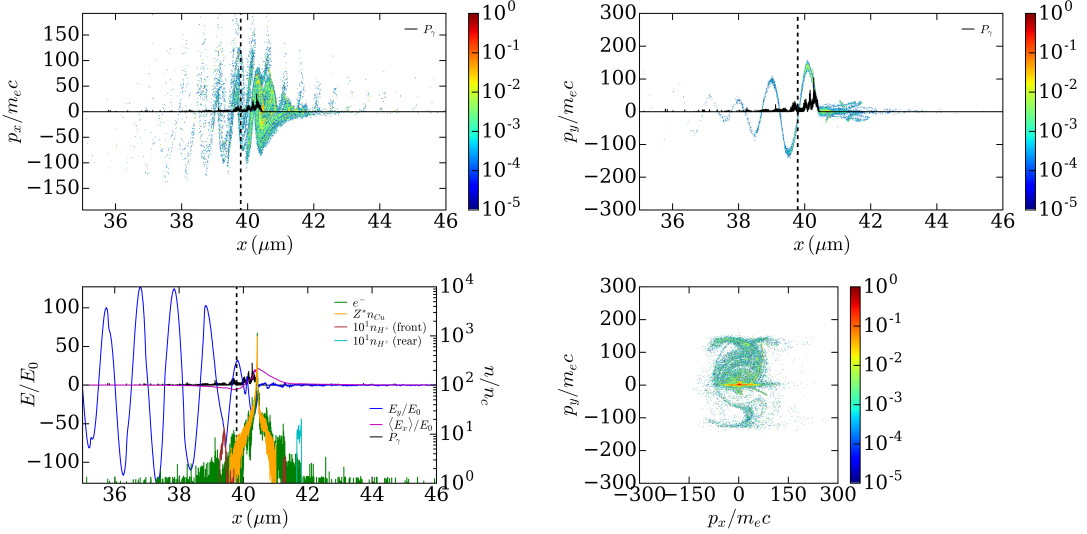


Figure 4.24: 1D simulation of a $l = 16 \text{ nm}$ target. (a) $x - p_x$ electron phase. (b) Spatial profiles of the particle charge densities, E_y and $\langle E_x \rangle$ fields and synchrotron radiated power density. All quantities are recorded at $t = -15 \text{ fs}$.

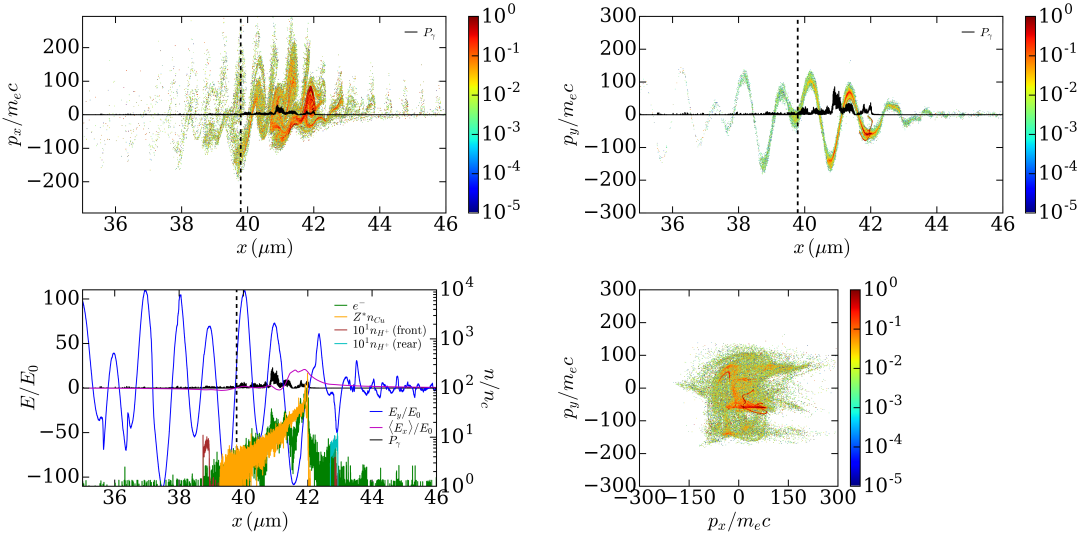


Figure 4.25: 1D simulation of a $l = 16 \text{ nm}$ target. (a) $e - p_x$ electron phase. (b) Spatial profiles of the particle charge densities, E_y and $\langle E_x \rangle$ fields and synchrotron radiated power density. All quantities are recorded at $t = +3 \text{ fs}$.

enable laser transmission: the laser front has then moved $\sim 1 \mu\text{m}$ from the density spike. Synchrotron emission, which is at its highest [see Figs. 4.22(c) and 4.23(b)], takes place in the relativistically undercritical front-side region ($10 \lesssim n_e/n_c \lesssim a_L$), which contains most of the target electrons, with peak emissivities occurring around $n_e \approx 10 - 20 n_c$. As the maximum electron density (and therefore the laser reflectivity) further decreases, the synchrotron spectrum is increasingly backward directed [Fig. 4.22(c)], in agreement with the results of Sec. 4.2.1.

Figure 4.23(b) shows that the Bremsstrahlung areal power density culminates slightly

prior to the laser peak, and that its time scale is somewhat longer than that of synchrotron emission, yet still comparable with the laser duration. Figure 4.22(d) reveals that its angular distribution significantly evolves in time: in the rising phase of the laser, it is peaked along the longitudinal axis (around $\theta_\gamma \approx 0$ and $\theta_\gamma \approx \pi$), while after the laser peak it is mainly concentrated at forward oblique angles ($0.5 \lesssim \theta_\gamma \lesssim 1.5$). This behavior can be easily understood from the following expression of the Bremsstrahlung areal power density, valid in the ultrarelativistic limit and neglecting electron screening (Quigg, 1968),

$$\frac{dE_{b,h}}{dt} = 12\alpha r_e^2 Z^2 m_e c^3 l \langle n_{\text{Cu}} \rangle \langle n_h \rangle \langle \gamma \rangle [\log(2\langle \gamma \rangle) + 0.92], \quad (4.42)$$

where l denotes the time-dependent width of the bulk copper plasma, with mean electron density $\langle n_e \rangle$, mean ion density $\langle n_{\text{Cu}} \rangle$, and mean electron energy $\langle \gamma \rangle$. Note that the mean energy of Bremsstrahlung photons is $\langle \hbar\omega \rangle \approx m_e c^2 \langle \gamma \rangle / 3$ (Dermer and Menon, 2009). At early times, the Cu density spike (from which most of the Bremsstrahlung power originates) is opaque to the laser field. Therefore, due to the 1D geometry, the electron p_y momenta locally vanish, and Bremsstrahlung photons are emitted (in both directions) along the laser propagation axis. Once the target turns transparent, the laser field extends over the whole plasma profile; hence, the electrons acquire comparable longitudinal and transverse momenta, $p_x/m_e c \sim p_y/m_e c \sim a_L$, and emit Bremsstrahlung photons at oblique angles.

Furthermore, since the areal density $n_{\text{Cu}} l$ is approximately constant, the Bremsstrahlung areal power density should vary as $dE_{b,h}/dt \sim \langle n_h \rangle \langle \gamma \rangle(t)$. Introducing E_h the total hot electron energy leads to $dE_b/dt \sim E_h(t)/l(t)$. This scaling is consistent with the decay rate of dE_b/dt over the time span $0 \leq t \leq 100$ fs [Fig. 4.23(b)]. Indeed, the bulk Cu plasma then expands by a factor ~ 50 , while, owing to energy transfer to ions, the total electron energy drops by a factor ~ 3 [Fig. 4.23(a)], so that $dE_{b,h}/dt$ should decay by a factor ~ 150 , close to the observed value (~ 100).

We now address the dynamics of a 32-nm-thick target as described by a 1D simulation. Figures 4.26-4.28 display the same quantities as before. The main difference with the $l = 16$ nm case is that the foil remains opaque to the laser field [Fig. 4.26(a)]. As before, the Cu ions carry away most of the absorbed laser energy [Fig. 4.23(a)]. A close-up of the irradiated plasma at $t = +3$ fs is provided in Figs. 4.28. The $x - p_x$ electron phase space shows the standard electrostatically confined distribution, modulated at $2\omega_0$ and with maximum momenta $|p_x| \sim 100m_e c$. The electrons are recirculating across the compressed ($Z^* n_{\text{Cu}} \approx 4000n_c$) Cu bulk layer, in which their density peaks at ‘only’ $n_e \approx 200n_c$ (due to their Debye length being much larger than the Cu layer width). The laser is prevented from shining through, which results in light-sail acceleration of the bulk target [Fig. 4.26(a)], up to a mean velocity $v_x \approx 0.4c$ consistent with Eq. (4.37).

As for the $l = 16$ nm foil before transparency, synchrotron emission occurs in the expanding plasma ($5 \lesssim n_e \lesssim 100n_c$) at the foot of the compressed layer [see also Fig. 4.26(b)]. This plasma ramp contains about one half of the plasma electrons, which explains why the synchrotron efficiency is roughly equal to that obtained at $l = 16$ nm (since in that case, following transparency, all plasma electrons eventually contribute to the emission). However, due to the enhanced laser reflectivity, the $p_x > 0$ and $p_x < 0$ electrons contribute similarly to the spectrum, which thus presents two broad angular maxima around $\theta_\gamma \approx 0.5$ and $\gamma_\gamma \approx 2.5$.

Figure 4.27(b) shows an approximate four-fold increase in the peak Bremsstrahlung power compared to $l = 16$ nm. This enhancement is consistent with Eq. (4.42), taking account of both twice larger thickness and mean electron density [as a consequence of

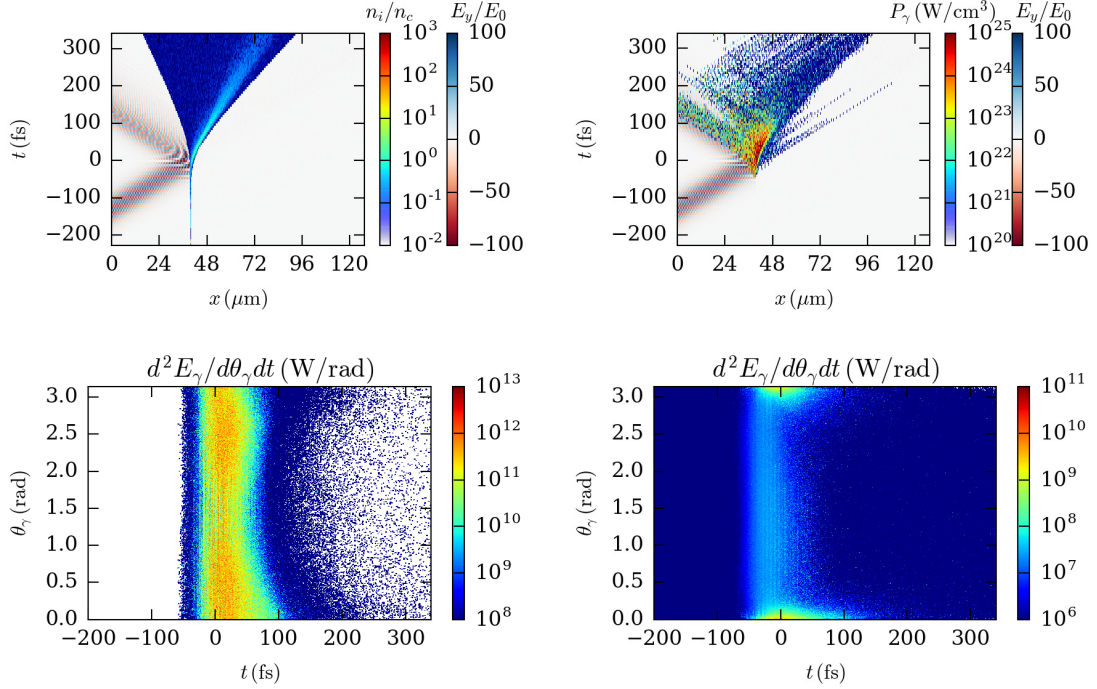


Figure 4.26: 1D simulation of a $l = 32 \text{ nm}$ target. (a) Space-time evolution of the ion density and E_y field. (b) Space-time evolution of the synchrotron radiated power density. Time evolution of the angle-resolved (c) synchrotron and (d) Bremsstrahlung energy spectra.

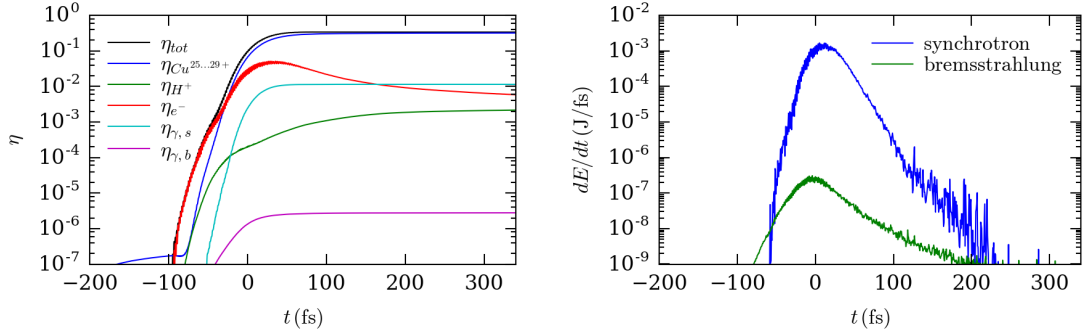


Figure 4.27: 1D simulation of a $l = 32 \text{ nm}$ target. (a) Time evolution of the total kinetic and photon energies normalized to the total injected laser energy. (b) Time evolution of the synchrotron and Bremsstrahlung radiated powers.

slower target decompression, compare Figs. 4.22(a) and 4.26(a)]. Despite reaching higher absolute values, the Bremsstrahlung radiated power exhibits a similar decay rate than with $l = 16 \text{ nm}$. Since the Cu plasma remains opaque during the Bremsstrahlung time scale, the transverse momenta of the radiating electrons vanish, leading to peaked forward and backward emission lobes [Fig. 4.26(d)]. Those lobes are superimposed on a rather uniform radiation background due to the isotropized lower-energy electron population.

We now present the results of the 2D simulation run with $l = 32 \text{ nm}$. It was noted in Sec. 4.3.2 that, although they give comparable synchrotron efficiencies and laser ab-

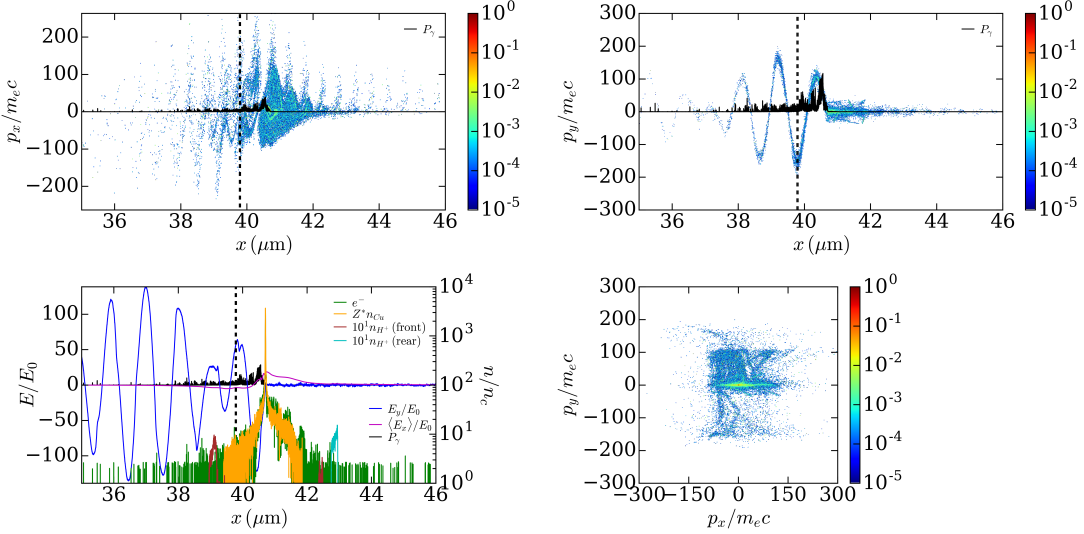


Figure 4.28: 1D simulation of a $l = 32$ nm target. (a) $x - p_x$ electron phase. (b) Spatial profiles of the particle charge densities, E_y and $\langle E_x \rangle$ fields and synchrotron radiated power density. All quantities are recorded at $t = +3$ fs.

sorption rates, the 1D and 2D simulations at $l = 32$ nm strongly differ in predicting the transparency or opacity of the target. Indeed, the 2D simulation reveals that the target becomes transparent near the pulse maximum, as shown in Figs. 4.29(a-c) and Fig. 4.30(b), all recorded at $t = +24$ fs (just after the time of peak synchrotron emission). Fast-growing Rayleigh-Taylor-like surface modulations with spatial scale $\sim \lambda_0$ [Fig. 4.30(b)] have enhanced the electron heating by breaking the translational invariance along y , and disrupted the 1D balance between the radiation and particle momentum fluxes. As a result, the laser absorption into electron kinetic energy is increased by a factor of ~ 3 [compare Figs. 4.32(a) and 4.27(a)], and the Cu plasma, initially accelerated through LSA, is bored through by the laser pulse. The on-axis particle density profiles plotted in Fig. 4.30(b) indicate that the heated foil has evolved, through TNSA, into a $\sim 3 \mu\text{m}$ thick plasma of maximum density $Z^*n_{Cu} \sim 20$. While quasineutrality is well fulfilled in the decompressed bulk Cu plasma, it obviously no longer holds beyond its expanding boundaries, notably around the detached proton layers (at $x \approx 21.5 \mu\text{m}$ and $x \approx 29 \mu\text{m}$). Synchrotron emission is concentrated in the laser-filled bulk plasma turned undercritical, in the density range $3 \lesssim n_e/n_c \lesssim 20$ [see Figs. 4.29(d) and 4.30(b)].

The evolution of the target at a later time ($t = +63$ fs) is depicted in Figs. 4.31(a-d). Most of the laser pulse has then broken out of the Cu plasma, whose density has further dropped to $Z^*n_{Cu} \approx 5n_c$ and which extends over $\sim 10 \mu\text{m}$. Figure 4.32 shows that, by then, the Cu kinetic energy has overtaken the electron kinetic energy. The ten-fold decrease in electron density has led to a comparable drop in the synchrotron radiated power density [Fig. 4.32(b)], in agreement with the expected scaling [Eq. (4.41)].

The time-resolved synchrotron energy spectrum, which is nearly isotropic in the laser's rising edge, increases in intensity and becomes mainly backward directed after the laser peak, *i.e.*, once the target turns transparent [Fig. 4.33(a)]. This behavior is confirmed by the integrated synchrotron energy-angle spectrum [Fig. 4.34(a)], which presents a broad maximum at backward angles. This emission is more backward directed than in 1D geometry: this is due to lower effective electron densities that favor emission from electrons

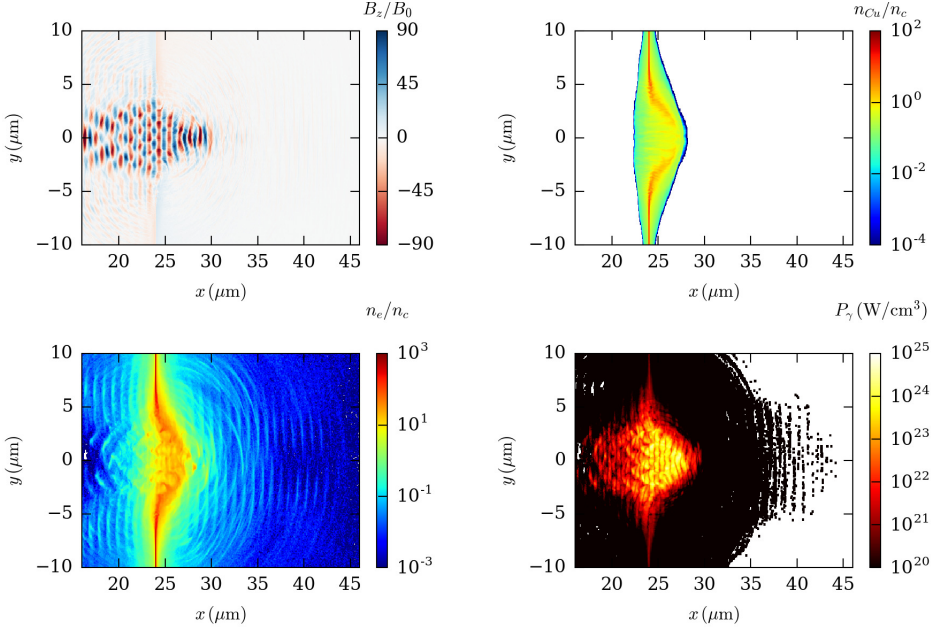


Figure 4.29: 2D simulation of a $l = 32$ nm target. (a) Magnetic field B_z . (b) Ion density n_{Cu} . (c) Electron density n_e . (d) Synchrotron radiated power density P_γ . All quantities are recorded near the time of peak synchrotron emission, $t = +24$ fs.

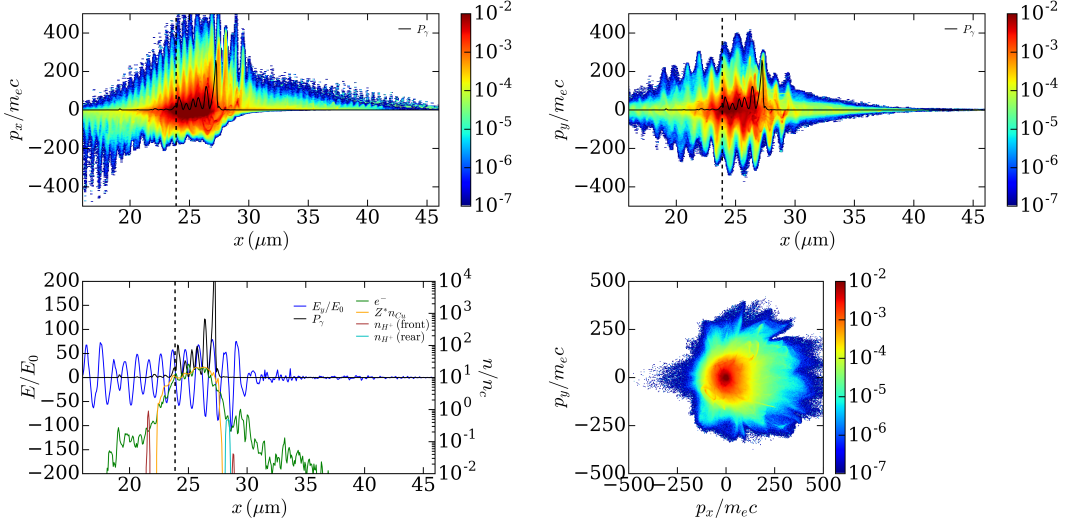


Figure 4.30: 2D simulation of a $l = 32$ nm target. (a) $x - p_x$ and (b) $x - p_y$ electron phase spaces. (c) Spatial profiles of the particle charge densities, E_y and $\langle E_x \rangle$ fields and synchrotron radiated power density. All quantities are recorded at $t = +24$ fs.

counterstreaming against the incident laser wave [Sec. 4.2.1].

Similarly to the synchrotron emission, the Bremsstrahlung radiated power culminates at the laser peak [Figs. 4.32(b)], yet decays away over a longer time scale (~ 50 fs vs. ~ 15 fs for synchrotron). This time scale also turns out to be longer than in 1D [Fig. 4.27(b)], as a result of a slower electron cooling and remaining dense Cu regions off axis. The Bremsstrahlung radiation is initially emitted preferentially in the $x > 0$ and $x < 0$ di-

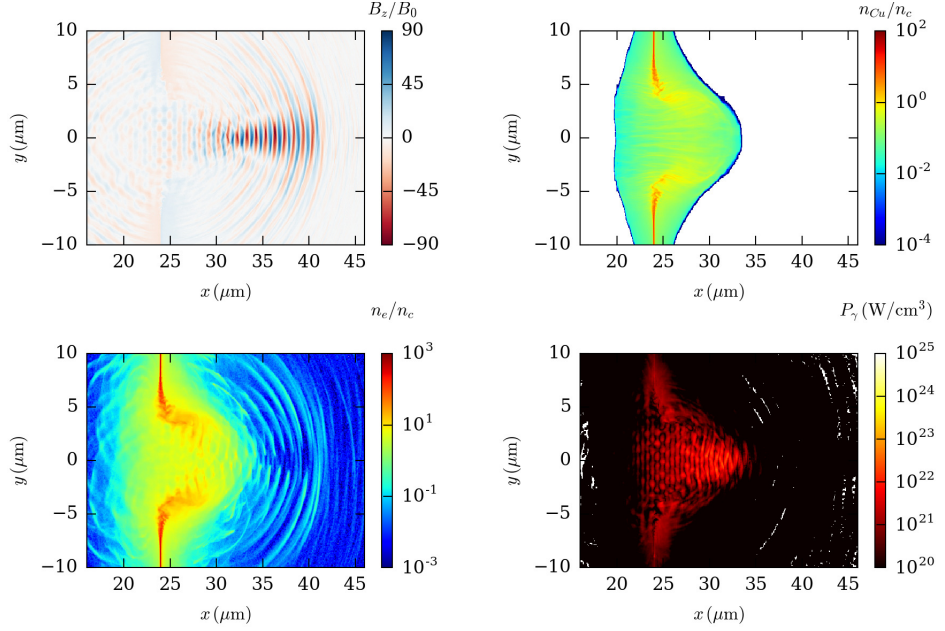


Figure 4.31: 2D simulation of a $l = 32 \text{ nm}$ target. (a) Magnetic field B_z . (b) Ion density n_{Cu} . (c) Electron density n_e . (d) Synchrotron radiated power density P_γ . All quantities are recorded at $t = +63 \text{ fs}$.

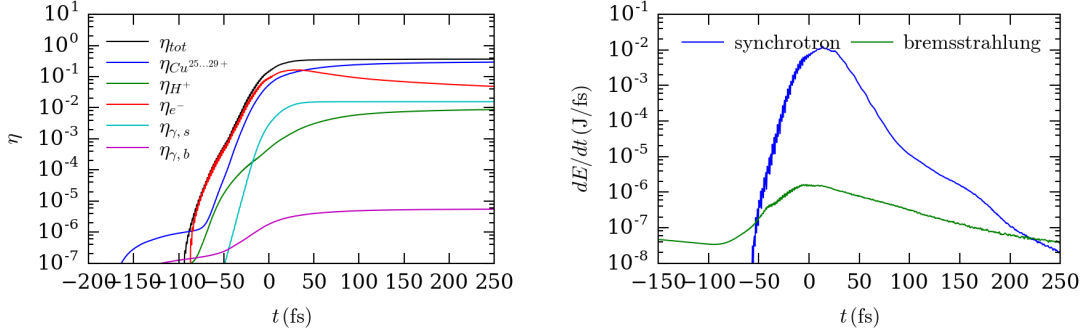


Figure 4.32: 2D simulation of a $l = 32 \text{ nm}$ target. (a) Time evolution of the total kinetic and photon energies normalized to the total injected laser energy. (b) Time evolution of the synchrotron and Bremsstrahlung radiated powers.

rections, and turns increasingly isotropic after the laser peak [Fig. 4.34(b)]. The quasi-isotropy of the resulting time-integrated energy-angle spectrum [4.34(b)] contrasts with the longitudinal emission observed in 1D. The reasons for this are two-fold: (i) While the relativistic electrons accelerated by the laser in the transparent regime have typical momenta $|p_x| \gtrsim |p_y| \gg m_e c$ [Fig. 4.30(a)], they lose more rapidly p_x momentum through driving the ion expansion; (ii) Electrons moving at oblique angles travel across dense Cu regions, and hence their Bremsstrahlung radiated power is enhanced.

4.3.4 Opaque targets

As a first illustration of radiation in the opaque regime, Figs. 4.35-4.36 depict the 1D dynamics of a $0.5 \mu\text{m}$ thick target. During the laser irradiation, both RPA and TNSA

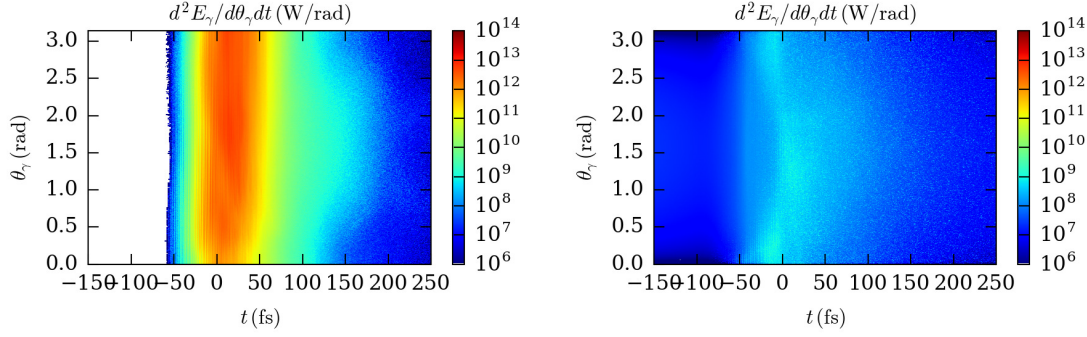


Figure 4.33: 2D simulation of a $l = 32$ nm target. Time evolution of the angle-resolved (a) synchrotron and (b) Bremsstrahlung energy spectra.

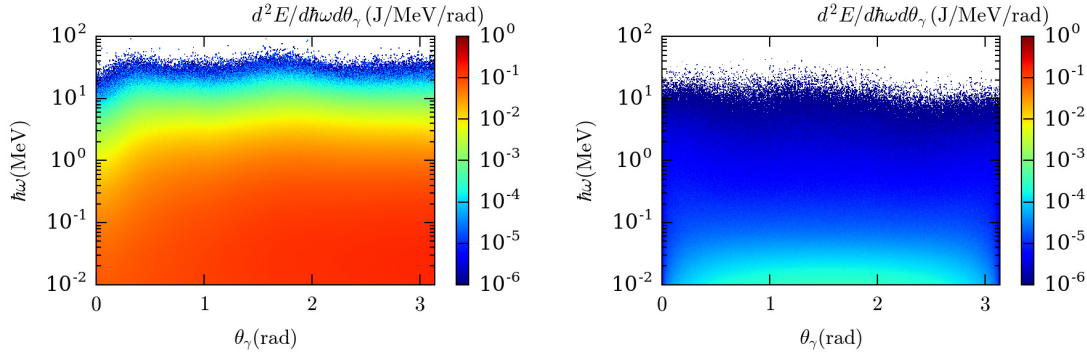


Figure 4.34: 2D simulation of a $l = 32$ nm target. Time-integrated (a) synchrotron and (b) Bremsstrahlung energy-angle spectra.

operate at the front and rear target sides, respectively [Fig. 4.35(a)]. The compression of the target front side associated with RPA is clearly seen in Fig. 4.36(b) at $t = +14$ fs, giving rise to maximum electron and Cu densities as high as $n_e \approx Z^* n_{\text{Cu}} \approx 9 \times 10^3 n_c$ (*i.e.*, about 4 times their initial value). At this instant, the front-side proton layer, which has been accelerated as a whole through RPA, is crossing the backside of the Cu foil, while the TNSA-accelerated rear-side protons are located about $1 \mu\text{m}$ further away. Synchrotron emission takes place in front of the compressed plasma boundary, where electrons are accelerated and/or reflected by the laser field. The resulting synchrotron spectrum shows two broad, forward and backward (slightly dominant) directed emission lobes.

As for $l = 32$ nm (and further shown below for $l = 5 \mu\text{m}$), the longitudinally peaked Bremsstrahlung spectrum [Fig. 4.35(d)] is an artefact of the reduced 1D geometry. A physically meaningful feature, however, is the significant isotropic background that is radiated from the start of the simulation. This signal is due to thermal electrons, and it can be approximated by the formula (Gould, 1980)

$$\frac{dE_{b,th}}{dt} = \left(\frac{32}{3}\right) \sqrt{\frac{2}{\pi}} \alpha r_e^2 Z^2 m_e c^3 l_0 n_{\text{Cu0}} n_{e0} \sqrt{\frac{T_{e0}}{m_e c^2}}, \quad (4.43)$$

where the subscript ‘0’ denotes initial values.

Finally, we describe the case of a $5 \mu\text{m}$ thick target, simulated in 2D geometry. Its dynamics, displayed in Figs. 4.37-4.44, shows the same qualitative behavior as for $l =$

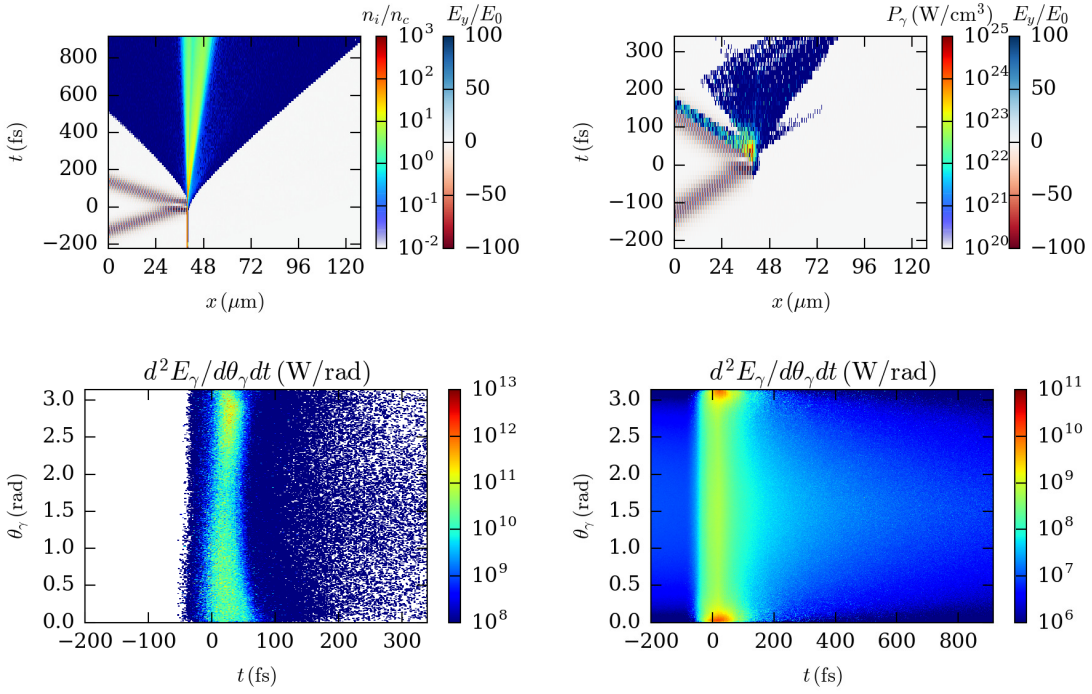


Figure 4.35: 1D simulation of a $l = 0.5 \mu\text{m}$ target. (a) Space-time evolution of the ion density and E_y field. (b) Space-time evolution of the synchrotron radiated power density. Time evolution of the angle-resolved (c) synchrotron and (d) Bremsstrahlung energy spectra.

$0.5 \mu\text{m}$. Most of the Cu ions located at the illuminated front side are pushed forward, while a fraction of them is expanding toward vacuum, as a consequence of escaping high-energy electrons [Figs. 4.38(a,b)]. Plasma expansion is faster at the rear side, where the hot-electron kinetic pressure is not counteracted by radiation pressure. A noticeable difference with thinner targets, which all lead to a rapidly dominant contribution of the Cu ions' kinetic energy to the total laser absorption, is that, up to $t = 250 \text{ fs}$, most of the absorbed laser energy is still carried by electrons [Fig. 4.41(a)]. This is caused by the slower TNSA-type expansion of the target, which essentially remains at solid density over the full simulation time.

Synchrotron photons are mainly radiated just in front of the compressed plasma boundary, where $10 \lesssim n_e/n_c \lesssim 100$ [see Figs. 4.37(d) and 4.38(d)]. Due to electromagnetic field fluctuations, synchrotron emission also arises inside the target bulk, yet with a two orders of magnitude lower power density [Figs. 4.38(d)]. The total synchrotron emission peaks at $t \approx 10 \text{ fs}$, at which time it is mainly forward directed ($\theta_\gamma \approx 0.5 - 1$) [Fig. 4.42(a)]. The backward spectral component abruptly rises by $t \approx 20 \text{ fs}$, *i.e.*, after a two-way transit time of the energetic electrons generated in the laser's rising edge. The time-integrated synchrotron spectrum is mainly concentrated at forward angles, with a secondary maximum in the backward direction [4.43(a)].

Similarly to the $l = 0.5 \mu\text{m}$ target, the Bremsstrahlung spectrum shows a significant signal prior to the interaction, due to thermal electrons in the initially warm Cu layer [Fig. 4.42(b)]. The Bremsstrahlung power increases suddenly during the pulse rise and essentially saturates after the pulse maximum. In such a thick target, the simulation time ($\sim 250 \text{ fs}$) is clearly too short for a quantitative evaluation of the total Bremsstrahlung

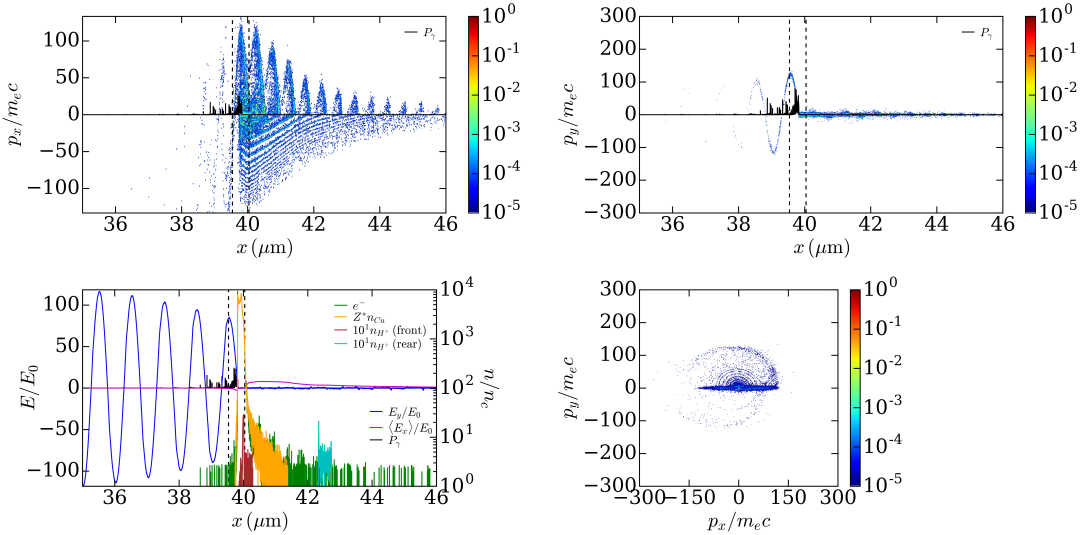


Figure 4.36: 1D simulation of a $l = 0.5 \mu\text{m}$ target. (a) $x - p_x$ electron phase. (b) Spatial profiles of the particle charge densities, E_y and $\langle E_x \rangle$ fields and synchrotron radiated power density. All quantities are recorded at the time of peak synchrotron emission, $t = +14$ fs

yield. As time passes, the Bremsstrahlung spectrum develops a more and more isotropic angular distribution. This behavior stems from the growing average isotropy of the electron distribution. To illustrate this, we plot in Fig. 4.44 the (spatially averaged) longitudinal (T_x) and transverse (T_y) electron temperatures as a function of time. For each quantity, we distinguish between those ('bulk') electrons initially contained in the pre-ionized Cu^{25+} layer and those ('fast') issued from the surface hydrogen layers and subsequent ionization of the Cu ions. As these electron groups are not defined according to their mean energy (or level of thermalization), they do not exactly correspond to the usual co-called thermal ('cold') and suprathermal ('hot') electron populations. Notably, the 'fast' population involves surface electrons directly laser-accelerated to high energies, but also relatively cold secondary electrons from the inner Cu plasma, and so its temperature should greatly underestimate that of the suprathermal electrons. Despite this caveat, we expect that Fig. 4.44 provides a qualitative picture of the electron relaxation dynamics. It can be seen that, for both electron groups, the longitudinal temperature grows initially the fastest. As expected, $T_{x,\text{fast}}$ peaks (at ~ 2 MeV) at the laser maximum, after which it steadily decreases down to ~ 0.7 MeV at $t = 250$ fs. Meanwhile, $T_{y,\text{fast}}$, which is about twice lower at the laser maximum, goes on rising up to $t \approx 70$ fs at which time it overtakes $T_{x,\text{fast}}$, and essentially stagnates later on. At the final time, the anisotropy remains quite weak ($T_{y,\text{fast}}/T_{x,\text{fast}} - 1 \approx 0.4$). This behavior is mainly attributed to preferentially longitudinal momentum losses to the expanding ions. It is more pronounced for the higher-energy electron fraction, as evidenced by the $x - p_x$ and $x - p_y$ electron phase spaces at $t = +7$ fs [Figs. 4.39(a,b)] and $t = 250$ fs [Figs. 4.40(a,b)]. It is clearly seen that the ultrarelativistic electrons ($p/m_ec \gtrsim 50$), initially characterized by $p_x > |p_y|$, develop a strong anisotropy along the transverse direction. For the 'bulk' electrons, T_x and T_y culminate at $t \approx 25$ fs and $t \approx 70$ fs, respectively. Due to collisional scattering off Cu ions, isotropization is reached at $t \approx 90$ fs, and is maintained during the subsequent cooling of the bulk electrons.

As a result, the time-integrated Bremsstrahlung energy-angle spectrum plotted in Fig. 4.43(b) shows a nearly isotropic shape, up to photon energies ~ 1 MeV. By contrast,

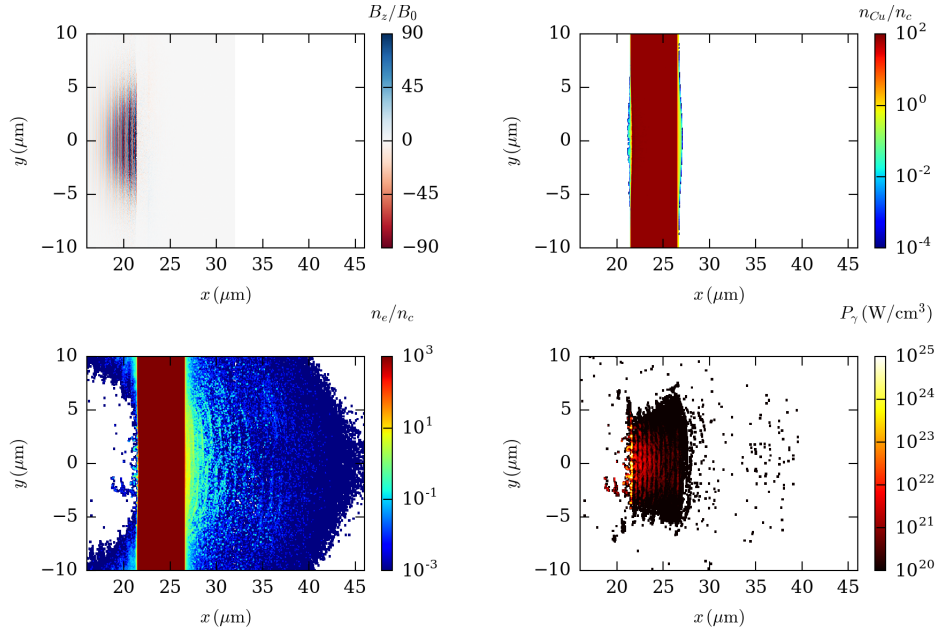


Figure 4.37: 2D simulation of a $l = 5 \mu\text{m}$ target. (a) Magnetic field B_z . (b) Ion density n_{Cu} . (c) Electron density n_e . (d) Synchrotron radiated power density P_γ . All quantities are recorded at $t = +7 \text{ fs}$.

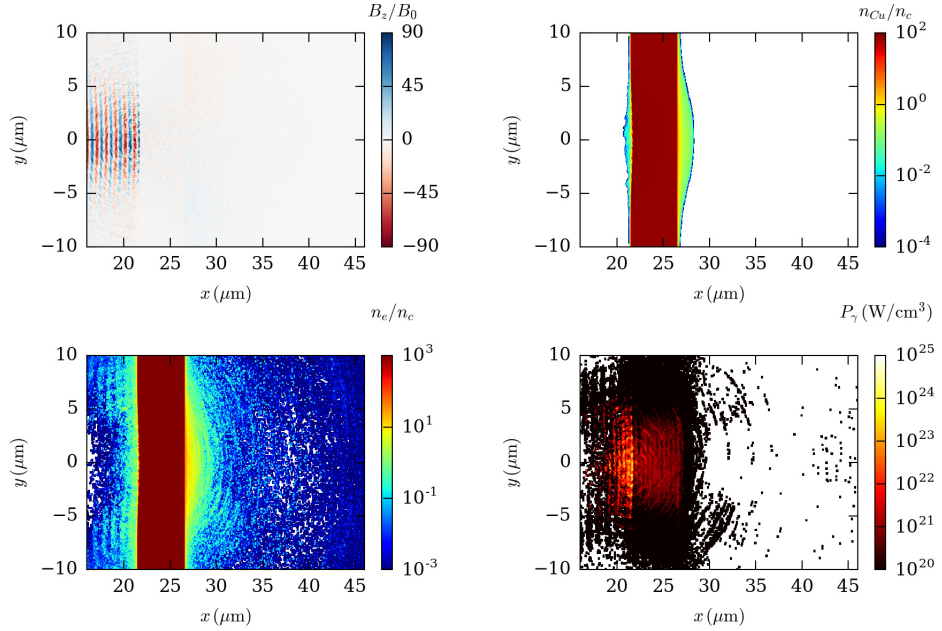


Figure 4.38: Same as in Fig. 4.37 but at $t = +33 \text{ fs}$.

the higher-energy photons, which are emitted by ultrarelativistic electrons (recalling that $\langle \hbar\omega \rangle \approx m_ec^2\gamma/3$), during the first $\sim 50 \text{ fs}$ [Fig. 4.42(b)], appear to be collimated in the longitudinal (forward and backward) directions. Yet they carry only a very weak fraction ($\lesssim 1\%$) of the total Bremsstrahlung energy. The late-time transverse anisotropy of the ultrarelativistic electrons [Fig. 4.40(a,b)] does not lead to a measurable signal because of their much reduced density fraction.

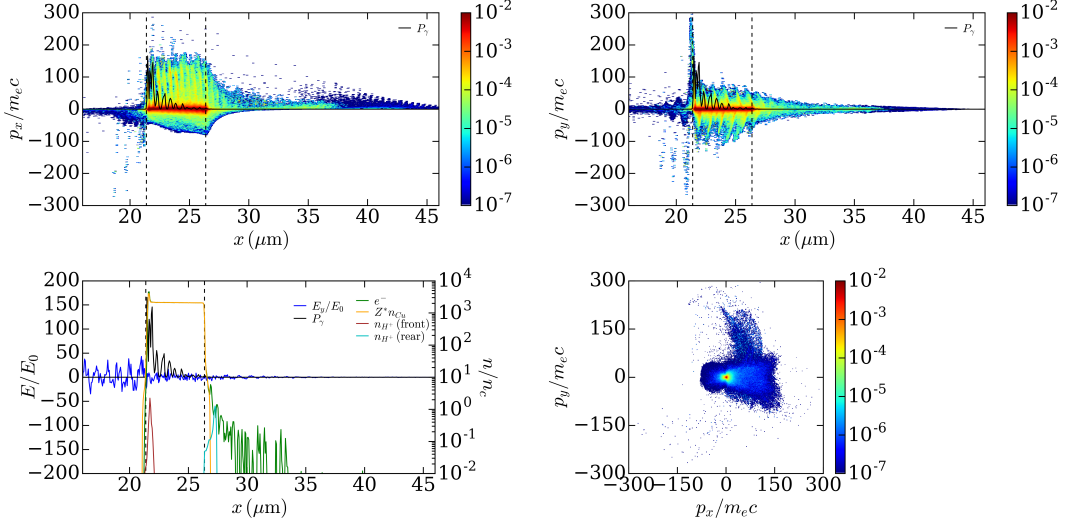


Figure 4.39: 2D simulation of a $l = 5 \mu\text{m}$ target. (a) $x - p_x$ and (b) $x - p_y$ electron phase spaces. (c) Spatial profiles of the particle charge densities, E_y field and synchrotron radiated power density. All quantities are recorded at $t = +7 \text{ fs}$.

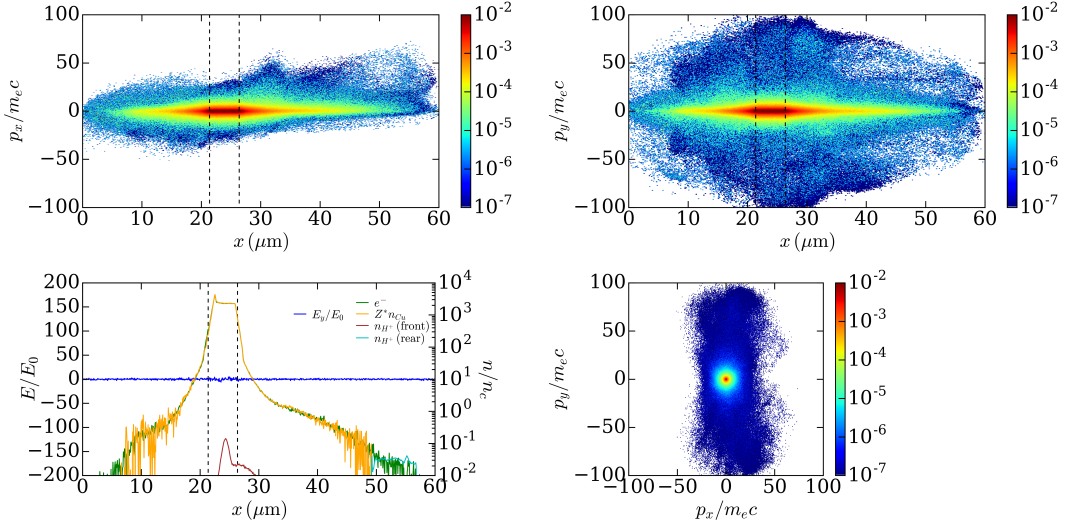


Figure 4.40: 2D simulation of a $l = 5 \mu\text{m}$ target. (a) $x - p_x$ and (b) $x - p_y$ electron phase spaces. (c) Spatial profiles of the particle charge densities, E_y field and synchrotron radiated power density. All quantities are recorded at $t = +250 \text{ fs}$.

4.3.5 Target thickness dependence of the radiation spectra

The radiation spectral properties predicted by our 2D simulations are summarized in Figs. 4.45(a,b) and Figs. 4.46(a,b), which gather the energy and angular spectra characterizing the synchrotron the Bremsstrahlung radiations, respectively. Those graphs further illustrate the trends discussed above.

The synchrotron energy spectra [Fig. 4.45(a)] confirm that the maximum yield is achieved at $l = 32 \text{ nm}$, and is almost reproduced at $l = 51 \text{ nm}$. While the highest photon cutoff energies ($\sim 40 \text{ MeV}$) are observed at these optimal thicknesses, the cutoff energies

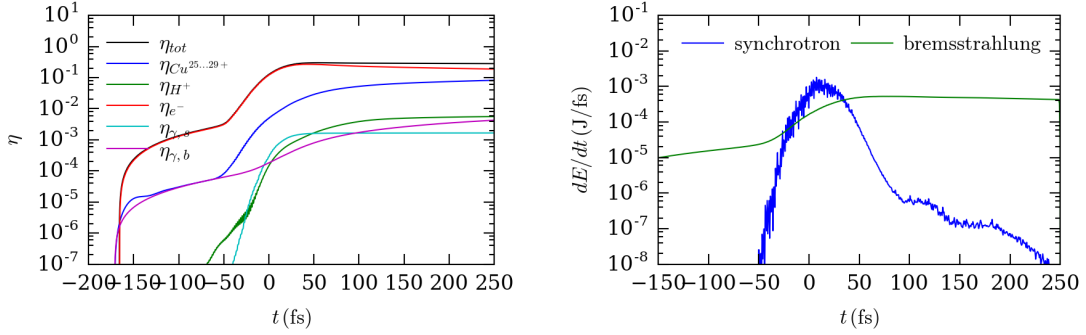


Figure 4.41: 2D simulation of a $l = 5 \mu\text{m}$ target.(a) Time evolution of the total kinetic and photon energies normalized to the total injected laser energy. (b) Time evolution of the synchrotron and Bremsstrahlung radiated powers.

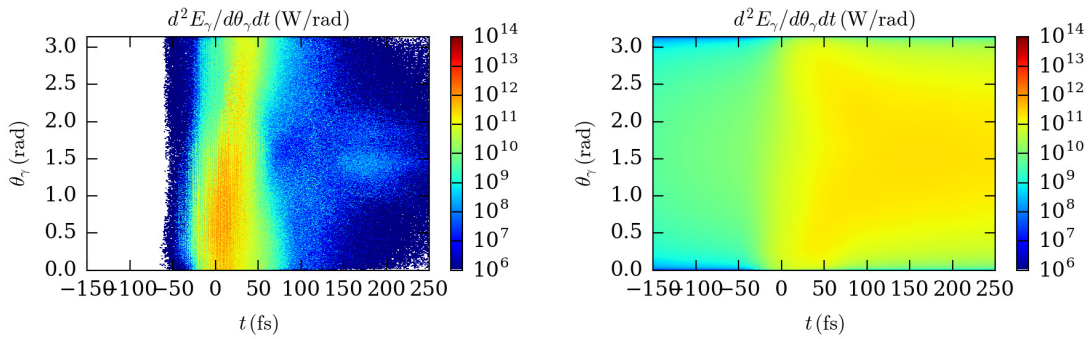


Figure 4.42: 2D simulation of a $l = 5 \mu\text{m}$ target. Time evolution of the angle-resolved (a) synchrotron and (b) Bremsstrahlung energy spectra.

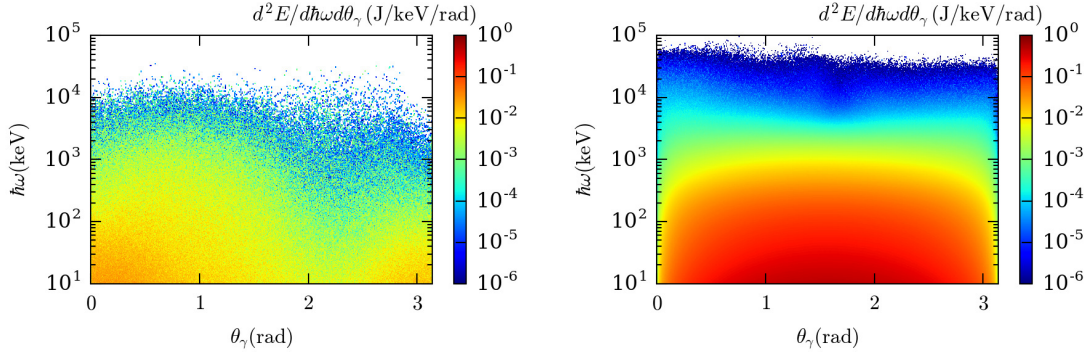


Figure 4.43: 2D simulation of a $l = 5 \mu\text{m}$ target. Time-integrated (a) synchrotron and (b) Bremsstrahlung energy-angle spectra.

produced in either thinner (16 nm) or thicker ($0.5 - 5 \mu\text{m}$) foils are only half lower. Figure 4.45(b) clearly evidences a transition between two distinct angular patterns when the target is made thicker: (i) A dominantly backward/transverse emission at $l = 16 - 51 \text{ nm}$, with an oblique forward lobe emerging at larger l ; (ii) A mainly oblique forward emission at $l = 0.5 - 5 \mu\text{m}$, with a weaker backward lobe, due to refluxing electrons and diminishing at larger l .

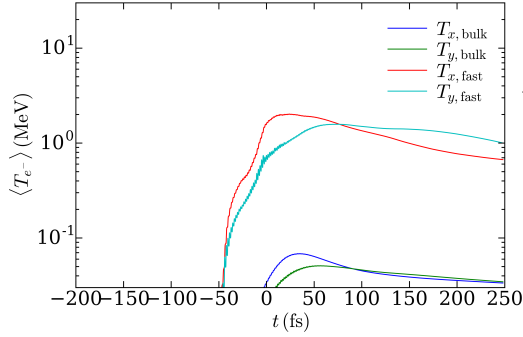


Figure 4.44: 2D simulation of a $l = 5 \mu\text{m}$ target. Time evolution of the longitudinal (T_x) and transverse (T_y) temperatures. We distinguish between the ('bulk') electrons initially contained in the pre-ionized Cu^{2+} layer and the ('fast') electrons originating from the surface hydrogen layers and subsequent ionization of the Cu ions.

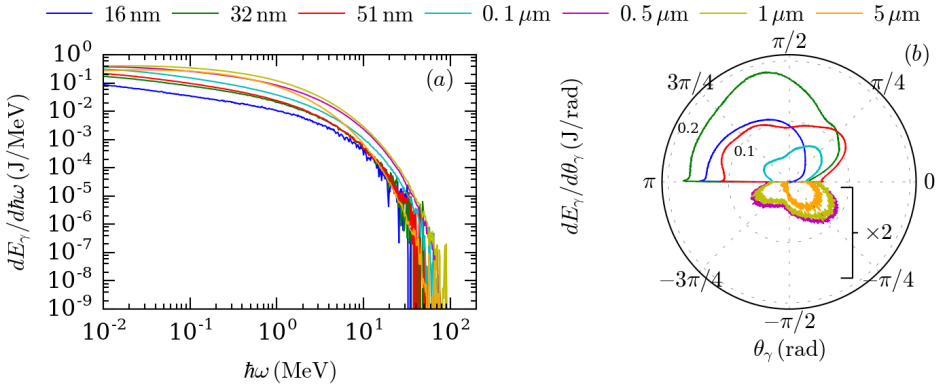


Figure 4.45: Variations of the synchrotron radiation with the target thickness l . (a) Energy-resolved and (b) angle-resolved radiated energy spectra (for $> 10 \text{ keV}$ photon energies). Each color represents a different value of l . All plotted quantities are integrated in time and over the simulation domain. Angles in (b) are defined as $\theta_\gamma = \arccos(k_{\gamma,x}/k_\gamma) \in (0, \pi)$, and the resulting angular distributions are symmetrized with respect to $\theta_\gamma = 0$. For better visibility, a $\times 2$ factor is applied to the $l = 0.5, 1$ and $5 \mu\text{m}$ curves.

The energy spectra displayed in Fig. 4.46(a) evidence the growing trend of the Bremsstrahlung yield with l . The angular distributions are computed in Fig. 4.46(b,c) for two photon groups. The radiation emitted into $\hbar\omega \geq 10 \text{ keV}$ photons is isotropic (or close to isotropic) at all thicknesses, except for $l = 51 \text{ nm}$, where it is maximized in the forward direction. This is due to rapidly isotropized high-energy electrons in nanometric foils, and to the dominant contribution of low- or medium-energy electrons in micrometric foils. By contrast, the radiation emitted by highly relativistic electrons at $\hbar\omega \geq 5 \text{ MeV}$ energies is increasingly directed along the longitudinal direction at larger thickness. This is explained by the fact that those electrons can recirculate a few times across the solid target (hence the forward and backward lobes visible at $l = 5 \mu\text{m}$) before losing longitudinal momentum through ion expansion (slowed down at large l) or collisions.

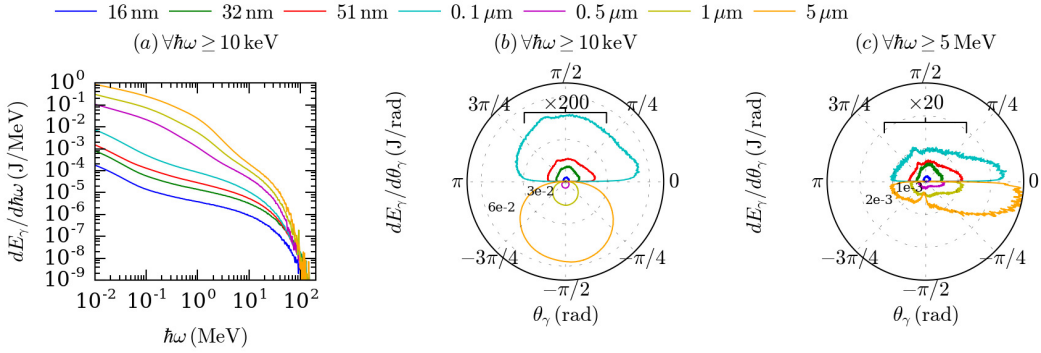


Figure 4.46: Variations of the Bremsstrahlung radiation with the target thickness l . (a) Energy-resolved and (b,c) angle-resolved radiated energy spectra. The angular spectra are shown for photon energies $\hbar\omega \geq 10$ keV in (b) and $\hbar\omega \geq 5$ MeV in (c). Each color represents a different value of l . All plotted quantities are integrated in time and over the simulation domain. For better visibility, a $\times 300$ (resp. $\times 50$) factor is applied to the $l = 16, 32$ and 51 nm curves in (b) [resp. (c)].

4.3.6 Conclusions

To conclude, by means of self-consistent 1D and 2D PIC simulations, we have investigated the Bremsstrahlung and synchrotron emissions driven by a $10^{22} \text{ W cm}^{-2}$ intensity, 50 fs laser pulse focused onto solid copper foils, with thicknesses ranging from a few 10 nm to a few μm . We have examined in great detail the dynamics and spectral properties of both radiation processes, and correlated them with the ultrafast evolution of the energized target electrons and ions. We have found that the synchrotron efficiency is maximized in $\sim 30 - 50$ nm thick foils which, owing to relativistic and expansion effects, transition from being opaque to transparent during the laser pulse. In this interaction regime, the synchrotron emission takes place throughout the expanding bulk plasma, and is dominated by ultrarelativistic electrons counterpropagating against the incoming wave. The rapid drop in plasma densities then leads to very weak Bremsstrahlung radiation. As the target is made thicker and opaque to the laser pulse, both hot-electron generation and synchrotron emission get localized around the target front side. The synchrotron spectrum is then mainly forward directed, yet may also feature a backward lobe mainly due to electron refluxing during the laser irradiation. As the target expands more slowly with larger thickness, the energized electrons experience higher average densities, which enables efficient Bremsstrahlung over longer time scales. While most of the Bremsstrahlung energy into ≥ 10 keV photons is radiated isotropically due to the prevailing contribution of relatively low-energy isotropized electrons, its high-energy (≥ 5 MeV) fraction is emitted within increasingly collimated forward and backward lobes.

Chapter 5

Improving the synchrotron process efficiency with nanowire arrays

Introduction

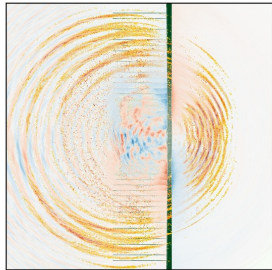


Figure 5.1: γ -ray generation from a nanowire array irradiated by an intense laser as simulated by the PIC code CALDER.

The interaction of an intense laser field with a plasma is known to generate a population of relativistic electrons that can radiate their energy through several mechanisms, as explained in the introduction of Chap. 4. For next generation laser systems ($I \geq 10^{22} \text{ W/cm}^2$) electrons are expected to radiate their energy mostly through the synchrotron process (Zhidkov *et al.*, 2002; Kirk *et al.*, 2009; Ji *et al.*, 2014b; Grismayer *et al.*, 2016; Lobet *et al.*, 2017) rather than the Bremsstrahlung or the radiative relaxation of excited atomic states.

The ultra-short and bright photon sources generated via the laser-induced synchrotron process can be employed for various purposes. The first one is the basic study of the radiation friction force on the electron dynamic in the quantum regime (Blackburn *et al.*, 2014; Ji *et al.*, 2014b; Wang *et al.*, 2015b; Niel *et al.*, 2018). This force is induced by the radiation emitted by a relativistic electron and is experimentally accessible in the collision of a relativistic electron beam and an intense laser pulse. While this experimental scheme has been exploited in previous years to generate hard x-rays and even γ -rays (Phuoc *et al.*, 2012; Chen *et al.*, 2013; Powers *et al.*, 2014; Sarri *et al.*, 2014; Yu *et al.*, 2016; Yan *et al.*, 2017), a clear evidence of radiation reaction in the quantum regime was only recently put forward (Poder *et al.*, 2018; Cole *et al.*, 2018). A second application lies in the anticipation of future experiments involving multi-petawatt lasers. Indeed, the radiative loss suffered by electrons can significantly alter their dynamic and subsequently the relativistic transparency threshold of a plasma (Zhang *et al.*, 2015) or ion acceleration via the Radiative Pressure Acceleration mechanism (Naumova *et al.*, 2009; Bulanov *et al.*, 2010; Tamburini *et al.*, 2012). The third application of γ -rays produced by the synchrotron

process is related to the creation of electron-positron pairs (Bell and Kirk, 2008; Nerush *et al.*, 2011; Ridgers *et al.*, 2012; Ji *et al.*, 2014c; Zhu *et al.*, 2016; Grismayer *et al.*, 2017; Jirka *et al.*, 2017). Such electron-positron jets, clouds or plasmas are present in various scenarios of astrophysical interest. For example, relativistic shocks and magnetic reconnection in active galaxy nuclei or pulsar wind nebulae are held responsible for the generation of nonthermal particles and radiation (Liang, 2013; Lobet *et al.*, 2015; Kagan *et al.*, 2016).

While the range of applications of laser-driven synchrotron sources is wide, only few experiments were successfully conducted to date (Poder *et al.*, 2018; Cole *et al.*, 2018). There is a critical need to gather more data by improving the synchrotron process efficiency, *i.e.* the fraction of laser energy converted into high-energy photons. With uniform plasmas, several radiation regimes have been identified depending on the laser intensity and plasma density. Above the relativistic critical density, an electromagnetic standing wave is formed at the laser-irradiated target front. The resulting synchrotron radiation is referred to as skin depth emission (SDE) regime (Ridgers *et al.*, 2012) and is mainly emitted in a forward-directed cone, yet remains relatively weak (with a $\lesssim 1\%$ conversion efficiency at laser intensities $I \sim 10^{22} \text{ W/cm}^2$). In relativistically near-critical or undercritical plasmas, the radiation is predominantly emitted in the transversally oscillating electron emission (TOEE) regime (Chang *et al.*, 2017) or in the reinjected electron synchrotron emission (RESE) regime (Brady *et al.*, 2012). The radiation yield has been found to be maximized in the RESE regime, with a $\sim 1\%$ conversion efficiency predicted at $I \sim 10^{22} \text{ W/cm}^2$ and 45% at $I \sim 7 \times 10^{23} \text{ W/cm}^2$ (Brady *et al.*, 2014). Strategies to enhance the synchrotron emission or improve its properties have been proposed, taking advantage of preplasmas (Nakamura *et al.*, 2012), plasma channels (Stark *et al.*, 2016; Huang *et al.*, 2017), or structured targets such as gratings (Pan *et al.*, 2015), cone targets (Zhu *et al.*, 2015; Liu *et al.*, 2016; Zhu *et al.*, 2016), clusters (Iwata *et al.*, 2016), micro-plasma waveguides (Yi *et al.*, 2016), or nanowire arrays (Andreev and Platonov, 2016; Lecz and Andreev, 2017; Wang *et al.*, 2018). The purpose of this chapter is to further explore the potential of the latter target type for high-energy synchrotron radiation.

In past years nanowire arrays have been used in several experiments and can be manufactured by an increasing number of laboratories. Because of their particular geometry, nanowire arrays enable a volumetric interaction and strongly increase the absorption of moderately relativistic ($I \sim 10^{17} - 10^{19} \text{ Wcm}^{-2}$) short-pulse lasers into fast electrons. As a result, the temperature of the electrons as well as their number is increased and drives bright Bremsstrahlung or X-ray line emission (Zhao *et al.*, 2010; Ovchinnikov *et al.*, 2011; Mondal *et al.*, 2011; Ivanov *et al.*, 2017), enhances ion acceleration by the Target Normal Sheath Acceleration (Khaghani *et al.*, 2017; Bin *et al.*, 2018), triggers fusion reactions (Curtis *et al.*, 2018) and, above all, enable a volumetric heating ($\sim 1 - 10 \text{ keV}$) of $\sim 10^{23} \text{ cm}^{-3}$ density plasmas (Purvis *et al.*, 2013; Bargsten *et al.*, 2017; Hollinger *et al.*, 2017; Samsonova *et al.*, 2017). The presence of surface return currents also allows for the generation of magneto-static fields which enable long-distance collimated transport of fast electrons (Ji *et al.*, 2010; Chatterjee *et al.*, 2012; Tian *et al.*, 2014). This interesting property of nanowire arrays is of interest in the context of fast ignition (Tabak *et al.*, 1994).

Along with the aforementioned experimental works, a number of PIC simulation studies have examined the dependencies of the laser absorption and fast-electron generation on the nanowire array parameters (Cao *et al.*, 2010b,a; Yi *et al.*, 2016; Lecz and Andreev, 2017; Cristoforetti *et al.*, 2017). These works suggest that the laser absorption can reach values as high as 90% at $I \sim 10^{19}-10^{20} \text{ W/cm}^2$ and interwire spacings in the $\sim 0.1-1 \mu\text{m}$

range. The possibility of triggering betatron electron acceleration in the superimposed laser and quasistatic fields around the wires has also been demonstrated under specific conditions, e.g. a 10^{19} W/cm^2 laser pulse irradiating 60 nm diameter wires (Andreev and Platonov, 2016; Lecz and Andreev, 2017). These trends, revealed at relatively moderate laser intensities, make nanowire arrays promising setups for developing ultraintense synchrotron sources at extreme laser intensities ($I > 10^{22} \text{ W/cm}^2$). Another argument in their favor is that the strong magnetostatic fields they give rise to (Kaymak *et al.*, 2016) may, if sustained long enough, significantly enhance the synchrotron emission compared to that induced by the sole laser field. A similar scenario of synchrotron radiation boosted by quasistatic fields has been numerically evidenced in a plasma channel (Stark *et al.*, 2016).

In this chapter we are eager to study the behavior of nanowire arrays for the forthcoming ultra-intense laser intensities ($I \simeq 10^{21-23} \text{ W.cm}^{-2}$) that are expected to boost the synchrotron emission. In Sec. 5.1 we investigate the electron heating mechanisms under such conditions, thus extending the previous studies conducted at lower intensities (Jiang *et al.*, 2016; Cristoforetti *et al.*, 2017). Section 5.2 illustrates the main plasma processes fostering the synchrotron photon emission in laser nanowire interaction. In Sec. 5.3, we perform a parametric scan by varying the target's characteristics and we analyse the synchrotron emission in light of the processes previously identified. In addition, we compare the performance of nanowire targets with that of uniform plasma of varying density. In Sec. 5.4, we show that placing a solid foil at the backside of the nanowire array can notably increase the photon source efficiency. We also address the changes brought by a finite laser spot size and an oblique incidence angle. Finally preliminary results on ion acceleration with nanowire arrays are presented in Sec. 5.5.

5.1 Preliminary investigation of electron heating

In this Section, we show that the electron heating proceeds through various stages during the interaction of an ultraintense laser pulse with a nanowire array. This is done in light of a reference 2D PIC simulation parameterized as follows.

5.1.1 2D PIC simulation setup

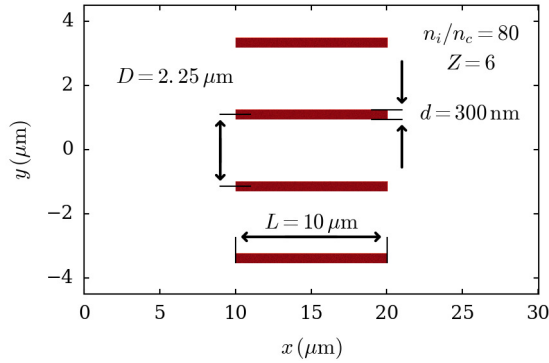


Figure 5.2: Schematic of the reference simulation setup.

The laser pulse is modeled as a planar electromagnetic wave, propagating along the x axis, linearly polarized along the y direction and with a central wavelength $\lambda_0 = 1 \mu\text{m}$. It has a Gaussian temporal profile with a FWHM duration of 30 fs and a peak intensity

$I = 10^{22} \text{ Wcm}^{-2}$ (corresponding to a dimensionless field strength $a_L = 85$). As depicted in Fig. 5.2, the target consists of a periodic array of solid-density carbon nanowires. The carbon atoms, of atomic number $Z = 6$, and mass number $A = 12$, are initially unionized with an atomic density $n_C = 80n_c$ ($n_c \simeq 1.1 \times 10^{21} \text{ cm}^{-3}$ is the nonrelativistic critical density). The wires have a length $L = 10 \mu\text{m}$, a width (diameter in 3D) $d = 0.3 \mu\text{m}$ and the interwire spacing is $D = 2.25 \mu\text{m}$. The wire width is equal to that considered by [Kaymak et al. \(2016\)](#), where it was shown to give rise to strong quasistatic fields at $I = 5 \times 10^{21} \text{ Wcm}^{-2}$ (for circular polarization). The absence of a substrate at the backside of the wires, which could absorb and reflect the laser pulse, allows us to isolate the effects induced by the sole wires. The simulation domain has dimensions $L_x \times L_y = 30 \mu\text{m} \times 9 \mu\text{m}$, with a spatial resolution $\Delta x = \Delta y = \lambda_0/210$. The temporal resolution is $\Delta t = \tau_0/314$ (where $\tau_0 = \lambda_0/c = 3.3 \text{ fs}$ is the optical cycle) and the simulation is run over $25\,000\Delta t$. The boundary conditions are taken to be absorbing along x and periodic along y for both fields and particles, and 50 macro-particles per cell and per species are used. The peak of the laser pulse hits the tips of the wires at time $t = 0$.

Section	$I (\text{W}/\text{cm}^2)$	Z	inter-spacing D	thickness d	length L
Sec. 5.3.1	10^{22}	6	$0 \rightarrow 9 \mu\text{m}$	300 nm	$10 \mu\text{m}$
Sec. 5.3.2	10^{22}	6	$1 \mu\text{m}$	$15 \text{ nm} \rightarrow 1 \mu\text{m}$	$10 \mu\text{m}$
Sec. 5.3.3	10^{22}	6, 29, 79	$1 \mu\text{m}$	36 nm	$10 \mu\text{m}$
Sec. 5.3.3	$10^{21} \rightarrow 10^{23}$	6	$1 \mu\text{m}$	100 and 300 nm	$10 \mu\text{m}$

Table 5.1: Overview of the parametric scan performed in Sec. 5.1 (hot electron generation) and Sec. 5.3 (photon generation). All other parameters are detailed in those sections.

This illustrative simulation, as every other performed in this study, takes into account Coulomb binary collisions between charged particle species, field and impact ionization and synchrotron radiation. The synchrotron module implemented in CALDER by [Lobet et al. \(2016\)](#) combines a continuous radiation reaction model by [Sokolov et al. \(2009\)](#) for electrons with a low quantum parameter ($\chi_e \leq 10^{-3}$) and a stochastic quantum description by [Duclous et al. \(2011\)](#) for electrons with a higher quantum parameter ($\chi_e \geq 10^{-3}$). We recall that the electron quantum parameter, which determines the radiation characteristics, is defined as $\chi_e = \gamma[(\mathbf{E}_\perp + \mathbf{v} \times \mathbf{B})^2 + E_\parallel^2/\gamma^2]^{1/2}/E_S \simeq \gamma|\mathbf{E}_\perp + \mathbf{v} \times \mathbf{B}|/E_S$, where \mathbf{v} is the electron velocity, γ its Lorentz factor, \mathbf{B} is the magnetic field, \mathbf{E}_\parallel is the electric field component parallel to \mathbf{v} , \mathbf{E}_\perp the electric field component normal to \mathbf{v} , and $E_S = m_e^2 c^3 / \hbar e = 1.3 \times 10^{18} \text{ Vm}^{-1}$ is the Schwinger field. The chosen threshold value between the classical and quantum regimes ($\chi_e = 10^{-3}$) is quite arbitrary, yet ensures that the quantum regime is accurately described. Bremsstrahlung emission, pair production from Breit-Wheeler and Bethe-Heitler processes are not simulated for the moment. Since we are not interested in pair creation and in order to reduce the computational load, the radiated photons are not advanced on the simulation grid (but their energy and emission angle are recorded).

5.1.2 Evidence of different electron heating mechanisms with nanowires

In this subsection we show three different electron heating/acceleration mechanisms one can identify during laser nanowire-array interaction. We emphasize that electron heating can be achieved by the ponderomotive force of the laser or take place in the Relativistically Self-Induced Transparency (RSIT) regime and even through Direct Laser Acceleration

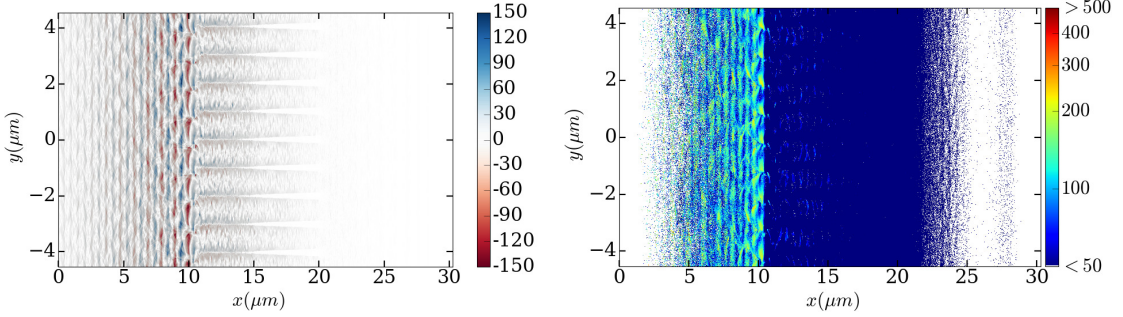


Figure 5.3: (a) Laser field distribution (B_z/B_0 , red/blue colorbar); (b) Lorentz factor at time $t = 13 \text{ fs}$. The copper wires ($n_e/n_c = 480$) are characterized by a spacing of $D = 1 \mu\text{m}$, a width of $d = 300 \text{ nm}$ and a length of $L = 10 \mu\text{m}$. The laser peak intensity is 10^{22} W/cm^2 ($a_L = 85$).

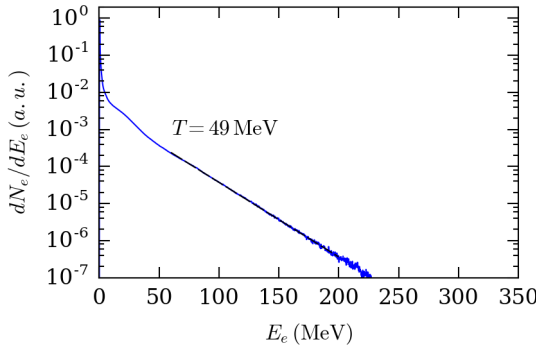


Figure 5.4: Energy-resolved electron spectra for wires expanding to a relativistically over-critical plasma and blocking the laser propagation. The copper wires ($n_e/n_c = 480$) are characterized by a spacing of $D = 1 \mu\text{m}$, a width of $d = 300 \text{ nm}$ and a length of $L = 10 \mu\text{m}$ (average density $n_{av}/n_c \simeq 144$). The laser peak intensity is 10^{22} W/cm^2 ($a_L = 85$).

(DLA) if the nanowire array geometry is well-chosen.

The first case we study is exemplified in Fig. 5.2, except we use a wire spacing $D = 1 \mu\text{m}$. The wire width is $d = 300 \text{ nm}$ and their length is $L = 10 \mu\text{m}$. The laser pulse front can propagate between the wires and accelerate electrons from the wire's edges. This tends to rise the electron density between the wires. We estimate from field reflection and plasma density levels that the electron density between the wires becomes relativistically overcritical to the laser field for $t \geq -10 \text{ fs}$ (before the pulse peak on target). Most of electron heating takes place after this time and is illustrated in Fig. 5.3(a), 13 fs after the arrival of the pulse peak on the nanowires. One can see that the laser pulse (of normalized intensity $a_L = 85$) is indeed reflected at the beginning of the wires, located at abscissa $x = 10 \mu\text{m}$. Parallel to this in Fig. 5.3(b), we represent the Lorentz factor of electrons above 25 MeV. Electron heating takes place in the preplasma formed in front of the wires (between abscissa 5 and $10 \mu\text{m}$) and in the plasma skin depth (at an abscissa of $10 \mu\text{m}$). Electron bunches accelerated forward by the ponderomotive force can propagate between the wires and one can note their trace between abscissa 10 and $15 \mu\text{m}$. They are not very visible since their length is comparable to the diagnostic resolution along x axis (3 mesh cells along x axis). The energy-resolved spectra of electrons at time $t = 13 \text{ fs}$ displayed in Fig. 5.4 is best-fitted with a Maxwellian distribution of temperature 49 MeV. This value

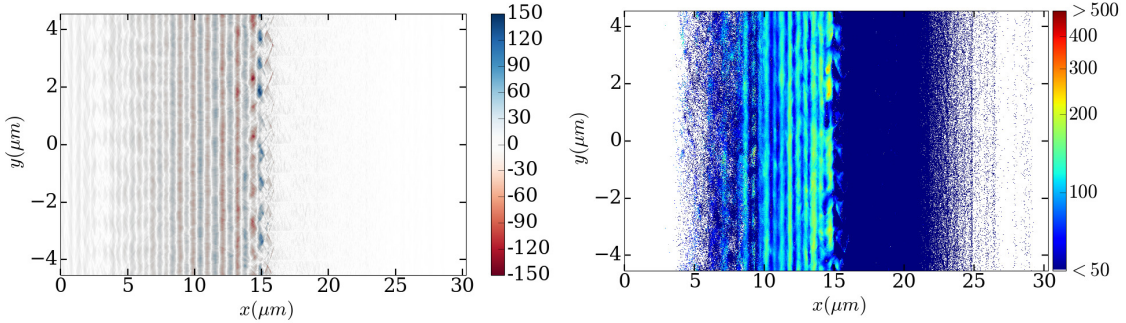


Figure 5.5: (a) Laser field distribution (B_z/B_0 , red/blue colorbar); (b) Lorentz factor at time $t = 13 \text{ fs}$. The copper wires ($n_e/n_c = 480$) are characterized by a spacing of $D = 1 \mu\text{m}$, a width of $d = 36 \text{ nm}$ and a length of $L = 10 \mu\text{m}$ (average density $n_{av}/n_c \simeq 17$). The laser peak intensity is 10^{22} W/cm^2 ($a_L = 85$).

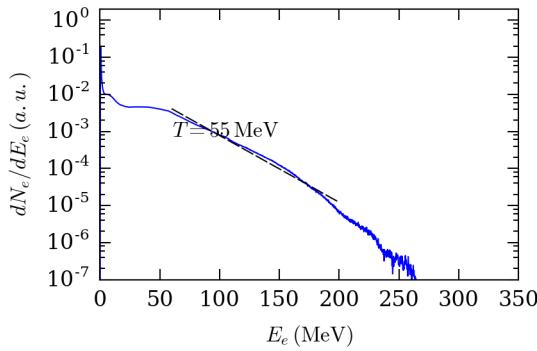


Figure 5.6: Energy-resolved electron spectra for wires expanding on the laser pulse time scale to a relativistically undercritical plasma of average density $n_{av}/n_c \simeq 17$. The copper wires ($n_e/n_c = 480$) are characterized by a spacing of $D = 1 \mu\text{m}$, a width of $d = 36 \text{ nm}$ and a length of $L = 10 \mu\text{m}$. The laser peak intensity is 10^{22} W/cm^2 ($a_L = 85$).

falls within the range provided by the scaling of [Wilks *et al.* \(1992\)](#): $(\sqrt{1 + a_L^2} - 1)mc^2 = 43 \text{ MeV}$ and the one from [Haines *et al.* \(2009\)](#): $(\sqrt{1 + \sqrt{2}a_L^2} - 1)mc^2 = 51 \text{ MeV}$. Those scalings are derived for lower laser intensities and overcritical planar targets but they still provide a good estimate in our case. This comes from the fact that most of the laser pulse interacts with a relativistically overcritical plasma generated by the early expansion of the wire's.

The second electron heating regime observed takes place for thin wires. We now consider wires with a width $d = 36 \text{ nm}$ and keep the spacing $D = 1 \mu\text{m}$ and the length $L = 10 \mu\text{m}$. The electron density in the wires is still $n_e/n_c = 480$, such that the average density of electrons is relativistically undercritical ($n_{av}/a_L n_c \simeq 0.2$). In this particular regime of thin wires, all electrons are removed from the wires by the laser pulse front ramp and form a plasma layer of modulated density of average value $n_{av}/n_c \simeq 17$. Since this density is below the relativistic transparency threshold, the laser pulse can propagate as seen in Fig. 5.5(a) where we represent the laser field distribution. One can note that at time $t = 13 \text{ fs}$ it has propagated $5 \mu\text{m}$ deep in the plasma which is initially located between abscissa 10 and $20 \mu\text{m}$. This regime is significantly different from the previous one. Indeed the strong field heats the whole plasma volume (see Fig. 5.5(b)) instead of

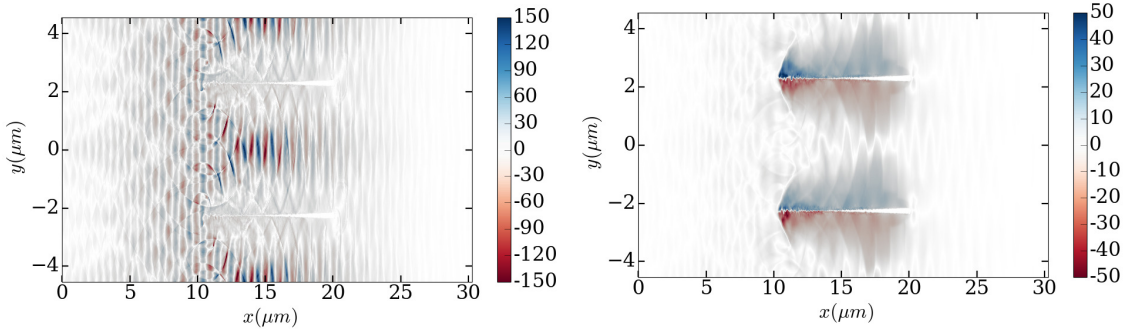


Figure 5.7: (a) Laser field distribution (B_z/B_0 , red/blue colorbar); (b) Laser-cycle averaged $\langle B_z \rangle / B_0$ field at time $t = 13$ fs. The copper wires ($n_e/n_c = 480$) are characterized by a spacing of $D = 4.5 \mu\text{m}$, a width of $d = 300 \text{ nm}$ and a length of $L = 10 \mu\text{m}$. The laser peak intensity is 10^{22} W/cm^2 ($a_L = 85$).

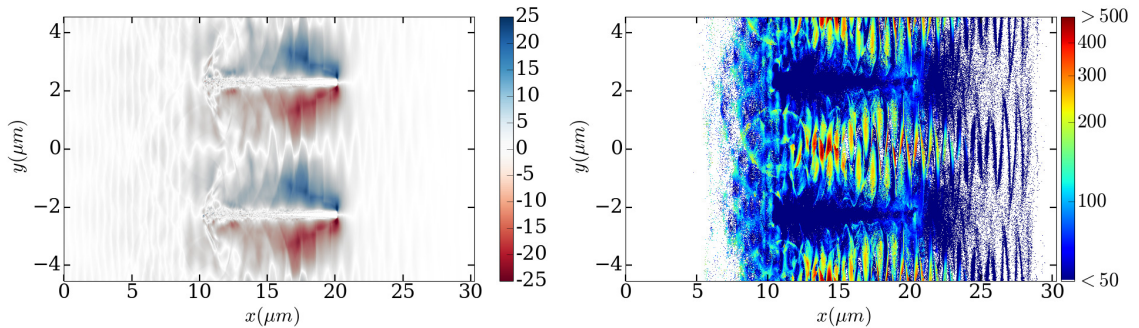


Figure 5.8: (a) Laser-cycle averaged $\langle E_y \rangle / E_0$ field and (b) Lorentz factor at time $t = 13$ fs. The copper wires ($n_e/n_c = 480$) are characterized by a spacing of $D = 4.5 \mu\text{m}$, a width of $d = 300 \text{ nm}$ and a length of $L = 10 \mu\text{m}$. The laser peak intensity is 10^{22} W/cm^2 ($a_L = 85$).

just a preplasma and the skin depth. The fraction of electrons with a high energy is therefore higher in the transparency case than in the opacity one as seen by comparing Figs. 5.4 and 5.6. This energy-resolved electron spectra in the RSIT regime attests that the electron temperature is 55 MeV, which is not significantly higher than in the opacity regime (49 MeV) given the uncertainty related to the fitting procedure. The cutoff value of electron energy corroborates the idea of a better acceleration in the RSIT regime than in the opacity one since it is 15% higher ($\simeq 220 \rightarrow 260$ MeV).

The third process identified is Direct Laser Acceleration (DLA). To observe this, we consider a nanowire array with a large spacing $D = 4.5 \mu\text{m}$ a wire width $d = 300 \text{ nm}$ and a length $L = 10 \mu\text{m}$. For this configuration, they are only two nanowires in the simulation domain and the laser pulse (wavelength $\lambda_0 = 1 \mu\text{m}$) can propagate between them. We first describe the electron acceleration and then explain why it can be interpreted as DLA. The laser propagation is illustrated in Fig. 5.7(a) at time $t = 13$ fs. The pulse is deflected because of the wires expansion but it is mainly transmitted. Electrons are transversally accelerated by the E_y component of the laser field and re-directed in the $+x$ direction by its B_z component. They are therefore injected in the laser pulse with a velocity close to c and in the same direction as the laser pulse. They are extracted from the thin layer of the wire's edge that experiences the laser field. This particular localization of the electron depletion generates a return current localized in the wires' edge, generating a quasistatic magnetic field $\langle B_z \rangle$ observed in Fig. 5.7(b). The amplitude of this field is

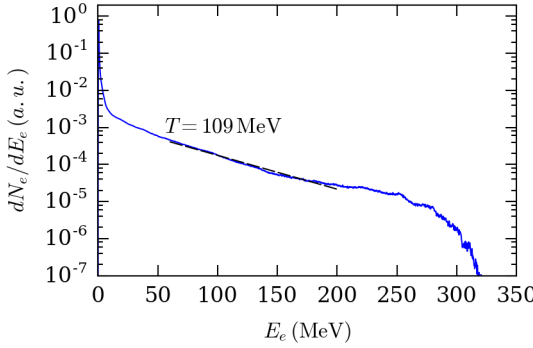


Figure 5.9: Energy-resolved electron spectra showing a super-ponderomotive population of electrons. The copper wires ($n_e/n_c = 480$) are characterized by a spacing of $D = 4.5 \mu\text{m}$, a width of $d = 300 \text{ nm}$ and a length of $L = 10 \mu\text{m}$ (average density $n_{av}/n_c \simeq 32$). The laser peak intensity is 10^{22} W/cm^2 .

obtained by averaging the magnetic field over a laser period and is comparable to the laser field amplitude $\langle B_z \rangle / B_0 a_L \simeq 0.6$. This strong quasistatic field surrounds the wires and tends to pinch them as seen between abscissa 10 and $15 \mu\text{m}$. The charge separation created by the sudden electron extraction from the wires edges also generates a strong electrostatic field $\langle E_y \rangle$ observed in Fig. 5.8(a). Its amplitude is lower than the $\langle B_z \rangle$ field but reaches a significant fraction of the laser field amplitude $\langle E_y \rangle / a_L \simeq 0.3$.

Having this picture of the electron acceleration in the case of a large interspacing one can draw a parallel with DLA. The basic idea consists in dropping an electron in a laser pulse and continuously accelerates it, which we observe in our simulations. This acceleration is efficient only if the electron can keep an adequate phase with the laser pulse. Keeping this phase-match condition on a long distance requires to inject electrons with a velocity close to c and to maintain their velocity parallel to the laser pulse propagation direction. In order to achieve this, some solutions have been suggested. In the specific case of a plasma channel (Arefiev *et al.*, 2012), the transverse electrostatic field is shown to limit the electron dephasing and to generate superponderomotive electrons. In our case, we observe such transverse electrostatic fields as well as magnetostatic fields in Fig. 5.7(b) and Fig. 5.8(a). However, the wires are quite short and therefore limit the propagation distance of electrons. A first evidence of the presence of DLA is illustrated in Fig. 5.8(b). Most energetic electrons ($\gamma_e \geq 400$) overlap with the laser field as expected in the DLA mechanism (see Fig. 5.7(a)). Another strong evidence of the presence of DLA comes from the super-ponderomotive electron population observed in the energy-resolved spectra in Fig. 5.9. They reach a temperature of 109 MeV and cutoff energies of 320 MeV. This temperature is the double of the ponderomotive scaling ($\simeq 50 \text{ MeV}$) and this high energy electron exceeds by 50% the one reached in the opaque regime.

5.1.3 Dependence of electron heating on the nanowire parameters

We detailed three mechanisms of electron heating/acceleration for three particular nanowire array geometries. We now adopt a more general perspective and report which one prevails depending on the wire parameters. To this purpose, the variations of $\langle \gamma_e \rangle$ with the nanowire parameters are shown in Figs. 5.10 and 5.11. For each simulation, we report the average kinetic energy of fast electrons ($> 0.511 \text{ MeV}$) when it reaches its maximum, close to time $t \simeq 0 \text{ fs}$.

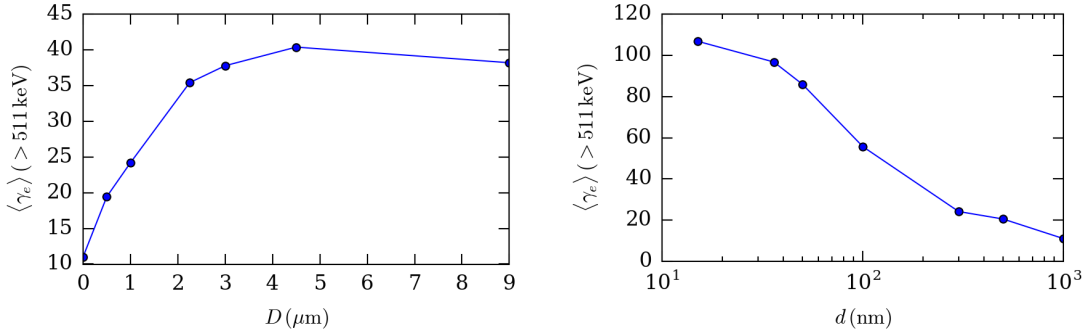


Figure 5.10: Scalings of the fast electron ($> 511 \text{ keV}$) average energy as a function of (a) nanowire spacing; (b) nanowire width. For each panel the nanowire array parameters are detailed in the text.

We start from the reference setup presented in Fig. 5.2 and first vary the nanowire spacing D in the range $D = 0.5 - 9 \mu\text{m}$ [Fig. 5.10 (a)]. We observe a clear correlation between the rise of the average electron energy and of the wires' spacing. The reason is that for a large spacing, electrons can be stuck in phase with the laser field and be continuously accelerated in a DLA regime as shown previously in Sec. 5.1.2. This phenomenon is quite robust since the average kinetic energy remains around $\simeq 40 \text{ MeV}$ as long as the wires' spacing is above $2.25 \mu\text{m}$. This value does not match the one seen in Fig. 5.9 since we include lower electron energies in the average switching from an interval $\gamma_e \geq 2$ to $120 < \gamma_e < 400$. This acceleration process prevails provided that the transverse spacing between the wires is large enough ($\geq 2 \mu\text{m}$ in this case) as observed in Fig. 5.10(a). In the laser intensity range $10^{18} - 10^{21} \text{ W cm}^{-2}$, it was shown that increasing the wire spacing enables the electrons to reach higher energies (Jiang *et al.*, 2016; Lecz and Andreev, 2017; Cristoforetti *et al.*, 2017)). Our results partially corroborate this behavior at $I = 10^{22} \text{ W cm}^{-2}$: the mean energy of the electrons above 511 keV is found to increase from $\langle E_e \rangle = m_e c^2 \langle \gamma \rangle \simeq 5 \text{ MeV}$ at $D = 0$ to $\langle E_e \rangle \simeq 15 \text{ MeV}$ at $D = 2.25 \mu\text{m}$. At larger spacings, $2.25 \leq D \leq 9 \mu\text{m}$, the mean hot-electron energy is found to saturate at $\langle E_e \rangle \simeq 20 \text{ MeV}$. We recall that those values are lower than the ponderomotive scaling $\simeq 40 \text{ MeV}$ evidenced by Wilks *et al.* (1992) since we consider not only the most energetic electrons ($E_e > 50 \text{ MeV}$) but also moderately relativistic ones ($E_e > 0.511 \text{ MeV}$) which are more numerous. Rising the threshold to 50 MeV , one finds $\langle E_e \rangle \simeq 120 \text{ MeV}$ for $D \geq 2.25 \mu\text{m}$.

We fix the spacing at $D = 1 \mu\text{m}$ and vary the nanowire's width d in the range $d = 15 - 500 \text{ nm}$. As we will see in Sec. 5.3 this choice maximizes the synchrotron efficiency. The average kinetic energy of electrons is reported in Fig. 5.10 (b) and attests for a clear increase as the wires get thinner. We already identified previously in Sec. 5.1.2 that for thin wires ($d = 36 \text{ nm}$, $n_{av}/n_c = 17$) the laser can propagate in the RSIT regime and lead to a volumetric heating. This mechanism was shown to be more efficient than for thicker wires ($d = 300 \text{ nm}$, $n_{av}/n_c = 144$) where the plasma expands to a relativistically overcritical density level and leads to a less efficient ponderomotive surface heating.

We now keep the spacing $D = 1 \mu\text{m}$ and fix the wires' width to $d = 36 \text{ nm}$. This geometry will be observed to maximize the synchrotron efficiency in Sec. 5.3. We then change the ion mass from carbon ($n_i = 80 n_c$) to copper ($n_i = 80 n_c$) and gold ($n_i = 60 n_c$) and measure the average kinetic energy of electrons in Fig. 5.11 (a). In all cases the target atoms are almost completely ionized: the mean ionization degree attains $Z^* \simeq 6$ in C, $Z^* \simeq 29$ in Cu and $Z^* \simeq 70$ in Au. This implies a strong rise of the expanded electron

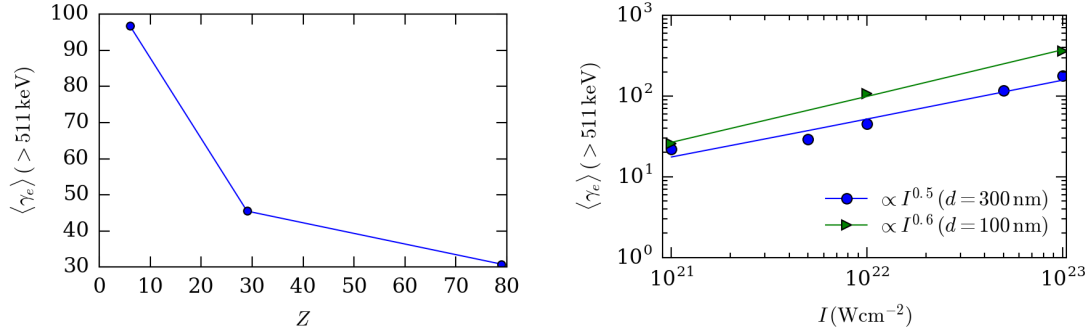


Figure 5.11: Scalings of the fast electron ($> 511 \text{ keV}$) average energy as a function of (a) ion mass; (b) laser intensity. For each panel the nanowire array parameters are detailed in the text.

density $n_{e,av} = 15 \rightarrow 200n_c$ when one rises the atomic number $Z = 6 \rightarrow 79$. Therefore, regarding the laser interaction, we observe a transition between RSIT for carbon to a highly overcritical plasma for gold. In the RSIT regime, the electron heating takes place in the whole plasma volume, which explains the rather high average kinetic energy ($\simeq 50 \text{ MeV}$). In the overdense plasma the heating by the ponderomotive force is confined into the plasma skin-depth and preplasma, consequently leading to lower average kinetic energies ($\simeq 15 \text{ MeV}$).

We are finally interested in the scaling of the average electron energy as a function of laser intensity. We consider wires with a spacing $D = 1 \mu\text{m}$, a length $L = 10 \mu\text{m}$ and a width $d = 100$ or 300 nm . The variations of the mean hot-electron energy $\langle E_e \rangle$ (counting all electrons above 0.511 MeV) as a function of the laser intensity is highlighted in Fig. 5.11(b) for the wire widths $d = 100 \text{ nm}$ (green triangles) and $d = 300 \text{ nm}$ (blue circles). Both curves are consistent with an approximate scaling $\langle E_e \rangle \propto I^{0.5-0.6}$, quite close to the fit $\langle E_e \rangle \propto I^{0.4}$, reported at lower intensities ($10^{18} \leq I \leq 3 \times 10^{20} \text{ Wcm}^{-2}$) by Cao *et al.* (2010a). The fact that $\langle E_e \rangle$ roughly obeys the well-known ponderomotive law of Wilks *et al.* (1992) for $d = 300 \text{ nm}$ can be understood since, the expanded plasma ($n_{av}/n_c = 144$) becomes overcritical over the whole range of laser intensity $10^{21} \leq I \leq 10^{23} \text{ W/cm}^2$. For $d = 100 \text{ nm}$ one should take the scaling with caution since it only relies on three points. For $I = 10^{23} \text{ W/cm}^2$ we observe a significant laser transmission whereas for $I = 10^{21}$ and 10^{22} W/cm^2 it is negligible and the laser mainly interacts with an overcritical density plasma. This regime of opacity can once again explain why the scaling obtained is so close to the ponderomotive one.

5.2 Identification of the main synchrotron radiation regimes

This section focuses on the plasma processes underpinning the synchrotron photon generation. The simulation setup is the one presented in Sec. 5.1.1, that is, wires are spaced by a period of $D = 2.25 \mu\text{m}$, their width is $d = 300 \text{ nm}$, their length is $L = 10 \mu\text{m}$ and are composed of carbon ions at solid density $n_i = 80n_c$.

We recall that since we run 2D simulations, all quantities describing the spectral properties of the photons are obtained per unit length of the third dimension $z (\text{m})$ but are normalized per μm of transverse direction. This choice is convenient since the usual focal spots of such lasers have a few microns length. For example in Fig. 5.16(a), the ordi-

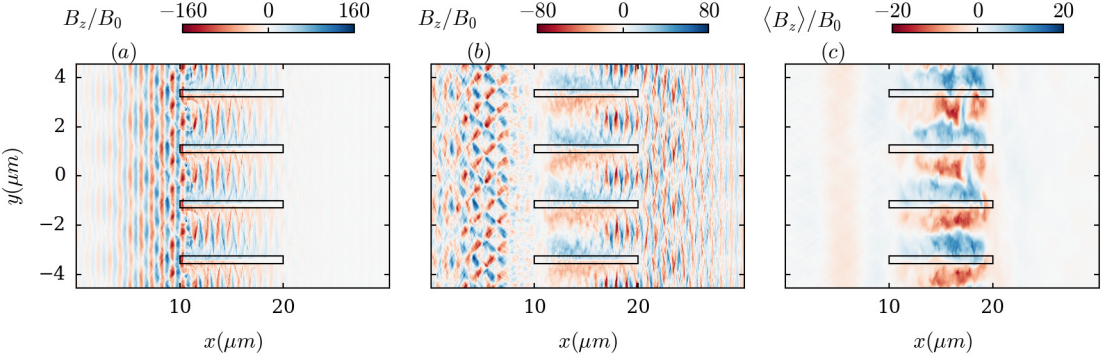


Figure 5.12: Maps of the magnetic field B_z (normalized to $B_0 = m_e \omega_0 / e \simeq 1.1 \times 10^4$ T) at three different times: (a) $t = 8$ fs (during plasma filling of the interstices), (b) $t = 40$ fs (after the left-hand side of the plasma-filled interstices have become opaque to the laser) and (c) $t = 167$ fs (final simulation time). The peak of the laser pulse hits the wire tips at $t = 0$. Panel (c) displays the magnetostatic field, $\langle B_z \rangle$, averaged over an optical cycle. The black rectangles plot the initial location of the wires.

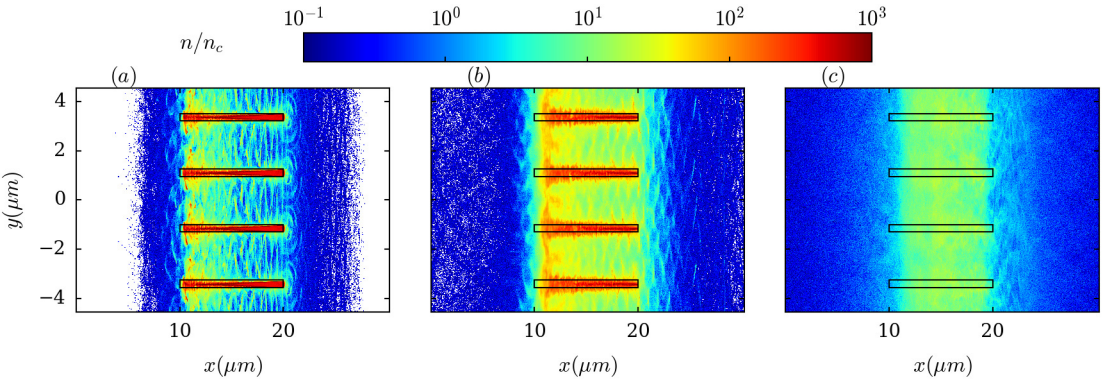


Figure 5.13: Maps of the electron density n_e (normalized to the nonrelativistic critical density $n_c \simeq 1.1 \times 10^{21} \text{ cm}^{-3}$) at (a) $t = 8$ fs and (b) $t = 40$ fs. Panel (c) displays the ion density n_i at $t = 167$ fs (final simulation time).

inate axis is in W/rad but corresponds to W/rad/μm of transverse direction. Similarly in Fig. 5.16(b), the ordinate axis is in J/MeV but corresponds to J/MeV/μm of transverse direction. The same rule applies for all figures representing spectral properties of the photons in the following sections of this chapter.

Figures 5.12(a-c) display maps of the magnetic field (B_z) at three successive times, visualizing the penetration of the laser wave through the interwire gaps and the generation of quasistatic fields. The magnetic field is normalized to $B_0 = m_e \omega_0 / e = 1.1 \times 10^4$ T (where m_e is the electron mass, e is the elementary charge, and ω_0 is the laser angular frequency). The expansion dynamics of the wires is illustrated by the electron and ion density maps shown in Figs. 5.13(a-c). At the beginning of the interaction, the electrons are pulled over a $\sim 1 \mu\text{m}$ distance from the wire surface by the E_y component of the laser field, and accelerated in the forward direction by its B_z component. As a result, the interwire gaps are filled with a population of energized electrons bunched at the laser wavelength λ_0 . Figure 5.13(a) is recorded shortly after the on-target laser peak ($t = +8$ fs), at which time the electron density in the interstices near the tips of the

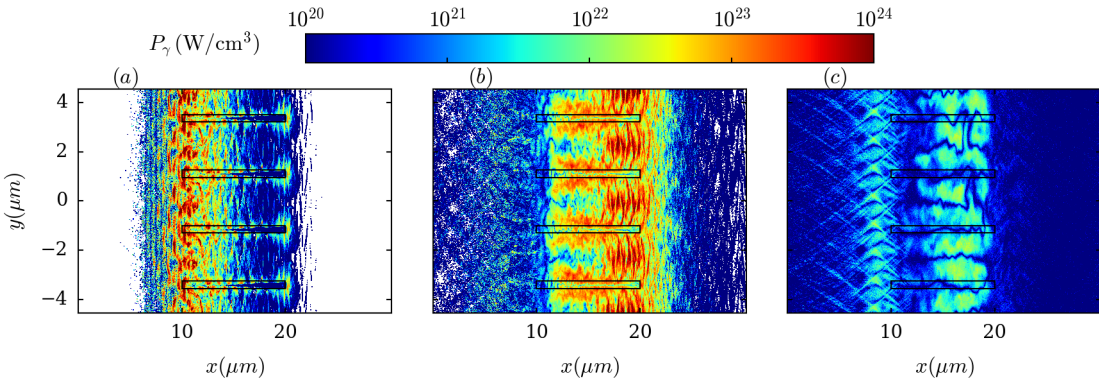


Figure 5.14: Maps of the radiated power density, P_γ , at three different times: (a) $t = 8$ fs (during plasma filling of the vacuum gaps), (b) $t = 40$ fs (after the left-hand side of the plasma-filled interstices have become opaque to the laser) and (c) $t = 167$ fs (final simulation time).

wires is of $\sim 50n_c$, *i.e.*, approaches the relativistic critical density $n_{cr} \simeq a_L n_c$ (see also Sec. 5.3.4). Figure 5.12(a) shows that, up to this time, the interstices have remained (partially) transparent to the laser wave. The hot-electron current flowing in the interstices induces a magnetostatic field that is screened inside the wires by a return current carried by bulk electrons (of density $n_e \simeq Zn_C = 480n_c$). The amplitude of this field can be estimated by noting that the laser-accelerated electrons are initially extracted from a layer of thickness $\delta_{acc} \simeq a_L(n_c/n_e)c/\omega_0 \simeq 30$ nm (assuming immobile ions and a balance between the transverse laser and space-charge fields). These electrons generate a magnetostatic field of normalized strength $\langle B_z \rangle / B_0 \simeq \langle v_x/c \rangle (n_e/n_c) \delta_{acc} \omega_0 / c \simeq a_L \langle v_x/c \rangle$, with $\langle v_x \rangle \simeq c$ the mean longitudinal fast-electron velocity. One therefore expects the strength of the self-induced magnetostatic field to be comparable with that of the laser field, in agreement with the maximum value $\langle B_z \rangle \simeq 0.7a_L$ measured at the laser peak. At laser intensities (resp. wire width) high (resp. small) enough that $\delta_{acc} \gtrsim d/4$, the number of electrons remaining inside the wires becomes lower than those expelled by the laser, so that current balance between the forward-moving hot electrons and the backward-moving core electrons can no longer be maintained in the vicinity of a wire, as noted previously by [Kaymak et al. \(2016\)](#). In the planar-wave case under consideration, this leads to $\langle B_z \rangle$ dropping with decreasing $d \lesssim 4\delta_{acc}$, from $\langle B_z \rangle / B_0 \simeq (n_e/n_c)d\omega_0/4c$ down to zero in the fully depleted regime ($d \lesssim 2\delta_{acc}$).

[Kaymak et al. \(2016\)](#) reported that the magnetostatic field setup around the wires tends to deflect inwards the bulk electrons, resulting in the pinching of the wire cores. This transverse magnetic compression occurs early in time, as shown in Fig. 5.13(a) where one can note a contraction of the wires compared to their initial position (solid black lines). Simultaneously, the space-charge sheath field $\langle E_y \rangle / B_0 c \simeq (n_e/n_c) \delta_{acc} \omega_0 / c$ transversely accelerates the ions from the outer wire regions, and hence an increasingly dense plasma progressively fills up the interwire gaps. At $t = +40$ fs, the bulk electrons have expanded enough to form in the wire interstices a relativistically overcritical plasma ($n_e \geq n_{cr}$) opaque to the laser light [Fig. 5.13(b)]. This causes the splitting of the laser pulse into a transmitted part and a reflected one, as seen in Fig. 5.12(b). The density modulations at the vacuum/plasma interface arising from the incomplete homogenization of the wires account for the reflection interference pattern seen in front of the target. Given the relatively large interwire spacing considered here, the laser transmission across the target

is significant ($\simeq 13\%$). Figure 5.13 shows that, by $t = +167\text{ fs}$ (about 85 fs after the laser pulse has exited the simulation domain), the nanostructure has been completely homogenized, the ion density then tending to the average density $n_i d / D = 11n_c$.

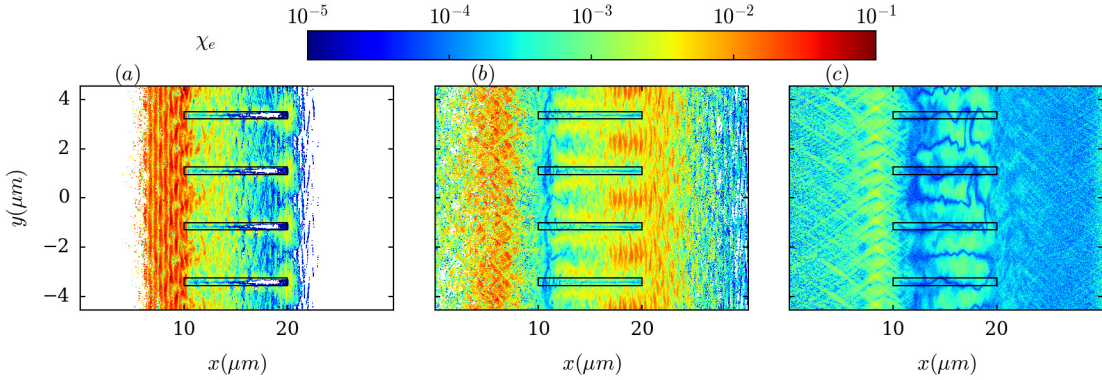


Figure 5.15: Maps of the electron quantum parameter, χ_e , at three different times: (a) $t = 8\text{ fs}$, (b) $t = 40\text{ fs}$ and (c) $t = 167\text{ fs}$ (final simulation time).

Figure 5.12(c) plots the quasistatic magnetic field $\langle B_z \rangle$, averaged over an optical cycle, at $t = 167\text{ fs}$. It demonstrates the relatively slow decay of the magnetostatic modulations sustained by the homogenized target electrons. At this instant, these modulations have a strength $\langle B_z \rangle \simeq 15B_0 \simeq 0.18a_L$, which remains an appreciable fraction of the laser field strength, and a typical length $L_B \sim 0.5\text{ μm}$. Electrons are considered to be magnetized when their Larmor radius $R\omega_0/c = \beta_e \gamma_e B_0/B_z$ becomes smaller than L_B . This criterion leads to magnetization of electrons with up to $\sim 25\text{ MeV}$ energies, and therefore of the vast majority of the plasma electrons, of mean energy $\langle \gamma \rangle m_e c^2 \simeq 12\text{ MeV}$.

Let us now examine the synchrotron emission that takes place during and after the laser-nanowire interaction. To provide insight into the radiative processes, we plot the spatial distribution of the averaged (over the local electron distribution) radiated power density in Figs. 5.14(a-c) and of the averaged electron quantum parameter, χ_e in Figs. 5.15(a-c), at the same times as in Figs. 5.12(a-c). We remind that the power radiated by a single electron can be expressed as $P = (2/3) \alpha_f m_e c^2 \chi_e^2 g(\chi_e) / \tau_C$, with $\tau_C = \hbar/m_e c^2$ the Compton time, α_f the fine structure constant, and $g(\chi_e)$ a quantum correction first introduced by [Kirk et al. \(2009\)](#). The scaling $P \propto \chi_e^2$ is a good approximation in the classical regime ($\chi_e \lesssim 0.05$). These maps will help analyze the time evolution of the angle-resolved radiated power and the photon energy spectra (integrated over different time intervals) plotted in Figs. 5.16(a,b). The angle θ_γ denotes the angle of the photon momentum \mathbf{k}_γ relative to the laser axis (x), *i.e.*, $\theta_\gamma = \arccos(k_{\gamma,x}/k_\gamma) \in (0, \pi)$.

Figure 5.16(a) indicates that the emission initially occurs in the laser direction ($\theta_\gamma = 0$) with an increasingly broad angular distribution. As expected, the emission strongly increases at the laser peak, and is at its brightest in the time period $5 \lesssim t \lesssim 20\text{ fs}$. Figure 5.16(b) shows that the spectrum radiated from the start of the interaction up to $t = +25\text{ fs}$ extends to $\hbar\omega_{\max} \simeq 60\text{ MeV}$, and makes up $\sim 40\%$ of the total radiated energy. The radiated power is then contained in a forward cone of $\sim 45^\circ$ half angle and is modulated at twice the laser frequency. This oscillation is typical of the synchrotron radiation from a relativistically overdense plasma layer in the SDE regime described by [Ridgers et al. \(2012\)](#). Consistently, Fig. 5.14(a), recorded at $t = +8\text{ fs}$, shows that the emission then mainly occurs at the front side of the plasma (with electron density $n_e \simeq 10 - 50n_c$) filling the wire gaps, where relatively high values $\chi_e \simeq 5 \times 10^{-2} - 10^{-1}$ are

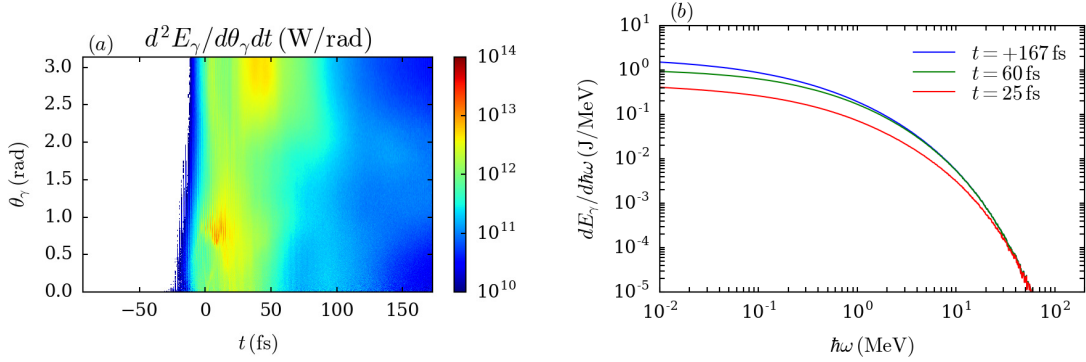


Figure 5.16: (a) Time evolution of the angle-resolved radiated power and (b) photon energy spectra integrated from the start of the iteration up to three different times: $t = +25$ fs (red curve), $+60$ fs (green curve) and $+167$ fs (blue curve). Angles in (a) are defined as $\theta_\gamma = \arccos(k_{\gamma,x}/k_\gamma) \in (0, \pi)$.

found. Deeper into the array ($15 \leq x \leq 20 \mu\text{m}$), the more dilute, λ_0 -periodic electron bunches that move along the laser wave present a weaker quantum parameter, $\chi_e < 10^{-2}$ (due to compensating electric and magnetic forces), and hence weakly radiate. Note, however, the relatively bright synchrotron spots at the right-hand tips of the wires, where quasistatic fields deflect the electrons at an angle to the laser direction, hence increasing their quantum parameter and radiation efficiency (see below).

Figure 5.16(a) reveals that a secondary emission burst occurs in the time interval $25 \lesssim t \lesssim 60$ fs, when the transmitted laser pulse travels across the target backside. In contrast to the first emission burst, this emission takes place in the backward direction ($\theta_\gamma \simeq \pi$). It originates from the interaction of the transmitted part of the laser pulse with the fast electrons reflected at the target backside by the space-charge field. Such a counterpropagating geometry maximizes the quantum parameter $\chi_e \simeq 2\gamma E_\perp/E_S$ (where E_\perp is the laser electric field). This mechanism is supported by Fig. 5.14(b), which shows a volumetric emission between (and near the backside of) the wires, where χ_e values of $\sim 10^{-2}$ are reached [Fig. 5.15(b)]. About 45 % of the synchrotron yield is radiated during this stage (with maximum photon energies ~ 60 MeV, similar to those in the primary stage). Of course, this phenomenon will be altered in the presence of a substrate coated at the target backside (see Sec. 5.4). We note that relatively high χ_e values ($\sim 10^{-2}$) are also reached in the dilute plasma formed in front of the target, yet the electron density, $n_e \simeq 0.1n_c$ [Fig. 5.13(b)] is there too low to yield significant emission.

Following the laser irradiation ($t \gtrsim 60$ fs), the radiated power strongly drops, yet, in similar fashion to the work of Stark *et al.* (2016), the remaining magnetostatic fields can sustain additional radiation [Fig. 5.16(a)]. Figure 5.15(c) thus indicates that, at $t = +167$ fs, χ_e attains values $\sim 10^{-3}$ in the magnetic modulations. The weaker power radiated at such low χ_e values [Fig. 5.14(c)] is partially compensated for by the longer duration of this emission stage, which makes up ~ 15 % of the total yield in the time period $60 \lesssim t \lesssim 167$ fs [Fig. 5.16(b)]. Since the magnetostatic fields build up early in the laser irradiation, their contribution is *a priori* not limited to the final times of the simulation. Yet their effect is initially mitigated by the transverse electrostatic field ($\langle E_y \rangle$) around the wires, which tends to weaken the quantum parameter; as the wires radially expand and mix [Fig. 5.13(c)], however, $\langle E_y \rangle$ diminishes and becomes small compared to $\langle B_z \rangle$, so that $\chi_e \simeq \langle \gamma \rangle \langle B_z \rangle c/E_S$. At $t = 167$ fs, we have $\langle B_z \rangle \simeq 15B_0$ and a mean electron energy $\langle \gamma_e \rangle \simeq 23$ in the expanded plasma, which implies $\chi_e \simeq 8 \times 10^{-4}$, consistent with

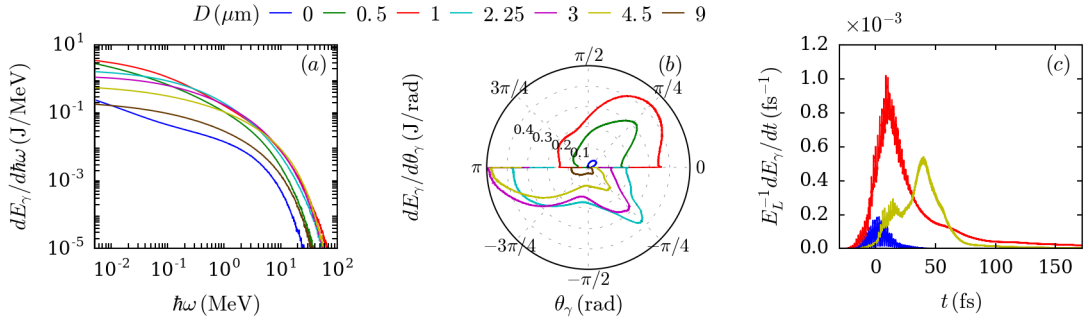


Figure 5.17: Variations of the synchrotron emission with the interwire spacing D : (a) energy spectra, (b) angle-resolved radiated energy and (c) time-resolved radiated power (and normalized to the total laser energy E_L). Each color represents a different value of D (in μm units) as indicated in the legend of panel (a). Angles in (b) are defined as $\theta_\gamma = \arccos(k_{\gamma,x}/k_\gamma) \in (0, \pi)$ and the resulting angular distribution is symmetrized with respect to $\theta_\gamma = 0$. All plotted quantities are integrated over the simulation domain.

Fig. 5.15(c).

Our reference simulation has allowed us to pinpoint important processes affecting the synchrotron radiation in the interaction of a 10^{22} Wcm^{-2} femtosecond laser pulse with a nanowire array of micron-scale interspacing. We will now examine the dependencies of the emission on the wire and laser parameters.

5.3 Variations of the synchrotron yield with the nanowire parameters

In the following, we explore the dependency of the angle-energy spectra of the synchrotron radiation on the nanowire spacing (D), width (d) and material (Z), as well as on the laser intensity (I). Except for the varied parameter, the numerical setup is identical to that presented in Sec. 5.1.1. Our parametric scan will encompass various regimes of synchrotron radiation, which will be interpreted in light of the processes revealed in the reference case of Sec. 5.2 and previous simulation works by Cao *et al.* (2010b); Brady *et al.* (2012); Andreev and Platonov (2016) and Lecz and Andreev (2017).

5.3.1 Variation of the interwire spacing: from forward to backward directed radiation

In our simulations, the interwire spacing has been varied over the set of values $D \in [0, 0.5, 1, 2.25, 3, 4.5, 9] \mu\text{m}$. Note that $D = 0 \mu\text{m}$ corresponds to a planar target. The chosen values exactly divide the transverse size of the domain ($L_y = 9 \mu\text{m}$) so as to keep the periodic condition valid. The other target parameters are set to $d = 0.3 \mu\text{m}$, $L = 10 \mu\text{m}$, $Z = 6$ and the laser intensity is $I = 10^{22} \text{ Wcm}^{-2}$.

The energy-resolved photon spectra recorded for various interwire spacings are plotted in Fig. 5.17(a). We see that the cutoff photon energy weakly varies for $1 \leq D \leq 4.5 \mu\text{m}$, where it reaches a maximum value $\hbar\omega_{\max} \simeq 50 \text{ MeV}$, approximately twice that found at uniform density ($\simeq 23 \text{ MeV}$). Figure 5.17(b), which displays the angle-resolved energy spectra, shows a transition from a mainly forward-directed emission at $D \leq 1 \mu\text{m}$ to an

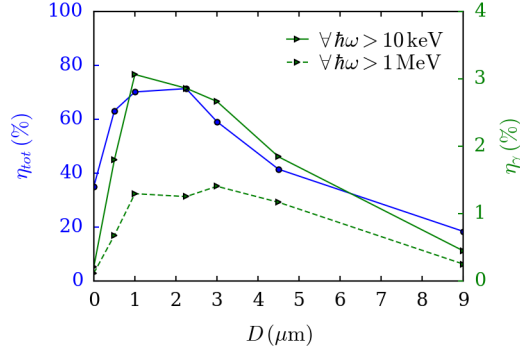


Figure 5.18: Variations with the interwire spacing (D) of the total absorbed laser energy fraction (η_{tot} , blue circles) and radiation conversion efficiency (η_γ , green triangles). The radiation conversion efficiency is computed for two photon energy thresholds: $\hbar\omega \geq 10 \text{ keV}$ (green solid) and $\hbar\omega \geq 1 \text{ MeV}$ (green dashed). All quantities are integrated over the simulation duration.

increasingly backward-directed emission at larger spacings. The two lobes of emission found at $D \geq 2.25 \mu\text{m}$ around the directions $\theta_\gamma \simeq 45^\circ$ and $\theta \simeq 180^\circ$ originate from the same mechanisms discussed in Sec. 5.2. In particular, we emphasize that the backward emission follows from the electrons refluxing in the $-x$ direction and colliding head-on with the transmitted part of the laser pulse. This results in a secondary backward-directed γ -ray burst after the primary (and weaker) forward-directed burst. This is evidenced in Fig. 5.17(c) where is plotted the time evolution of the radiated power: the curve at $D = 4.5 \mu\text{m}$ presents two distinct emission peaks, the second, brighter one taking place at $t \simeq 40 \text{ fs}$, *i.e.*, as the laser pulse exits the target.

At narrower spacings ($D \leq 1 \mu\text{m}$), the interstices fill up with opaque plasma increasingly early before the laser pulse maximum. Looking at the increase in the instantaneous laser reflectivity, we find that the transparency-opacity transition occurs at $\tau_f \simeq -8 \text{ fs}$ for $D = 0.5 \mu\text{m}$ and $\tau_f \simeq 3 \text{ fs}$ for $D = 1 \mu\text{m}$. The energy fraction and mean intensity of the transmitted light then diminishes with decreasing D , which greatly weakens the aforementioned backward emission mechanism. At $D = 2.25 \mu\text{m}$, about 13 % of the laser energy is transmitted, and this fraction becomes negligible for $D \leq 1 \mu\text{m}$. The time history of the radiated power at $D = 1 \mu\text{m}$, plotted in Fig. 5.17(c), thus presents a single maximum, occurring at $t \simeq 10 \text{ fs}$, just after the overdense plasma filling of the vacuum gaps. The primary radiation burst observed at $D = 4.5 \mu\text{m}$ occurs approximately at the same time: both signals exhibit a $2\omega_0$ modulation, characteristic of SDE in an overcritical plasma as outlined by Brady *et al.* (2013). The photons are then emitted in a large forward cone, as seen in the upper part of Fig. 5.17(b).

As pointed out in the introduction, the interest for nanowire targets as potentially efficient radiation sources arose from their well-established capability in yielding high laser absorption fractions. Since the latter usually translate in large numbers of energetic electrons, it is tempting to predict that the laser absorption and radiation yield are correlated. To check this scenario, we plot in Fig. 5.18 the variations of the total absorbed laser energy fraction (η_{tot} , defined as the energy absorbed by all the particle and photon species, normalized to the laser energy) and the laser-to-photon energy conversion efficiency (η_γ) with the interwire spacing. To discriminate between the contributions of the ‘low’ and ‘high’ energy photons in the radiation yield, the green solid and dashed η_γ curves are computed

applying lower-energy cutoffs $\hbar\omega = 10 \text{ keV}$ and 1 MeV , respectively. We note that the laser absorption rises from $\sim 35\%$ at uniform solid density to $\sim 70\%$ at $D = 2.25 \mu\text{m}$, with a plateau above $\sim 60\%$ in the range $1 \leq D \leq 3 \mu\text{m}$. While the η_{tot} and η_γ curves look similar, a few quantitative differences are discernible. Both η_γ curves starting from very low values ($\sim 0.2\%$ for $\hbar\omega \geq 10 \text{ keV}$ and $\sim 0.1\%$ for $\hbar\omega \geq 1 \text{ MeV}$) at uniform solid density, they present a steeper rise at low D values ($\leq 1 \mu\text{m}$) than η_{tot} . Also, η_γ attains its maximum ($\sim 3\%$, for $\hbar\omega \geq 10 \text{ keV}$) at $D = 1 \mu\text{m}$, lower than the value optimizing η_γ . For $\hbar\omega \geq 1 \text{ MeV}$, we find $\eta_\gamma \simeq 1\%$ in a broader range of interwire spacings, $1 \leq D \leq 4.5 \mu\text{m}$, with a weakly pronounced optimum at $D = 3 \mu\text{m}$.

The overall evolution of the total laser absorption, as depicted in Fig. 5.18, is consistent with the results obtained by [Cao et al. \(2010b\)](#) at lower laser intensity ($I = 5 \times 10^{19} \text{ W/cm}^2$) and in the sub-micron range $0.24 \leq D \leq 0.8 \mu\text{m}$ (with $d = 0.16 \mu\text{m}$). In our work, by considering larger interwire spacings, we allow greater fractions of the laser light to be transmitted through the target, thus enabling the secondary radiation burst at the target backside discussed above.

To summarize, we have identified two distinct regimes of synchrotron radiation by varying the interwire spacing. For narrowly spaced wires ($D \leq 1 \mu\text{m}$), the vacuum gaps rapidly fill up with overdense plasma before the on-target laser peak, causing the emission to be concentrated at the target front and be mainly forward directed, similarly to what occurs in a uniform overdense plasma. At larger interwire spacings ($D \geq 2.25 \mu\text{m}$), this mechanism is progressively superseded by an additional emission taking place at the target backside, which results from the interaction of the transmitted laser light with the refluxing fast electrons. This backward-directed emission is distinct from the RESE mechanism highlighted by [Brady et al. \(2012\)](#) (see Sec. 4.2), which occurs at the moving laser front in relativistically underdense plasmas. To achieve the dilute plasma conditions required by the latter mechanism during the laser pulse, the wire width must be reduced, as is done in the next Section.

5.3.2 Variation of the wire width: from RESE to SDE, through TOEE

We now set the interwire spacing to the value maximizing the radiation efficiency, $D = 1 \mu\text{m}$, and vary the wire width in the set of values $d \in (15, 36, 50, 100, 300, 500, 1000) \text{ nm}$. Note that the value $d = 1 \mu\text{m}$ corresponds to a uniform solid-density target. The resulting energy-angle photon spectra and radiation dynamics are displayed in Fig. 5.19(a-c).

For $d \lesssim \delta_{acc} \simeq 30 \text{ nm}$, most of the electrons are expelled from the wires by the laser field, hence leading to fast (*i.e.*, before ion expansion) homogenization of the plasma profile at the average density $n_{av} = n_e d / D$. For $d = 15 \text{ nm}$, one has $n_{av} \simeq 7n_c$, which falls into the regime of relativistic self-induced transparency (RSIT). [Brady et al. \(2012\)](#) have shown that such plasma conditions favor the RESE process: the electrons, pushed by the ponderomotive force at the laser front, are periodically reinjected back into the laser wave by the charge separation field. Their momentum ($\sim a_L m_e c$) then forms an angle of $\sim \pi$ with the laser wavevector, which maximizes the quantum parameter $\chi_e \sim 2a_L^2 c B_0 / E_S \sim 5 \times 10^{-6} a_L^2$ and the subsequent synchrotron radiation in the backward direction. Figure 5.19(b) confirms this prediction, showing that practically all the radiation is then directed backwards. In Fig. 5.19(c), we observe a temporal modulation of the radiated power at a period of $\sim 15 \text{ fs}$, of the same order as the theoretical estimate $\tau_{RESE} = a_L / (n_e \omega_0) \simeq 7 \text{ fs}$ derived for RESE in uniform plasmas by [Brady et al. \(2012\)](#). This period is significantly larger than that of the $2\omega_0$ oscillations arising in the SDE regime (see the curve with $d = 500 \text{ nm}$, corresponding to $n_{av} = 240n_c$).

As discussed below [see Fig. 5.25(a) in Sec. 5.3.4], we have checked the occurrence of

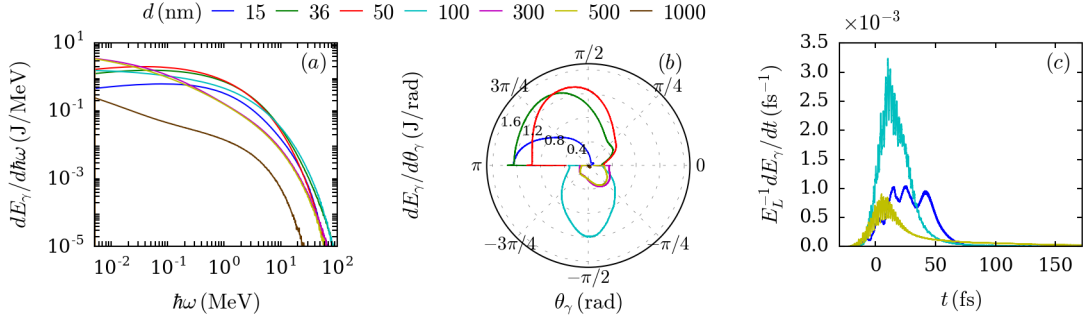


Figure 5.19: Variations of the synchrotron emission with the wire width d : (a) energy spectra, (b) angle-resolved radiated energy and (c) time-resolved radiated power (normalized to the total laser energy E_L). Each color represents a different value of d (in nm units) as indicated in the legend of panel (a). Angles in (b) are defined as $\theta_\gamma = \arccos(k_{\gamma,x}/k_\gamma) \in (0, \pi)$ and the resulting angular distribution is then symmetrized with respect to $\theta_\gamma = 0$. All plotted quantities are integrated over the simulation domain.

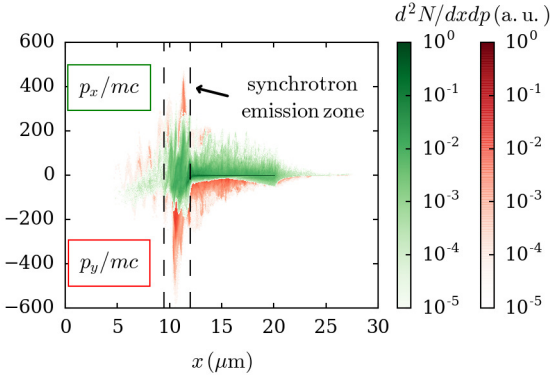


Figure 5.20: Electron $x - p_x$ (green colormap) and $x - p_y$ (red colormap) phase spaces at $t = +40$ fs. The nanowire-array parameters are $d = 100$ nm, $D = 1$ μm and $L = 10$ μm , giving rise to transversally oscillating electron synchrotron emission (TOEE).

RSIT by measuring the effective propagation velocity of the laser front in the homogenized plasma, in similar fashion to Weng *et al.* (2012b). RSIT is found to occur for $d \lesssim 50 - 100$ nm, thus leading to significant laser transmission across the plasma. For wire widths $\gtrsim 100$ nm, the homogenized plasma becomes opaque to the laser light, which then propagates at a much reduced speed through hole boring (HB).

The synchrotron spectra of Fig. 5.19(a) show that the maximum photon energy weakly varies ($\hbar\omega_{\max} \simeq 50 - 70$ MeV), and in a non-monotonic way, for $15 \leq d \leq 300$ nm. The most notable variation occurs when the wire width is increased from $d = 300$ nm to $d = 500$ nm, leading to $\hbar\omega_{\max}$ decreasing from ~ 50 MeV to ~ 20 MeV. More interestingly, it is found that the mean photon energy is maximized in the RSIT regime: for $d = 15$ nm, we obtain $\langle \hbar\omega \rangle \simeq 0.45$ MeV, much higher than for $d \geq 300$ nm, which leads to a relativistically overdense homogenized plasma ($n_{av} = 144n_c$) and $\langle \hbar\omega \rangle \simeq 0.14$ MeV.

The case of $d = 100$ nm, close to the RSIT/HB threshold, yields the highest maximum photon energies [Fig. 5.19(a)] but also, and more significantly, to a radiated energy concentrated in the transverse direction, $\theta_\gamma = \pi/2$ [Fig. 5.19(b)]. This particular radi-

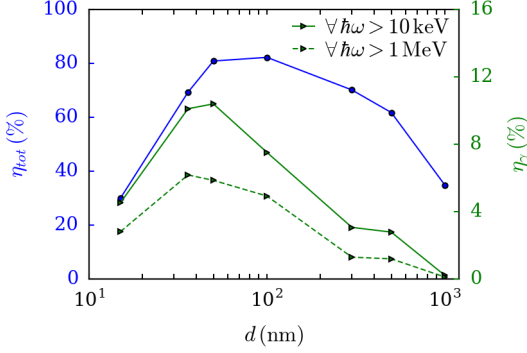


Figure 5.21: Variations with the wire width (d) of the total absorbed laser energy fraction (η_{tot} , blue circles) and radiation conversion efficiency (η_γ , green triangles). The radiation conversion efficiency is computed for two photon energy thresholds: $\hbar\omega \geq 10$ keV (green solid) and $\hbar\omega \geq 1$ MeV (green dashed). All quantities are integrated over the whole simulation duration.

ation pattern corresponds to the TOEE regime evidenced by Chang *et al.* (2017). In this mechanism, an approximate balance is established between the laser ponderomotive force and the charge-separation field at the irradiated plasma front. This causes the electrons to predominantly oscillate in the transverse plane, thus inducing a mainly transverse synchrotron emission. This particular electron dynamics stands out in Fig. 5.20, which superimposes the $x - p_x$ (green colormap) and $x - p_y$ (red colormap) electron phase spaces at $t = +40$ fs. Around the front side of the target where most of the radiation is emitted, the electron distribution is clearly more extended in the transverse direction than in the longitudinal direction.

As the wire width is decreased (resp. increased) from $d \simeq 100$ nm, the radiation pattern is shifted to the backward (resp. forward) direction, characteristic of the RESE (resp. SDE) mechanism.

Figure 5.21 displays the wire-width dependence of the total laser absorption (η_{tot}) and radiation conversion efficiencies (η_γ) into > 10 keV and > 1 MeV energy photons. The laser absorption rises from $\eta_{tot} \sim 30\%$ at $d = 15$ nm to a maximum of $\sim 80\%$ at $d = 50-100$ nm, before dropping to $\sim 35\%$ in the uniform-density case ($d = 1\mu\text{m}$). While the increase in η_{tot} at low wire widths is accompanied by similar rises in the η_γ curves, the latter attain their maxima (at $d \simeq 36-50$ nm) slightly before η_{tot} . A peak value of $\eta_\gamma \sim 10.4\%$ (resp. 6.1%) for $\hbar\omega \geq 10$ keV (resp. > 1 MeV) is obtained at $d = 50$ nm (resp. $d = 36$ nm). Moreover, the two η_γ curves show a faster decrease at large d than η_{tot} . To quantify this, let us compare the cases of $d = 36$ nm and $d = 300$ nm: although both widths give rise to similar absorption fractions ($\eta \simeq 70\%$), the photon yield at $d = 36$ nm is ~ 3 times larger than at $d = 300$ nm. This marked difference follows from the distinct plasmas produced by the electron-depleted exploding wires: at $d = 36$ nm, a relativistically undercritical plasma ($n_{av} = 17n_c$) forms, which triggers a RESE-type mechanism more efficient than SDE that arises in the overcritical plasma ($n_{av} = 144n_c$) generated at $d = 300$ nm. Finally, we note that at $d = 15$ nm, a sizable fraction ($\sim 70\%$) of the laser energy is transmitted across the array, which mechanically reduces the radiated energy fraction.

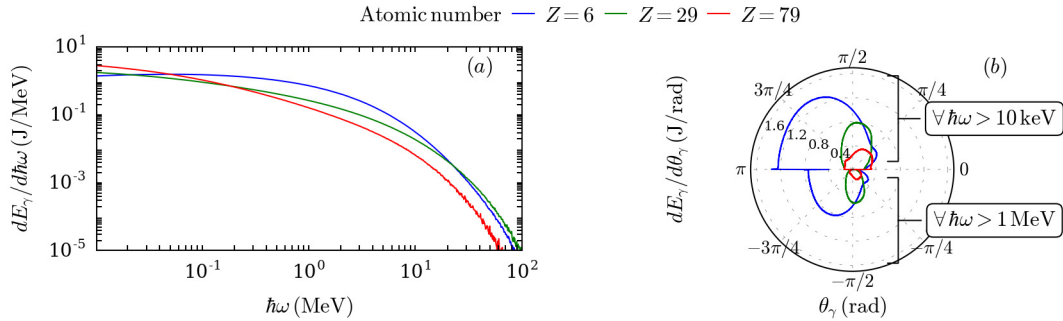


Figure 5.22: Wire-material dependence of the (a) energy-resolved and (b) angle-resolved radiated energy. The blue, green and red curves correspond, respectively, to C, Cu and Au wires. The top (resp. bottom) half of panel (b) is associated with a photon energy threshold of 10 keV (resp. 1 MeV). All spectra are integrated over the simulation duration. Angles in (b) are defined as $\theta_\gamma = \arccos(k_{\gamma,x}/k_\gamma) \in (0, \pi)$, and the resulting angular distribution is symmetrized with respect to $\theta_\gamma = 0$.

5.3.3 Changing the ion mass and the laser intensity

We now demonstrate that modifying other key parameters of the interaction such as the wire material or the laser intensity can also enable switching between the previously discussed radiation mechanisms. To this goal, we first replace, in the most efficient configuration for γ -ray production ($D = 1 \mu\text{m}$, $d = 36 \text{ nm}$), the neutral carbon atoms ($Z = 6$) by either copper ions ($Z = 29$) with a 5+ initial ionization degree and a solid density $n_{Cu} = 80n_c$, or gold ions ($Z = 79$) with a 14+ initial ionization degree and a solid density $n_{Au} = 55n_c$. Second, we vary the laser intensity in the range $I = 10^{21} - 10^{23} \text{ Wcm}^{-2}$ for two values of the wire widths: $d = 100 \text{ nm}$ and $d = 300 \text{ nm}$.

The energy-resolved radiated energy displayed in Fig. 5.22(a) indicates that the average photon energy is decreased by the use of copper (0.27 MeV) and gold (0.14 MeV) compared to carbon (0.41 MeV). The radiation efficiency above 10 keV also drops with increasing atomic number (from $\sim 10.1\%$ in carbon to 4.6% in copper and 2.9% in gold), in spite of a slightly enhanced laser absorption in copper and gold ($\eta_{tot} \sim 80\%$) than in carbon ($\sim 70\%$, see Fig. 5.21). In light of our previous results, the reason for this difference is that the homogenized electron density ($n_{av} = 17n_c$) in the carbon wires lies in the RSIT regime, prone to RESE. In contrast, the copper (resp. gold) wires produce a higher-density plasma, $n_{av} = 80n_c$ (resp. $n_{av} = 3000n_c$), opaque to the laser field, which favours TOEE (resp. SDE). This transition from RESE to SDE through TOEE is supported by the angular radiation patterns shown in Fig. 5.22(b): both for the 10 keV and 1 MeV photon energy thresholds, we clearly see that the emission evolves from a mainly backward radiation in the carbon target to a predominantly transverse radiation in copper and to a forward directed radiation in gold.

In the gold case, we observe ionization rates up to $Z^* = 70$ at the laser-target interface, consistent with the work of Bargsten *et al.* (2017) where a similar setup is numerically considered (yet without describing synchrotron emission). Also, the synchrotron photon yield above 1 MeV ($\sim 1.9\%$) is about 60% of the yield above 10 keV, similarly to the carbon and copper targets. Although this performance is not optimal due to too dense a homogenized plasma, it can be put in perspective with the record $\sim 20\%$ conversion efficiency into $> 1 \text{ keV}$ photons which has been recently reported using gold nanowires

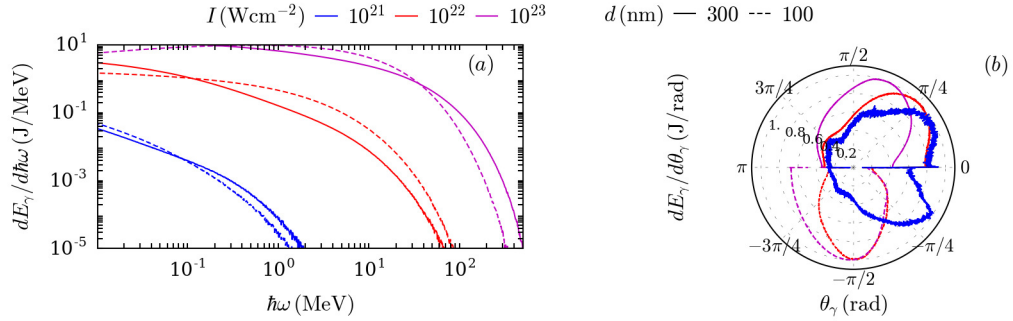


Figure 5.23: Laser-intensity dependence of (a) the energy-resolved and (b) angle-resolved radiated energy (above 10 keV). Each color stands for a particular value of I as indicated in the legend. The solid (resp. dashed) curves correspond to a wire width $d = 300$ nm (resp. 100 nm). The interwire spacing is set to $D = 1 \mu\text{m}$. Angles in (b) are defined as $\theta_\gamma = \arccos(k_{\gamma,x}/k_\gamma) \in (0, \pi)$, and the resulting angular distribution is symmetrized with respect to $\theta_\gamma = 0$.

driven by a $4 \times 10^{19} \text{ Wcm}^{-2}$, 55 fs laser pulse by Hollinger *et al.* (2017). Rather than synchrotron emission, X-ray radiation in this experiment is caused by atomic physics processes (atomic line emissions, photorecombination and Bremsstrahlung). Another difference with our study is that, due to lower laser intensity, and hence slower nanowire expansion, the highest X-ray yield is found for significantly smaller interspacings ($\sim 0.1 \mu\text{m}$). The measured X-ray yield, however, rapidly drops with increasing photon energies (below 1 % for $\hbar\omega > 6 \text{ keV}$). These results should stimulate further theoretical work on the radiation efficiencies of atomic physics and synchrotron processes as functions of the laser and nanowire parameters.

We now return to carbon nanowires and examine the photon distributions produced in the laser intensity range $10^{21} \leq I \leq 10^{23} \text{ Wcm}^{-2}$. Figure 5.23(a) reveals that the photon generation at $I = 10^{21} \text{ Wcm}^{-2}$ occurs with the same efficiency for the two chosen values of the wire width, $d = 100$ nm (dashed lines $\eta_\gamma \simeq 0.09 \%$) and $d = 300$ nm (solid lines $\eta_\gamma \simeq 0.08 \%$). The case of $d = 300$ nm, however, leads to higher maximum ($\hbar\omega_{\max} = 1.4 \rightarrow 1.8 \text{ MeV}$) and average ($\langle \hbar\omega \rangle = 32 \rightarrow 42 \text{ keV}$) photon energies. At higher intensity ($I \geq 10^{22} \text{ Wcm}^{-2}$), by contrast, the average photon energy is much larger at $d = 100$ nm than at $d = 300$ nm (400 keV *vs.* 140 keV). This stems from the fact that the expanded plasma then becomes relativistically transparent, whereas it remains opaque at $d = 300$ nm (even at $I = 10^{23} \text{ Wcm}^{-2}$). Furthermore, the fraction of laser energy converted into $\geq 10 \text{ keV}$ photons is always higher at $d = 100$ nm whatever the laser intensity in the studied range.

In Fig. 5.23(b), it is seen that the emission cone angle increases with increasing laser intensity. While at $d = 300$ nm the radiation remains forward-directed up to $I = 10^{23} \text{ Wcm}^{-2}$, at $d = 100$ nm it is forward directed at $I = 10^{21} \text{ Wcm}^{-2}$, becomes concentrated in the transverse direction at $I = 10^{22} \text{ Wcm}^{-2}$, and is mainly confined within angles $\geq \pi/2$ at $I = 10^{23} \text{ Wcm}^{-2}$. Once again we stress that this evolution from SDE to RESE results from the onset of RSIT at high enough laser intensity. In the latter case, the radiation is mostly carried by γ -ray photons: the radiation conversion efficiency above 1 MeV indeed reaches $\sim 43 \%$, hardly lower than the $\sim 47 \%$ conversion fraction in $\geq 10 \text{ keV}$ photons.

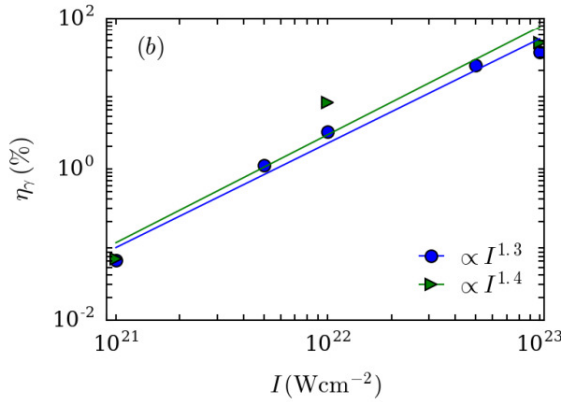


Figure 5.24: Radiation conversion efficiency into $> 10 \text{ keV}$ photons as a function of the laser intensity. The green triangles (resp. blue circles) correspond to a wire width $d = 100 \text{ nm}$ (resp. 300 nm). The interwire spacing is set to $D = 1 \mu\text{m}$.

In Fig. 5.24 is plotted the radiation conversion efficiency (counting all photons above 10 keV) as a function of the laser intensity. The results can be approximately fitted to $\eta_\gamma \propto I^{1.3-1.4}$. This scaling happens to fall in between the one found by [Brady et al. \(2012\)](#) at undercritical densities in the RESE regime, $\eta_\gamma \propto I$, and the one observed by [Ji et al. \(2014a\)](#) at overcritical densities in the SDE regime, $\eta_\gamma \propto I^{3/2}$. This behavior could be expected since both radiation regimes can arise in our broad intensity range. Regarding the radiation efficiency, these two mechanisms mainly differ in the typical number of radiating electrons (N_e). In the underdense plasma, this number is proportional to the areal density crossed by the laser, $N_e \propto n_e$; in an overdense plasma, this number scales as the areal density of the compressed electron layer at the target front, $N_e \propto I^{1/2}$. Since $\eta_\gamma \propto N_e \chi_e^2 / I$ and $\chi_e \propto \langle \gamma_e \rangle I^{1/2}$, we can employ the scaling fitted from simulations (see Sec. 5.1.3) stating that $\langle \gamma_e \rangle \propto I^{1/2}$ we thus expect $\chi_e \propto I$ and therefore $\eta_\gamma \propto I$ for RESE and $\eta_\gamma \propto I^{3/2}$ for SDE. For more details on this derivation, the reader is referred to Sec. 4.2.

5.3.4 Comparison with uniform-density targets

The dominant radiation processes that we have highlighted in nanowire arrays appear similar to those identified in previous simulation studies considering uniform plasmas. This is so because, under the present ultra-high-intensity interaction conditions, the nanostructure is largely smoothed out during the laser pulse, so that a large part of it experiences a significantly homogenized plasma. One may then question the advantage, regarding synchrotron radiation, of using nanowire arrays compared to uniform plasmas at sub-solid densities. To answer this question, we have conducted a set of simulations considering a $10 \mu\text{m}$ -thick carbon layer of uniform (free electron) density varying from $Zn_i = 7n_c$ to $480n_c$ (solid density). This density range corresponds to that achieved in fully homogenized nanowire arrays ($n_{av} = Zn_C d/D$) when increasing the wire width from $d = 15 \text{ nm}$ to $1 \mu\text{m}$ at fixed spacing $D = 1 \mu\text{m}$. The laser intensity is set to $I = 10^{22} \text{ Wcm}^{-2}$.

First, we examine the transition between plasma transparency (RSIT) and opacity (HB), which appears critical in determining the properties of the synchrotron emission. To properly identify the regime of laser-plasma interaction, we have tracked the position of the laser front in the target, $x_f(t)$, defined such that $a(x_f(t), t) = \max_x a(x, t)/2$, with $a(x, t)$ being the y -averaged dimensionless laser field. This definition is similar to that used by [Weng et al. \(2012b\)](#) except that, due to our short pulse duration, we use

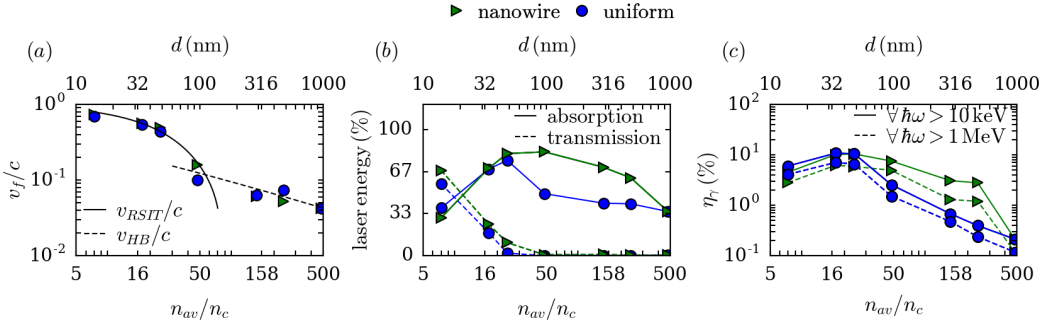


Figure 5.25: Comparison between carbon nanowire arrays (green triangles) and uniform-density targets (blue circles): (a) propagation velocity of the laser front; (b) total laser absorption (solid lines) and transmission (dashed lines); (c) radiative conversion efficiencies into $> 10 \text{ keV}$ (solid lines) and $> 1 \text{ MeV}$ photons (dashed lines). Results from nanowire-array (resp. uniform-density) targets are plotted as functions of the wire width d (resp. the average electron density n_{av}). In (a), the black solid and dashed lines plot the theoretical front velocities v_{RSIT} and v_{HB} , respectively (see text). In (b) and (c), all quantities are integrated over the simulation duration.

$\max_x a(x, t)/2$ instead of $a_L/2$ as is relevant to a semi-infinite pulse. For each simulation, v_f is evaluated from a linear regression fit of $x_f(t)$. Figure 5.25(a) plots v_f as a function of the wire width (d) in the nanowire-array case, and of the electron density ($n_e \equiv n_{av}$) in the uniform-plasma case. Both target types lead to a similarly decreasing curve for v_f , which drops from $v_f/c \simeq 0.7$ at $n_{av} = 7n_c$ down to $v_f/c \simeq 0.2$ at $n_{av} = 32n_c$. This parameter range corresponds to RSIT, and we have further checked that, as expected in this regime, the laser wave then overlaps with the plasma electrons and ions (Siminos *et al.*, 2017). Nanowire arrays tend to yield slightly faster laser propagation, which is ascribed to inhomogeneity effects. For completeness, we have plotted (as a black solid line) the front velocity estimated by Weng *et al.* (2012b) in a simpler setting (1D geometry, semi-infinite pulse, no synchrotron losses), $v_{RSIT}/c \simeq \exp(-2n_{av}/n_{cr})\sqrt{1 - n_{av}/n_{cr}}$, where $n_{cr} \simeq 0.89a_Ln_c$ in the ultrarelativistic regime. Despite the short duration and time-varying intensity of our laser pulse, correct agreement is found between v_f and v_{RSIT} up to $n_{av} \simeq 48n_c$ (or $d \simeq 100 \text{ nm}$), where the transition from RSIT to HB occurs, also corresponding to the transition threshold between RESE and SDE [see Figs. 5.19(b) and 5.20]. At higher n_{av} or d , the front velocity approximately matches the theoretical HB velocity, recalled in Robinson *et al.* (2008), (black dashed line), $v_{HB}/c \simeq \Pi/(1 + \Pi)$, where $\Pi = \sqrt{IZ/Am_en_{av}c^3}$ (see Sec. 4.1.5).

In Fig. 5.25(b) are plotted the absorbed and transmitted laser energy fractions as functions of the wire width (d) in the nanowire-array case, and of the plasma density ($n_e \equiv n_{av}$) in the uniform-target case. Similarly, Fig. 5.25(c) plots, for both target types, the variations with n_{av} and d of the conversion efficiencies into $> 10 \text{ keV}$ and $> 1 \text{ MeV}$ photons. In uniform targets, the laser absorption strongly increases (from $\eta_{tot} \sim 35 \%$ to $\sim 75 \%$) with increasing density in the range $7 \leq n_{av} \leq 24n_c$. Similar variations are found in nanowire arrays with same equivalent density (*i.e.*, $15 \leq d \leq 50 \text{ nm}$), with the differences, however, that η_{tot} is a bit smaller ($\sim 30 \%$) at $n_{av} = 7n_c$, but larger ($\sim 80 \%$) at $n_{av} = 24n_c$. In this parameter range, the interaction takes place in the RSIT regime in both targets and the transmitted laser fraction is always a bit larger in nanowire

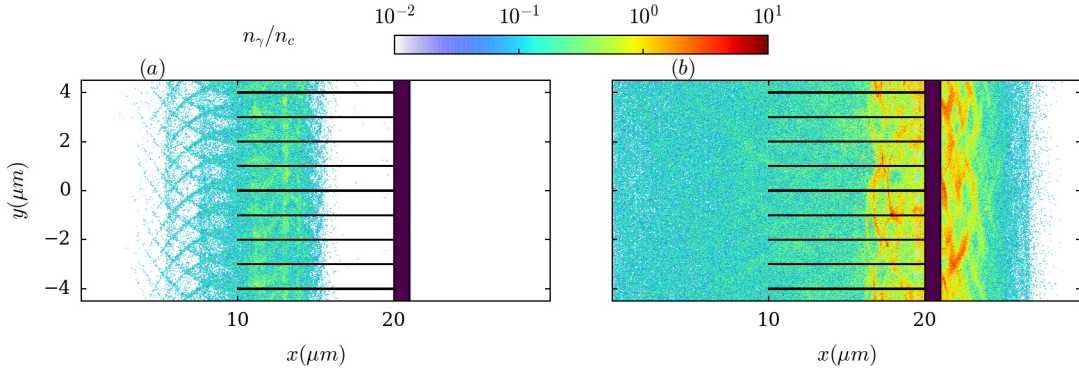


Figure 5.26: Normalized density (n_γ/n_c) of the high-energy ($> 1 \text{ MeV}$) photons (a) before ($t = +13 \text{ fs}$) and (b) after the reflection ($t = +56 \text{ fs}$) of the laser pulse off the copper foil at the target backside. The initial target shape is shown in dark red.

arrays, reaching $\sim 70\%$ at $n_{av} = 7n_c$ and $\sim 10\%$ at $n_{av} = 24n_c$). The most pronounced difference between the two target types arises at larger n_{av} or d : while the laser absorption in uniform targets abruptly drops beyond $n_{av} = 24n_c$, (down to $\eta_{tot} \simeq 45\%$ at $n_{av} = 64n_c$, and $\eta_{tot} \simeq 35\%$ at solid density), it stays at a high level ($\gtrsim 70\%$) up to $n_{av} = 144n_c$ (*i.e.*, $d = 300 \text{ nm}$).

The general trends observed for the laser absorption also hold for the synchrotron radiation. While uniform targets yield slightly better radiation efficiencies at $n_{av} = 7n_c$ ($\eta_\gamma \simeq 6\%$ *vs.* $\sim 4.5\%$, for $\hbar\omega > 10 \text{ keV}$), both setups give very similar maximum efficiencies, $\eta_\gamma \simeq 10\%$ (*resp.* $\sim 6\%$) for $\hbar\omega > 10 \text{ keV}$ (*resp.* $> 1 \text{ MeV}$) in the range $n_{av} = 17\text{--}24n_c$ (*i.e.*, $d = 36\text{--}50 \text{ nm}$). The robustness of the laser absorption enhancement in nanowire arrays of relatively large density ($n_{av}/n_c \geq 50$) is accompanied by a similar robustness of the radiation efficiency, which remains relatively high, $\eta_\gamma > 3\%$ (*resp.* $> 1\%$) for $\hbar\omega > 10 \text{ keV}$ (*resp.* $> 1 \text{ MeV}$) up to $n_{av} = 240n_c$ ($d = 500 \text{ nm}$). By contrast, the radiation yield from uniform targets decreases rapidly after its maximum: η_γ drops by a factor ~ 2.5 when n_{av} is increased from $24n_c$ to $32n_c$, and falls below 3% for $n_{av} \geq 64n_c$.

If we restrict our analysis to the forward radiation ($\theta_\gamma \leq 30^\circ$), we find that the highest yield into $> 1 \text{ MeV}$ photons ($\eta_\gamma \simeq 0.4\%$) is provided by a nanowire array of width $d = 36 \text{ nm}$, yet with little variation ($< 10\%$) in the $36 \leq d \leq 100 \text{ nm}$ range. Also, the highest yield into $> 10 \text{ keV}$ photons is observed for $d = 300 \text{ nm}$ ($\eta_\gamma \simeq 0.7\%$), with $< 10\%$ variation in the $36 \leq d \leq 300 \text{ nm}$ range.

5.4 Extension to more realistic setups

5.4.1 Radiation enhancement by a reflective substrate

We now investigate whether a more realistic setup, whereby the nanowire array is coated on a solid-density substrate, may substantially improve the synchrotron process. The rationale for this is that, for the parameters (carbon wires with $D = 1 \mu\text{m}$ and $d = 36\text{--}100 \text{ nm}$) previously found to yield the highest radiation efficiencies ($\eta_\gamma \geq 8\%$), a sizable fraction of the laser energy (*e.g.*, $\sim 25\%$ at $d = 36 \text{ nm}$) shines through the target via RSIT. Making this transmitted light reflect off a plasma mirror so as to interact with the hot electrons filling the nanowire array could sustain the synchrotron emission, and hence increase its efficiency.

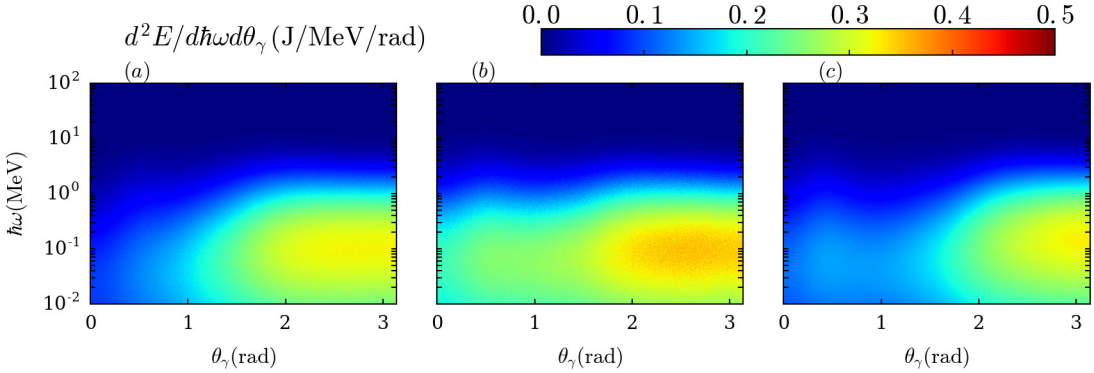


Figure 5.27: Energy-angle spectrum of the radiated energy for (a) the optimized nanowire array ($d = 36 \text{ nm}$, $D = 1 \mu\text{m}$) without substrate, (b) the optimized nanowire array target with substrate, and (c) the optimized (and density-equivalent) uniform plasma ($n_e = 16n_c$). Angles are defined by $\theta_\gamma = \arccos(k_{\gamma,x}/k_\gamma) \in (0, \pi)$. All spectra are integrated over the simulation duration.

To test this scenario, we have performed a simulation in which a $1 \mu\text{m}$ -thick copper foil is placed at the backside of a carbon wire array with $D = 1 \mu\text{m}$, $d = 36 \text{ nm}$ and $L = 10 \mu\text{m}$. The Cu ions are initialized with 5+ charge state and a density $n_{Cu} = 80n_c$. As before, collisional and field ionizations are described. The laser pulse maximum (10^{22} Wcm^{-2}) strikes the Cu foil at $t_r = +33 \text{ fs}$. For this simulation only, the γ -ray photons ($\hbar\omega \geq 1 \text{ MeV}$) are advanced (ballistically) on the simulation domain. The evolution of their density is depicted in Figs. 5.26(a,b). At $t = +13 \text{ fs} < t_r$ [Fig. 5.26(a)], the wires have rapidly expanded (in the leading edge of the laser) to form a relativistically underdense plasma ($n_e \simeq 17n_c$), in which synchrotron emission occurs volumetrically mainly through RESE, as analyzed in Sec. 5.3.2. At $t = +56 \text{ fs} > t_r$ [Fig. 5.26(b)], high-density ($\sim 10n_c$) photon bunches are seen to radiate from the target backside.

The resulting time-integrated energy-angle radiation spectrum is displayed in Fig. 5.27(b), and compared with that obtained from the sole nanowire array [Fig. 5.27(a)]. Comparison of the two spectra reveals the generation of two distinct photon groups. The first one originates from the interaction with the expanded wires, and is broadly distributed in the backward direction ($\theta_\gamma = 2 - 3 \text{ rad}$) with mean energies $\sim 0.4 \text{ MeV}$ (resp. $\sim 2.5 \text{ MeV}$) for $\hbar\omega > 10 \text{ keV}$ (resp. $> 1 \text{ MeV}$). The second one follows the reflection of the laser head off the foil, and its interaction with the electrons still accelerated in the laser tail. As already stressed, the quantum parameter is maximized for the forward-moving electrons that stream against the reflected pulse. Consequently, in this emission stage the radiated energy is mainly, but not entirely, forward-directed, as seen by comparing Figs. 5.27(a) and (b). This secondary emission stage increases the integrated radiation efficiency to $\sim 13\%$ (vs. $\sim 10\%$ without substrate, for $\hbar\omega > 10 \text{ keV}$). Closer analysis reveals that out of the $\sim 26\%$ of laser energy hitting the Cu foil, approximately 13% is further gained by electrons and ions, 3% is converted into photons, and 10% escapes through the target front side.

Finally, we show in Fig. 5.27(c) the energy-angle spectrum recorded from the optimized uniform-density target ($n_e = 16n_c$), giving a radiation efficiency $\eta_\gamma \sim 11\%$ into $> 10 \text{ keV}$ photons. It corroborates our previous findings that optimized nanowire arrays and uniform targets of same average density yield similar photon distributions. Notable differences, however, are visible: the backward-emission cone angle is slightly narrower,

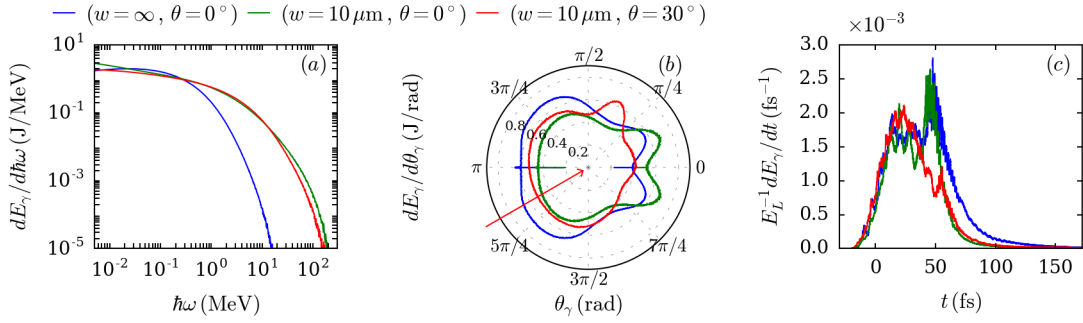


Figure 5.28: Variations of the synchrotron emission with the laser spot size (w) and incidence angle (θ_0): (a) energy spectra, (b) angle-resolved radiated energy and (c) time-resolved radiated power (normalized to the total laser energy E_L). Each color represents a different case as indicated in the legend of panel (a). $w = \infty$ corresponds to the planar wave case. Angles in (b) are defined as $\theta_\gamma = \arctan(k_{\gamma,y}/k_{\gamma,x}) \in (0, 2\pi)$. The red arrow indicates the $\theta_0 = 30^\circ$ incidence angle. All plotted quantities are integrated over the simulation domain.

and is complemented by a distinct, albeit weaker, forward emission around $\theta_\gamma \sim \pi/4$ rad.

While the optimized nanowire array with substrate yields the highest radiation conversion efficiency, $\eta_\gamma = 13\%$ (for $\hbar\omega > 10), its performance falls by an order of magnitude, as does that of the two other types, if we consider only photon energies $> 1 and forward emission angles $\leq 30^\circ$ (as would be relevant for, *e.g.*, creating electron-positron pairs in a thicker high- Z substrate): one then obtains $\eta_\gamma \sim 1.2\%$ with a substrate and $\eta_\gamma \simeq 0.9\%$ from the uniform target.$$

5.4.2 Effect of a finite focal spot and an oblique incidence angle

All the results of the previous sections correspond to a planar laser wave normally incident on a nanowire array. One may wonder whether they still hold in the more realistic case of a focused, possibly obliquely incident, laser beam. The variations of the synchrotron yield with the laser incidence angle have been recently investigated by [Serebryakov and Nerush \(2016\)](#), but this study considered planar targets irradiated at a very high laser intensity ($1.3 \times 10^{23} \text{ W cm}^{-2}$). The strongest emission was found for an incidence angle $\theta_0 \simeq 30\%$ and an electron density $n_{av} \simeq 100n_c$. Our goal here is not to extend this detailed study to the case of nanowire arrays but, rather, to examine briefly how the use of an obliquely incident, focused laser pulse may alter the properties of the emission compared to the optimal planar-wave configuration. To this end, we have run additional simulations in which the $10^{22} \text{ W cm}^{-2}$, 30 fs laser pulse has an 8th-order hyper-Gaussian transverse profile of FWHM $w = 10 \mu\text{m}$, and impinges onto the target at an angle $\theta_0 = 0^\circ$ or 30° . The choice of a hyper-Gaussian transverse profile aims at minimizing intensity gradient effects, thus easing comparison with the planar-wave results. The laser electric field is in the xy plane (p polarization). The target consists of the highest-yield nanowire setup ($d = 36 \text{ nm}$, $D = 1 \mu\text{m}$, $L = 10 \mu\text{m}$ with a Cu substrate) as previously identified.

The changes induced by the laser's finite focal spot size and oblique incidence angle on the synchrotron radiation are displayed in Figs. 5.28(a-c). Since the problem is no longer symmetric relative to the x -axis, the photon emission angles are now defined as $\theta_\gamma = \arctan(k_{\gamma,y}/k_{\gamma,x}) \in (0, 2\pi)$. A striking result [Fig. 5.28(a)] is that a $10 \mu\text{m}$ laser

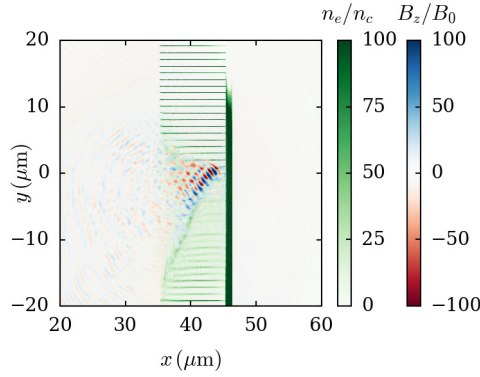


Figure 5.29: Propagation of an obliquely incident, focused laser pulse ($I = 10^{22} \text{ W/cm}^2$) with $w = 10 \mu\text{m}$ and $\theta_0 = 30^\circ$: magnetic field (B_z/B_0 , red-blue colormap) and electron density (n_e/n_c , green colormap) at $t = 83 \text{ fs}$ after the on-target laser peak.

focal spot leads to a 10-fold increase in the cutoff photon energy, which attains $\hbar\omega_{\max} \simeq 150 - 180 \text{ MeV}$ (weakly dependent on θ_0) compared to $\hbar\omega_{\max} \simeq 16 \text{ MeV}$ for a plane wave. The mean photon energies are also increased, albeit to a lower extent, from $\langle \hbar\omega \rangle \simeq 2.5 \text{ MeV}$ (above 1 MeV) for a plane wave to $\langle \hbar\omega \rangle \simeq 3.5 \text{ MeV}$ in the focused case.

These enhanced photon energies stem for the relativistic self-focusing undergone by the finite-spot laser pulse in the homogenized plasma, as observed and exploited by [Bin et al. \(2015\)](#). This phenomenon is illustrated in Fig. 5.29, which displays the maps of the magnetic field and electron density in the $\theta_0 = 30^\circ$ case at $t = 83 \text{ fs}$ after the on-target laser peak. We see that the laser beam has self-focused to a $\sim 2 \mu\text{m}$ spot where it reaches a maximum field strength of $B_z/B_0 \simeq 100$, consistent with the $\sim 75\%$ absorption it has then experienced. At final simulation time, almost $\sim 85\%$ of the laser energy is absorbed. The laser self-focusing significantly affects the electron energy spectra, as shown in Fig. 5.30 at $t = 83 \text{ fs}$. While the electron energy spectra produced by the focused beams show similar temperatures ($T \simeq 65 \text{ MeV}$, such that $dN_e/dE_e \propto \exp(-E_e/T)$) to the planar wave case up to $E_e \simeq 140 \text{ MeV}$, they present additional hotter, high-energy tails, extending up to $E_e \simeq 400 \text{ MeV}$.

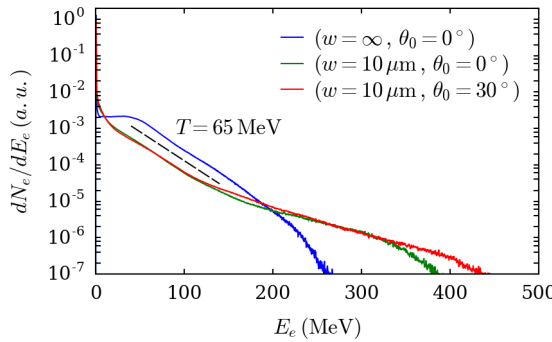


Figure 5.30: Variations of the electron energy spectra dN_e/dE_e with the laser spot size (w) and incidence angle (θ_0). The best-fitting temperature $T = 65 \text{ MeV}$ is computed in the $40 \leq E_e \leq 140 \text{ MeV}$ range.

As a result, the angle-resolved photon spectra obtained with the focused beams show

notable differences with the planar-wave case [Fig 5.28(b)]. At $\theta_0 = 0^\circ$, the backward emission is reduced while the forward radiation is enhanced and emitted into smaller-angle emission lobes ($\theta_\gamma \simeq \pm 20^\circ$). As for the planar wave, the time-resolved radiated power presents two successive maxima corresponding to the laser interaction with the homogenized nanowires and the substrate [Fig. 5.28(c)]. The overall conversion efficiency is found to be slightly lower than that observed using a planar wave ($\eta_\gamma \sim 10.2\% vs. \sim 13\%$), with a larger fraction emitted in the forward ($\theta_\gamma < 90^\circ$) direction ($\sim 49\% vs. \sim 42\%$). At $\theta_0 = 30^\circ$, the backward emission is also lowered (though less than at $\theta_0 = 0^\circ$), yet the main difference concerns the forward emission, peaked at angles $\theta_\gamma \simeq 0^\circ$ and $\theta_\gamma \simeq 67^\circ$. Another difference is the much reduced second maximum in the time-resolved radiated power. This follows from the longer penetration length, and hence increased absorption of the obliquely propagating laser pulse across the nanowires, which therefore interacts at a lower intensity with the substrate. This weakened secondary radiation, however, is compensated for by a strengthened radiation throughout the nanowires, thus leading to a total radiation efficiency ($\sim 10.3\%$) equal to that obtained at normal incidence.

Overall, those results show that the salient radiation properties evidenced in the planar-wave case are significantly, but not strongly, affected by using a few nanowires wide focal spot and a moderately oblique incidence angle.

5.5 Ion acceleration in nanowire arrays

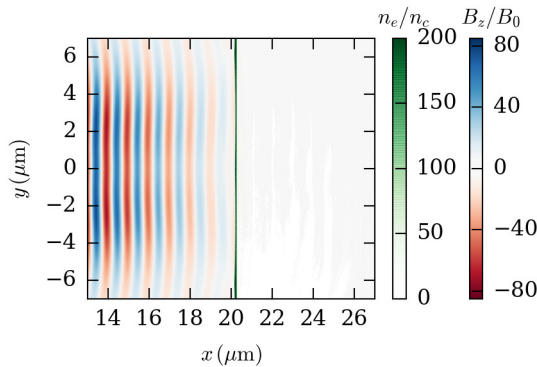


Figure 5.31: Numerical setup for ion acceleration study. The laser has a peak intensity $I = 10^{22} \text{ W/cm}^2$, a 30 fs FWHM duration, a $5 \mu\text{m}$ FWHM focal spot. The figure is plotted at time $t = -33 \text{ fs}$ and zooms in on the sub-domain $(x, y) \in (13, 27) \mu\text{m} \times (-7, 7) \mu\text{m}$ in order to distinguish the thin CH_2 target of length $l = 200 \text{ nm}$ and density $n_e/n_c = 200$.

As mentioned in the introduction of this chapter, ion acceleration in nanostructured targets has already been investigated experimentally and numerically. Studies with foam-attached targets were conducted by [Passoni et al. \(2014\)](#) and [Prencipe et al. \(2016\)](#) (in the intensity range $I = 10^{16-20} \text{ W/cm}^{-2}$), with micro-pillars by [Khaghani et al. \(2017\)](#) ($I = 10^{17-18} \text{ W/cm}^{-2}$), with carbon-nanotube foams attached to micron-size-substrate ([Bin et al., 2015](#)) and even to nano-size-substrates ([Bin et al., 2018](#)) at intensities of approximately $I \simeq 2 \times 10^{20} \text{ W/cm}^{-2}$. Those works are conducted in various irradiation conditions and therefore do not provide a clear evidence for an optimum ion acceleration regime. The record proton energies obtained from relatively long (600 fs) high-intensity ($1.5 \times 10^{20} \text{ W/cm}^2$) pulses interacting with structured target can reach $\simeq 70 \text{ MeV}$ ([Gaillard et al., 2011](#)).

With flat foils, there is a concensus on the fact that proton acceleration is maximized for thin foils, (tens of nm) for a short (25 fs) and moderately intense laser pulse ($I \simeq 10^{19} \text{ W/cm}^2$) (Loch *et al.*, 2016). For higher laser intensity, $I \simeq 3 \times 10^{20} \text{ W/cm}^2$, the best performance obtained so far is $\simeq 100 \text{ MeV}$ (Higginson *et al.*, 2018). Using structured targets at higher laser intensity $I = 10^{22} \text{ W/cm}^2$ may improve the proton acceleration compared to the optimum nanometric flat foils. For this reason, we investigate the proton acceleration induced by an intense (10^{22} W/cm^2) laser pulse interacting with nanowire arrays.

Firstly, we recall the results obtained for flat foils where optimum acceleration conditions have already been identified by Esirkepov *et al.* (2006) and Brantov *et al.* (2015). Secondly, we investigate how ion acceleration changes by varying the substrate length or the nanowire length. We finally initiate a comparison with uniform foams and illustrate on an example that differences can arise even with equivalent nanowire arrays which have the same length and average density.

As we are limited to a 2D geometry that is well-known to over-estimates the ion acceleration due to an unexact treatment of electron dilution and spatial decay of space charge fields, we will not directly focus on the peak performances of ion acceleration. Instead we will underline its relative variations with the problem's parameters. In this section we are particularly interested in the evolution of the maximum proton energy (E_{H^+}).

5.5.1 Numerical setup and optimized regime for flat targets

In what follows, the laser pulse is modeled as a focused electromagnetic wave with a Gaussian transverse profile of $5 \mu\text{m}$ FWHM, propagating along the x axis, linearly polarized along the y direction and with a central wavelength $\lambda_0 = 1 \mu\text{m}$. The laser pulse has a Gaussian temporal profile with a 30 fs FWHM and a peak intensity $I = 10^{22} \text{ Wcm}^{-2}$ (corresponding to a dimensionless field amplitude $a_L = 85$). The foil is made of solid density ($n_e/n_c = 200$) fully ionized CH₂ and has a thickness denoted by l which is $l = 200 \text{ nm}$. The 2D simulation domain has dimensions $L_x \times L_y = 80 \mu\text{m} \times 80 \mu\text{m}$, with a spatial resolution $\Delta x = \Delta y = \lambda_0/140$. The temporal resolution is $\Delta t = \tau_0/250$ (where $\tau_0 = \lambda_0/c = 3.3 \text{ fs}$ is the optical cycle) and the simulation is run over $30\,000\Delta t$. The boundary conditions are taken to be absorbing along x and y for both fields and particles. We use 250 to 100 macro-particles per cell per species for the substrate, depending on its length which varies from 100 to 400 nm. The total number of macro-particles per species is 9×10^7 . The peak of the laser pulse hits the substrate at time $t = 0$. This setup is illustrated in Fig. 5.31.

	CH ₂ thin foil
Sec. 5.5.1	length $l = 100 \rightarrow 400 \text{ nm}$

Table 5.2: Overview of the parametric scan performed in Sec. 5.5.1. The length l of a CH₂ thin foil is varied with all other parameters fixed and detailed in the text.

Using 2D and 3D simulations, an optimum regime of ion acceleration in thin foils has already been identified by Esirkepov *et al.* (2006) and Brantov *et al.* (2015). For a laser pulse of maximum field strength a_L and a target of initial electron density n_{e0} , the optimal target thickness is found to be

$$l_{opt} \simeq 0.5a_L \frac{n_c}{n_{e0}} \lambda_0 \quad (5.1)$$

This condition is similar to that derived by Vshivkov *et al.* (1998), yielding strong laser

	nanowire array ($Z = 6$)			substrate (CH_2)
	inter-spacing D	thickness d	length L	length l
Sec. 5.5.2	1 μm	36 nm	10 μm	100 \rightarrow 300 nm
Sec. 5.5.3	1 μm	36 nm	0 \rightarrow 10 μm	200 nm

Table 5.3: Overview of the parametric scan performed in Sec. 5.5.2 and Sec. 5.5.3. The main parameters of the wire array and substrate are summarised and the other parameters are detailed in the text.

transmission across a thin foil. While a significant laser transmission ensures a volumetric heating of the target electrons, which favors ion acceleration, the optimum condition may be given a more meaningful interpretation. To this purpose, let us consider a thin foil of initial electron density n_{e0} . Let us now assume that the target electrons are volumetrically heated to a mean energy $\langle \gamma_e \rangle \simeq a_L$, and subsequently expand to a cloud of typical length equal to their Debye length $L_D \omega_0 / c = (\langle \gamma_e \rangle n_c / n_e)^{1/2}$. Here n_e is the typical density of the hot electron cloud. Charge conservation implies initially $n_{e0} l = n_e L_D$. Volumetric heating of the target involves laser transmission $n_e \leq a_L n_c$, so that $l_{opt} \leq a_L (n_c / n_{e0}) (c / \omega_0)$ as expected. Setting $l = l_{opt}$ ensures both volumetric heating and a maximal electrostatic field seen by the target ions, this field is given by $E_x = e n_{e0} l / 2\epsilon_0$. In Eq. (5.1) the coefficient 0.5 best fits the 3D PIC simulations of [Brantov et al. \(2015\)](#) for CH_2 targets and $a_L = 1 \rightarrow 100$. For our parameters ($a_L = 85$, $n_e = 200$), which lie in this range (except for the 2D geometry), the predicted optimum thickness is

$$l_{opt} = 210 \text{ nm} \quad (5.2)$$

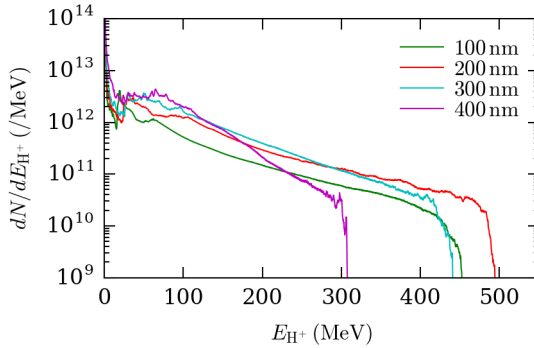


Figure 5.32: Proton energy spectra from the interaction of a 10^{22} W/cm^2 , 30 fs laser pulse with flat CH_2 foils of increasing length ($l = 100, 200$ and 300 nm). The spectra are reported at the final time $t = 240$ fs.

We report the proton energy spectra as a function of the substrate length ($l = 100, 200, 300$ and 400 nm) in Fig.5.32. We observe that the optimum thickness found numerically (200 nm) is in fair agreement with the expected estimate (210 nm) provided by formula (5.2). The highest energy protons ($\simeq 500$ MeV) are still gaining energy at time $t = 240$ fs, when they are leaving the simulation domain. One should consider their maximum energy carefully for two reasons. Firstly, because the 2D geometry overestimates the electron density and heating in the polarization plane and the subsequent ion acceleration, as underlined by [Stark et al. \(2017\)](#). Secondly, because 3D effects will prevail at some point

and strongly mitigate ion acceleration so that carrying the 2D simulation further becomes unphysical (Prencipe *et al.*, 2016). A criterion employed by Brantov *et al.* (2015) is to state that 3D effects prevail as the ions have been accelerated on a distance approximately equal to the laser focal spot.

The mechanism at the origin of such a high ion acceleration has been identified. We present in Figs. 5.33(a,b) and in Figs. 5.34(a,b) the ion acceleration mechanism before the on-target pulse peak ($t \leq 0$ fs). We then detail the effect of laser transmission (taking place for $t \geq 3.5$ fs) on this mechanism in Figs. 5.35(a,b) and Figs. 5.36(a,b).

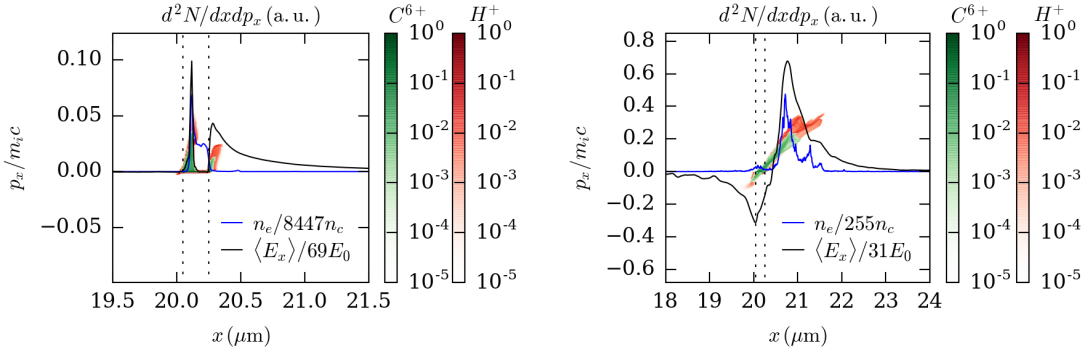


Figure 5.33: $x - p_x$ phase space of H^+ (red colorbar) and C^{6+} (green colorbar) with the longitudinal accelerating electrostatic field $\langle E_x \rangle / E_0$ on axis ($y = 0$, black curve) and the electron density on axis ($y = 0$, blue curve) at times (a) $t = -26$ fs and (b) $t = 0$ fs. The flat CH_2 foil has a thickness $l = 200$ nm and its initial position is marked by the dotted lines. The peak laser intensity is 10^{22} W/cm^2 ($a_L = 85$).

The laser has a 30 fs FWHM so that at time $t = -26$ fs represented in Fig. 5.33(a) the laser intensity is $\simeq 10^{20} \text{ W/cm}^2$. In Figs. 5.33(a,b) the 2D colormaps represent $x - p_x$ phase spaces of protons (red colorbar) and carbon ions (green colorbar) at times $t = -26$ and 0 fs. The electron density n_e/n_c and longitudinal electrostatic field $\langle E_x \rangle / E_0$ are taken on the laser axis ($y = 0$), superimposed and re-scaled by an adequate factor so that they share their y axis with $p_x/m_i c$. We see in those figures that the electrons located in the plasma skin depth (abscissa $x = 20.05 \mu\text{m}$) are compressed and form an overdense layer ($n_e/n_c = 0.06 \times 8447 \simeq 507$). The ions therefore see a charge separation field ($\langle E_x \rangle / E_0 = 0.1 \times 0.69 \simeq 6.9$) and are accelerated in a RPA regime with momentum $p_x/m_{Hc} = 0.05$ for protons and $p_x/m_{Cc} = 0.035$ for carbon ions (see Sec. 4.1.5 for a clear explanation of RPA mechanism). The fast electrons generated at the rear side of the target (abscissa $x = 20.25 \mu\text{m}$) also create a charge separation field ($\langle E_x \rangle / E_0 = 0.05 \times 69 \simeq 3.5$) accelerating protons ($p_x/m_{Hc} = 0.022$) and carbon ions ($p_x/m_{Cc} = 0.012$) through the TNSA mechanism (see Sec. 4.1.5 for details about this process). The ions pushed at the front of the target catch up with the ions accelerated at the back at time $t = 0$ fs (see Fig. 5.33(b)). The two fields previously observed are now merged and reach a strength $\langle E_x \rangle / E_0 = 0.7 \times 31 \simeq 22$, one quarter of the laser field strength. The two populations of ions accelerated via TNSA and RPA both benefit from this merged field structure. Since both RPA and TNSA driven protons caught up, the target is moving as a whole in a Light Sail Acceleration (LSA) regime (see Sec. 4.1.5 for an introduction to LSA). It is characterized in Fig. 5.34(a,b). One can see in Fig. 5.34(a) that the laser is pushing forward a thin layer of electrons which has an overcritical density ($n_e/n_c \simeq 130$). Fig. 5.34(b) evidences the motion of the whole target with the carbon and hydrogen density. During this LSA phase, starting at $t \simeq 0$ fs, protons reach longitudinal momentum $p_x/m_{Hc} = 0.35$

and carbon ions $p_x/m_{CC} = 0.21$ (see Fig. 5.33(b)). This dynamic transition from mixed RPA-TNSA to LSA was already reported by [Qiao et al. \(2012\)](#).

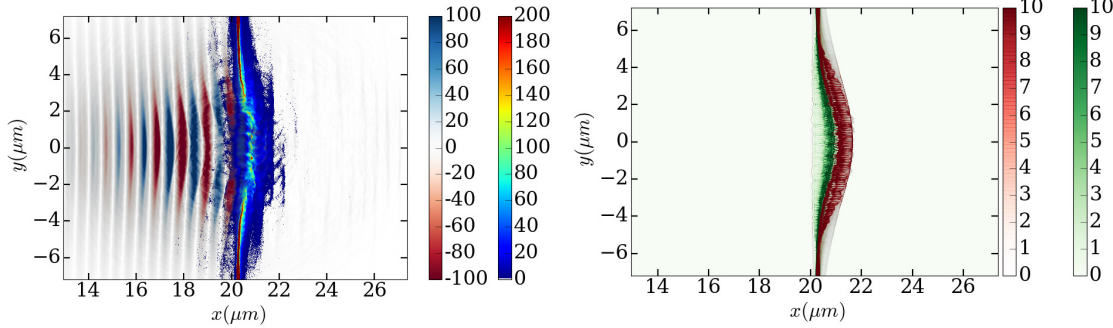


Figure 5.34: (a) Laser field distribution (B_z/B_0 , red/blue colorbar) and electron density n_e/n_c (rainbow colorbar); (b) Proton density (red colorbar) and copper density (green colorbar). Both pictures are taken at the pulse peak on target $t = 0$ fs. The flat CH₂ foil has an initial thickness $l = 200$ nm. The peak laser intensity is 10^{22} W/cm² ($a_L = 85$).

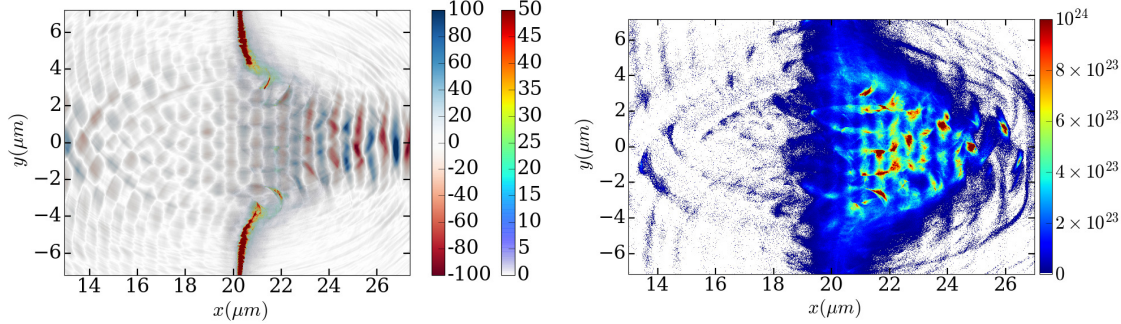


Figure 5.35: (a) Laser field distribution (B_z/B_0 , red/blue colorbar) and electron density n_e/n_c (rainbow colorbar); (b) Energy density of electrons Een_e (MeV/cm³). Both images are represented at time $t = 26$ fs. The CH₂ foil has an initial thickness $l = 200$ nm. The peak laser intensity is 10^{22} W/cm² ($a_L = 85$).

For a time $t = 3.5 \pm 3.5$ fs, the electron density bump seen in Figs. 5.34(a) decreases below the transparency threshold. The laser is then transmitted. A few laser cycles after this ($t = 26$ fs), we clearly observe this transparency in Fig. 5.35(a) where the laser field and the electron density are both represented. The laser transmission gives rise to an efficient electron heating as noted on the electron energy density in Fig. 5.35(b). This additional electron heating amplifies the accelerating field $\langle E_x \rangle$ which reaches a maximum $\langle E_x \rangle \simeq 10E_0$ at time $t = 26$ fs (see Fig. 5.36(a)). We can see the effect of this accelerating field on the protons and carbon ions in their $x - p_x$ phase space plotted in Fig. 5.36(b). They overlap with the strong $\langle E_x \rangle \simeq 10E_0$ field and subsequently reach high longitudinal momentum $p_x/m_{HC} = 0.6$ and $p_x/m_{CC} = 0.4$. At final simulation time ($t = 240$ fs) their respective longitudinal momentum are $p_x/m_{HC} = 1.15$ and $p_x/m_{CC} = 0.49$.

We evidenced two mechanisms enhancing ion acceleration during the interaction of an intense laser with a thin foil. Firstly, the RPA-driven ions coming from the target front can benefit from the TNSA-driven accelerating field if they catch up with TNSA-driven ions at the rear side of the foil, conducting to a LSA regime. Secondly, the onset of RSIT leads to an efficient volumetric heating of target electrons which can in return

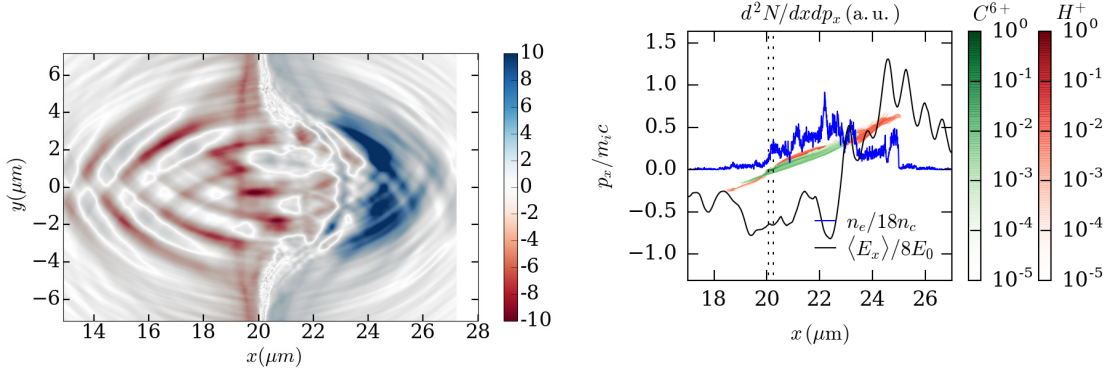


Figure 5.36: (a) Longitudinal electrostatic field $\langle E_x \rangle / E_0$ at time $t = 26$ fs; (b) $x - p_x$ phase space of H^+ (red colorbar) and C^{6+} (green colorbar) with the longitudinal static electric field $\langle E_x \rangle / E_0$ on axis ($y = 0$, black curve) and the electron density on axis ($y = 0$, blue curve). Both images are represented at time $t = 26$ fs. The CH₂ foil has a thickness $l = 200$ nm and its initial position is marked by the dotted lines.

transfer their energy to ions via the longitudinal electrostatic field. Understanding in details how the relative effectiveness of those two processes evolve with the target thickness is challenging. We provide one reason why it can be maximized for $l = 200$ nm in Fig. 5.37. We plot the evolution of the maximum ion energy and add the estimated time for the laser transparency to take place with errorbars. In particular for $l = 200$ nm the transparency occurs at the pulse peak on target, thus maximizing the coupling between the laser energy and the hot electrons boosting proton acceleration. The catch-up dynamic between RPA and TNSA-driven ions is more complex to evaluate because of the spatial extend of the proton bunches. One can emphasize that for the optimum case ($l = 200$ nm) it takes place relatively close (\simeq one laser cycle) to the laser transparency.

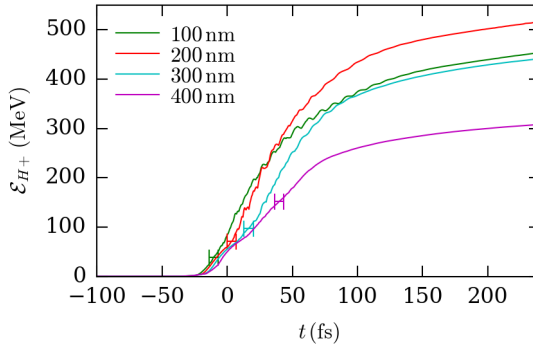


Figure 5.37: Evolution of the maximum proton energy as a function of the foil thickness varying from $l = 100$ to 400 nm. The laser peak intensity (10^{22} W/cm^2) arrival on target is set to $t = 0$ fs. The estimated transparency time is showed with an horizontal error bar.

There are other possible explanations in the literature to explain this ion acceleration enhancement due to the laser transmission through the target plasma. [Yin et al. \(2006\)](#) suggested that the difference between the drift velocities of the fast electrons and ions triggers a relativistic Buneman instability that induces an efficient energy transfer from electrons to ions. On the experimental side, [Higginson et al. \(2018\)](#) evidenced that ions accelerated by the RPA mechanism catch up with the ones accelerated by the TNSA to

form a single bunch. We do observe that behavior in Fig. 5.36(b) for protons. However this study ignores the interplay with the carbon ions and we note in Fig. 5.36(b) that they modify substantially the accelerating field $\langle E_x \rangle$ that presents several oscillations. Heavy ions were demonstrated to play a substantial role on proton acceleration by [Bulanov et al. \(2008\)](#). Indeed they modify the charge separation field which accelerates the proton acceleration. An additional argument confirms the feedback between the two ion species as we note in Fig. 5.36(b) that they overlap.

Overall we recalled and characterized the best case scenario for ion acceleration from a flat foil. We will now examine the potential benefit of adding a nanowire array onto a nanometric foil.

5.5.2 Substrate length dependence of ion acceleration

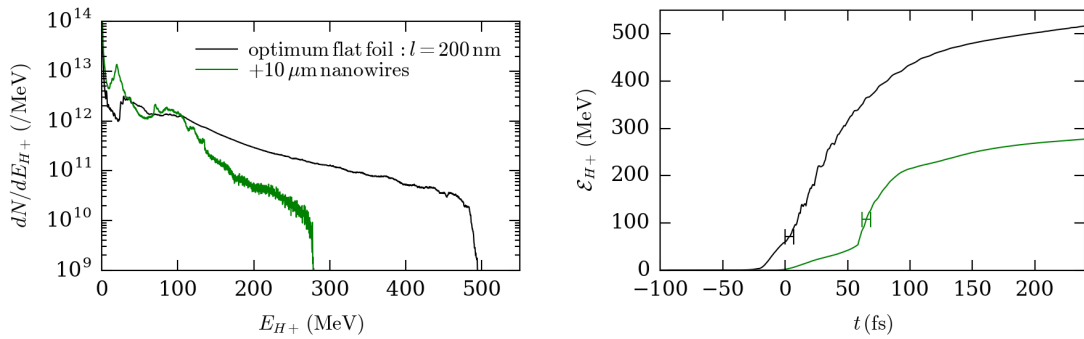


Figure 5.38: (a) Energy-resolved proton spectra at $t = 240$ fs; (b) evolution of maximum proton energy for the optimum flat foil ($l = 200$ nm) and with wires attached to this foil ($+10 \mu\text{m}$ wires). The nanowires' width, interspacing and length are set to $d = 36$ nm , $D = 1 \mu\text{m}$ and $L = 10 \mu\text{m}$. The laser peak intensity (10^{22} W/cm^2) arrival on the flat CH_2 foil (or the wires) is set to $t = 0$ fs. The estimated transparency times are showed with horizontal error bars.

We have demonstrated in Sec. 5.3.4 that a nanowire array target can be very beneficial to laser absorption which can be as high as $\simeq 80\%$ in $10 \mu\text{m}$ long nanowire-array of optimized width and interspacing. Since this enhancement mainly originates from an improved coupling with the wires' electrons, it is tempting to examine whether it could favor the acceleration of protons from a thin foil attached to the nanowire array.

To investigate this problem, we consider the setup that maximizes the laser absorption: it is composed of carbon wires, measuring $L = 10 \mu\text{m}$, with a diameter $d = 36$ nm and with a spacing $D = 1 \mu\text{m}$ (Section 5.3.4). We attach it to a flat CH_2 substrate of length $l = 200$ nm that is known to maximize proton acceleration from Section 5.5.1. In simulations with nanowire arrays, the time $t = 0$ fs denotes the arrival time of the pulse peak at the wires entrance, and not on the substrate.

Fig. 5.38(a) compares the proton energy spectra obtained with or without the nanowire-array. We see that the maximum proton energy is dramatically reduced from $\simeq 500$ MeV to $\simeq 280$ MeV. In the optimum thin foil case, efficient proton acceleration proceeds through both the interplay of RPA and TNSA (*i.e.*, the frontside protons driven by the laser piston overtake the TNSA backside protons, hence taking advantage of the hot electron induced sheath field) and the onset of RSIT at the laser peak, which further heats the electrons and sustains the sheath field.

The generation of hot electrons (≥ 25 MeV) mainly occurs in the nanowire region: their total number (8×10^{11}) is largely increased compared to the isolated foil (2×10^{11}), but their density around the backside of the substrate is reduced ($n_h \simeq n_{av} \simeq 17n_c$ vs $n_h \simeq 120n_c$). A significant number of hot electrons is also produced during the laser-substrate interaction, but due to the then reduced laser energy, this process is less efficient than in the isolated foil, and those electron rapidly mix with the electrons originating from the nanowires.

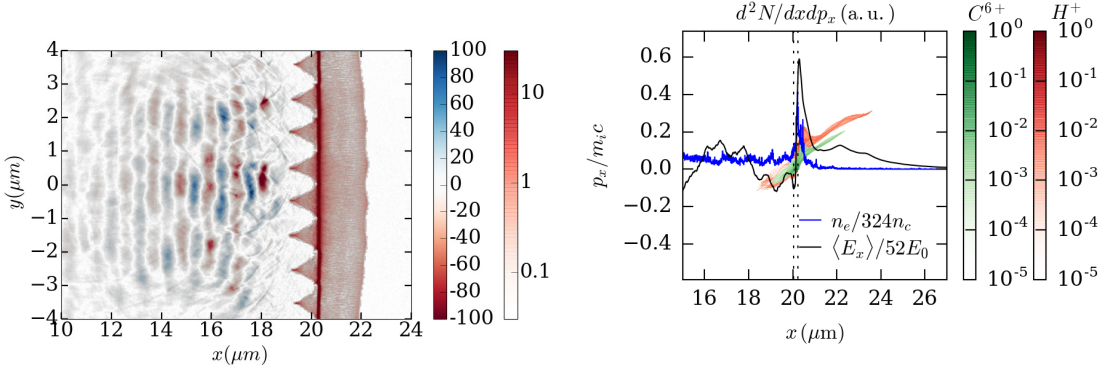


Figure 5.39: (a) Laser field distribution (B_z/B_0 , red/blue colorbar) and proton density n_H/n_c (red colorbar) before the pulse peak hits the substrate at time $t = 35$ fs; (b) Weak RPA observed from $x - p_x$ phase space of H^+ (red colorbar) and C^{6+} (green colorbar) with the longitudinal static electric field $\langle E_x \rangle/E_0$ on axis ($y = 0$, black curve) and the electron density on axis ($y = 0$, blue curve) at time $t = 53$ fs. The nanowires' width, interspacing and length are set to $d = 36$ nm, $D = 1 \mu\text{m}$ and $L = 10 \mu\text{m}$, the CH_2 substrate has a thickness $l = 200$ nm.

The RPA driven by the partially absorbed laser pulse is weakened, there is indeed 50% of absorption in the wires before the pulse arrival on the substrate. It starts as the laser hits the substrate for $t = 53$ fs and is illustrated in Fig. 5.39(b). We clearly see a compression of the electrons $n_e/n_c \simeq 80$ associated with a strong accelerating field $\langle E_x \rangle/E_0 \simeq 30$, approximately one third of the laser field amplitude. The RPA is strong enough to allow the protons from the foil's front side to catch up with those expanding in the backside TNSA field (at $t \simeq 170$ fs). While reproducing the hybrid RPA/TNSA process found to be optimum in the isolated foil, the nanowire-array target is less efficient because both mechanisms are then weakened. The 'poor' performance of RPA is expected because $v_{HB} \propto a_L$; that of TNSA is also anticipated. Indeed fast electrons from the wires ($\beta \simeq 1$) propagate faster than the laser ($\simeq 0.5c$) and pre-heat the substrate, leading to its premature expansion. We observe this premature expansion of protons in Fig. 5.39(a) and recall that it mitigates TNSA acceleration since the measured rear-side proton density scale length $\simeq 1.6c/\omega_0$ is comparable to the electrons Debye length $\lambda_{dh} \simeq 2.2c/\omega_0$. The proton expansion seen in front of the substrate is driven by the neutralizing return currents of electrons localized in the edges of the wires. The acceleration dynamic of the foil's protons is plotted in Fig. 5.38(b) with or without the nanowire array. As expected, the protons are accelerated more rapidly at early times in the simple foil case. One can observe a steeper slope of the curve representing the evolution of the maximum proton energy between times $t \simeq 60$ and 100 fs with wires. It is attributed to the plasma transparency (signaled with the horizontal errorbar). The transmitted fraction of the laser is therefore superimposed with the electrons forming the TNSA accelerating field and heats them, which subsequently rises the accelerating field, since $\langle E_x \rangle/E_0 \propto \sqrt{n_h \gamma_h/n_c}$. This behavior was already evidenced

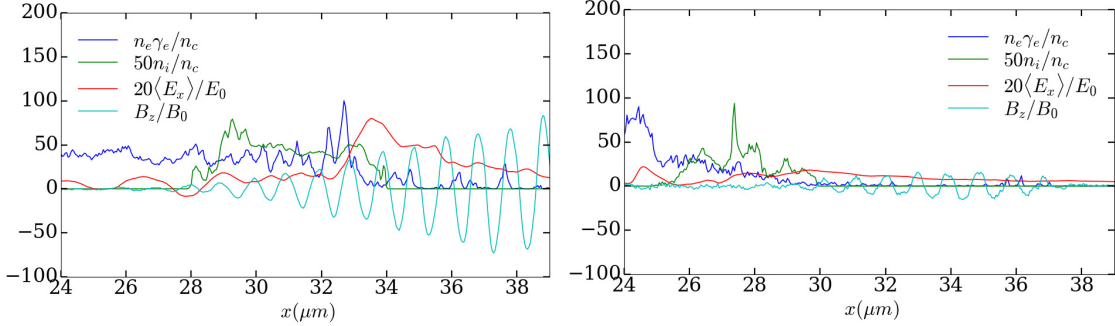


Figure 5.40: Electron energy density ($n_e \gamma_e / n_c$), ion density (n_i / n_c), electrostatic field ($\langle E_x \rangle / E_0$), laser field (B_z / B_0) on axis ($y = 0$) at time $t = 106$ fs (a) for the optimum (200 nm-long) flat foil made of CH_2 (b) with 10 μm -long wires attached to it. The nanowires' width and interspacing are set to $d = 36$ nm and $D = 1$ μm .

for the optimum flat foil ($l = 200$ nm, see Figs. 5.35 and 5.36). There are, however, two major differences during this phase of acceleration which explain why it remains more efficient with the simple foil than with the nanowire array. Firstly, the nanowires absorb a significant fraction of the laser energy (50%) such that the transmitted laser field is much lower than for the simple flat foil as seen in Fig. 5.40(a,b) on the light blue curves. As a consequence the potential energy transfer between electrons and ions is mitigated with the nanowire array compared to the flat foil. Secondly, protons acquire a higher longitudinal momentum with the flat foil than with the nanowire array. The result is that their dephasing length with the transmitted laser field is longer and that they take advantage of it on a longer time.

In the nanowire case, the late-time ($t \geq 150$ fs) acceleration seems to proceed at a faster rate: $a c \omega_0 = 1.3 \times 10^{-4}$ vs $a c \omega_0 = 8.0 \times 10^{-5}$ for the flat foil. At the final simulation time ($t = 240$ fs after the on-target peak) maximum proton energy is still about half that obtained with the simple foil. One could argue that the proton acceleration in the nanowire-foil target is handicapped by too short simulation time; the proton front, however, has then moved a distance of $25 - 30 \mu\text{m}$, higher than the transverse size of the sheath field, and so we expect that, in a realistic 3D geometry, the sheath field would decay faster than in the present 2D simulations, and hence, it does not seem physically meaningful to increase their duration.

We now compare ion acceleration for increasing substrate length from $l = 100$ to 300 nm. To this purpose, we report the proton dynamics in Figs. 5.41(a,b). The instant when the substrate becomes transparent to the laser field is reported in Fig. 5.41(b) by an horizontal error bar. For a substrate of length $l = 100$ nm, the substrate electron density, initially at a level of $n_e / n_c = 200$, falls close to the RSIT threshold ($n_e / n_c \simeq 75$) before the pulse arrival on the substrate as illustrated in Fig. 5.42(a). The substrate electron density decrease is driven by its early heating driven by fast electrons generated in the wires and by return currents localized on the edges of the wires. Those currents tend to neutralize the charge separation field induced by the interaction of the intense laser with the wires. The peak of the laser pulse shines through the substrate without driving RPA (see Fig. 5.42(b)). As the substrate length is $l = 200$ nm, the exploded foil is still opaque (see the phase space in Fig. 5.43(a)) thus giving rise to RPA (see Fig. 5.43(b)), albeit with reduced efficiency due to partially depleted laser pulse. RSIT occurs in the laser down-ramp; by then the RPA driven protons are moving faster than the TNSA-driven ones (see Fig. 5.43(b)). The extra electron heating associated with RSIT takes place in

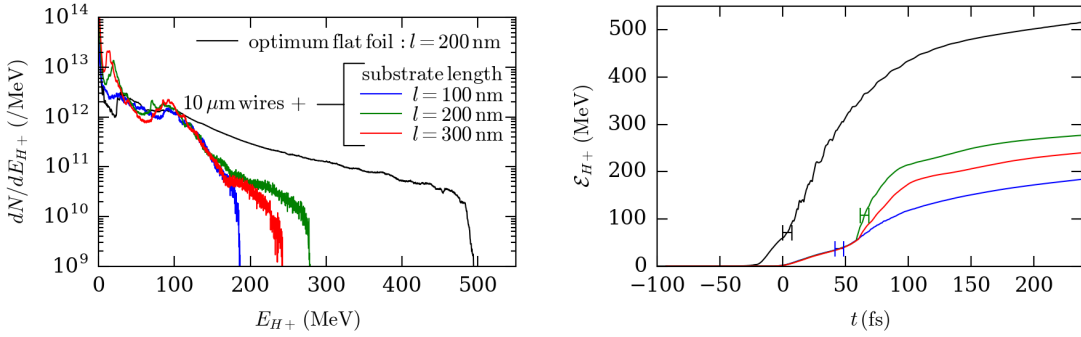


Figure 5.41: (a) Energy-resolved proton spectra at $t = 240$ fs; (b) evolution of maximum proton energy for substrates of varying length ($l = 100$, 200, and 300 nm). The nanowires' width, interspacing and length are set to $d = 36$ nm, $D = 1$ μm and $L = 10$ μm . The laser peak intensity (10^{22} W/cm^2) arrival on the flat CH_2 foil (or the wires) is set to $t = 0$ fs. The estimated transparency times are showed with horizontal error bars.

a plasma profile with a larger length scale than the isolated foil case, which mitigates its beneficial effect (the RPA protons are lagging behind the outermost TNSA protons). For a substrate length $l = 300$ nm the premature expansion of the substrate, which is less pronounced than for a substrate length $l = 200$ nm as seen in Fig. 5.44(a), decreases the efficiency of RPA since the hole boring velocity scales as $\propto n_i^{-1/2}$. The proton phase spaces in Fig. 5.43(b) and in Fig. 5.44(b) show longitudinal momentum $p_x/m_{Hc} \simeq 0.5$ for the 300 nm-thick substrate while it peaks at $p_x/m_{Hc} \simeq 0.6$ for the 200 nm-thick one. In addition, the beneficial effect of transparency does not take place at all for the 300 nm-thick substrate as it remains opaque as seen in Figs. 5.44(b).

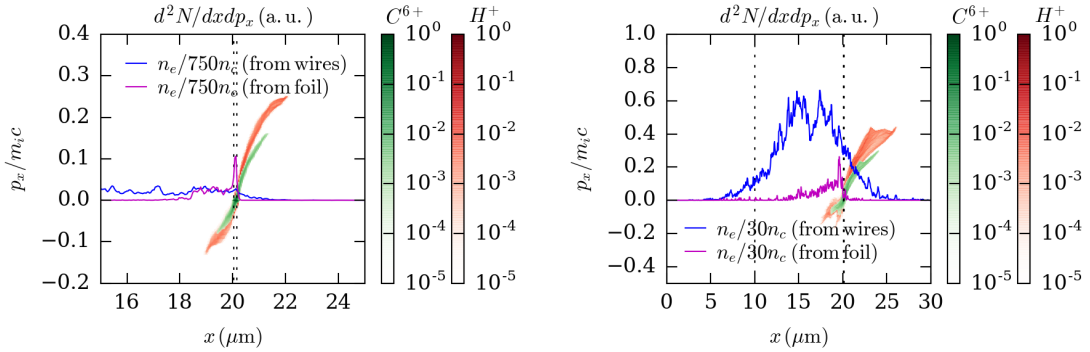


Figure 5.42: $x - p_x$ phase space of protons (red colorbar) and carbon ions (green colorbar), on-axis density of electrons initially in the wires (blue curve) and initially in the substrate (purple curve) (a) at time $t = 35$ fs (before pulse arrival on substrate) and (b) at time $t = 77$ fs (after laser transparency). The nanowires' width, interspacing and length are set to $d = 36$ nm, $D = 1$ μm and $L = 10$ μm , the CH_2 substrate has a thickness $l = 100$ nm. The laser peak intensity (10^{22} W/cm^2) arrival on the wires is set at time $t = 0$ fs.

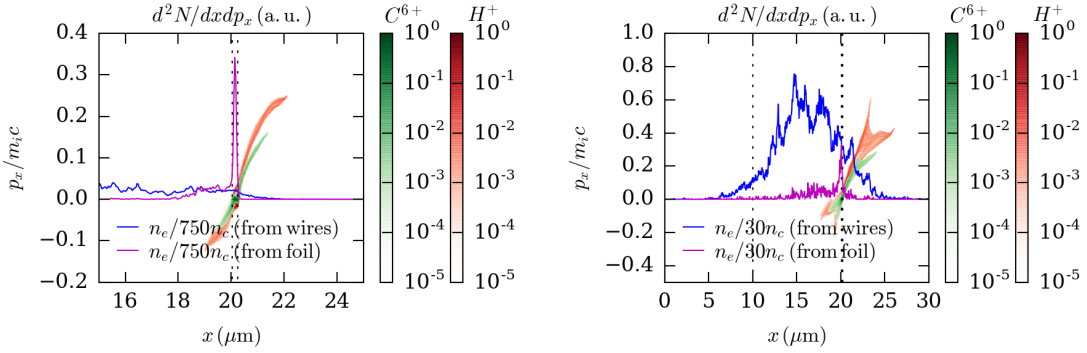


Figure 5.43: $x - p_x$ phase space of protons (red colorbar) and carbon ions (green colorbar), on-axis density of electrons initially in the wires (blue curve) and initially in the substrate (purple curve) (a) at time $t = 35$ fs (before pulse arrival on substrate) and (b) at time $t = 77$ fs (after laser transparency). The nanowires' width, interspacing and length are set to $d = 36$ nm, $D = 1 \mu\text{m}$ and $L = 10 \mu\text{m}$, the CH₂ substrate has a thickness $l = 200$ nm. The laser peak intensity (10^{22} W/cm^2) arrival on the wires is set at time $t = 0$ fs

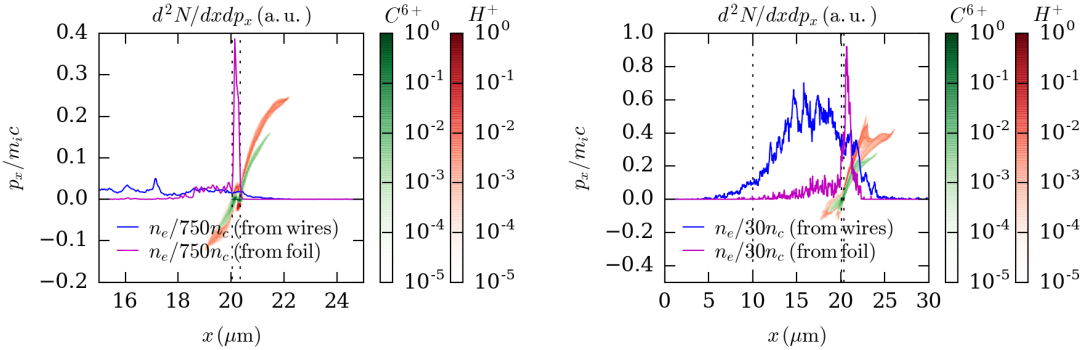


Figure 5.44: $x - p_x$ phase space of protons (red colorbar) and carbon ions (green colorbar), on-axis density of electrons initially in the wires (blue curve) and initially in the substrate (purple curve) (a) at time $t = 35$ fs (before pulse arrival on substrate) and (b) at time $t = 77$ fs (the substrate remains overcritical). The nanowires' width, interspacing and length are set to $d = 36$ nm, $D = 1 \mu\text{m}$ and $L = 10 \mu\text{m}$, the CH₂ substrate has a thickness $l = 300$ nm. The laser peak intensity (10^{22} W/cm^2) arrival on the wires is set at time $t = 0$ fs

5.5.3 Nanowire length dependence of ion acceleration

We now address the variations of proton acceleration with the nanowire's length. The CH₂ substrate is the one optimizing the proton cutoff energy ($\simeq 500$ MeV) in the absence of nanowires.

The proton energy spectra obtained for $L = 1, 3, 5$ and $10 \mu\text{m}$ are plotted in Fig. 5.45(a) with the optimum flat foil case for reference (equivalent to $L = 0 \mu\text{m}$). The $L = 10 \mu\text{m}$ setup, considered previously, is clearly not the optimum one. The maximum proton energy ($E_{H^+}^{\max} \simeq 500$ MeV) is recorded for $L = 3 \mu\text{m}$ and associated with a spectra very close to the flat foil case. Surprisingly, the $L = 3 \mu\text{m}$ configuration appears to be a local optimum as the $L = 1$ and $5 \mu\text{m}$ cases show slightly reduced performances: ($E_{H^+}^{\max} \simeq 460$ MeV) in both cases, with similar spectra except very near the energy cutoff. In the range $0 \leq L \leq 5 \mu\text{m}$

the proton cutoff energy varies less than 10%. The weak dependence of the proton spectra

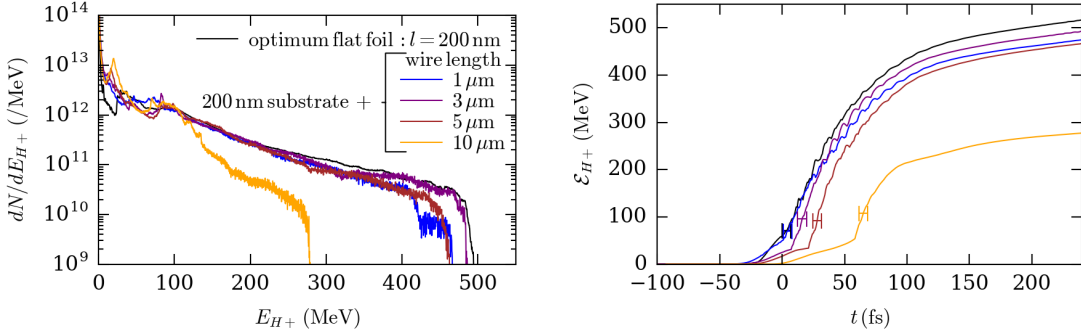


Figure 5.45: (a) Energy-resolved proton spectra at $t = 240$ fs; (b) evolution of maximum proton energy for nanowire arrays targets of varying length ($L = 1, 3, 5$ and $10 \mu\text{m}$), the nanowires' width and interspacing are set to $d = 36 \text{ nm}$ and $D = 1 \mu\text{m}$. The laser peak intensity (10^{22} W/cm^2) arrival on the flat CH_2 foil (or the wires) is set to $t = 0$ fs. The estimated transparency times are showed with horizontal error bars.

in the range $0 \leq L \leq 5 \mu\text{m}$ suggests that, despite variations in each of the acceleration process (RPA, TNSA, more or less boosted by the laser transparency), the efficiency of their combination is essentially unchanged. In the optimum case $L = 3 \mu\text{m}$ we underline that the transparency occurs at a time $t \simeq 15$ fs (see the errorbar in Fig. 5.45(b)). To understand how the previously identified mechanisms operate with shorter wires ($L = 3 \mu\text{m}$), we illustrate in Figs. 5.46(a,b) the proton phase space before ($t = 3$ fs) and after ($t = 30$ fs) transparency. We superimpose this phase space with the laser field distribution on axis (B_z/B_0), the accelerating field on axis ($\langle E_x \rangle/E_0$) and the electron density on axis (n_e/n_c). Contrary to the $10 \mu\text{m}$ -long wire case, the laser still carries enough energy to strongly accelerate protons by the RPA mechanism (see Fig. 5.46(a) illustrating the interaction before transparency at $t = 3$ fs). A few laser cycles after transparency takes place (at time $t = 30$ fs), the RPA-driven protons are seen to catch-up with the TNSA protons and thus benefit form the TNSA accelerating field. While transparency occurs before the two ion populations catch-up with the optimal nanowire-array target, it takes place after for the optimal flat foil case.

From Fig. 5.47, illustrating the wire's length dependence of the laser transmission through the nanowire array target, one can understand that employing short wires ($0 \leq L \leq 5 \mu\text{m}$) is a good mean to observe a significant transparency. The ability for the laser to go through the expanded substrate has a beneficial effect on electron heating and therefore on proton acceleration (see Section 5.5.1). Increasing the wire's length up to $L = 5 \mu\text{m}$ enhances the laser absorption into hot electron and subsequently maintains an efficient proton acceleration (see Section 5.5.2). However, if the wire's length is too high ($L = 10 \mu\text{m}$), the transmission rate drops to $\simeq 5\%$, mitigating its positive impact. In addition, the laser depletion in the wires decreases the efficiency of the RPA and TNSA processes, leading to dramatically reduced peak proton energies from $\simeq 500 \text{ MeV}$ (for $L \leq 5 \mu\text{m}$) to $\simeq 280 \text{ MeV}$ (for $L \leq 10 \mu\text{m}$).

5.5.4 Comparison of nanowire-foil and foam-foil targets

In Sec. 5.3.4, it was shown that nanowire and uniform targets of same average density $n_{av}/n_c \leq 50$ (*i.e.* $d \leq 100 \text{ nm}$ with a spacing $D = 1 \mu\text{m}$) behave similarly in terms of

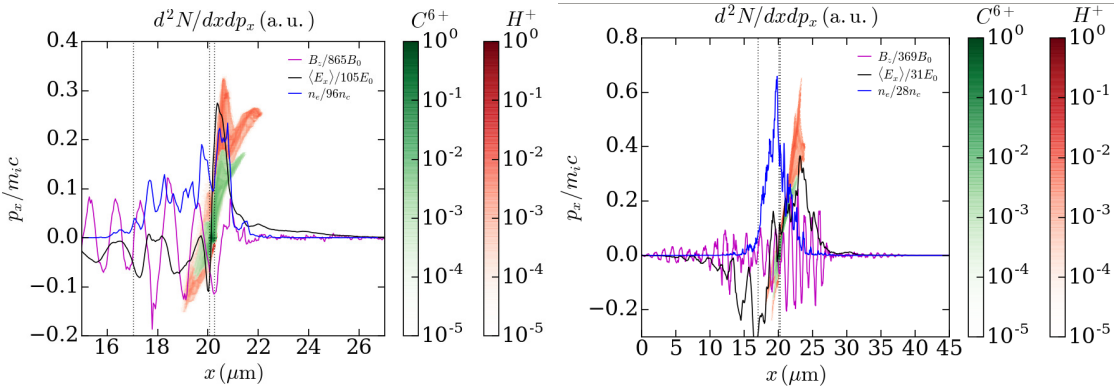


Figure 5.46: $x - p_x$ phase space of H^+ (red colorbar) and C^{6+} (green colorbar) with the longitudinal static electric field $\langle E_x \rangle / E_0$ on axis ($y = 0$, black curve), the electron density on axis ($y = 0$, blue curve) and the laser field distribution on axis ($y = 0$, purple curve) at time (a) $t = 3$ fs and (b) $t = 30$ fs. The nanowires' width, interspacing and length are set to $d = 36$ nm, $D = 1$ μm and $L = 3$ μm , the CH_2 substrate has a thickness $l = 200$ nm.

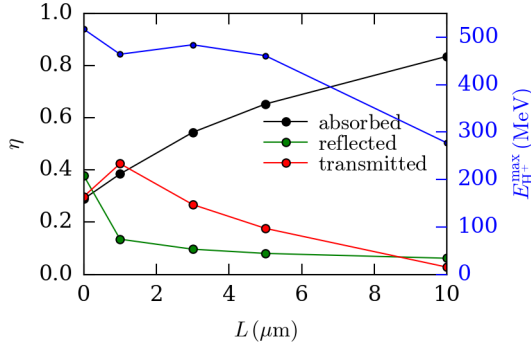


Figure 5.47: Fraction of absorbed, reflected, transmitted laser energy and maximum proton energy as a function of the wires' length $0 \leq L \leq 10$ μm . The nanowires' width and interspacing are set to $d = 36$ nm and $D = 1$ μm . The laser peak intensity is 10^{22} W/cm^2 . The proton energy is reported at the final time $t = 240$ fs.

laser absorption, electron energization and synchrotron emission. Here, we will show that, despite such similarities, those two target types can exhibit significant differences in proton acceleration.

To illustrate this, we consider the optimum 200 nm CH_2 flat foil, which we attach either to a carbon nanowire array with a wire's length $L = 10$ μm , a spacing $D = 1$ μm , a width $d = 36$ nm and an electron density of $n_e/n_c = 480$ in the wires ($\rightarrow n_{av}/n_c = 17$) or to a carbon foam with the same length $L = 10$ μm and same average electron density $n_{av}/n_c = 17$ (total electron density at full ionization).

The proton spectra obtained 240 fs after the on-target laser peak from the simple foil, the nanowire-foil and the foam-foil targets are displayed in Fig. 5.48. The foam-foil target yields a proton cutoff energy much larger than the nanowire-foil target ($\simeq 460$ vs $\simeq 280$ MeV) and only slightly less than the optimum flat foil $\simeq 500$ MeV. The much better performance of the foam-attached foil is not intuitive since the two plasmas formed in front of the foil share the same average electron density ($n_{av}/n_c = 17$) and dimensions (length $L = 10$ μm), yielding similar absorption rates ($\simeq 80\%$). Looking more closely at the laser

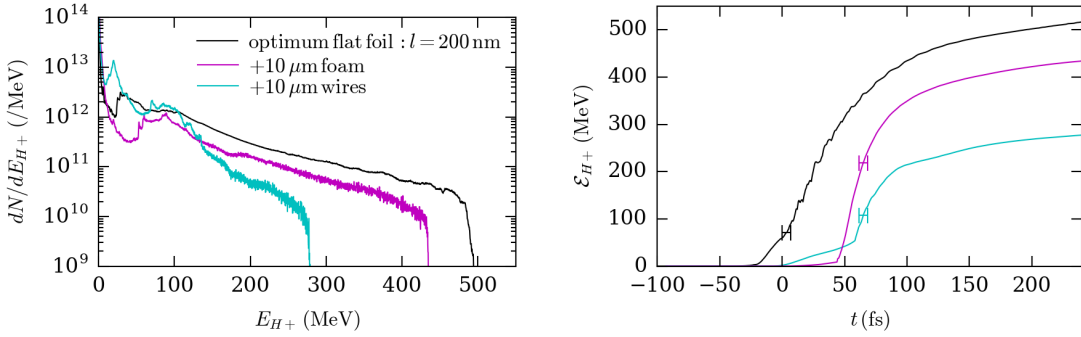


Figure 5.48: (a) Energy-resolved proton spectra at $t = 240$ fs; (b) evolution of maximum proton energy for nanowire-foil and foam-foil targets. The nanowires and the foam have the same average density ($n_{av}/n_c = 17$) and the same length ($L = 10 \mu\text{m}$). The laser peak intensity (10^{22} W/cm^2) arrival on the foam (or the wires) is set to $t = 0$ fs. The estimated transparency times are showed with horizontal error bars.

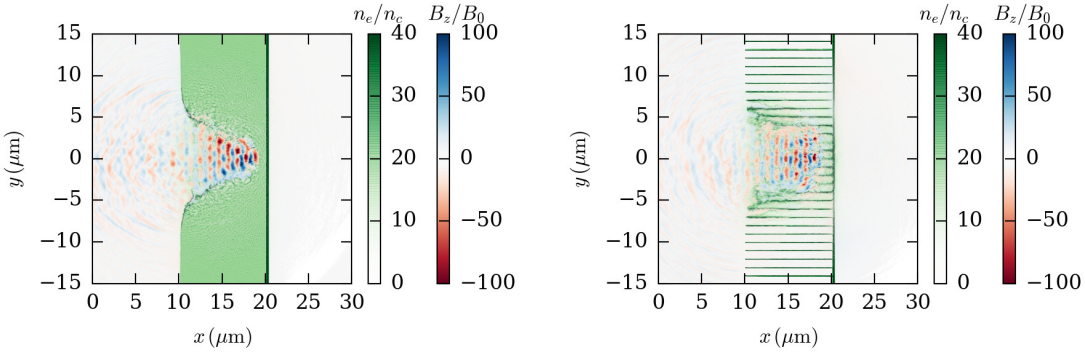


Figure 5.49: (a) Strong laser autofocusing with a uniform foam (b) Much weaker autofocusing with a nanowire array. The density and field amplitude are reported at time $t = 35$ fs. Both nanostructures have the same average density ($n_{av}/n_c = 17$) and the same length ($L = 10 \mu\text{m}$).

dynamics, we observe that the process of self-focusing significantly differs between the two cases. This is illustrated in Fig. 5.49(a,b) which plots the B_z field distribution at $t = 35$ fs (*i.e.* just before the laser pulse hits the substrate) in the foam (a) and nanowire (b) targets. In the foam case, the head of the laser pulse has focused to a $\simeq 2 \mu\text{m}$ (FWHM) spot where local intensity reaches $I \simeq 2.5 \times 10^{22} \text{ W/cm}^2$ ($a_L = 135$). By contrast, when propagating through the exploding nanowires, the laser head fragments into several filaments due to transverse density modulations, and hence does not shrink down to a single bright spot. Its transverse profile has an approximate $4 \mu\text{m}$ width, with $\simeq 2.2 \times 10^{22} \text{ W/cm}^2$ local intensity maxima ($a_L = 125$). The enhancement of the laser intensity amplitude and of its transverse uniformity in the foam-foil target strengthen the RPA in the CH_2 substrate, as shown in the $x - p_x$ ion phase spaces (overlaid with the E_x accelerating field) in Fig. 5.50(a,b). We illustrate the proton and carbon phase spaces for the foam-foil target at times $t = 66$ and 106 fs, in order to directly compare them to the wire-foil case (see Fig. 5.40). At time $t = 66$ fs, RPA-driven protons from the foam-foil target have a much higher longitudinal momentum ($p_x/m_{HC} \simeq 0.83$) than from the wire-foil target ($p_x/m_{HC} \simeq 0.51$). Moreover, they have already catch-up with the TNSA-accelerated

protons at the rear side of the substrate, and can therefore take advantage of the TNSA accelerating field. As we already emphasized, laser transparency can additionally improve proton acceleration. This boost process is enhanced if at transparency time, protons already have a higher velocity. Indeed, they can take advantage of the transmitted laser energy on a longer time via the electrons propagating with them.

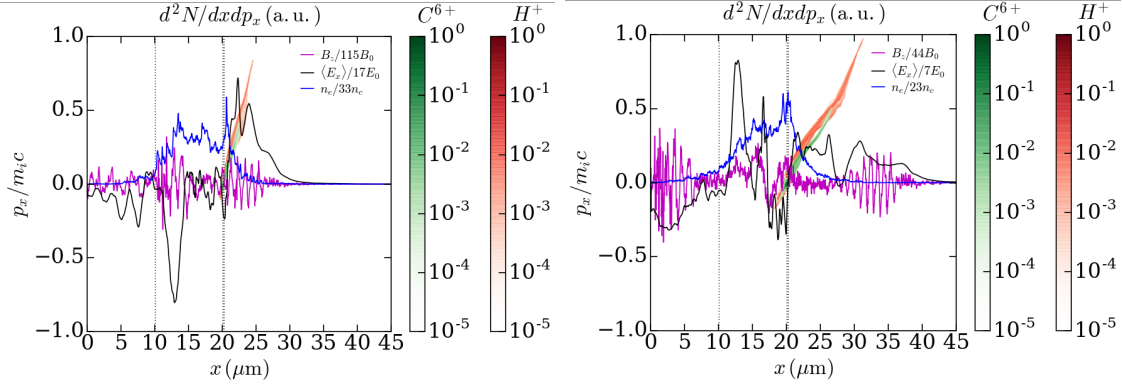


Figure 5.50: $x - p_x$ phase space of H^+ (red colorbar) and C^{6+} (green colorbar) with the longitudinal static electric field $\langle E_x \rangle / E_0$ on axis ($y = 0$, black curve), the electron density on axis ($y = 0$, blue curve) and the laser field distribution on axis ($y = 0$, purple curve) at time (a) $t = 66$ fs and (b) $t = 106$ fs. The foam's average density is $n_e/n_c = 17$ and its length is $L = 10 \mu\text{m}$, the CH_2 substrate has a thickness $l = 200 \text{ nm}$.

For the nanowire-foil target we mentioned the detrimental impact of the premature expansion of the substrate protons. For a foam-foil target, this effect is significantly weaker. We checked it by representing the proton density before the pulse peak hit the substrate in the nanowire-foil and foam-foil cases in Fig. 5.51(a,b). A zoom is performed in order to distinguish the incoming laser pulse (Red/Blue colormap) and the proton density (Red colormap). The rear-side of the substrate is more expanded with wires than foam ($\simeq 2 \mu\text{m}$ vs $\simeq 1 \mu\text{m}$). For the wire-foil target, we also witness a saw-tooth-like periodic acceleration pattern in front of the substrate. It comes from the charge separation field driven by the neutralizing return current of electrons localized in the wires'edges which spacing $D = 1 \mu\text{m}$, explains the periodicity observed.

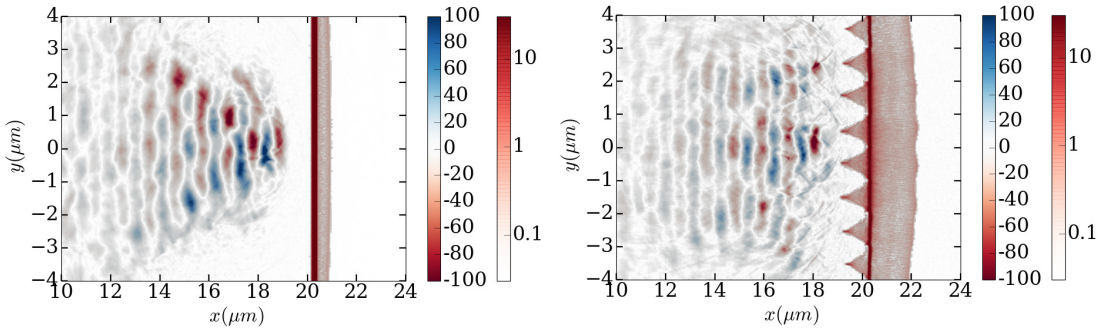


Figure 5.51: Laser field distribution (B_z/B_0 , red/blue colormap) and proton density n_H/n_c (red colormap) before the pulse peak hits the substrate at time $t = 35$ fs. A zoom is performed in the area $16 \leq x \leq 24 \mu\text{m}$ $-4 \leq y \leq 4 \mu\text{m}$. (a) foam-foil target and (b) wire-foil target.

We have examined the benefit of adding nanowire array onto a nanometric CH_2 foil for

enhancing the laser-driven proton acceleration. First, we have identified the target thickness optimizing the cutoff proton energy for a simple flat foil. Our findings corroborates that of [Esirkepov et al. \(2006\)](#) and [Brantov et al. \(2015\)](#), namely $l_{opt} \simeq 0.5a_L\lambda_0n_c/n_{e0}$. This optimum thickness gives rise to an efficient coupling of RPA and TNSA, followed by a short LSA regime, further enhanced by the onset of RSIT at the laser peak. In the presence of a $10\text{ }\mu\text{m}$ -long nanowire array, the hot electrons generated by the laser ramp in the nanowires cause the foil to expand early in time. Also, the propagation velocity of the laser peak is slower in the near-critical ($n_{av}/n_c = 17$) plasma formed due to the ultra-fast expansion of the wires' expansion. When hitting the substrate, the laser pulse has suffered significant depletion through the nanowires, and so drives a less efficient RPA. The enhancement of the TNSA field at the target's rear is also weakened due to its premature expansion. Overall the net effect is to reduce by a factor 2 the maximum proton energy attained $\simeq 250\text{ fs}$ after the pulse peak. Such mitigation of the proton acceleration efficiency can be overcome by using shorter wires. This limit the time-of-flight difference between the pre-heating fast electrons and the laser pulse at the foil's front side, while ensuring an enhanced laser absorption through the nanowires. We have found that in the range $0 \leq L \leq 5\text{ }\mu\text{m}$ the proton acceleration is optimized and weakly varies $E_{\text{H}^+}^{\text{max}} \simeq 500\text{ MeV}$. This value should be considered an upper limit due to the 3D effects bound to arise when the proton have moved a distance comparable to the transverse size of the accelerating electric field.

Finally we have briefly compared the proton acceleration achieved in non-uniform nanowire-foil (with a length $L = 10\text{ }\mu\text{m}$) and a uniform foam-foil target of same average density and dimensions. We have shown that the foam-foil target favors the relativistic laser self-focusing but also limits the level of pre-heating fast electrons, thus improving the resulting proton acceleration. This study should be extended to a broader parameter range in order to conclude about the relative performance of the two target types.

Conclusions

We conducted a comprehensive work on the interaction of an intense and short laser pulse with nanowire arrays in this chapter. We successively identified the main generation mechanisms of energetic particles (electrons, photons and protons) depending on the nanowire array geometry and compared them more or less extensively to uniform flat targets.

In a first part we showed that Direct Laser Acceleration can take place for wires with a large spacing. As soon as the electron density in the nanowires' interspacing raises, the laser interacts with an expanded plasma. This gives rise to an electron heating that is typical of the Relativistic Self Induced Transparency (RSIT) or opacity regimes, depending on the expanded plasma density and transverse modulations.

Nanowire arrays were shown to be efficient photon sources that can convert up to $\simeq 10\%$ (resp. 6%) of the laser energy into energy photons higher than 10 keV (resp. 1 MeV). This peak performance is comparable to the one obtained for uniform foams of equivalent density and takes place for average densities $n_{av}/n_c \simeq 20$ for a laser pulse of top intensity $I = 10^{22}\text{ W.cm}^{-2}$ and short duration (30 fs). We evidenced that the emission is more robust with the nanowire array than the uniform foams since it remains at a higher level for large average densities $n_{av}/n_c \geq 50$.

We finally focused our attention on proton acceleration in such nanowire-array targets, still irradiated by a short (30 fs) and intense laser ($I = 10^{22}\text{ W.cm}^{-2}$). Through 2D PIC simulations we found an optimum regime by studying the different acceleration mechanisms as a function of the substrate and wires' length. The maximum proton energy ($\simeq 500\text{ MeV}$) inferred with nanowire arrays are demonstrated to be at the same level than an optimized flat foil. On these aspects they do not embody a promising way to significantly enhance proton acceleration. Overall this last study is not complete and may be carried on as a future perspective.

Conclusions and perspectives

Conclusions

This PhD work is centered on the generation of high-energy photon and positron arising during relativistic laser plasma interactions. It leads to the implementation and validation of new modules in the PIC code CALDER developed at CEA and to several investigations summarized below. The first goal of this PhD is to provide self-consistent and coherent simulations tools to prepare the physics of the next generation PW and multi-PW laser systems.

In Chap. 1, we recall the numerical scheme employed to simulate laser plasma interactions: the particle-in-cell method. It is based on the Maxwell-Klimontovich equations and the main steps of the time loop are detailed: the charge and current assignation, the resolution of Maxwell's equations, the interpolation of fields at the particles' position and the resolution of particle motion. In addition, we highlight that this kind of code lacks some physical effects such as elastic deflections, the emission of high energy photons (by Bremsstrahlung or by synchrotron) and of electron-positron pairs. The latter cannot be described by the large discretization of PIC codes and must be accounted for by new modules. While the essence of this new implementation is provided at the end of Chap. 1, a comprehensive study of processes induced in an electromagnetic (resp. Coulomb) field is provided in Chap. 2 (resp. in Chap. 3).

Processes induced in an electromagnetic field are described in Chap. 2. As we will only tackle the synchrotron emission in the frame of this PhD, it is put forward compared to the Breit-Wheeler and electromagnetic Trident pair generation. We explain how the synchrotron process is modeled and provide its emission rate in the classical and quantum regimes. Its implementation in both regimes, either by adding a term in the motion equation or by performing a Monte-Carlo sampling, is detailed. The modeling of the Breit-Wheeler mechanism is then given. Overall its implementation is similar to the synchrotron process. While the electromagnetic Trident process is illustrated, its implementation is not reported in this PhD. There are indeed less theoretical works on this process.

The results presented in Chap. 3 aim to enrich the simulation capabilities of PIC codes to relevant Coulomb-mediated processes. We successively examine major mechanisms induced in an atomic Coulomb field during relativistic laser-plasma interaction. These include elastic scattering, impact ionization, the generation of photons by Bremsstrahlung and of electron-positron pairs by Bethe-Heitler/Trident. We emphasize that only the three latter processes were implemented in the frame of this PhD and that the two first were already treated ([Pérez et al., 2012](#)). For two of these processes (Bremsstrahlung and Bethe-Heitler), we derived cross-sections accounting for electron shielding in both the low and high ionization limit of the atom. This specific impact of electron screening is also tackled, introducing a heuristic model, for electron-ion elastic scattering. After systematically checking the accuracy of each updated or newly implemented Coulomb-mediated processes

in the PIC code CALDER, we consider the classical problem of fast electron relaxation in a thin copper foil ($5 - 15 \mu\text{m}$). The goal is to understand the competition between the direct (Coulomb Trident) and indirect (Bethe-Heitler) production of positrons. While our self-consistent simulations reproduce qualitatively a 0D model (Myatt *et al.*, 2009), they also highlight that energy transfers from electrons to ions, via the acceleration of the latter, can limit the generation of photons and pairs.

Chapter 4 considers laser-plasma interaction in the context of short and mid term experiments where laser intensities may reach the unprecedented level of 10^{22} W/cm^2 . This is motivated by the observation that the relative importance of Bremsstrahlung and synchrotron emission is poorly known for this regime of laser intensities. Few previous works investigated the competition between the two radiative processes, evidencing the impact of laser intensity (Pandit and Sentoku, 2012) or the target material (Wan *et al.*, 2017). We progressively introduce key concepts to grasp the issues at stake during the interaction of such short (tens of fs) and intense lasers with a solid foil. In particular, the notions of relativistic transparency, fast electron generation and ion acceleration are summarized. We then illustrate and analyze how synchrotron emission proceeds in a basic scenario of laser plasma interaction. Among the detailed analysis done for different plasma densities, we bring forward an enhanced comprehension of how emission operates for near-critical plasmas ($n_e/n_c \simeq 15 - 20$) which are known to maximize the synchrotron process efficiency (Brady *et al.*, 2012, 2014). We also point out the impact of the target breakout by the laser on the spectral signature of photons. Having in mind this background, we consider synchrotron emission from thin solid density copper foils irradiated by a short (50 fs) and intense laser ($I = 10^{22} \text{ W/cm}^2$). While those measuring tens of nm rapidly expand, giving rise to relativistic transparency and subsequently maximize the synchrotron emission, the Bremsstrahlung prevails for larger thicknesses ($> 2 \mu\text{m}$). The spectral features of both processes are analysed and related to the target expansion dynamic.

Chapter 5 explores the possibility to generate better synchrotron photon sources by employing nanowire arrays. While they present unique properties already experienced for more accessible laser intensities ($I \leq 10^{21} \text{ W/cm}^2$), we are eager to investigate whether they can be extended for $10^{21} \leq I \leq 10^{23} \text{ W/cm}^2$. Overall nanowires were shown to bring almost complete laser absorption as their inter-wire gaps enable a volumetric interaction with the laser, contrary to a solid flat foil where it remains on its surface (Purvis *et al.*, 2013). We begin by illustrating fast electron generation in nanowire arrays, depending on their geometry. We then exemplify the spectral evolution of the photon emission on a test case. In light of this example, the synchrotron process is analyzed for a broad range of parameters. For $I = 10^{22} \text{ W/cm}^2$, the optimum nanowire array geometry enables to convert up to 10% of the laser energy into X-rays ($\geq 10 \text{ keV}$) and 6% into γ -rays ($\geq 1 \text{ MeV}$). It consists in thin carbon wires expanding in the laser front, such that the main part of the laser interacts with an almost homogenized relativistically undercritical plasma of density $n_e/n_c \simeq 15 - 20$. A comparison between the performances achieved with nanowire arrays and equivalent uniform density plasmas is carried. It sorts out that for average densities n_e/n_c below 50, both types of targets bring similar results whereas for higher average densities ($n_e/n_c \geq 50$) nanowires are better. The high level of photon production in nanowire arrays is successfully generalized to a more realistic scenario involving a finite focal spot and an oblique incidence angle of the laser. The potential of nanowire arrays is also examined regarding proton acceleration. Even though we show that nanowire arrays generate protons as energetic as optimized flat foils, the range of parameters explored in this prospective work remains limited and to be completed.

Perspectives

The first perspective one can think of is to further extend the capacity of PIC codes. From a physical point of view, it can be worth to add more processes describing atomic physics with Auger electrons or K- α emission and photon transport such as photo-ionization and Compton effect ([Del Gaudio *et al.*, 2017](#)). This can be done with the Monte-Carlo macro-particle pairing scheme already implemented in the PIC code CALDER. It is however necessary to extend the existing algorithm to account for the presence of bound states of atoms. Such phenomena are useful to understand the interaction of X-ray Free-Electron Lasers (XFEL) with solid material samples for applications related to high-energy density plasmas. Such states of matter are present in the interior of stars and planets of our solar system ([Chabrier, 2009](#)) and are also of interest for inertial confinement fusion ([Atzeni and Meyer-ter-Vehn, 2004](#)). A recent study suggests another way to tackle this problem by coupling a PIC and a photon transport code ([Royle *et al.*, 2017](#)). The latter accounts for energy transfers via emissivity and opacity coefficients determined from the PIC code output. From a numerical point of view, the addition of several new modules implies a growing number of macro-particles and increases significantly the simulation time. The best way to limit the inflation of secondary particles is to merge them ([Vranic *et al.*, 2015](#)). The main difficulty with this kind of algorithm is to conserve quantities such as the statistical weight, momentum and energy of macro-particles.

During this PhD thesis, we compare two processes that lead to the generation of high energy photons: the synchrotron and the Bremsstrahlung. We put forward the impact of the plasma length on their relative efficiency. Other laser-plasma parameters, such as the laser duration, the target profile or composition, are however expected to alter this result. It is worth to address such issue in the context of laser-solid interaction in short and mid term experiments. It may also be interesting to extend this comparison to pair creation processes with the Bethe-Heitler, the Breit-Wheeler, electromagnetic and Coulomb Trident. While it is known that the Bethe-Heitler and Coulomb Trident prevail for laser intensities $\leq 10^{21} \text{ W/cm}^2$ it is also expected that the Breit-Wheeler and electromagnetic Trident will prevail for a laser intensity of $10^{22} - 10^{23} \text{ W/cm}^2$. Regarding our results in Chap. 4, it can be expected that for plasmas thick enough, the Bethe-Heitler dominates the Breit-Wheeler process, even at high laser intensities. The influence of other laser plasma parameter remains unexplored yet and this opens up the opportunity to tackle an issue barely addressed in the literature. Indeed the comparison between electromagnetic and Coulomb induced processes requires to model, implement and validate them all. Another difficulty lies in the growing computational time of such simulations. Only a few codes can claim to address such issues which is the case of the code CALDER developed at CEA, now accounting for all these mechanisms (except the electromagnetic Trident). The main motivation to compare all the pair production effects comes from the growing interest of several groups to bring forward the first experimental evidence of a pair generation process known as two photon (or linear) Breit-Wheeler process ([Pike *et al.*, 2014; Ribeyre *et al.*, 2016; Yu *et al.*, 2018](#)). As it produces less pairs than the Bethe-Heitler and Trident processes in such experiments, its detection remains a challenge to be faced, calling for a clear understanding of the relative effectiveness of all those mechanisms.

Given the efforts carried out to put forward an efficient γ -ray source, it is of interest to employ it to generate an efficient electron-positron pair source using, for example, a high-Z mm-thick converter target. This would, however, require more resources since it is necessary to couple PIC and particle transport codes. Those efforts are worth to pursue as they contribute to a global growing interest for the experimental realisation of

electron-positron plasmas carried by, among others, [Liang et al. \(2015\)](#); [Chen et al. \(2015\)](#); [Sarri et al. \(2015\)](#). The first step is to produce gamma-rays via the synchrotron emission during the interaction of an intense laser with a foam or nanostructured target. As already proven via Particle-In-Cell numerical simulations, gamma-ray synchrotron sources induced by those plasmas can present a high conversion efficiency into a forward ($\pm 45^\circ$) cone angle ([Brady et al., 2014](#)): 1% for a 10^{22} W/cm^2 laser interacting either with a uniform relativistically undercritical plasma ($\sim 2 \times 10^{22} / \text{cm}^3$) or with an optimized nanowire array ([Martinez et al., 2018](#)). The rather high angular and energy spread which characterizes the photons produced can be reduced by employing a preformed plasma channel. In this particular context, up to 10% of a $5 \times 10^{22} \text{ W/cm}^2$ laser can be converted into a directed γ -ray burst ([Stark et al., 2016](#)). Once γ -rays are produced, they can be converted into e^-e^+ pairs using a high-Z (gold or tantalum) target. The thickness of this converter target can be varied in order to achieve quasi-neutral e^-e^+ beams or plasmas, as done previously by [Liang et al. \(2015\)](#). The expected optimum length is a few mm. One of the main issues is to assess whether the e^-e^+ cloud formed has the right density and dimensions to be considered as a plasma, i.e. its spatial extent must be higher than the relativistic skin depth of the pair cloud.

The best γ -ray source identified with nanowires for a laser intensity of 10^{22} W/cm^2 presents a spectrum extending to $\sim 100 \text{ MeV}$ energies. This opens up the possibility to create neutron sources driven by photo-nuclear reactions. Such reactions are already employed to diagnose the high-energy tail of Bremsstrahlung photons in experiments with $\hbar\omega \geq 10 \text{ MeV}$ for $^{63}\text{Cu}(\gamma, n)^{62}\text{Cu}$ and $\hbar\omega \geq 19 \text{ MeV}$ for $^{12}\text{C}(\gamma, n)^{11}\text{C}$ ([Courtois et al., 2009](#)). A recent experiment, based on copper activation, lead to the generation of $\sim 10^9$ neutrons per shot ([Pomerantz et al., 2014](#)). Another promising way to generate neutrons comes from the interaction of laser-accelerated ion beams with, for example, beryllium targets ([Roth et al., 2013](#)) which provides more neutrons, up to $\sim 10^{10} \text{ n/sr}$. Potential applications of neutron sources range from material testing for fusion research ([Perkins et al., 2000](#)), fast neutron radiography ([Loveman et al., 1995](#)) or the treatment of cancer ([Gray and Read, 1943](#)). The implementation within a PIC code of photo-nuclear reactions was done recently for carbon and beryllium ([Nakamura and Hayakawa, 2015](#)). Overall, there are very few works suggesting to generate neutrons via photo-nuclear reactions compared to nuclear reactions such as $^7\text{Li}(d, n)^8\text{Be}$. This adds an interesting perspective to this PhD work which may take part in the global effort to drive efficient and compact neutron sources using relativistic laser-plasma interactions.

Appendices

Appendix A

Laser normalisation

	Variable	Value ($\lambda_0 = 1 \mu\text{m}$)
Density	n_c	$1.11 \times 10^{27} / \text{m}^3$
Velocity	c	$3.00 \times 10^8 \text{ m/s}$
Distance	c/w_0	$1.59 \times 10^{-7} \text{ m}$
Time	w_0^{-1}	$5.31 \times 10^{-16} \text{ s}$
Mass	m_e	$9.11 \times 10^{-31} \text{ kg}$
Impulsion	$m_e c$	$2.73 \times 10^{-22} \text{ kg.m/s}$
Energy	$m_e c^2$	$8.20 \times 10^{-14} \text{ J}$
Current density	$n_c e c$	$5.34 \times 10^{16} \text{ A/m}^2$
Magnetic field	$B_0 = m_e \omega_0 / e$	$1.07 \times 10^4 \text{ T}$
Electric field	$E_0 = m_e \omega_0 c / e$	$3.21 \times 10^{12} \text{ V/m}$

Appendix B

Screening angle in the limit of weak and strong ionization

We present the calculation of an integral denoted by $I_{\alpha\beta}$ and defined as

$$I_{\alpha\beta} = \int_0^\pi \frac{\sin \vartheta (1 - \cos \vartheta)}{(4 \sin^2 \frac{\vartheta}{2} + \vartheta_\alpha^2) (4 \sin^2 \frac{\vartheta}{2} + \vartheta_\beta^2)} d\vartheta \quad (\text{B.1})$$

In this expression ϑ_α and ϑ_β are fixed parameters on which the value of the integral $I_{\alpha\beta}$ depends. It is involved in the determination of an adequate description of screening effects in angular deflections detailed in chapter 4. The first step is to do the substitution $u = \sin(\vartheta/2)$ which provides a simpler expression without trigonometric functions

$$I_{\alpha\beta} = \int_0^1 \frac{8u^3}{(4u^2 + \vartheta_\alpha^2)(4u^2 + \vartheta_\beta^2)} du \quad (\text{B.2})$$

Firstly we treat the particular case where $\alpha = \beta$. Physically speaking, it corresponds to a Fermi or a Debye screening which have an exponential form. Then we generalise the calculation to the case $\alpha \neq \beta$ which matches the case of the mixed Fermi-Debye potential which is the sum of two exponentials.

B.1 Particular case of a single exponential potential

In the case $\alpha = \beta$ calculations are much simpler and they enable to have a good intuition for the generalisation to the other case $\alpha \neq \beta$. We are willing to determine the closed form of expression

$$I_{\alpha\alpha} = \int_0^1 \frac{8u^3}{(4u^2 + \vartheta_\alpha^2)^2} du \quad (\text{B.3})$$

We do the substitution $v = 2u/\vartheta_\alpha$ and obtain

$$2I_{\alpha\alpha} = \int_0^{2/\vartheta_\alpha} \frac{v^3}{(1 + v^2)^2} dv \quad (\text{B.4})$$

The key to integrate this expression is to decompose v^3 as $= v(1 + v^2) - v$ which leads to a simplification

$$2I_{\alpha\alpha} = \int_0^{2/\vartheta_\alpha} \frac{v(1+v^2)}{(1+v^2)^2} dv - \int_0^{2/\vartheta_\alpha} \frac{v}{(1+v^2)^2} dv \quad (\text{B.5})$$

The remaining terms are straightforward to integrate and provide

$$I_{\alpha\alpha} = \frac{1}{4} \left\{ \ln(4 + \vartheta_\alpha^2) + \frac{\vartheta_\alpha^2}{4 + \vartheta_\alpha^2} - 1 - 2 \ln \vartheta_\alpha^2 \right\} \quad (\text{B.6})$$

Equation (B.6) represents the closed form of the initial integral we are willing to derive and defined in equation (B.3). In the physical scenario of interest the variable ϑ_α is a screening angle which is small with typically $\vartheta_\alpha \ll 1$. A limited developement of equation (B.2) for $\vartheta_\alpha \ll 1$ provides a much simpler expression for the integral $I_{\alpha\alpha}$

$$I_{\alpha\alpha} = \frac{1}{2} \ln \vartheta_\alpha^{-1} + O(1) \quad (\text{B.7})$$

B.2 Generalisation to a double exponential potential

We would like now to generalize the former calculation and derive the closed-form of the following integral

$$I_{\alpha\beta} = \int_0^1 \frac{8u^3}{(4u^2 + \vartheta_\alpha^2)(4u^2 + \vartheta_\beta^2)} du \quad (\text{B.8})$$

The key step is to get rid of the product in the denominator of the expression we want to integrate in equation (B.8). From the result in the case $\alpha = \beta$ we are able to integrate an expression of the form $u^3 / (4u^2 + \vartheta_\alpha^2)^2$. For this reason we look for a decomposition of the denominator involving this type of expression. More precisely we look for four variables denoted by A , B , C and D as follows

$$\frac{8u^3}{(4u^2 + \vartheta_\alpha^2)(4u^2 + \vartheta_\beta^2)} = \frac{Au^3 + Bu}{(4u^2 + \vartheta_\alpha^2)^2} + \frac{Cu^3 + Du}{(4u^2 + \vartheta_\beta^2)^2} \quad (\text{B.9})$$

The resolution of equation (B.9) for A , B , C and D leads to a system of 4 equations with 4 unknown that can be written under the following form

$$\begin{bmatrix} 16 & 0 & 16 & 0 \\ 8\vartheta_\beta^2 & 16 & 8\vartheta_\alpha^2 & 16 \\ \vartheta_\beta^4 & 8\vartheta_\beta^2 & \vartheta_\alpha^4 & 8\vartheta_\alpha^2 \\ 0 & \vartheta_\beta^4 & 0 & \vartheta_\alpha^4 \end{bmatrix} \begin{pmatrix} A \\ B \\ C \\ D \end{pmatrix} = \begin{pmatrix} 128 \\ 32(\vartheta_\alpha^2 + \vartheta_\beta^2) \\ 8\vartheta_\alpha^2\vartheta_\beta^2 \\ 0 \end{pmatrix} \quad (\text{B.10})$$

and resolved provided the determinant of the matrix is not null $\leftrightarrow \vartheta_\alpha^2 \neq \vartheta_\beta^2$. As the parameters ϑ_α and ϑ_β are both positive, it is equivalent to $\vartheta_\alpha \neq \vartheta_\beta$. We have already treated the particular case where $\vartheta_\alpha = \vartheta_\beta$ above and can therefore go on with the case $\vartheta_\alpha \neq \vartheta_\beta$ without loss of generality. The resolution is done by classical means and leads to

$$\begin{pmatrix} A \\ B \\ C \\ D \end{pmatrix} = \frac{2}{\vartheta_\alpha^2 - \vartheta_\beta^2} \begin{pmatrix} 4\vartheta_\alpha^2 \\ \vartheta_\alpha^4 \\ -4\vartheta_\beta^2 \\ -\vartheta_\beta^4 \end{pmatrix} \quad (\text{B.11})$$

Having now the expression of the parameters A , B , C and D , we can integrate the right

hand side of equation (B.9). Let us detail the method for the first term of the right hand side of equation (B.9). The second term will be integrated following the same method. As we substitute the expression of the coefficient $B = \vartheta_\alpha^2 A/4$ in the first term of the right hand side of equation (B.9) we obtain a simplification

$$\forall u \in (0, 1) \quad \frac{Au^3 + Bu}{(4u^2 + \vartheta_\alpha^2)^2} = \frac{A}{4} \frac{u(4u^2 + \vartheta_\alpha^2)}{(4u^2 + \vartheta_\alpha^2)^2} = \frac{A}{4} \frac{u}{4u^2 + \vartheta_\alpha^2} \quad (\text{B.12})$$

which is now straightforward to integrate. The calculation provides the following result

$$\int_0^1 \frac{Au^3 + Bu}{(4u^2 + \vartheta_\alpha^2)^2} = \frac{1}{4} \frac{\vartheta_\alpha^2}{(\vartheta_\alpha^2 - \vartheta_\beta^2)} \ln \left[\left(1 + \frac{4}{\vartheta_\alpha^2} \right) \right] \quad (\text{B.13})$$

The method to integrate the second term of the right hand side off equation (B.9) is strictly the same. We direclty report the sum of the two expressions and obtain the final expression of the integral $I_{\alpha\beta}$ which is

$$I_{\alpha\beta} = \frac{1}{4} \frac{1}{\vartheta_\alpha^2 - \vartheta_\beta^2} \{ \vartheta_\alpha^2 [\ln(4 + \vartheta_\alpha^2) - 2 \ln \vartheta_\alpha] - \vartheta_\beta^2 [\ln(4 + \vartheta_\beta^2) - 2 \ln \vartheta_\beta] \} \quad (\text{B.14})$$

Equation (B.14) represents the closed form of the initial integral we are willing to derive and defined in equation (B.1). In the physical scenario of interest the variables ϑ_α and ϑ_β are screening angles which are small with typically $\vartheta_\alpha, \vartheta_\beta \ll 1$. A limited developement of equation (B.14) for $\vartheta_\alpha, \vartheta_\beta \ll 1$ provides the following expression for the integral $I_{\alpha\beta}$

$$I_{\alpha\beta} = \frac{1}{2} \ln \left[\vartheta_\alpha^{\frac{1}{(\vartheta_\beta^2/\vartheta_\alpha^2 - 1)}} \vartheta_\beta^{\frac{1}{(\vartheta_\alpha^2/\vartheta_\beta^2 - 1)}} \right] + O(1) \quad (\text{B.15})$$

Appendix C

List of communications

C.1 First author articles in peer-reviewed journals

B. Martinez, M. Lobet, E. d’Humières, L. Gremillet Synchrotron emission from nanowire-array targets irradiated by intense laser pulses, *Plasma Physics and Controlled Fusion* **60**, 074009 (2018).

B. Martinez, E. d’Humières, L. Gremillet High-Energy Radiation and Pair Production by Coulomb Processes in Particle-in-Cell Simulations, *to be submitted to Physics of Plasmas*.

C.2 Oral presentations

B. Martinez, E. d’Humières, and L. Gremillet *Radiative effects in the interaction of an intense laser with flat and nanowire-array targets*, University of Chalmers, Gteborg (2018) (invited oral).

B. Martinez, E. d’Humières, and L. Gremillet *Radiative and QED effects in relativistic laser plasma interaction*, seminar at CEA, Bruyères-le-Châtel (2018) (oral).

B. Martinez, E. d’Humières, and L. Gremillet *Radiative and QED effects in relativistic laser plasma interaction*, seminar at LULI Laboratory, Palaiseau (2018) (oral).

L. Gremillet, B. Martinez, M. Lobet, and E. d’Humières, *High-energy radiation sources from nano-structured and thin targets irradiated by ultraintense lasers*, 27th Annual International Laser Physics Workshop (LPHYS’18), Nottingham (2018) (invited oral).

B. Martinez, E. d’Humières, and L. Gremillet *Synchrotron emission from nanowire-array targets irradiated by ultraintense laser pulses*, 45th EPS Conference on Plasma Physics, Prague (2018) (poster).

L. Gremillet, B. Martinez, M. Lobet, and E. d’Humières, *High-energy radiation sources from structured and thin targets irradiated by ultraintense lasers*, 12th International Conference on High Energy Density Laboratory Astrophysics (HEDLA), Kurashiki (2018) (invited oral).

B. Martinez, M. Lobet, E. d’Humières, and L. Gremillet, *Synchrotron sources from nanowire-array targets irradiated by intense lasers*, 15è Congrès Plasmas de la Société Française de Physique, Bordeaux (2018) (oral).

B. Martinez, M. Lobet, E. d’Humières, and L. Gremillet. *Synchrotron sources from nanowire-array targets irradiated by intense lasers*, 8th Conference on Plasma Physics by Lasers and Application, Messina (2017) (oral).

B. Martinez, M. Lobet, E. d’Humières, and L. Gremillet, *High-energy radiation and pair production in particle-in-cell simulations*, National Terawatt Facility, Reno (2016)

(invited seminar).

C.3 Poster presentations

L. Gremillet, B. Martinez, and E. d'Humières, *Synchrotron radiation from nanowire targets irradiated by intense lasers*, 2nd Conference on Extremely High Intensity Laser Physics (ExHILP), Lisbon (2017).

B. Martinez, L. Gremillet and E. d'Humières, *Synchrotron emission from nanowire-array targets irradiated by ultraintense laser pulses*, Summer School Atoms and plasmas in super-intense laser fields, Erice (2017).

B. Martinez, E. d'Humières, and L. Gremillet, *Synchrotron emission from nanowire-array targets irradiated by ultraintense laser pulses*, Winter School :Matter in extreme conditions, Modane (2017).

B. Martinez, E. d'Humières, and L. Gremillet, *Synchrotron emission from nanowire-array targets irradiated by ultraintense laser pulses*, 8è Forum ILP, Aussois (2017).

B. Martinez, M. Lobet, E. d'Humières, and L. Gremillet, *High-energy radiation and pair production in particle-in-cell simulations*, PHARE kickoff meeting, Paris (2016).

B. Martinez, M. Lobet, E. d'Humières, and L. Gremillet, *High-energy radiation and pair production in particle-in-cell simulations*, 43rd EPS Conference on Plasma Physics, Leuven (2016).

B. Martinez, M. Lobet, E. d'Humières, and L. Gremillet, *High-energy radiation and pair production in particle-in-cell simulations*, 14è Congrès Plasmas de la Société Française de Physique Nancy (2016).

Bibliography

- “APOLLON: laser system at the Commissariat à l’Énergie Atomique,” <https://cilexsaclay.fr/>.
- “ARC: laser system at the Lawrence Livermore National Laboratory,” <https://lasers.llnl.gov/>.
- “BELLA: Berkeley Laboratory Laser Accelerator,” <https://www.clpu.es/>.
- “ELI-BL: Extreme Light Infrastructure Beamlines,” <https://www.eli-beams.eu/>.
- “ELI-NP: Extreme Light Infrastructure Nuclear Physics,” <http://www.eli-np.ro/>.
- “LMJ: laser system at the Commissariat à l’energie Atomique,” <http://www-lmj.cea.fr/>.
- “NIF: laser system at the Lawrence Livermore National Laboratory,” <https://lasers.llnl.gov/>.
- “OMEGA-EP: laser system at the Laboratory for Laser Energetics,” <http://www.lle.rochester.edu/>.
- “ORION: laser system at the Atomic Weapon Establishment,” <https://www.awe.co.uk/>.
- “PETAL: PETawatt Aquitaine Laser,” <http://www.enseignementsup-recherche.gouv.fr/>.
- “VEGA: laser system at the Centro de Laseres Pulsados,” <http://www.enseignementsup-recherche.gouv.fr/>.
- “VULCAN: laser system at the Rutherford Appleton Laboratory,” <https://www.clf.stfc.ac.uk/>.
- “XCELS: Exawatt Center for Extreme Light Studies,” <http://www.xcels.iapras.ru/>.
- Abraham, M., and A. Föppl (1918), *Theorie der Elektrizität* (Leipzig : B.G. Teubner, University of Toronto).
- Adam, J. C., A. Héron, and G. Laval, Phys. Rev. Lett. **97**, 205006 (2006).
- Aleksandrov, I. A., G. Plunien, and V. M. Shabaev, ArXiv e-prints , [arXiv:1811.01419](https://arxiv.org/abs/1811.01419) (2018).
- Andreev, A. A., and K. Y. Platonov, IEEE J. Quant. Electron. **46** (2), 109 (2016).

BIBLIOGRAPHY

- Antonelli, L., S. Atzeni, A. Schiavi, S. D. Baton, E. Brambrink, M. Koenig, C. Rousseaux, M. Richetta, D. Batani, P. Forestier-Colleoni, E. Le Bel, Y. Maheut, T. Nguyen-Bui, X. Ribeyre, and J. Trela, Phys. Rev. E **95**, 063205 (2017).
- Antonsen, T. M., and P. Mora, Phys. Rev. Lett. **69**, 2204 (1992).
- Arefiev, A. V., B. N. Breizman, M. Schollmeier, and V. N. Khudik, Phys. Rev. Lett. **108**, 145004 (2012).
- Atzeni, S., and J. Meyer-ter-Vehn (2004), *The Physics of Inertial Fusion: Beam Plasma Interaction, Hydrodynamics, Hot Dense Matter* (Oxford University Press, New York).
- Audebert, P., P. Renaudin, S. Bastiani-Ceccotti, J.-P. Geindre, C. Chenais-Popovics, S. Tzortzakis, V. Nagels-Silvert, R. Shepherd, I. Matsushima, S. Gary, F. Girard, O. Peyrusse, and J.-C. Gauthier, Phys. Rev. Lett. **94** (2), 025004 (2005).
- Azechi, H., K. Mima, Y. Fujimoto, S. Fujioka, H. Homma, M. Isobe, A. Iwamoto, T. Jitsuno, T. Johzaki, R. Kodama, M. Koga, K. Kondo, J. Kawanaka, T. Mito, N. Miyanaga, O. Motojima, M. Murakami, H. Nagatomo, K. Nagai, M. Nakai, H. Nakamura, T. Nakamura, T. Nakazato, Y. Nakao, K. Nishihara, H. Nishimura, T. Norimatsu, T. Ozaki, H. Sakagami, Y. Sakawa, N. Sarukura, K. Shigemori, T. Shimizu, H. Shiraga, A. Sunahara, T. Taguchi, K. Tanaka, and K. Tsubakimoto, Nuclear Fusion **49** (10), 104024 (2009).
- Baeva, T., S. Gordienko, A. P. L. Robinson, and P. A. Norreys, Phys. Plasmas **18** (5), 056702 (2011).
- Baier, V. N., and V. M. Katkov, J. Exp. Theor. Phys. Lett. **88**, 80 (2008).
- Balabanski, D. L., R. Popescu, D. Stutman, K. A. Tanaka, O. Tesileanu, C. A. Ur, D. Ursescu, and N. V. Zamfir, EPL **117**, 28001 (2017).
- Bargsten, C., R. Hollinger, M. G. Capeluto, V. Kaymak, A. Pukhov, S. Wang, A. Rockwood, Y. Wang, D. Keiss, R. Tommasini, R. London, J. Park, M. Busquet, M. Klapisch, V. N. Shlyaptsev, and J. J. Rocca, Sci. Adv. **3** (1) (2017).
- Barr, H. C., P. Mason, and D. M. Parr, Phys. Plasmas **7**, 2604 (2000).
- Barthélémy, R. (2005), *Le problème de conservation de la charge dans le couplage des équations de Vlasov et de Maxwell*, Ph.D. thesis (Université de Strasbourg, Département de Mathématiques).
- Bauer, D., and P. Mulser, Phys. Plasmas **14** (2), 023301 (2007).
- Bauer, D., P. Mulser, and W. H. Steeb, Phys. Rev. Lett. **75**, 4622 (1995).
- Bearden, J. A., and A. F. Burr, Rev. Mod. Phys. **39**, 125 (1967).
- Bell, A. R., and J. G. Kirk, Phys. Rev. Lett. **101**, 200403 (2008).
- Berger, M. J., M. Inokuti, H. H. Anderson, H. Bichsel, J. A. Dennis, D. Powers, S. M. Seltzer, and J. E. Turner, Journal of the ICRU **os19** (2) (1984).
- Bethe, H. A., Phys. Rev. **89**, 1256 (1953).
- Bethe, H. A., and N. F. Mott, Proc. Cambridge Philos. Soc. **30**, 524 (1934).

- Bhabha, H. J., Proc. R. Soc. London A **152** (877), 559 (1935).
- Bin, J. H., W. J. Ma, H. Y. Wang, M. J. V. Streeter, C. Kreuzer, D. Kiefer, M. Yeung, S. Cousens, P. S. Foster, B. Dromey, X. Q. Yan, R. Ramis, J. Meyer-ter Vehn, M. Zepf, and J. Schreiber, Phys. Rev. Lett. **115**, 064801 (2015).
- Bin, J. H., M. Yeung, Z. Gong, H. Y. Wang, C. Kreuzer, M. L. Zhou, M. J. V. Streeter, P. S. Foster, S. Cousens, B. Dromey, J. Meyer-ter Vehn, M. Zepf, and J. Schreiber, Phys. Rev. Lett. **120**, 074801 (2018).
- Birdsall, C. K., and A. B. Langdon (1991), *Plasma Physics via Computer Simulation, The Adam Hilger Series on Plasma Physics*, edited by C. Birdsall, A. Langdon. Adam Hilger, Bristol, England.
- Blackburn, T. G., C. P. Ridgers, J. G. Kirk, and A. R. Bell, Phys. Rev. Lett. **112**, 015001 (2014).
- Blandford, R. D., and C. F. McKee, Monthly Notices of the Royal Astronomical Society **180** (3), 343 (1977).
- Blumenthal, G. R., and R. J. Gould, Rev. Mod. Phys. **42**, 237 (1970).
- Boris, J. P., R. A. Shanny, U. S. O. of Naval Research, and N. R. Laboratory, “Proceedings : fourth conference on numerical simulation of plasmas, november 2, 3, 1970,” .
- Bourdier, A., D. Patin, and E. Lefebvre, Physica D: Nonlinear Phenomena **206** (1), 1 (2005).
- Brady, C. S., C. P. Ridgers, T. D. Arber, and A. R. Bell, Plasma Phys. Control. Fusion **55** (12), 124016 (2013).
- Brady, C. S., C. P. Ridgers, T. D. Arber, and A. R. Bell, Phys. Plasmas **21** (3), 033108 (2014).
- Brady, C. S., C. P. Ridgers, T. D. Arber, A. R. Bell, and J. G. Kirk, Phys. Rev. Lett. **109**, 245006 (2012).
- Brambrink, E., H. G. Wei, B. Barbrel, P. Audebert, A. Benuzzi-Mounaix, T. Boehly, T. Endo, C. D. Gregory, T. Kimura, R. Kodama, N. Ozaki, H.-S. Park, and M. Koenig, Phys. Rev. E **80**, 056407 (2009).
- Brantov, A. V., E. A. Govras, V. Y. Bychenkov, and W. Rozmus, Phys. Rev. ST Accel. Beams **18**, 021301 (2015).
- Breit, G., and J. A. Wheeler, Phys. Rev. **46**, 1087 (1934).
- Brunel, F., Phys. Rev. Lett. **59**, 52 (1987).
- Bulanov, S. S., A. Brantov, V. Y. Bychenkov, V. Chvykov, G. Kalinchenko, T. Matsuoka, P. Rousseau, S. Reed, V. Yanovsky, D. W. Litzenberg, K. Krushelnick, and A. Maksimchuk, Phys. Rev. E **78**, 026412 (2008).
- Bulanov, S. V., E. Y. Echkina, T. Z. Esirkepov, I. N. Inovenkov, M. Kando, F. Pegoraro, and G. Korn, Phys. Rev. Lett. **104** (13), 135003 (2010).

BIBLIOGRAPHY

- Bulanov, S. V., T. Z. Esirkepov, M. Kando, J. K. Koga, and S. S. Bulanov, Phys. Rev. E **84**, 056605 (2011).
- Cao, L., Y. Gu, Z. Zhao, L. Cao, W. Huang, W. Zhou, H. B. Cai, X. T. He, W. Yu, and M. Y. Yu, Phys. Plasmas **17** (10), 103106 (2010a).
- Cao, L., Y. Gu, Z. Zhao, L. Cao, W. Huang, W. Zhou, X. T. He, W. Yu, and M. Y. Yu, Phys. Plasmas **17** (4), 043103 (2010b).
- Carlson, T. A., C. Nestor, N. Wasserman, and J. McDowell, At. Data Nucl. Data Tables **2**, 63 (1970).
- Cattani, F., A. Kim, D. Anderson, and M. Lisak, Phys. Rev. E **62**, 1234 (2000).
- Ceccotti, T., A. Lévy, H. Popescu, F. Réau, P. D’Oliveira, P. Monot, J. P. Geindre, E. Lefebvre, and P. Martin, Phys. Rev. Lett. **99** (18), 185002 (2007).
- Chabrier, G., Plasma Physics and Controlled Fusion **51** (12), 124014 (2009).
- Chang, H. X., B. Qiao, Y. X. Zhang, Z. Xu, W. P. Yao, C. T. Zhou, and X. T. He, Phys. Plasmas **24** (4), 043111 (2017).
- Chatterjee, G., P. K. Singh, S. Ahmed, A. P. L. Robinson, A. D. Lad, S. Mondal, V. Narayanan, I. Srivastava, N. Koratkar, J. Pasley, A. K. Sood, and G. R. Kumar, Phys. Rev. Lett. **108**, 235005 (2012).
- Chen, C. D., P. K. Patel, D. S. Hey, A. J. Mackinnon, M. H. Key, K. U. Akli, T. Bartal, F. N. Beg, S. Chawla, H. Chen, R. R. Freeman, D. P. Higginson, A. Link, T. Y. Ma, A. G. MacPhee, R. B. Stephens, L. D. Van Woerkom, B. Westover, and M. Porkolab, Phys. Plasmas **16** (8), 082705 (2009).
- Chen, H., F. Fiuzza, A. Link, A. Hazi, M. Hill, D. Hoarty, S. James, S. Kerr, D. D. Meyerhofer, J. Myatt, J. Park, Y. Sentoku, and G. J. Williams, Phys. Rev. Lett. **114** (21), 215001 (2015).
- Chen, H., S. C. Wilks, J. D. Bonlie, E. P. Liang, J. Myatt, D. F. Price, D. D. Meyerhofer, and P. Beiersdorfer, Phys. Rev. Lett. **102**, 105001 (2009).
- Chen, H., S. C. Wilks, D. D. Meyerhofer, J. Bonlie, C. D. Chen, S. N. Chen, C. Courtois, L. Elberson, G. Gregori, W. Kruer, O. Landoas, J. Mithen, J. Myatt, C. D. Murphy, P. Nilson, D. Price, M. Schneider, R. Shepherd, C. Stoeckl, M. Tabak, R. Tommasini, and P. Beiersdorfer, Phys. Rev. Lett. **105**, 015003 (2010).
- Chen, S., N. D. Powers, I. Ghebregziabher, C. M. Maharjan, C. Liu, G. Golovin, S. Banerjee, J. Zhang, N. Cunningham, A. Moorti, S. Clarke, S. Pozzi, and D. P. Umstadter, Phys. Rev. Lett. **110**, 155003 (2013).
- Chung, H.-K., M. Chen, W. Morgan, Y. Ralchenko, and R. Lee, High Energy Density Physics **1** (1), 3 (2005).
- Cole, J. M., K. T. Behm, E. Gerstmayer, T. G. Blackburn, J. C. Wood, C. D. Baird, M. J. Duff, C. Harvey, A. Ilderton, A. S. Joglekar, K. Krushelnick, S. Kuschel, M. Marklund, P. McKenna, C. D. Murphy, K. Poder, C. P. Ridgers, G. M. Samarin, G. Sarri, D. R. Symes, A. G. R. Thomas, J. Warwick, M. Zepf, Z. Najmudin, and S. P. D. Mangles, Phys. Rev. X **8**, 011020 (2018).

- Compart La Fontaine, A., C. Courtois, and E. Lefebvre, Phys. Plasmas **19** (2), 023104 (2012).
- Courtois, C., R. Edwards, A. C. L. Fontaine, C. Aedy, M. Barbotin, S. Bazzoli, L. Biddle, D. Brebion, J. L. Bourgade, D. Drew, M. Fox, M. Gardner, J. Gazave, J. M. Lagrange, O. Landoas, L. L. Dain, E. Lefebvre, D. Mastrosimone, N. Pichoff, G. Pien, M. Ramsay, A. Simons, N. Sircombe, C. Stoeckl, and K. Thorp, Phys. Plasmas **18** (2), 023101 (2011).
- Courtois, C., R. Edwards, A. C. L. Fontaine, C. Aedy, S. Bazzoli, J. L. Bourgade, J. Gazave, J. M. Lagrange, O. Landoas, L. L. Dain, D. Mastrosimone, N. Pichoff, G. Pien, and C. Stoeckl, Phys. Plasmas **20** (8), 083114 (2013).
- Courtois, C., A. C. L. Fontaine, O. Landoas, G. Lidove, V. Mot, P. Morel, R. Nuter, E. Lefebvre, A. Boscheron, J. Grenier, M. M. Alonard, M. Gerbaux, F. Gobet, F. Hannachi, G. Malka, J. N. Scheurer, and M. Tarisien, Physics of Plasmas **16** (1), 013105 (2009).
- Cowan, T. E., A. W. Hunt, T. W. Phillips, S. C. Wilks, M. D. Perry, C. Brown, W. Fountain, S. Hatchett, J. Johnson, M. H. Key, T. Parnell, D. M. Pennington, R. A. Snavely, and Y. Takahashi, Phys. Rev. Lett. **84**, 903 (2000).
- Cowan, T. E., M. D. Perry, M. H. Key, T. R. Ditmire, S. P. Hatchett, E. A. Henry, J. D. Moody, M. J. Moran, D. M. Pennington, T. W. Phillips, T. C. Sangster, J. A. Sefcik, M. S. Singh, R. A. Snavely, M. A. Stoyer, S. C. Wilks, P. E. Young, Y. Takahashi, B. Dong, W. Fountain, T. Parnell, J. Johnson, A. W. Hunt, and T. Kühl, Laser & Part. Beams **17**, 773 (1999).
- Cristoforetti, G., P. Londrillo, P. K. Singh, F. Baffigi, G. D'Arrigo, A. D. Lad, R. G. Milazzo, A. Adak, M. Shaikh, D. Sarkar, G. Chatterjee, J. Jha, M. Krishnamurthy, G. R. Kumar, and L. A. Gizzi, Sci. Reports **7**, 1479 (2017).
- Curtis, A., C. Calvi, J. Tinsley, R. Hollinger, V. Kaymak, A. Pukhov, S. Wang, A. Rockwood, Y. Wang, V. N. Shlyaptsev, and J. J. Rocca, Nature Comm. **9**, 1077 (2018).
- Daido, H., M. Nishiuchi, and A. S. Pirozhkov, Rep. Prog. Phys. **75** (5), 056401 (2012).
- Das, M., B. K. Sahoo, and S. Pal, Phys. Rev. A **93** (5), 052513 (2016).
- Davies, J. R., Plasma Phys. Control. Fusion **51** (1), 014006 (2009).
- Debayle, A., J. J. Honrubia, E. d'Humières, and V. T. Tikhonchuk, Phys. Rev. E **82**, 036405 (2010).
- Debayle, A., F. Mollica, B. Vauzour, Y. Wan, A. Flacco, V. Malka, X. Davoine, and L. Gremillet, New J. Phys. **19** (12), 123013 (2017).
- Debayle, A., J. Sanz, L. Gremillet, and K. Mima, Phys. Plasmas **20** (5), 053107 (2013).
- Del Gaudio, F., T. Grismayer, R. Fonseca, and L. Silva (2017), in *APS Meeting Abstracts*, p. BP11.030.
- Del Gaudio, F., T. Grismayer, R. A. Fonseca, W. B. Mori, and L. O. Silva, ArXiv e-prints , arXiv:1807.06968 (2018).

BIBLIOGRAPHY

- Dermer, C. D., and G. Menon (2009), *High energy radiation from black holes: Gamma rays, Cosmic rays, and Neutrinos*, Princeton series in Astrophysics (Princeton University Press, Princeton, NJ).
- d'Humières, E., E. Lefebvre, L. Gremillet, and V. Malka, Phys. Plasmas **12** (6), 062704 (2005).
- Di Piazza, A., C. Müller, K. Z. Hatsagortsyan, and C. H. Keitel, Rev. Mod. Phys. **84**, 1177 (2012).
- Di Piazza, A., M. Tamburini, S. Meuren, and C. H. Keitel, Phys. Rev. A **98**, 012134 (2018).
- Diaw, A., and P. Mora, Phys. Rev. E **84** (3), 036402 (2011).
- Diaw, A., and P. Mora, Phys. Rev. E **86**, 026403 (2012).
- Dirac, P. A., Proceedings of the Royal Society of London A: Mathematical, Physical and Engineering Sciences **167** (929), 148 (1938).
- Dorozhkina, D. S., and V. E. Semenov, Phys. Rev. Lett. **81**, 2691 (1998).
- Drouin, M. (2009), *Vers la simulation particulaire réaliste de l'interaction laser-plasma surcritique : conception d'un schéma implicite avec amortissement ajustable et fonctions de forme d'ordre élevé*, Ph.D. thesis (École normale supérieure de Cachan).
- Duclos, R., J. G. Kirk, and A. R. Bell, Plasma Phys. Control. Fusion **53** (1), 015009 (2011).
- Edwards, R. D., M. A. Sinclair, T. J. Goldsack, K. Krushelnick, F. N. Beg, E. L. Clark, A. E. Dangor, Z. Najmudin, M. Tatarakis, B. Walton, M. Zepf, K. W. D. Ledingham, I. Spencer, P. A. Norreys, R. J. Clarke, R. Kodama, Y. Toyama, and M. Tampo, Applied Physics Letters **80**, 2129 (2002).
- Eliasson, B., New J. Phys. **17** (3), 033026 (2015).
- Elwert, G. (1939), *Verschärft Berechnung von Intensität und Polarisation im kontinuierlichen Röntgenspektrum* (Annalen der Physik).
- Embréus, O., L. Hesslow, M. Hoppe, G. Papp, K. Richards, and T. Fülöp, Journal of Plasma Physics **84** (5) (2018).
- Erber, T., Rev. Mod. Phys. **38**, 626 (1966).
- Eremin, V. I., A. V. Korzhimanov, and A. V. Kim, Phys. Plasmas **17** (4), 043102 (2010).
- Esarey, E., C. B. Schroeder, and W. P. Leemans, Rev. Mod. Phys. **81**, 1229 (2009).
- Esarey, E., P. Sprangle, J. Krall, and A. Ting, IEEE Transactions on Plasma Science **24**, 252 (1996).
- Esirkepov, T., Computer Physics Communications **135** (2), 144 (2001).
- Esirkepov, T., B. M., S. V. Bulanov, G. Mourou, and T. Tajima, Phys. Rev. Lett. **92**, 175003 (2004).
- Esirkepov, T., M. Yamagiwa, and T. Tajima, Phys. Rev. Lett. **96**, 105001 (2006).

- Faure, J., Y. Glinec, A. Pukhov, S. Kiselev, S. Gordienko, E. Lefebvre, J.-P. Rousseau, F. Burgy, and V. Malka, *Nature* **431**, 541 (2004).
- Ferri, J., L. Senje, M. Dalui, K. Svensson, B. Aurand, M. Hansson, A. Persson, O. Lundh, C.-G. Wahlström, L. Gremillet, E. Siminos, T. C. DuBois, L. Yi, J. L. Martins, and T. Fülöp, *Phys. Plasmas* **25** (4), 043115 (2018).
- Frankel, N. E., K. C. Hines, and R. L. Dewar, *Phys. Rev. A* **20**, 2120 (1979).
- Fuchs, J., P. Antici, E. D'Humières, E. Lefebvre, M. Borghesi, E. Brambrink, C. A. Cecchetti, M. Kaluza, V. Malka, M. Mancossi, S. Meyroneinc, P. Mora, J. Schreiber, T. Toncian, H. Pépin, and P. Audebert, *Nature Phys.* **2**, 48 (2006).
- Gahn, C., G. Pretzler, A. Saemann, G. D. Tsakiris, K. J. Witte, D. Gassmann, T. Schtz, U. Schramm, P. Thirolf, and D. Habs, *Appl. Phys. Lett.* **73** (25), 3662 (1998).
- Gahn, C., G. D. Tsakiris, G. Pretzler, K. J. Witte, C. Delfin, C.-G. Wahlström, and D. Habs, *Appl. Phys. Lett.* **77**, 2662 (2000).
- Gahn, C., G. D. Tsakiris, A. Pukhov, J. Meyer-ter Vehn, G. Pretzler, P. Thirolf, D. Habs, and K. J. Witte, *Phys. Rev. Lett.* **83**, 4772 (1999).
- Gaillard, S. A., T. Kluge, K. A. Flippo, M. Bussmann, B. Gall, T. Lockard, M. Geissel, D. T. Offermann, M. Schollmeier, Y. Sentoku, and T. E. Cowan, *Phys. Plasmas* **18** (5), 056710 (2011).
- Galy, J., M. Mau, D. J. Hamilton, R. Edwards, and J. Magill, *New. J. Phys.* **9**, 23 (2007).
- Geddes, C. G. R., C. Toth, J. van Tilborg, E. Esarey, C. B. Schroeder, D. Bruhwiler, C. Nieter, J. Cary, and W. P. Leemans, *Nature* **431**, 538 (2004).
- Gibbon, P., *Phys. Rev. Lett.* **73**, 664 (1994).
- Gibbon, P. (2005), *Short Pulse Laser Interactions with Matter: An Introduction* (Imperial College Press).
- Glinec, Y., J. Faure, L. L. Dain, S. Darbon, T. Hosokai, J. J. Santos, E. Lefebvre, J. P. Rousseau, F. Burgy, B. Mercier, and V. Malka, *Phys. Rev. Lett.* **94**, 025003 (2005).
- Gonoskov, A. (2013), *Ultra-intense laser-plasma interaction for applied and fundamental physics*, Ph.D. thesis (Ume University, Department of Physics).
- Gonoskov, A. A., A. V. Korzhimanov, A. V. Kim, M. Marklund, and A. M. Sergeev, *Phys. Rev. E* **84** (4), 046403 (2011).
- Gould, R. J., *Astr. Phys. J.* **238**, 1026 (1980).
- Gray, L. H., and J. Read, *Nature* **152**, 53 (1943).
- Gremillet, L. (2001), *Étude théorique et expérimentale du transport des électrons rapides dans l'interaction laser-solide à très haut flux*, Ph.D. thesis (École Polytechnique).
- Grismayer, T., P. Mora, J. C. Adam, and A. Héron, *Phys. Rev. E* **77** (6), 066407 (2008).
- Grismayer, T., M. Vranic, J. L. Martins, R. A. Fonseca, and L. O. Silva, *Phys. Plasmas* **23**, 056706 (2016).

BIBLIOGRAPHY

- Grismayer, T., M. Vranic, J. L. Martins, R. A. Fonseca, and L. O. Silva, Phys. Rev. E **95**, 023210 (2017).
- Gryaznykh, D. A., Y. Z. Kandiev, and V. A. Lykov, JETP Lett. **67** (4), 257 (1998).
- Gurevich, A. V., L. V. Pariiskaya, and L. P. Pitaevskii, Sov. Phys. JETP **22**, 449 (1966).
- Haines, M. G., M. S. Wei, F. N. Beg, and R. B. Stephens, Phys. Rev. Lett. **102**, 045008 (2009).
- Hatchett, S. P., C. G. Brown, T. E. Cowan, E. A. Henry, J. S. Johnson, M. H. Key, J. A. Koch, A. B. Langdon, B. F. Lasinski, R. W. Lee, A. J. Mackinnon, D. M. Pennington, M. D. Perry, T. W. Phillips, M. Roth, T. C. Sangster, M. S. Singh, R. A. Snavely, M. A. Stoyer, S. C. Wilks, and K. Yasuike, Phys. Plasmas **7**, 2076 (2000).
- Heitler, W. (1954), *The Quantum Theory of Radiation*, Monographs on Physics (Oxford University Press).
- Hellwarth, R. W. (1961), in *Advances in Quantum Electronics*, edited by J. R. Singer, p. 334.
- Higginson, A., R. J. Gray, M. King, R. J. Dance, S. D. R. Williamson, N. M. H. Butler, R. Wilson, R. Capdessus, C. Armstrong, J. S. Green, S. J. Hawkes, P. Martin, W. Q. Wei, S. R. Mirfayzi, X. H. Yuan, S. Kar, R. J. Borghesi, M. and Clarke, D. Neely, and P. McKenna, Nature Comm. **9**, 724 (2018).
- Hollinger, R., C. Bargsten, V. N. Shlyaptsev, V. Kaymak, A. Pukhov, M. G. Capeluto, S. Wang, A. Rockwood, Y. Wang, A. Townsend, A. Prieto, P. Stockton, A. Curtis, and J. J. Rocca, Optica **4** (11), 1344 (2017).
- Huang, T. W., C. T. Zhou, H. Zhang, S. Z. Wu, B. Qiao, X. T. He, and S. C. Ruan, Appl. Phys. Lett. **110** (2), 021102 (2017).
- Hubbell, J. H., H. A. Gimm, and I. Overbo, Journal of Physical and Chemical Reference Data **9** (4), 1023 (1980).
- Ilderton, A., B. King, and D. Seipt, ArXiv e-prints , [arXiv:1808.10339](https://arxiv.org/abs/1808.10339) (2018).
- Ivanov, K. A., D. A. Gozhev, S. P. Rodichkina, S. V. Makarov, S. S. Makarov, M. A. Dubatkov, S. A. Pikuz, D. E. Presnov, A. A. Paskhalov, N. V. Eremin, V. Y. Brantov, A. V. and Bychenkov, R. V. Volkov, V. Y. Timoshenko, S. I. Kudryashov, and A. B. Savel'ev, Appl. Phys. B **123** (10), 252 (2017).
- Iwata, N., H. Nagatomo, Y. Fukuda, R. Matsui, and Y. Kishimoto, Phys. Plasmas **23** (6), 063115 (2016).
- Jarrott, L. C., A. J. Kemp, L. Divol, D. Mariscal, B. Westover, C. McGuffey, F. N. Beg, M. Suggit, C. Chen, D. Hey, B. Maddox, J. Hawreliak, H.-S. Park, B. Remington, M. S. Wei, and A. MacPhee, Phys. Plasmas **21** (3), 031211 (2014).
- Ji, L., A. Pukhov, E. Nerush, I. Kostyukov, K. Akli, and B. Shen, Eur. Phys. J. Spec. Top. **223** (6), 1069 (2014a).
- Ji, L. L., A. Pukhov, I. Y. Kostyukov, B. F. Shen, and K. Akli, Phys. Rev. Lett. **112**, 145003 (2014b).

- Ji, L. L., A. Pukhov, E. N. Nerush, I. Y. Kostyukov, B. F. Shen, and K. U. Akli, Phys. Plasmas **21** (2), 023109 (2014c).
- Ji, Y., G. Jiang, W. Wu, C. Wang, Y. Gu, and Y. Tang, Appl. Phys. Lett. **96** (4), 041504 (2010).
- Jiang, S., L. L. Ji, H. Audesirk, K. M. George, J. Snyder, A. Krygier, P. Poole, C. Willis, R. Daskalova, E. Chowdhury, N. S. Lewis, D. W. Schumacher, A. Pukhov, R. R. Freeman, and K. U. Akli, Phys. Rev. Lett. **116**, 085002 (2016).
- Jirka, M., O. Klímo, M. Vranic, S. Weber, and G. Korn, Sci. Reports **7**, 15302 (2017).
- Joshi, C., Phys. Plasmas **14** (5), 055501 (2007).
- Kagan, D., L. Sironi, B. Cerutti, and D. Giannios (2016), “Relativistic magnetic reconnection in pair plasmas and its astrophysical applications,” in *The Strongest Magnetic Fields in the Universe*, edited by V. Beskin, A. Balogh, M. Falanga, M. Lyutikov, S. Mereghetti, T. Piran, and R. Treumann (Springer New York, New York, NY) pp. 555–583.
- Kaw, P., and J. Dawson, The Physics of Fluids **13** (2), 472 (1970).
- Kaymak, V., A. Pukhov, V. N. Shlyaptsev, and J. J. Rocca, Phys. Rev. Lett. **117**, 035004 (2016).
- Kemp, A. J., and L. Divol, Physics of Plasmas **23** (9), 090703 (2016).
- Kemp, A. J., F. Fiuzza, A. Debayle, T. Johzaki, W. B. Mori, P. K. Patel, Y. Sentoku, and L. O. Silva, Nucl. Fusion **54** (5), 054002 (2014).
- Kemp, A. J., Y. Sentoku, and M. Tabak, Phys. Rev. E **79**, 066406 (2009).
- Khaghani, D., M. Lobet, B. Borm, L. Burr, F. Gärtner, L. Gremillet, L. Movsesyan, O. Rosmej, M. E. Toimil-Molares, F. Wagner, and P. Neumayer, Sci. Reports **7**, 11366 (2017).
- Kim, I. J., K. H. Pae, C. M. Kim, H. T. Kim, J. H. Sung, S. K. Lee, T. J. Yu, I. W. Choi, C.-L. Lee, K. H. Nam, P. V. Nickles, T. M. Jeong, and J. Lee, Phys. Rev. Lett. **111**, 165003 (2013).
- Kim, Y.-K., J. P. Santos, and F. Parente, Phys. Rev. A **62**, 052710 (2000).
- Kirk, J. G., A. R. Bell, and I. Arka, Plasma Phys. Control. Fusion **51** (8), 085008 (2009).
- Klím, O., J. Psikal, J. Limpouch, and V. T. Tikhonchuk, Phys. Rev. Accel. Beams **11** (3), 031301 (2008).
- Kmetec, J. D., C. L. Gordon, J. J. Macklin, B. E. Lemoff, G. S. Brown, and S. E. Harris, Phys. Rev. Lett. **68**, 1527 (1992).
- Koch, H. W., and J. W. Motz, Rev. Mod. Phys. **31**, 920 (1959).
- Koga, J., Phys. Rev. E **70** (4), 046502 (2004).
- Kruer, W. L., and K. Estabrook, Phys. Fluids **28** (1), 430 (1985).

BIBLIOGRAPHY

- Landau, L. D., and E. M. Lifshitz (1975), *Course of theoretical physics - Pergamon International Library of Science, Technology, Engineering and Social Studies, Oxford: Pergamon Press, 1975, 4th rev.engl.ed.*
- Le Garrec, B., S. Sebban, D. Margarone, M. Precek, S. Weber, O. Klimo, G. Korn, and B. Rus (2014), in *High Energy/Average Power Lasers and Intense Beam Applications VII*, Proc. SPIE, Vol. 8962, p. 89620I.
- Lecherbourg, L., P. Renaudin, S. Bastiani-Ceccotti, J.-P. Geindre, C. Blancard, P. Cossé, G. Faussurier, R. Shepherd, and P. Audebert, High. Energ. Dens. Phys. **3**, 175 (2007).
- Lecz, Z., and A. Andreev, Phys. Plasmas **24** (3), 033113 (2017).
- Lécz, Z., O. Boine-Frankenheim, and V. Kornilov, Nucl. Instrum. Methods Phys. Res. A **727**, 51 (2013).
- Ledingham, K. W. D., P. McKenna, and R. P. Singhal, Science **300**, 1107 (2003).
- Ledingham, K. W. D., I. Spencer, T. McCanny, R. P. Singhal, M. I. K. Santala, E. Clark, I. Watts, F. N. Beg, M. Zepf, K. Krushelnick, M. Tatarakis, A. E. Dangor, P. A. Norreys, R. Allott, D. Neely, R. J. Clark, A. C. Machacek, J. S. Wark, A. J. Cresswell, D. C. W. Sanderson, and J. Magill, Phys. Rev. Lett. **84**, 899 (2000).
- Lee, Y. T., and R. M. More, Phys. Fluids **27**, 1273 (1984).
- Leemans, W. P., A. J. Gonsalves, H.-S. Mao, K. Nakamura, C. Benedetti, C. B. Schroeder, C. Tóth, J. Daniels, D. E. Mittelberger, S. S. Bulanov, J.-L. Vay, C. G. R. Geddes, and E. Esarey, Phys. Rev. Lett. **113**, 245002 (2014).
- Leemans, W. P., B. Nagler, A. J. Gonsalves, C. Tóth, K. Nakamura, C. G. R. Geddes, E. Esarey, C. B. Schroeder, and S. M. Hooker, Nature Phys. **2**, 696 (2006).
- Lefebvre, E., and G. Bonnaud, Phys. Rev. Lett. **74**, 2002 (1995).
- Lefebvre, E., and G. Bonnaud, Phys. Rev. E **55**, 1011 (1997).
- Lehe, R., A. Lifschitz, C. Thaury, V. Malka, and X. Davoine, Phys. Rev. ST Accel. Beams **16**, 021301 (2013).
- Liang, E., High. Energ. Dens. Phys. **9**, 425 (2013).
- Liang, E., T. Clarke, A. Henderson, W. Fu, W. Lo, D. Taylor, P. Chaguine, S. Zhou, Y. Hua, X. Cen, X. Wang, J. Kao, H. Hasson, G. Dyer, K. Serratto, N. Riley, M. Donovan, and T. Ditmire, Sci. Reports **5**, 13968 (2015).
- Liang, E. P., S. C. Wilks, and M. Tabak, Phys. Rev. Lett. **81**, 4887 (1998).
- Lindl, J., Physics of Plasmas **2** (11), 3933 (1995).
- Liu, J.-J., T.-P. Yu, Y. Yin, X.-L. Zhu, and F.-Q. Shao, Opt. Express **24** (14), 15978 (2016).
- Lobet, M. (2015), *Radiative and quantum electrodynamics effects in extreme intensity laser-matter interaction*, Ph.d. thesis (Université de Bordeaux).

- Lobet, M., X. Davoine, E. d'Humières, and L. Gremillet, Phys. Rev. Accel. Beams **20**, 043401 (2017).
- Lobet, M., E. d'Humières, M. Grech, C. Ruyer, X. Davoine, and L. Gremillet, J. Phys. Conf. Ser. **688** (1), 012058 (2016).
- Lobet, M., C. Ruyer, A. Debayle, E. d'Humières, M. Grech, M. Lemoine, and L. Gremillet, Phys. Rev. Lett. **115**, 215003 (2015).
- Loch, R. A., T. Ceccotti, F. Qur, H. George, G. Bonnaud, F. Rau, P. D'Oliveira, M. J. H. Luttkhof, F. Bijkerk, K.-J. Boller, G. Blaclar, and P. Combis, Physics of Plasmas **23** (9), 093117 (2016).
- Lorentz, H. A. (1916), *The theory of electrons and its applications to the phenomena of light and radiant heat* (Leipzig : B.G. Teubner ; New York : G.E. Stechert).
- Loveman, R., J. Bendahan, T. Gozani, and J. Stevenson, Nuclear Instruments and Methods in Physics Research Section B: Beam Interactions with Materials and Atoms **99** (1), 765 (1995), application of Accelerators in Research and Industry '94.
- Lu, W., M. Tzoufras, C. Joshi, F. S. Tsung, W. B. Mori, J. Vieira, R. A. Fonseca, and L. O. Silva, Phys. Rev. ST Accel. Beams **10**, 061301 (2007).
- Lundh, O., J. Lim, C. Rechatin, L. Ammoura, A. Ben-Ismaïl, X. Davoine, G. Gallot, J.-P. Goddet, E. Lefebvre, V. Malka, and J. Faure, Nature Phys. **7**, 219 (2011).
- Macchi, A., High Power Laser Science and Engineering **2**, e10 (2014).
- Macchi, A., M. Borghesi, and M. Passoni, Rev. Mod. Phys. **85**, 751 (2013).
- Macchi, A., F. Cattani, T. V. Liseykina, and F. Cornolti, Phys. Rev. Lett. **94**, 165003 (2005).
- Macchi, A., C. Livi, and A. Sgattoni, J. Instrum. **12** (04), C04016 (2017).
- Macchi, A., S. Veghini, and F. Pegoraro, Phys. Rev. Lett. **103**, 085003 (2009).
- Mackenroth, F., N. Neitz, and A. Di Piazza, Plasma Phys. Control. Fusion **55** (12), 124018 (2013).
- Maiman, T. H., Nature **187**, 493 (1960).
- Malka, V., S. Fritzler, E. Lefebvre, M.-M. Aléonard, F. Burgy, J.-P. Chambaret, J.-F. Chemin, K. Krushelnick, G. Malka, S. P. D. Mangles, Z. Najmudin, M. Pittman, J.-P. Rousseau, J.-N. Scheurer, B. Walton, and A. E. Dangor, Science **298**, 1596 (2002).
- Mangles, S. P. D., C. D. Murphy, Z. Najmudin, A. G. R. Thomas, J. L. Collier, A. E. Dangor, E. J. Divall, P. S. Foster, J. G. Gallacher, C. J. Hooker, D. A. Jaroszynski, A. J. Langley, W. B. Mori, P. A. Norreys, F. S. Tsung, R. Viskup, B. R. Walton, and K. Krushelnick, Nature **431**, 535 (2004).
- March, N. H., Adv. Phys. **6**, 1 (1957).
- Martinez, B., E. dHumires, and L. Gremillet, Plasma Physics and Controlled Fusion **60** (7), 074009 (2018).

BIBLIOGRAPHY

- Martinolli, E., M. Koenig, S. D. Baton, J. J. Santos, F. Amiranoff, D. Batani, E. Perelli-Cippo, F. Scianitti, L. Gremillet, R. Mélizzi, A. Decoster, C. Rousseaux, T. A. Hall, M. H. Key, R. Snavely, A. J. MacKinnon, R. R. Freeman, J. A. King, R. Stephens, D. Neely, and R. J. Clarke, Phys. Rev. E **73** (4), 046402 (2006).
- Marx, G., Nature **211**, 22 (1966).
- May, J., J. Tonge, F. Fiuzza, R. A. Fonseca, L. O. Silva, C. Ren, and W. B. Mori, Phys. Rev. E **84**, 025401 (2011).
- Meadcroft, A. L., and R. D. Edwards, IEEE Transactions on Plasma Science **40**, 1992 (2012).
- Mihalas, D. (1978), *Stellar atmospheres* (San Francisco, W. H. Freeman and Co.).
- Mishra, R., F. Fiuzza, and S. Glenzer, New J. Phys. **20** (4), 043047 (2018).
- Mishra, R., Y. Sentoku, and A. J. Kemp, Phys. Plasmas **16** (11), 112704 (2009).
- Mocker, H. W., and R. J. Collins, Appl. Phys. Lett. **7** (10), 270 (1965).
- Modena, A., Z. Najmudin, A. E. Dangor, C. E. Clayton, K. A. Marsh, C. Joshi, V. Malka, C. B. Darrow, C. Danson, D. Neely, and F. N. Walsh, Nature **377**, 606 (1995).
- Molière, G., Zeitschrift Naturforschung Teil A **2**, 133 (1947).
- Mondal, S., I. Chakraborty, S. Ahmad, D. Carvalho, P. Singh, A. D. Lad, V. Narayanan, P. Ayyub, G. R. Kumar, J. Zheng, and Z. Sheng, Phys. Rev. B **83**, 035408 (2011).
- Mora, P., Phys. Rev. Lett. **90**, 185002 (2003).
- Mora, P., Phys. Rev. E **72**, 056401 (2005).
- More, R., Adv. At. Mol. Phys. **21**, 305 (1985).
- Motz, J. W., H. A. Olsen, and H. W. Koch, Rev. Mod. Phys. **41**, 581 (1969).
- Mourou, G. A., T. Tajima, and S. V. Bulanov, Rev. Mod. Phys. **78**, 309 (2006).
- Mulser, P., and D. Bauer (2010), *High power laser-matter interaction*, Springer tracts in modern physics (Springer, Berlin).
- Mulser, P., D. Bauer, and H. Ruhl, Phys. Rev. Lett. **101**, 225002 (2008).
- Murota, T., A. Ueda, and H. Tanaka, Prog. Theor. Phys. **16** (5), 482 (1956).
- Myatt, J., J. A. Delettrez, A. V. Maximov, D. D. Meyerhofer, R. W. Short, C. Stoeckl, and M. Storm, Phys. Rev. E **79**, 066409 (2009).
- Nakamura, T., and T. Hayakawa, Phys. Plasmas **22** (8), 083113 (2015).
- Nakamura, T., J. K. Koga, T. Z. Esirkepov, M. Kando, G. Korn, and S. V. Bulanov, Phys. Rev. Lett. **108**, 195001 (2012).
- Nanbu, K., Phys. Rev. E **55**, 4642 (1997).
- Nanbu, K., and S. Yonemura, J. Comput. Phys. **145** (2), 639 (1998).

- Nardi, E., E. Y. Maron, and D. H. H. Hoffmann, *Laser & Part. Beams* **25**, 489 (2007).
- Nardi, E., and Z. Zinamon, *Phys. Rev. A* **18**, 1246 (1978).
- Naumova, N., T. Schlegel, V. T. Tikhonchuk, C. Labaune, I. V. Sokolov, and G. Mourou, *Phys. Rev. Lett.* **102**, 025002 (2009).
- Nerush, E. N., I. Y. Kostyukov, A. M. Fedotov, N. B. Narozhny, N. V. Elkina, and H. Ruhl, *Phys. Rev. Lett.* **106**, 035001 (2011).
- Nerush, E. N., I. Y. Kostyukov, L. Ji, and A. Pukhov, *Phys. Plasmas* **21** (1), 013109 (2014).
- Niel, F., C. Riconda, F. Amiranoff, R. Duclous, and M. Grech, *Phys. Rev. E* **97**, 043209 (2018).
- Nikishov, A. I., and V. I. Ritus, *Sov. Phys. JETP* **19**, 529 (1964).
- Ovchinnikov, A., O. Kostenko, O. Chefonov, O. Rosmej, N. Andreev, M. Agranat, J. Duan, J. Liu, and V. Fortov, *Laser & Part. Beams* **29** (2), 249 (2011).
- Pak, A., K. A. Marsh, S. F. Martins, W. Lu, W. B. Mori, and C. Joshi, *Phys. Rev. Lett.* **104**, 025003 (2010).
- Pan, K. Q., C. Y. Zheng, D. Wu, L. H. Cao, Z. J. Liu, and X. T. He, *Appl. Phys. Lett.* **107** (18), 183902 (2015).
- Pandit, R. R., and Y. Sentoku, *Phys. Plasmas* **19** (7), 073304 (2012).
- Paradkar, B. S., M. S. Wei, T. Yabuuchi, R. B. Stephens, M. G. Haines, S. I. Krasheninnikov, and F. N. Beg, *Phys. Rev. E* **83**, 046401 (2011).
- Park, H.-S., B. R. Maddox, E. Giraldez, S. P. Hatchett, L. T. Hudson, N. Izumi, M. H. Key, S. Le Pape, A. J. MacKinnon, A. G. MacPhee, P. K. Patel, T. W. Phillips, B. A. Remington, J. F. Seely, R. Tommasini, R. Town, J. Workman, and E. Brambrink, *Phys. Plasmas* **15** (7), 072705 (2008).
- Passoni, M., A. Zani, A. Sgattoni, D. Dellasega, A. Macchi, I. Prencipe, V. Floquet, P. Martin, T. V. Liseykina, and T. Ceccotti, *Plasma Phys. Control. Fusion* **56** (4), 045001 (2014).
- Peano, F., M. Marti, L. O. Silva, and G. Coppa, *Phys. Rev. E* **79**, 025701 (2009).
- Pegoraro, F., and S. V. Bulanov, *Phys. Rev. Lett.* **99**, 065002 (2007).
- Pérez, F., L. Gremillet, A. Decoster, M. Drouin, and E. Lefebvre, *Phys. Plasmas* **19** (8), 083104 (2012).
- Perkins, L., B. Logan, M. Rosen, M. Perry, T. D. de la Rubia, N. Ghoniem, T. Ditmire, P. Springer, and S. Wilks, *Nuclear Fusion* **40** (1), 1 (2000).
- Perry, M. D., J. A. Sefcik, T. Cowan, S. Hatchett, A. Hunt, M. Moran, D. Pennington, R. Snavely, and S. C. Wilks, *Review of Scientific Instruments* **70** (1), 265 (1999).
- Phuoc, K. T., S. Corde, C. Thaury, V. Malka, A. Tafzi, J. P. Goddet, R. C. Shah, S. Sebban, and A. Rousse, *Nature Phys.* **6**, 308-311 (2012).

BIBLIOGRAPHY

- Pike, O. J., F. Mackenroth, E. G. Hill, and S. J. Rose, *Nature Photon.* **8**, 434-436 (2014).
- Pisani, F., A. Bernardinello, D. Batani, A. Antonicci, E. Martinolli, M. Koenig, L. Gremillet, F. Amiranoff, S. Baton, J. Davies, T. Hall, D. Scott, P. Norreys, A. Djaoui, C. Rousseaux, P. Fews, H. Bandulet, and H. Pepin, *Phys. Rev. E* **62**, R5927 (2000).
- Poder, K., M. Tamburini, G. Sarri, A. Di Piazza, S. Kuschel, C. D. Baird, K. Behm, S. Bohlen, J. M. Cole, D. J. Corvan, M. Duff, E. Gerstmayr, C. H. Keitel, K. Krushelnick, S. P. D. Mangles, P. McKenna, C. D. Murphy, Z. Najmudin, C. P. Ridgers, G. M. Samarin, D. R. Symes, A. G. R. Thomas, J. Warwick, and M. Zepf, *Phys. Rev. X* **8**, 031004 (2018).
- Pomerantz, I., E. McCary, A. R. Meadows, A. Arefiev, A. C. Bernstein, C. Chester, J. Cortez, M. E. Donovan, G. Dyer, E. W. Gaul, D. Hamilton, D. Kuk, A. C. Lestrade, C. Wang, T. Ditmire, and B. M. Hegelich, *Phys. Rev. Lett.* **113**, 184801 (2014).
- Powers, N. D., I. Ghebregziabher, G. Golovin, C. Liu, S. Chen, S. Banerjee, J. Zhang, and D. P. Umstadter, *Nature Phys.* **8**, 28-31 (2014).
- Prencipe, I., A. Sgattoni, D. Dellasega, L. Fedeli, L. Cialfi, I. W. Choi, I. J. Kim, K. A. Janulewicz, K. F. Kakolee, H. W. Lee, J. H. Sung, S. K. Lee, C. H. Nam, and M. Passoni, *Plasma Phys. Control. Fusion* **58** (3), 034019 (2016).
- Pukhov, A., *J. Plasma Phys.* **61**, 425 (1999).
- Pukhov, A., and J. Meyer-ter-Vehn, *Applied Physics B: Lasers and Optics* **74**, 355 (2002).
- Pukhov, A., Z.-M. Sheng, and J. Meyer-ter Vehn, *Physics of Plasmas* **6** (7), 2847 (1999).
- Purvis, M. A., V. N. Shlyaptsev, R. Hollinger, C. Bargsten, A. Pukhov, A. Prieto, Y. Wang, B. M. Luther, L. Yin, S. Wang, and J. J. Rocca, *Nature Phys.* **7**, 796-800 (2013).
- Qiao, B., S. Kar, M. Geissler, P. Gibbon, M. Zepf, and M. Borghesi, *Phys. Rev. Lett.* **108**, 115002 (2012).
- Quesnel, B., and P. Mora, *Phys. Rev. E* **58**, 3719 (1998).
- Quigg, C., *Astr. Phys. J.* **151**, 1187 (1968).
- Ravasio, A., M. Koenig, S. Le Pape, A. Benuzzi-Mounaix, H. S. Park, C. Cecchetti, P. Patel, A. Schiavi, N. Ozaki, A. Mackinnon, B. Loupias, D. Batani, T. Boehly, M. Borghesi, R. Dezulian, E. Henry, M. Notley, S. Bandyopadhyay, R. Clarke, and T. Vinci, *Phys. Plasmas* **15** (6), 060701 (2008).
- Reiss, H. R., *Journal of Mathematical Physics* **3** (1), 59 (1962).
- Ribeyre, X., E. d'Humières, O. Jansen, S. Jequier, V. T. Tikhonchuk, and M. Lobet, *Phys. Rev. E* **93**, 013201 (2016).
- Ridgers, C. P., T. G. Blackburn, D. Del Sorbo, L. E. Bradley, C. Slade-Lowther, C. D. Baird, S. P. D. Mangles, P. McKenna, M. Marklund, C. D. Murphy, and A. G. R. Thomas, *J. Plasma Phys.* **83** (5), 715830502 (2017).
- Ridgers, C. P., C. S. Brady, R. Duclous, J. G. Kirk, K. Bennett, T. D. Arber, A. P. L. Robinson, and A. R. Bell, *Phys. Rev. Lett.* **108**, 165006 (2012).
- Ritus, V. I., *Journal of Soviet Laser Research* **6** (5), 497 (1985).

- Robinson, A. P. L., A. V. Arefiev, and V. N. Khudik, Phys. Plasmas **22** (8), 083114 (2015).
- Robinson, A. P. L., P. Gibbon, M. Zepf, S. Kar, R. G. Evans, and C. Bellei, Plasma Phys. Control. Fus. **51** (2), 024004 (2009).
- Robinson, A. P. L., M. Zepf, S. Kar, R. G. Evans, and C. Bellei, New Journal of Physics **10** (1), 013021 (2008).
- Robson, L., P. T. Simpson, R. J. Clarke, K. W. D. Ledingham, F. Lindau, O. Lundh, T. McCanny, P. Mora, D. Neely, C.-G. Wahlström, M. Zepf, and P. McKenna, Nature Phys. **3**, 58 (2007).
- Roth, M., D. Jung, K. Falk, N. Guler, O. Deppert, M. Devlin, A. Favalli, J. Fernandez, D. Gautier, M. Geissel, R. Haight, C. E. Hamilton, B. M. Hegelich, R. P. Johnson, F. Merrill, G. Schaumann, K. Schoenberg, M. Schollmeier, T. Shimada, T. Taddeucci, J. L. Tybo, F. Wagner, S. A. Wender, C. H. Wilde, and G. A. Wurden, Phys. Rev. Lett. **110**, 044802 (2013).
- Royle, R., Y. Sentoku, R. C. Mancini, I. Paraschiv, and T. Johzaki, Phys. Rev. E **95**, 063203 (2017).
- Rozsnyai, B. F., J. Quant. Spec. Radiat. Transf. **22**, 337 (1979).
- Samsonova, Z., S. Höfer, A. Hoffmann, B. Landgraf, M. Zürch, I. Uschmann, D. Khaghani, O. Rosmey, P. Neumayer, R. Röder, L. Trefflich, C. Ronning, E. Förster, C. Spielmann, and D. Kartashov, AIP Conference Proceedings **1811** (1), 180001 (2017).
- Santala, M. I. K., M. Zepf, I. Watts, F. N. Beg, E. Clark, M. Tatarakis, K. Krushelnick, A. E. Dangor, T. McCanny, I. Spencer, R. P. Singhal, K. W. D. Ledingham, S. C. Wilks, A. C. Machacek, J. S. Wark, R. Allott, R. J. Clarke, and P. A. Norreys, Phys. Rev. Lett. **84**, 1459 (2000).
- Sanz, J., A. Debayle, and K. Mima, Phys. Rev. E **85**, 046411 (2012).
- Sarri, G., D. J. Corvan, W. Schumaker, J. M. Cole, A. Di Piazza, H. Ahmed, C. Harvey, C. H. Keitel, K. Krushelnick, S. P. D. Mangles, Z. Najmudin, D. Symes, A. G. R. Thomas, M. Yeung, Z. Zhao, and M. Zepf, Phys. Rev. Lett. **113**, 224801 (2014).
- Sarri, G., K. Poder, J. Cole, W. Schumaker, A. Di Piazza, B. Reville, D. Doria, B. Dromey, L. Gizzi, A. Green, G. Grittani, S. Kar, C. H. Keitel, K. Krushelnick, S. Kushel, S. Mangles, Z. Najmudin, A. G. R. Thomas, M. Vargas, and M. Zepf, Nature Comm. **6** (2015).
- Sarri, G., W. Schumaker, A. Di Piazza, M. Vargas, B. Dromey, M. E. Dieckmann, V. Chvykov, A. Maksimchuk, V. Yanovsky, Z. H. He, B. X. Hou, J. A. Nees, A. G. R. Thomas, C. H. Keitel, M. Zepf, and K. Krushelnick, Phys. Rev. Lett. **110** (25), 255002 (2013).
- Schlegel, T., N. Naumova, V. T. Tikhonchuk, C. Labaune, I. V. Sokolov, and G. Mourou, Phys. Plasmas **16** (8), 083103 (2009).
- Schnürer, M., M. P. Kalashnikov, P. V. Nickles, T. Schlegel, W. Sandner, N. Demchenko, R. Nolte, and P. Ambrosi, Phys. Plasmas **2** (8), 3106 (1995).
- Schwinger, J., Phys. Rev. **82**, 664 (1951).

BIBLIOGRAPHY

- Schwoerer, H., F. Ewald, R. Sauerbrey, J. Galy, J. Magill, V. Rondinella, R. Schenkel, and T. Butz, *Europhys. Lett.* **61**, 47 (2003).
- Sefkow, A. B., G. R. Bennett, M. Geissel, M. Schollmeier, B. C. Franke, and B. W. Atherton, *Physical Review Letters* **106** (23), 235002 (2011).
- Seltzer, S. M., and M. J. Berger, *At. Data Nucl. Data Tables* **35** (3), 345 (1986).
- Sentoku, Y., and A. Kemp, *J. Comput. Phys.* **227** (14), 6846 (2008).
- Sentoku, Y., I. Paraschiv, R. Royle, R. C. Mancini, and T. Johzaki, *Phys. Rev. E* **90**, 051102 (2014).
- Serebryakov, D. A., and E. N. Nerush, *Quantum Electron.* **46** (4), 299 (2016).
- Serebryakov, D. A., E. N. Nerush, and I. Y. Kostyukov, *Phys. Plasmas* **22** (12), 123119 (2015).
- Sheng, Z.-M., K. Mima, Y. Sentoku, M. S. Jovanović, T. Taguchi, J. Zhang, and J. Meyerter Vehn, *Phys. Rev. Lett.* **88**, 055004 (2002).
- Sheng, Z.-M., S.-M. Weng, L.-L. Yu, W.-M. Wang, Y.-Q. Cui, M. Chen, and J. Zhang, *Chinese Physics B* **24** (1), 015201 (2015).
- Siminos, E., M. Grech, S. Skupin, T. Schlegel, and V. T. Tikhonchuk, *Phys. Rev. E* **86**, 056404 (2012).
- Siminos, E., M. Grech, B. S. Wettervik, and T. Fülöp, *New J. Physics* **19** (12), 123042 (2017).
- Simmons, J. F. L., and C. R. McInnes, *Am. J. Phys.* **61** (3), 205 (1993).
- Sokolov, I. V., N. M. Naumova, J. A. Nees, G. A. Mourou, and V. P. Yanovsky, *Phys. Plasmas* **16** (9), 093115 (2009).
- Sorokovikova, A., A. V. Arefiev, C. McGuffey, B. Qiao, A. P. L. Robinson, M. S. Wei, H. S. McLean, and F. N. Beg, *Phys. Rev. Letters* **116** (15), 155001 (2016).
- Spohn, H., *Europhys. Lett.* **50** (3), 287 (2000).
- Stark, D. J., T. Toncian, and A. V. Arefiev, *Phys. Rev. Lett.* **116**, 185003 (2016).
- Stark, D. J., L. Yin, B. J. Albright, and F. Guo, *Physics of Plasmas* **24** (5), 053103 (2017).
- Stephens, R. B., R. A. Snavely, Y. Aglitskiy, F. Amiranoff, C. Andersen, D. Batani, S. D. Baton, T. Cowan, R. R. Freeman, T. Hall, S. P. Hatchett, J. M. Hill, M. H. Key, J. A. King, J. A. Koch, M. Koenig, A. J. MacKinnon, K. L. Lancaster, E. Martinolli, P. Norreys, E. Perelli-Cippo, M. Rabec Le Gloahec, C. Rousseaux, J. J. Santos, and F. Scianitti, *Phys. Rev. E* **69** (6), 066414 (2004).
- Strickland, D., and G. Mourou, *Optics Communications* **55**, 447 (1985).
- Sudan, R. N., *Phys. Rev. Lett.* **70**, 3075 (1993).
- Sung, J. H., H. W. Lee, J. Y. Yoo, J. W. Yoon, C. W. Lee, J. M. Yang, Y. J. Son, Y. H. Jang, S. K. Lee, and C. H. Nam, *Opt. Lett.* **42** (11), 2058 (2017).

- Tabak, M., J. Hammer, M. E. Glinsky, W. L. Kruer, S. C. Wilks, J. Woodworth, E. M. Campbell, M. D. Perry, and R. J. Mason, Physics of Plasmas **1** (5), 1626 (1994).
- Tajima, T., and J. M. Dawson, Phys. Rev. Lett. **43**, 267 (1979).
- Takizuka, T., and H. Abe, J. Comput. Phys. **25** (3), 205 (1977).
- Tamburini, M., T. V. Liseykina, F. Pegoraro, and A. Macchi, Phys. Rev. E **85**, 016407 (2012).
- Tamburini, M., F. Pegoraro, A. Di Piazza, C. H. Keitel, and A. Macchi, New J. Phys. **12** (12), 123005 (2010).
- Teychenné, D., G. Bonnaud, and J.-L. Bobin, Phys. Rev. E **48**, R3248 (1993).
- Thaury, C., E. Guillaume, A. Lifschitz, K. Ta Phuoc, M. Hansson, G. Grittani, J. Gautier, J.-P. Goddet, A. Tafzi, O. Lundh, and V. Malka, Sci. Rep. **5**, 16310 (2015).
- The Nobel Prize in Physics,, NobelPrize.org Nobel Media AB 2018 (2018), Thu. 8 Nov 2018.
- Thévenet, M., A. Leblanc, H. Kahaly, H. Vincenti, A. Vernier, F. Quéré, and J. Faure, Nature Phys. **12**, 355-360 (2015).
- Tian, Y., J. Liu, W. Wang, C. Wang, X. Lu, Y. Leng, X. Liang, R. Li, and Z. Xu, Plasma Phys. Control. Fusion **56** (7), 075021 (2014).
- Tsai, Y. S., Rev. Mod. Phys. **46**, 815 (1974).
- Vaughan, D. (1986), *X-ray data booklet, revision*, Tech. Rep.
- Villasenor, J., and O. Buneman, Computer Physics Communications **69** (2), 306 (1992).
- Vodopiyanova, I. B., J. R. Dwyer, E. S. Cramer, R. J. Lucia, and H. K. Rassoul, J. Geophys. Res. **120**, 800 (2015).
- Vranic, M., T. Grismayer, J. Martins, R. Fonseca, and L. Silva, Comp. Phys. Comm. **191**, 65 (2015).
- Vranic, M., J. Martins, R. Fonseca, and L. Silva, Computer Physics Communications **204**, 141 (2016).
- Vranic, M., J. L. Martins, J. Vieira, R. A. Fonseca, and L. O. Silva, Phys. Rev. Lett. **113**, 134801 (2014).
- Vshivkov, V. A., N. M. Naumova, F. Pegoraro, and S. V. Bulanov, Physics of Plasmas **5** (7), 2727 (1998).
- Vyskočil, J., O. Klímo, and S. Weber, Plasma Phys. Control. Fusion **60** (5), 054013 (2018).
- Wallin, E., A. Gonoskov, and M. Marklund, Phys. Plasmas **22** (3), 033117 (2015).
- Wan, F., C. Lv, M. Jia, H. Sang, and B. Xie, The European Physical Journal D **71** (9), 236 (2017).

BIBLIOGRAPHY

- Wan, Y., C.-H. Pai, C. J. Zhang, F. Li, Y. P. Wu, J. F. Hua, W. Lu, Y. Q. Gu, L. O. Silva, C. Joshi, and W. B. Mori, Phys. Rev. Lett. **117**, 234801 (2016).
- Wang, H. Y., B. Liu, X. Q. Yan, and M. Zepf, Phys. Plasmas **22** (3), 033102 (2015a).
- Wang, H. Y., X. Q. Yan, and M. Zepf, Phys. Plasmas **22** (9), 093103 (2015b).
- Wang, W.-M., Z.-M. Sheng, P. Gibbon, L.-M. Chen, Y.-T. Li, and J. Zhang, Proc. Nat. Acad. Sci. **115** (40), 9911 (2018).
- Wang, X. L., Z. Y. Xu, W. Luo, H. Y. Lu, Z. C. Zhu, and X. Q. Yan, Physics of Plasmas **24** (9), 093105 (2017).
- Ward, R., and N. J. Sircombe, Tech. Rep. (2014).
- Waxer, L., D. Maywar, J. Kelly, T. Kessler, B. Kruschwitz, S. Loucks, R. McCrory, D. Meyerhofer, S. Morse, C. Stoeckl, and J. Zuegel, Opt. Photon. News **16** (7), 30 (2005).
- Weng, S. M., P. Mulser, and Z. M. Sheng, Phys. Plasmas **19** (2), 022705 (2012a).
- Weng, S. M., M. Murakami, P. Mulser, and Z. M. Sheng, New J. Phys. **14** (6), 063026 (2012b).
- Westover, B., A. MacPhee, C. Chen, D. Hey, T. Ma, B. Maddox, H.-S. Park, B. Remington, and F. N. Beg, Phys. Plasmas **17** (8), 082703 (2010).
- Wilks, S. C., W. L. Kruer, M. Tabak, and A. B. Langdon, Phys. Rev. Lett. **69**, 1383 (1992).
- Wilks, S. C., A. B. Langdon, T. E. Cowan, M. Roth, M. Singh, S. Hatchett, M. H. Key, D. Pennington, A. MacKinnon, and R. A. Snavely, Phys. Plasmas **8** (2), 542 (2001).
- Williams, G. J., D. Barnak, G. Fiksel, A. Hazi, S. Kerr, C. Krauland, A. Link, M. J.-E. Manuel, S. R. Nagel, J. Park, J. Peebles, B. B. Pollock, F. N. Beg, R. Betti, and H. Chen, Phys. Plasmas **23** (12), 123109 (2016).
- Xu, T., B. Shen, J. Xu, S. Li, Y. Yu, J. Li, X. Lu, C. Wang, X. Wang, X. Liang, Y. Leng, R. Li, and Z. Xu, Phys. Plasmas **23** (3), 033109 (2016).
- Yabe, T., T. Ishikawa, P. Wang, T. Aoki, Y. Kadota, and F. Ikeda, Computer Physics Communications **66** (2), 233 (1991).
- Yan, W., C. Fruhling, G. Golovin, D. Haden, J. Luo, P. Zhang, B. Zhao, J. Zhang, C. Liu, M. Chen, S. Chen, S. Banerjee, and D. Umstadter, Nature Photon. **11**, 514-520 (2017).
- Yan, X. Q., C. Lin, Z. M. Sheng, Z. Y. Guo, B. C. Liu, Y. R. Lu, J. X. Fang, and J. E. Chen, Phys. Rev. Lett. **100**, 135003 (2008).
- Yasuike, K., M. H. Key, S. P. Hatchett, R. A. Snavely, and K. B. Wharton, Rev. Sci. Instrum. **72**, 1236 (2001).
- Yee, K., IEEE Transactions on Antennas and Propagation **14** (3), 302 (1966).
- Yi, L., A. Pukhov, P. Luu-Thanh, and B. Shen, Phys. Rev. Lett. **116**, 115001 (2016).
- Yin, L., B. J. Albright, B. M. Hegelich, and J. C. Fernandez, Laser & Part. Beams **24** (2), 291 (2006).

- Yu, C., R. Qi, W. Wang, J. Liu, W. Li, C. Wang, Z. Zhang, J. Liu, Z. Qin, M. Fang, K. Feng, Y. Wu, Y. Tian, Y. Xu, F. Wu, Y. Leng, X. Weng, J. Wang, F. Wei, Y. Yi, Z. Song, R. Li, and Z. Xu, *Sci. Reports* **6**, 29518 (2016).
- Yu, J., H. Lu, T. Takahashi, R. Hu, Z. Gong, W. Ma, Y. Huang, and X. Yan, ArXiv e-prints , [arXiv:1805.04707](https://arxiv.org/abs/1805.04707) (2018).
- Yu, W., M. Y. Yu, Z. M. Sheng, and J. Zhang, *Phys. Rev. E* **58**, 2456 (1998).
- Zagorodnov, I., R. Schuhmann, and T. Weiland, *Journal of Computational Physics* **191** (2), 525 (2003).
- Zeitler, E., and H. Olsen, *Phys. Rev.* **136**, A1546 (1964).
- Zeng, X., K. Zhou, Y. Zuo, Q. Zhu, J. Su, X. Wang, X. Wang, X. Huang, X. Jiang, D. Jiang, Y. Guo, N. Xie, S. Zhou, Z. Wu, J. Mu, H. Peng, and F. Jing, *Opt. Lett.* **42** (10), 2014 (2017).
- Zhang, P., C. P. Ridgers, and A. G. R. Thomas, *New Journal of Physics* **17** (4), 043051 (2015).
- Zhao, Z., L. Cao, L. Cao, J. Wang, W. Huang, W. Jiang, Y. He, Y. Wu, B. Zhu, K. Dong, Y. Ding, B. Zhang, Y. Gu, M. Y. Yu, and X. T. He, *Phys. Plasmas* **17** (12), 123108 (2010).
- Zhidkov, A., J. Koga, A. Sasaki, and M. Uesaka, *Phys. Rev. Lett.* **88**, 185002 (2002).
- Zhu, X.-L., Y. Yin, T.-P. Yu, F.-Q. Shao, Z.-Y. Ge, W.-Q. Wang, and J.-J. Liu, *New J. Phys.* **17** (5), 053039 (2015).
- Zhu, X.-L., T.-P. Yu, Z.-M. Sheng, Y. Yin, I. C. E. Turcu, and A. Pukhov, *Nature Comm.* **7**, 13686 (2016).
- Zulick, C., B. Hou, F. Dollar, A. Maksimchuk, J. Nees, A. G. R. Thomas, Z. Zhao, and K. Krushelnick, *New J. Phys.* **15** (12), 123038 (2013).

Résumé : Effets radiatifs et d'électrodynamique quantique dans l'interaction laser-matière relativiste

Les futures installations laser multi-pétawatts, tel le projet Apollon (France) permettront d'atteindre des intensités sur cible dépassant 10^{22} W/cm^2 . Dans de telles conditions, l'interaction laser-matière met en jeu des processus plasmas ultra-relativistes couplés à des mécanismes radiatifs et d'électrodynamique quantique (QED). La plupart des études théoriques sur ce sujet ont porté sur l'émission synchrotron et la production de paires électron-positron par le processus de Breit-Wheeler, tous deux induits par un champ laser intense et censés dominer l'interaction à des intensités $> 10^{22} \text{ W/cm}^2$. À de plus faibles intensités ($\lesssim 10^{21} \text{ W/cm}^2$), l'émission de photons et la création de paires procèdent essentiellement du Bremsstrahlung et des processus de Bethe-Heitler/Trident, tous déclenchés sous l'action du champ Coulombien atomique. Cette thèse vise précisément à étudier ces processus à l'aide du code particle-in-cell (PIC) CALDER conçu au CEA/DAM.

Notre première étude permet d'étendre les capacités de simulation du code PIC CALDER à l'ensemble des mécanismes mentionnés ci-dessus. Nous nous intéressons ensuite à la compétition entre le Bremsstrahlung et l'émission synchrotron dans des feuilles de cuivre irradiées par un laser femtoseconde d'intensité 10^{22} W/cm^2 . Finalement, nous explorons le potentiel de cibles composées de nano-fils pour augmenter le rayonnement synchrotron.

Mots-clés : interaction laser-matière, plasma, électrodynamique quantique, Particle-In-Cell, Compton, Breit-Wheeler, Bremsstrahlung, Bethe-Heitler, nano-fils, Apollon.

Abstract: Radiative and quantum electrodynamic effects in relativistic laser-matter interaction

Forthcoming multi-petawatt laser systems, such as the French Apollon, are expected to deliver on-target laser intensities exceeding 10^{22} W/cm^2 . A novel regime of laser-matter interaction will ensue, where ultra-relativistic plasma effects are coupled with copious generation of high-energy photons and electron-positron pairs. In recent years, most theoretical studies performed in this field have focused on the impact of synchrotron photon emission and Breit-Wheeler pair generation, both directly induced by an intense laser field and believed to be dominant at intensities $> 10^{22} \text{ W/cm}^2$. At the lower intensities ($\lesssim 10^{21} \text{ W/cm}^2$) currently attainable, by contrast, photon and pair production mainly originate from, respectively, Bremsstrahlung and Bethe-Heitler/Trident processes, all triggered by atomic Coulomb fields. The purpose of this PhD is precisely to study those processes using the particle-in-cell CALDER code developed at CEA/DAM.

Our first study extends the simulation capabilities of CALDER to the whole range of photon and positron generation mechanisms aforementioned. We then address the competition between Bremsstrahlung and synchrotron emission from copper foils irradiated at 10^{22} W/cm^2 . Finally, we investigate the potential of nanowire-array targets to enhance the synchrotron yield of a 10^{22} W/cm^2 femtosecond laser pulse.

keywords: laser-matter interaction, plasma, quantum electrodynamics, Particle-In-Cell, Compton, Breit-Wheeler, Bremsstrahlung, Bethe-Heitler, nanowires, Apollon.